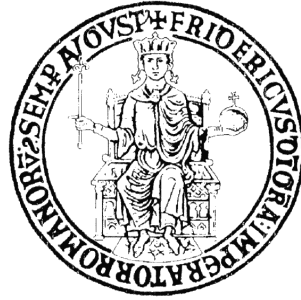


UNIVERSITY OF NAPLES FEDERICO II



Department of Structures for Engineering and Architecture

Ph.D. Program in Structural, Geotechnical and Seismic Engineering, XXIX Cycle

Ph.D. Program Coordinator: Prof. Luciano Rosati

Ph.D. Thesis

Mathematical Models and Numerical Methods for the Simulation of the Earthquake Response of Seismically Base-Isolated Structures

Advisor: Prof. Giorgio Serino

Ph.D. Student: Nicolò Vaiana

Co-advisor: Prof. Filip C. Filippou

March 2017

Dedicated to Professor Luciano Rosati and Professor Fabrizio Greco with gratitude for supporting me in completing my Ph.D. Program

“Earthquakes systematically bring out the mistakes made in design and construction - even the most minute mistakes; it is this aspect of Earthquake Engineering that makes it challenging and fascinating, and gives it an educational value far beyond its immediate objectives.”

Newmark and Rosenblueth

Acknowledgments

Gratitude, appreciation, giving thanks; it does not matter what words we use, they all mean the same thing: happiness. We are supposed to be happy and grateful for family, friends and those people who help us build our life. We have to be happy for experiences we live, whether we like them or not.

Finding gratitude and appreciation is the key to resilience. People who list things they are grateful for are happier and healthier.

Today is a day of celebration: a day to celebrate all the hard work that got me to this moment. Today is a day of thanks: a day to thank those who helped me get here, nurtured me, taught me and cheered me on. Today is a day of reflection because today marks the end of one era of my life and the beginning of something new.

First of all, my deepest gratitude goes to Professor *Luciano Rosati* and Professor *Fabrizio Greco* for supporting me when I was about to give up on my doctoral studies, for their dedication and passion, and for allowing me to understand that if we are not willing to keep looking for light in the darkest of places without stopping, even when it seems impossible, we will never succeed.

My sincere gratitude and appreciation also go to those people who made my Ph.D. course such an exciting and challenging journey around the world:

- Professor *Giorgio Serino*, for giving me the possibility to continue my postgraduate studies at the University of Naples Federico II, first as master student in Emerging Technologies for Construction, then as Ph.D. student in Structural, Geotechnical and Seismic Engineering. It has been such a great privilege teaching lectures for his undergraduate course of *Tecnica delle Costruzioni 2* and for his graduate course of *Earthquake Engineering and Structural Control*. Teaching allowed me to improve my skills, to become more self-confident and to share passion and knowledge with students. I learnt that teaching is a mission because it requires patience, perseverance and dedication. I am also grateful for the possibility he gave me to spend one academic year at the University of California at Berkeley and to present my research work in several international conferences in Europe.

- Professor *Filip C. Filippou*, my advisor during my research period at the University of California at Berkeley, for giving me the possibility to work on the simulation of the seismic response of base-isolated structures under his guidance. It has been a privilege to be in Berkeley, the place which has produced so many Nobel Prize winners, Turing Award winners, astronauts, members of Congress, Olympic gold medalists. The high level of concentration I had during my stay there allowed me to develop the main core of my Ph.D. thesis. I really miss watching the red sunset and the Golden Gate Bridge from my room in the International House and I miss the indescribable quiet and smell of the campus too. I am very grateful for his advice, lectures and for the time shared together during the lunches, coffee breaks and dinners he has kindly offered me.
- Professor *Luciano Nunziante*, my mentor during my first period at the Department of Structures for Engineering and Architecture of the University of Naples Federico II and my advisor during the second level master course in Emerging Technologies for Construction. I cannot find the right words to thank him for trusting in my skills, for the huge amount of time spent together in his office talking about stuff such as “the cause of the World Trade Center Tower collapse”, for his lectures, for the books he gave me as a present, for the possibility to teach lectures for his graduate course of Limit Analysis of Structures. It has been such a great privilege meeting him and learning from him.
- Professor *Anil K. Chopra*, for allowing me to attend his graduate course of Dynamics of Structures at the University of California at Berkeley.
- Engineer *Mariacristina Spizzuoco*, for her extraordinary effort and perseverance which allowed me to perform the experimental tests on Wire Rope Isolators. I am thankful for all the time spent working and conducting research together.
- Engineer *Francesco Marmo*, the best researcher I have ever met, for his challenging and interesting lectures of the FEM in Nonlinear Structural Analysis course. I am very grateful for his teachings because it could be practically impossible to develop the main core of my research work without them.
- Engineer *Salvatore Sessa*, for teaching me how to use OpenSees. I thank him for his advice and for the precious time he has spent for helping me.
- Professor *Paolo Lonetti*, for allowing me to teach several lectures on Seismic Isolation of Structures and Numerical Time Integration Methods for his graduate course of

Theory of Structures at the University of Calabria. I have really appreciated his great availability and kindness.

- Professors *Massimiliano Fraldi* and *Antonio Gesualdo*, for their precious and useful advice, patience and availability.
- Professor *Stefano Pagano* and Engineer *Salvatore Strano*, for their technical support during the experimental tests on Wire Rope Isolators carried out at the Department of Industrial Engineering of the University of Naples Federico II.
- Engineers *Mauro Fontana* and *Antonio Lagreca*, for helping me improve my skills during the internship at Powerflex S.r.l. (Limatola, Italy) and for providing and manufacturing the Wire Rope Isolators I needed for the experimental campaign.
- My friend *Marcello Maiorana*, for all the time spent together in San Francisco. Thank you so much for your hospitality, for helping me during my first weeks in the US. I will never forget the “homemade pizza” dinner we organized together with your friends, our cups of coffee in Contraband or in Blue Bottle, our very long walks from Pier 39 to the Golden Gate Bridge, the hundreds of pictures we took to the Pyramid Building, the Christmas time spent together in SF.
- My friend *Paolo Di Re*, for sharing the experience at the University of California at Berkeley with me. Thank you for the time spent together talking and walking around the campus, thinking about the future, looking for a way to survive. My dear, finally, we did! You allowed me to understand that it is the hard days, the times that challenge us to our very core, that will determine who we are. We will be defined not just by what we achieve, but by how we survive.
- My dear friends *Houman Hadad* and *Lukas Zett*, for all the time spent together in Naples. I am waiting for you here: my home is yours.
- My colleagues *Daniele Losanno*, *Iolanda Nuzzo*, *Cristoforo Demartino*, *Ingrid Madera* and *Akiko Suzuki*, for the time spent together at the Department of Structures for Engineering and Architecture of the University of Naples Federico II during our coffee breaks and lunches.
- My colleagues *Miquel Crusells-Girona*, *Than Do*, *Agustin Bertero* and *Magda Ntetsika*, for the time spent together in Berkeley during and after the weekly meetings with Professor *Filip C. Filippou*.
- My colleague *Arnkjell Løkke*, for the time spent together at the Department of Civil and Environmental Engineering of UC Berkeley.

- My friends *Adam Bodor, Daniela Sgambato, Chiara Rossi, Iris Caro, Nicola Giordano, Daniel Privitera, Kohei Kawabata, Nick Aguilera, Xavier Muntaner Sitges, Tobias Schuler, Simon Arch, Sophie von Pfaff, Scott Templin, Risa Hosoi, Fiona Russell, Paul Levasseur, Mathias Schmid, Mike Rosenblum, Catalina Moncada* and *Jan Kreibich*. You made my experience in Berkeley unforgettable.
- My friend *Ida Mascolo*, the best Structural Engineer I have ever met. Thank you for your precious advice and for the words you spent to support me when I was tired, nervous and frustrated.
- My friends *Pino Ieno* and *Alex Coppola*, for your hospitality in Rome and for supporting me to go on despite of the numerous obstacles.
- My friend *Fabrizio Mezza*, for supporting me during my stay in the US.
- My friends *Fabio Ragosta, Valerio Simonetti, Alessandro Zappia* and *Stefano Carrella*, for helping me find the peacefulness I needed to write my Ph.D. thesis during the last four months.
- Some of the best students I met in the last three years as teaching assistant: *Paolo De Lima Souza, Giuseppe Sellitto, Federico Di Carlo, Angelo Coppola, Alessandro De Fusco, Giuseppe L. Gargiulo, Luigi D'Esposito, Giuseppe Romano, Claudio Castiello, Marco Petrillo, Ciro Gallo, Marco Longobardo, Carlo Locascio* and *Salvatore Fioriniello*. I saw in you the same amount of passion I put in teaching. My best wishes for your careers.
- My father *Giorgio*, my mother *Maria*, my brother *Matteo*, my grandmother *Rosa*, and all the relative who really trust in me. If I am who I am is because of you and your sacrifices. There are no words I can find to thank you for what you did and what you are doing for helping me build my life and career, despite of the hard battles we have to fight every day.

Before greeting you all, I would like to remember you what *Benjamin Franklin* said a couple of hundred years ago: “*Never leave that till tomorrow which you can do today*”. What did he mean? He meant that knowing is better than wondering, waking is better than sleeping, and even the biggest failure, even the worst most intractable mistake beats the hell out of never trying.

Napoli, March 31, 2017

Nicolò Vaiana

Table of Contents

Acknowledgments	III
Table of Contents	VII
List of Figures	XI
List of Tables	XX
Chapter 1 Introduction	1
1.1 Mathematical Models	3
1.2 Numerical Method	4
1.3 Outline of the Dissertation	5
Chapter 2 Modeling of Base-Isolated Structures	7
2.1 Introduction	7
2.2 Modeling of the Superstructure	8
2.3 Modeling of the Base Isolation System	11
2.4 Dynamic Equilibrium Equations	13
Chapter 3 Seismic Isolation Bearings	15
3.1 Introduction	15
3.2 Elastomeric Bearings	16
3.2.1 Introduction	16
3.2.2 Low Damping Rubber Bearings	19
3.2.3 High Damping Rubber Bearings	20
3.2.4 Lead Rubber Bearings	23
3.2.5 Unbonded Elastomeric Bearings with Deformable Reinforcing Layers	25
3.2.5.1 Recycled Rubber-Fiber Reinforced Bearings	26
3.2.5.1.1 Introduction	26
3.2.5.1.2 Description of Tested Device	27
3.2.5.1.3 Experimental Tests Results	27
3.3 Sliding Bearings	29
3.3.1 Introduction	29
3.3.2 Flat Surface Sliding Bearings	29
3.3.3 Curved Surface Sliding Bearings	32

Table of Contents

3.4	Metal Devices	34
3.4.1	Wire Rope Isolators	34
3.4.1.1	Introduction	34
3.4.1.2	Description of Tested Devices	35
3.4.1.3	Experimental Study	37
3.4.1.3.1	Experimental Set-up	38
3.4.1.3.2	Dynamic Tests	40
3.4.1.3.3	Static Tests	40
3.4.1.4	Experimental Tests Results	41
3.4.1.4.1	Influence of Displacement Amplitude	42
3.4.1.4.2	Influence of Frequency	48
3.4.1.4.3	Influence of Vertical Load	50
3.4.1.4.4	Influence of WRI Geometrical Characteristics	56
3.4.1.4.5	Influence of Wire Rope Diameter	58
3.4.1.4.6	Comparison between Roll and Shear Dynamic Responses	60
3.4.1.4.7	Static Behavior	60
Chapter 4	Mathematical Modeling of Seismic Isolators	63
4.1	Introduction	63
4.2	Differential Equation Models	64
4.2.1	Uniaxial Models	64
4.2.1.1	Bouc-Wen Model	64
4.2.1.2	Modified Bouc-Wen Model	77
4.2.2	Biaxial Models	79
4.2.2.1	2d Bouc-Wen Model	79
4.3	Proposed Mathematical Models	82
4.3.1	Uniaxial Models	82
4.3.1.1	Nonlinear Exponential Model	82
4.3.1.2	Advanced Nonlinear Exponential Model	87
4.3.1.3	Parallel Model	92
4.3.1.3.1	Parallel Modeling of Inelastic Material Behavior	92
4.3.1.3.2	Application of Parallel Modeling to Seismic Isolators	95
4.3.1.4	Advanced Parallel Model	102
4.3.2	Biaxial Model	108
4.3.2.1	2d Parallel Model	108
4.3.2.1.1	Parallel Modeling of Inelastic Material Behavior	108
4.3.2.1.2	Application of Parallel Modeling to Seismic Isolators	111

Table of Contents

4.4	Comparisons between DEMs and Proposed Mathematical Models	114
4.4.1	Comparison between BWM and NEM	114
4.4.2	Comparison between BWM and PM	117
4.4.3	Comparison between MBWM and ANEM	124
4.4.4	Comparison between MBWM and APM	126
Chapter 5	 Verification of the Proposed Models	131
5.1	Introduction	131
5.2	Simulation of Experimental Response of WRIs	131
5.2.1	Advanced Nonlinear Exponential Model	131
5.2.1.1	WRI PWHS 16010	132
5.2.1.2	WRI PWHS 16040	137
5.2.1.3	WRI PWHS 16040 S	140
5.2.1.4	WRI PWHS 16060	143
5.2.1.5	Comparison with the MBWM	146
5.2.1.6	Limitation of the Proposed ANEM	148
5.2.2	Advanced Parallel Model	150
5.2.2.1	WRI PWHS 16010	150
5.2.2.2	WRI PWHS 16040	161
5.2.2.3	WRI PWHS 16040 S	164
5.2.2.4	WRI PWHS 16060	167
5.3	Simulation of Experimental Response of RR-FRB	170
5.3.1	Advanced Nonlinear Exponential Model	170
5.3.2	Advanced Parallel Model	179
Chapter 6	 Numerical Time Integration Methods	181
6.1	Introduction	181
6.2	Conventional Non-Partitioned Solution Approach	182
6.2.1	Introduction	182
6.2.2	Pseudo-Force Method	184
6.2.3	Solution Algorithm	186
6.3	Proposed Partitioned Solution Approach	188
6.3.1	Introduction	188
6.3.2	Proposed Mixed Explicit-Implicit Time Integration Method	190
6.3.2.1	Explicit Integration Substep	190
6.3.2.2	Implicit Integration Substep	192
6.3.3	Solution Algorithm	194

Table of Contents

6.4	Stability Aspects, Accuracy and Computational Efficiency of the MEIM	196
6.4.1	Introduction	196
6.4.2	Evaluation of the Critical Time Step	197
6.4.2.1	2d Base-Isolated Structures	197
6.4.2.2	3d Base-Isolated Structures	199
6.4.3	Numerical Applications	200
6.4.3.1	Analysis of Base-Isolated Structures with LRBS	200
6.4.3.1.1	Analyzed 3d Base-Isolated Structure A	200
6.4.3.1.2	Analyzed 3d Base-Isolated Structure B	203
6.4.3.1.3	Model Adopted for Lead Rubber Bearings	206
6.4.3.1.4	Numerical Results for Structure A	207
6.4.3.1.5	Numerical Results for Structure B	218
6.4.3.2	Analysis of Base-Isolated Structures with FPBS	229
6.4.3.2.1	Analyzed 3d Base-Isolated Structure A	229
6.4.3.2.2	Analyzed 3d Base-Isolated Structure B	230
6.4.3.2.3	Model Adopted for Friction Pendulum Bearings	231
6.4.3.2.4	Numerical Results for Structure A	232
6.4.3.2.5	Numerical Results for Structure B	242
Chapter 7	 Speeding Up Nonlinear Dynamic Analysis Using the MEIM and NEM	252
7.1	Introduction	252
7.2	Numerical Application	253
7.2.1	Analyzed 3d Base-Isolated Structure	253
7.2.2	Analytical Models Parameters	254
7.2.3	Dynamic Response of the 3d Base-Isolated Structure	255
Chapter 8	 Conclusions	266
8.1	Summary of the Dissertation	266
8.1.1	Mathematical Models	266
8.1.2	Numerical Method	267
8.1.3	Making the NLTHA almost as fast as a LTHA	269
8.2	Recommendations for Future Research	270
8.2.1	Mathematical Models	270
8.2.2	Numerical Method	270
References		271

List of Figures

Figure 2.1	3d discrete structural model of a two-story base-isolated structure	7
Figure 3.1	(a) Square and (b) circular elastomeric bearing	16
Figure 3.2	Behavior of elastomeric bearings in horizontal and vertical directions	17
Figure 3.3	(a) Dowelled and (b) bolted elastomeric bearing	18
Figure 3.4	Typical hysteresis loop displayed by LDRBs at relatively large displacements	19
Figure 3.5	Typical hysteresis loop displayed by HDRBs at (a) relatively large and (b) large displacements	21
Figure 3.6	Typical effect of scragging in a HDRB	22
Figure 3.7	(a) Square and (b) circular LRB	23
Figure 3.8	Typical hysteresis loop with bilinear characteristics displayed by LRBs at small and large displacements	24
Figure 3.9	Deformed configuration of (a) bonded steel reinforced elastomeric bearing and (b) unbonded elastomeric bearing with deformable reinforcing layers loaded in compression and shear	25
Figure 3.10	Tested RR-FRB	27
Figure 3.11	Loading directions	27
Figure 3.12	Experimental hysteresis loops of the tested RR-FRB obtained in (a) 0° and (b) 45° loading directions	28
Figure 3.13	FSSBs: (a) Pot and (b) Disk FSSB	29
Figure 3.14	Dependency of friction coefficient of PTFE-polished stainless steel interface on sliding velocity and normal load	30
Figure 3.15	Dependency of friction coefficient of PTFE-polished stainless steel interface on sliding velocity and temperature	31
Figure 3.16	Typical hysteresis loop with rigid-plastic characteristics displayed by FSSBs	31
Figure 3.17	CSSBs: (a) FPB and (b) DFPB	32
Figure 3.18	Typical hysteresis loop displayed by FPBs	33
Figure 3.19	(a) WRI; and (b) wire rope cross section	36
Figure 3.20	Schematic of WRIs PWHS 160: (a) lateral view; (b) section A-A'	37
Figure 3.21	TM adopted to perform experimental tests	38

List of Figures

Figure 3.22	WRI PWHS 16040 mounted in: (a) Roll and (b) Shear directions	39
Figure 3.23	Average dissipated energy in WRI PWHS 16040 along (a) Roll and (b) Shear directions	44
Figure 3.24	Experimental hysteresis loops of WRI PWHS 16040 obtained at small displacements in (a) Roll and (b) Shear directions	45
Figure 3.25	Experimental hysteresis loops of WRI PWHS 16040 obtained at relatively large displacements in (a) Roll and (b) Shear directions	46
Figure 3.26	Experimental hysteresis loops of WRI PWHS 16040 obtained at large displacements in (a) Roll and (b) Shear directions	47
Figure 3.27	Influence of frequency on WRI PWHS 16040 hysteresis loops obtained in (a) Roll and (b) Shear directions	49
Figure 3.28	Influence of vertical load on WRI PWHS 16040 hysteresis loops obtained at small displacements in (a) Roll and (b) Shear directions	52
Figure 3.29	Influence of vertical load on WRI PWHS 16040 hysteresis loops obtained at relatively large displacements in (a) Roll and (b) Shear directions	53
Figure 3.30	Influence of vertical load on WRI PWHS 16040 hysteresis loops obtained at large displacements in (a) Roll and (b) Shear directions	54
Figure 3.31	Influence of vertical load on WRI PWHS 16060 hysteresis loops obtained in Roll direction for (a) $A = 4$ cm and (b) $A = 8$ cm	55
Figure 3.32	Influence of WRI geometrical characteristics on hysteresis loops obtained in (a) Roll and (b) Shear directions	57
Figure 3.33	Influence of wire rope diameter on hysteresis loops obtained in Roll direction for: (a) $A = 3$ cm and (b) $A = 6$ cm	59
Figure 3.34	Force-displacement curves obtained for different vertical load values during static tests in Roll direction	61
Figure 3.35	WRI PWHS 16040 deformed shape displayed in Roll direction for $A = 6$ cm and $P_v = 0$ kN	62
Figure 4.1	Generic hysteresis loop obtained with the BWM	65
Figure 4.2	Influence of parameter n on the hysteresis loop shape in the BWM ($A = 1$, $\beta = \gamma = 0.5$)	67
Figure 4.3	Hysteresis loops obtained with the BWM for different values of pairs of parameters β and γ ($A = 1$, $n = 1$)	71
Figure 4.4	(a) Total nonlinear restoring force and its two components: (b) linear elastic force and (c) nonlinear hysteretic force	75
Figure 4.5	Total restoring force with (a) post-hardening and (b) post-softening characteristics at large displacements simulated by adopting the MBWM	78
Figure 4.6	Linear displacement path	79

List of Figures

Figure 4.7	Hysteretic behavior under linear path	80
Figure 4.8	Normalized hysteresis loop with (a) bilinear and (b) rigid-plastic characteristics	83
Figure 4.9	Tangent stiffness variation of the loading curve with (a) bilinear and (b) rigid-plastic characteristics	84
Figure 4.10	Normalized hysteresis loop with (a) post-hardening and (b) post-softening characteristics	87
Figure 4.11	Tangent stiffness variation of the loading curve with (a) post-hardening and (b) post-softening characteristics	88
Figure 4.12	Total restoring force components for hysteresis loop with (a) post-hardening and (b) post-softening characteristics	90
Figure 4.13	1d mechanical model	91
Figure 4.14	Parallel modeling of a 1d stress-strain curve for a work hardening material (two elements case)	94
Figure 4.15	Parallel modeling of a 1d stress-strain curve for a work hardening material (four elements case)	94
Figure 4.16	Plot of the tangent stiffness function $k_{t1}(u)$	95
Figure 4.17	Continuous and discretized tangent stiffness function $k_{t1}(u)$	96
Figure 4.18	Nonlinear hysteretic force $f_1(u)$ having bilinear characteristics simulated adopting (a) $N = 5$ and (b) $N = 50$	100
Figure 4.19	Nonlinear hysteretic force $f_1(u)$ having rigid-plastic characteristics simulated adopting (a) $N = 5$ and (b) $N = 50$	101
Figure 4.20	Plot of the tangent stiffness function $k_{t2}(u)$ obtained for $c_2 > 0$ and $c_3 > 0$	102
Figure 4.21	Continuous and discretized increasing tangent stiffness function $k_{t2}(u)$ obtained for $c_2 > 0$ and $c_3 > 0$	103
Figure 4.22	Total restoring force components for hysteresis loop with (a) post-hardening and (b) post-softening characteristics ($N = 5, M = 5$)	106
Figure 4.23	Total restoring force components for hysteresis loop with (a) post-hardening and (b) post-softening characteristics ($N = 50, M = 50$)	107
Figure 4.24	Symmetric softening hysteresis loop with bilinear characteristics simulated adopting the BWM and the proposed NEM	114
Figure 4.25	Symmetric softening hysteresis loop with bilinear characteristics and very high initial stiffness simulated adopting the BWM and the proposed NEM	115
Figure 4.26	Symmetric softening hysteresis loop with rigid-plastic characteristics simulated adopting the BWM and the proposed NEM	116
Figure 4.27	Symmetric softening hysteresis loop with bilinear characteristics simulated adopting the BWM and the proposed PM with $N = 50$	117

List of Figures

Figure 4.28	Symmetric softening hysteresis loop with bilinear characteristics simulated adopting the BWM and the proposed PM with (a) $N = 5$ and (b) $N = 100$	118
Figure 4.29	Symmetric softening hysteresis loop with bilinear characteristics and very high initial stiffness simulated adopting the BWM and the proposed PM with $N = 50$	119
Figure 4.30	Symmetric softening hysteresis loop with bilinear characteristics and very high initial stiffness simulated adopting the BWM and the proposed PM with (a) $N = 5$ and (b) $N = 100$	120
Figure 4.31	Symmetric softening hysteresis loop with rigid-plastic characteristics simulated adopting the BWM and the proposed PM with $N = 50$	121
Figure 4.32	Symmetric softening hysteresis loop with rigid-plastic characteristics simulated adopting the BWM and the proposed PM with (a) $N = 5$ and (b) $N = 100$	122
Figure 4.33	Symmetric hysteresis loop with post-hardening characteristics simulated adopting the MBWM and the proposed ANEM	124
Figure 4.34	Symmetric hysteresis loop with post-softening characteristics simulated adopting the MBWM and the proposed ANEM	125
Figure 4.35	Symmetric hysteresis loop with post-hardening characteristics simulated adopting the MBWM and the proposed APM with $N = 50$ and $M = 50$	126
Figure 4.36	Symmetric hysteresis loop with post-hardening characteristics simulated adopting the MBWM and the proposed APM with (a) $N = M = 5$ and (b) $N = M = 100$	127
Figure 4.37	Symmetric hysteresis loop with post-softening characteristics simulated adopting the MBWM and the proposed APM with $N = 50$ and $M = 50$	128
Figure 4.38	Symmetric hysteresis loop with post-softening characteristics simulated adopting the MBWM and the proposed APM with (a) $N = M = 5$ and (b) $N = M = 100$	129
Figure 5.1	Geometrical characteristics and principal horizontal directions of WRI PWHS 16010: (a) Roll and (b) Shear directions	132
Figure 5.2	Analytical and experimental hysteresis loops of WRI PWHS 16010 obtained for $A = 0.25$ cm, $f = 1$ Hz, and $P_v = 0$ kN in (a) Roll and (b) Shear directions	133
Figure 5.3	Analytical and experimental hysteresis loops of WRI PWHS 16010 obtained for $A = 0.5$ cm, $f = 1$ Hz, and $P_v = 0$ kN in (a) Roll and (b) Shear directions	134
Figure 5.4	Analytical and experimental hysteresis loops of WRI PWHS 16010 obtained for $A = 1$ cm, $f = 1$ Hz, and $P_v = 0$ kN in (a) Roll and (b) Shear directions	135
Figure 5.5	Analytical and experimental hysteresis loops of WRI PWHS 16010 obtained for $f = 1$ Hz and $P_v = 2$ kN in (a) Roll and (b) Shear directions	136
Figure 5.6	Geometrical characteristics and principal horizontal directions of WRI PWHS 16040: (a) Roll and (b) Shear directions	137
Figure 5.7	Analytical and experimental hysteresis loops of WRI PWHS 16040 obtained for $f = 1$ Hz and $P_v = 0$ kN in (a) Roll and (b) Shear directions	138

List of Figures

Figure 5.8	Analytical and experimental hysteresis loops of WRI PWHS 16040 obtained for $f = 1$ Hz and $P_v = 3$ kN in (a) Roll and (b) Shear directions	139
Figure 5.9	Geometrical characteristics and principal horizontal directions of WRI PWHS 16040 S: (a) Roll and (b) Shear directions	140
Figure 5.10	Analytical and experimental hysteresis loops of WRI PWHS 16040 S obtained for $f = 1$ Hz and $P_v = 0$ kN in (a) Roll and (b) Shear directions	141
Figure 5.11	Analytical and experimental hysteresis loops of WRI PWHS 16040 S obtained for $f = 1$ Hz and $P_v = 2$ kN in (a) Roll and (b) Shear directions	142
Figure 5.12	Geometrical characteristics and principal horizontal directions of WRI PWHS 16060: (a) Roll and (b) Shear directions	143
Figure 5.13	Analytical and experimental hysteresis loops of WRI PWHS 16060 obtained for $f = 1$ Hz and $P_v = 0$ kN in (a) Roll and (b) Shear directions	144
Figure 5.14	Analytical and experimental hysteresis loops of WRI PWHS 16060 obtained for $f = 1$ Hz and $P_v = 2$ kN in (a) Roll and (b) Shear directions	145
Figure 5.15	Comparisons of analytical and experimental hysteresis loops of WRI PWHS 16010: (a) ANEM and (b) MBWM	147
Figure 5.16	Comparisons of analytical and experimental hysteresis loops of WRI PWHS 16040 obtained at large displacements in (a) Roll and (b) Shear directions	149
Figure 5.17	Experimental and mathematical hysteresis loops of WRI PWHS 16010 obtained for $A = 0.25$ cm, $f = 1$ Hz, and $P_v = 0$ kN ($N = 50$, $M = 50$) in (a) Roll and (b) Shear directions	151
Figure 5.18	Experimental and mathematical hysteresis loops of WRI PWHS 16010 obtained for $A = 0.5$ cm, $f = 1$ Hz, and $P_v = 0$ kN ($N = 50$, $M = 50$) in (a) Roll and (b) Shear directions	152
Figure 5.19	Experimental and mathematical hysteresis loops of WRI PWHS 16010 obtained for $A = 1$ cm, $f = 1$ Hz, and $P_v = 0$ kN ($N = 50$, $M = 50$) in (a) Roll and (b) Shear directions	153
Figure 5.20	Experimental and mathematical hysteresis loops of WRI PWHS 16010 obtained for $A = 0.25$ cm, $f = 1$ Hz, and $P_v = 0$ kN ($N = 5$, $M = 5$) in (a) Roll and (b) Shear directions	154
Figure 5.21	Experimental and mathematical hysteresis loops of WRI PWHS 16010 obtained for $A = 0.5$ cm, $f = 1$ Hz, and $P_v = 0$ kN ($N = 5$, $M = 5$) in (a) Roll and (b) Shear directions	155
Figure 5.22	Experimental and mathematical hysteresis loops of WRI PWHS 16010 obtained for $A = 1$ cm, $f = 1$ Hz, and $P_v = 0$ kN ($N = 5$, $M = 5$) in (a) Roll and (b) Shear directions	156
Figure 5.23	Experimental and mathematical hysteresis loops of WRI PWHS 16010 obtained for $A = 0.25$ cm, $f = 1$ Hz, and $P_v = 0$ kN ($N = 100$, $M = 100$) in (a) Roll and (b) Shear directions	157

List of Figures

Figure 5.24	Experimental and mathematical hysteresis loops of WRI PWHS 16010 obtained for $A = 0.5$ cm, $f = 1$ Hz, and $P_v = 0$ kN ($N = 100$, $M = 100$) in (a) Roll and (b) Shear directions	158
Figure 5.25	Experimental and mathematical hysteresis loops of WRI PWHS 16010 obtained for $A = 1$ cm, $f = 1$ Hz, and $P_v = 0$ kN ($N = 100$, $M = 100$) in (a) Roll and (b) Shear directions	159
Figure 5.26	Experimental and mathematical hysteresis loops of WRI PWHS 16010 obtained for $f = 1$ Hz and $P_v = 2$ kN ($N = 50$, $M = 50$) in (a) Roll and (b) Shear directions	160
Figure 5.27	Experimental and mathematical hysteresis loops of WRI PWHS 16040 obtained for $f = 1$ Hz and $P_v = 0$ kN ($N = 50$, $M = 50$) in (a) Roll and (b) Shear directions	162
Figure 5.28	Experimental and mathematical hysteresis loops of WRI PWHS 16040 obtained for $f = 1$ Hz and $P_v = 3$ kN ($N = 50$, $M = 50$) in (a) Roll and (b) Shear directions	163
Figure 5.29	Experimental and mathematical hysteresis loops of WRI PWHS 16040 S obtained for $f = 1$ Hz and $P_v = 0$ kN ($N = 50$, $M = 50$) in (a) Roll and (b) Shear directions	165
Figure 5.30	Experimental and mathematical hysteresis loops of WRI PWHS 16040 S obtained for $f = 1$ Hz and $P_v = 2$ kN ($N = 50$, $M = 50$) in (a) Roll and (b) Shear directions	166
Figure 5.31	Experimental and mathematical hysteresis loops of WRI PWHS 16060 obtained for $f = 1$ Hz and $P_v = 0$ kN ($N = 50$, $M = 50$) in (a) Roll and (b) Shear directions	168
Figure 5.32	Experimental and mathematical hysteresis loops of WRI PWHS 16060 obtained for $f = 1$ Hz and $P_v = 2$ kN ($N = 50$, $M = 50$) in (a) Roll and (b) Shear directions	169
Figure 5.33	(a) Tested RR-FRB and (b) horizontal loading directions	170
Figure 5.34	Analytical and experimental hysteresis loops of RR-FRB obtained for $A = 1$ cm, $f = 0.87$ Hz, and $P_v = 16.9$ kN in (a) 0° and (b) 45° loading directions	171
Figure 5.35	Analytical and experimental hysteresis loops of RR-FRB obtained for $A = 1.5$ cm, $f = 0.87$ Hz, and $P_v = 16.9$ kN in (a) 0° and (b) 45° loading directions	172
Figure 5.36	Analytical and experimental hysteresis loops of RR-FRB obtained for $A = 2$ cm, $f = 0.87$ Hz, and $P_v = 16.9$ kN in (a) 0° and (b) 45° loading directions	173
Figure 5.37	Analytical and experimental hysteresis loops of RR-FRB obtained for $A = 2.5$ cm, $f = 0.87$ Hz, and $P_v = 16.9$ kN in (a) 0° and (b) 45° loading directions	174
Figure 5.38	Analytical and experimental hysteresis loops of RR-FRB obtained for $A = 3$ cm, $f = 0.87$ Hz, and $P_v = 16.9$ kN in (a) 0° and (b) 45° loading directions	175
Figure 5.39	Analytical and experimental hysteresis loops of RR-FRB obtained for $A = 3.5$ cm, $f = 0.87$ Hz, and $P_v = 16.9$ kN in (a) 0° and (b) 45° loading directions	176
Figure 5.40	Analytical and experimental hysteresis loops of RR-FRB obtained for $A = 4$ cm, $f = 0.87$ Hz, and $P_v = 16.9$ kN in (a) 0° and (b) 45° loading directions	177

List of Figures

Figure 5.41	Analytical and experimental hysteresis loops of RR-FRB obtained for $A = 4.5$ cm, $f = 0.87$ Hz, and $P_v = 16.9$ kN in (a) 0° and (b) 45° loading directions	178
Figure 5.42	Experimental and mathematical hysteresis loops of RR-FRB obtained for $f = 0.87$ Hz and $P_v = 16.9$ kN ($N = 50$, $M = 50$) in (a) 0° and (b) 45° loading directions	180
Figure 6.1	Structure A: (a) typical floor plan; (b) base floor plan; (c) section A-A'	201
Figure 6.2	3d discrete structural model of Structure A	202
Figure 6.3	Structure B: (a) typical floor plan; (b) base floor plan; (c) section A-A'	204
Figure 6.4	3d discrete structural model of Structure B	205
Figure 6.5	(a) SN and (b) SP component of horizontal ground acceleration recorded at the Jensen Filter Plant station during the Northridge earthquake of January 17, 1994	207
Figure 6.6	Displacement time history of the base isolation system mass center in (a) x and (b) y directions (Structure A with LRBS)	210
Figure 6.7	Velocity time history of the base isolation system mass center in (a) x and (b) y directions (Structure A with LRBS)	211
Figure 6.8	Acceleration time history of the base isolation system mass center in (a) x and (b) y directions (Structure A with LRBS)	212
Figure 6.9	Displacement time history of the superstructure second story mass center in (a) x and (b) y directions (Structure A with LRBS)	213
Figure 6.10	Velocity time history of the superstructure second story mass center in (a) x and (b) y directions (Structure A with LRBS)	214
Figure 6.11	Acceleration time history of the superstructure second story mass center in (a) x and (b) y directions (Structure A with LRBS)	215
Figure 6.12	Hysteresis loop displayed by Isolator 1 in (a) x and (b) y directions (Structure A with LRBS)	216
Figure 6.13	Hysteresis loop displayed by Isolator 5 in (a) x and (b) y directions (Structure A with LRBS)	217
Figure 6.14	(a) SN and (b) SP component of horizontal ground acceleration recorded at the LGPC station during the Loma Prieta earthquake of October 17, 1989	218
Figure 6.15	Displacement time history of the base isolation system mass center in (a) x and (b) y directions (Structure B with LRBS)	221
Figure 6.16	Velocity time history of the base isolation system mass center in (a) x and (b) y directions (Structure B with LRBS)	222
Figure 6.17	Acceleration time history of the base isolation system mass center in (a) x and (b) y directions (Structure B with LRBS)	223
Figure 6.18	Displacement time history of the superstructure fourth story mass center in (a) x and (b) y directions (Structure B with LRBS)	224

List of Figures

Figure 6.19	Velocity time history of the superstructure fourth story mass center in (a) x and (b) y directions (Structure B with LRBS)	225
Figure 6.20	Acceleration time history of the superstructure fourth story mass center in (a) x and (b) y directions (Structure B with LRBS)	226
Figure 6.21	Hysteresis loop displayed by Isolator 1 in (a) x and (b) y directions (Structure B with LRBS)	227
Figure 6.22	Hysteresis loop displayed by Isolator 11 in (a) x and (b) y directions (Structure B with LRBS)	228
Figure 6.23	Displacement time history of the base isolation system mass center in (a) x and (b) y directions (Structure A with FPBS)	234
Figure 6.24	Velocity time history of the base isolation system mass center in (a) x and (b) y directions (Structure A with FPBS)	235
Figure 6.25	Acceleration time history of the base isolation system mass center in (a) x and (b) y directions (Structure A with FPBS)	236
Figure 6.26	Displacement time history of the superstructure second story mass center in (a) x and (b) y directions (Structure A with FPBS)	237
Figure 6.27	Velocity time history of the superstructure second story mass center in (a) x and (b) y directions (Structure A with FPBS)	238
Figure 6.28	Acceleration time history of the superstructure second story mass center in (a) x and (b) y directions (Structure A with FPBS)	239
Figure 6.29	Hysteresis loop displayed by Isolator 1 in (a) x and (b) y directions (Structure A with FPBS)	240
Figure 6.30	Hysteresis loop displayed by Isolator 5 in (a) x and (b) y directions (Structure A with FPBS)	241
Figure 6.31	Displacement time history of the base isolation system mass center in (a) x and (b) y directions (Structure B with FPBS)	244
Figure 6.32	Velocity time history of the base isolation system mass center in (a) x and (b) y directions (Structure B with FPBS)	245
Figure 6.33	Acceleration time history of the base isolation system mass center in (a) x and (b) y directions (Structure B with FPBS)	246
Figure 6.34	Displacement time history of the superstructure fourth story mass center in (a) x and (b) y directions (Structure B with FPBS)	247
Figure 6.35	Velocity time history of the superstructure fourth story mass center in (a) x and (b) y directions (Structure B with FPBS)	248
Figure 6.36	Acceleration time history of the superstructure fourth story mass center in (a) x and (b) y directions (Structure B with FPBS)	249
Figure 6.37	Hysteresis loop displayed by Isolator 1 in (a) x and (b) y directions (Structure B with FPBS)	250

List of Figures

Figure 6.38	Hysteresis loop displayed by Isolator 11 in (a) x and (b) y directions (Structure B with FPBS)	251
Figure 7.1	Hysteresis loop simulated using the BWM and the NEM	254
Figure 7.2	(a) X and (b) Y components of the applied horizontal harmonic ground acceleration	255
Figure 7.3	Displacement time history of the base isolation system mass center in (a) x and (b) y directions	258
Figure 7.4	Velocity time history of the base isolation system mass center in (a) x and (b) y directions	259
Figure 7.5	Acceleration time history of the base isolation system mass center in (a) x and (b) y directions	260
Figure 7.6	Displacement time history of the superstructure fourth story mass center in (a) x and (b) y directions	261
Figure 7.7	Velocity time history of the superstructure fourth story mass center in (a) x and (b) y directions	262
Figure 7.8	Acceleration time history of the superstructure fourth story mass center in (a) x and (b) y directions	263
Figure 7.9	Hysteresis loop displayed by Isolator 1 in (a) x and (b) y directions	264
Figure 7.10	Hysteresis loop displayed by Isolator 11 in (a) x and (b) y directions	265

List of Tables

Table 3.1	Geometrical characteristics of tested WRIs	36
Table 3.2	Dynamic displacement-controlled tests in Roll and Shear directions	40
Table 3.3	Static displacement-controlled tests in Roll and Shear directions	41
Table 3.4	Influence of displacement amplitude WRI PWHS 16040	43
Table 3.5	Influence of frequency WRI PWHS 16040	48
Table 3.6	Vertical strain of tested WRIs due to vertical load	50
Table 3.7	Influence of vertical load WRI PWHS 16040	51
Table 3.8	Influence of vertical load WRI PWHS 16060 (Roll direction)	54
Table 3.9	Influence of WRI geometrical characteristics	56
Table 3.10	Influence of wire rope diameter (Roll direction)	58
Table 3.11	Comparison between Roll and Shear dynamic responses	60
Table 3.12	Static tests results WRI PWHS 16040	61
Table 4.1	Tangent stiffness of the restoring force in the BWM	65
Table 4.2	BWM and NEM parameters Hysteresis loop with bilinear characteristics	114
Table 4.3	BWM and NEM parameters Loop with bilinear characteristics and high initial stiffness	115
Table 4.4	BWM and NEM parameters Hysteresis loop with rigid-plastic characteristics	115
Table 4.5	BWM and PM parameters Hysteresis loop with bilinear characteristics	117
Table 4.6	BWM and PM parameters Loop with bilinear characteristics and high initial stiffness	119
Table 4.7	BWM and PM parameters Hysteresis loop with rigid-plastic characteristics	121
Table 4.8	MBWM and ANEM parameters Hysteresis loop with post-hardening characteristics	124
Table 4.9	MBWM and ANEM parameters Hysteresis loop with post-softening characteristics	125
Table 4.10	MBWM and APM parameters Hysteresis loop with post-hardening characteristics	126
Table 4.11	MBWM and APM parameters Hysteresis loop with post-softening characteristics	128
Table 5.1	ANEM parameters for WRI PWHS 16010 ($P_v = 0$ kN)	132

List of Tables

Table 5.2	ANEM parameters for WRI PWHS 16010 ($P_v = 2$ kN)	132
Table 5.3	ANEM parameters for WRI PWHS 16040 ($P_v = 0$ kN)	137
Table 5.4	ANEM parameters for WRI PWHS 16040 ($P_v = 3$ kN)	137
Table 5.5	ANEM parameters for WRI PWHS 16040 S ($P_v = 0$ kN)	140
Table 5.6	ANEM parameters for WRI PWHS 16040 S ($P_v = 2$ kN)	140
Table 5.7	ANEM parameters for WRI PWHS 16060 ($P_v = 0$ kN)	143
Table 5.8	ANEM parameters for WRI PWHS 16060 ($P_v = 2$ kN)	143
Table 5.9	MBWM and ANEM parameters for WRI PWHS 16010 ($P_v = 0$ kN)	146
Table 5.10	APM parameters for WRI PWHS 16010 ($P_v = 0$ kN)	150
Table 5.11	APM parameters for WRI PWHS 16010 ($P_v = 2$ kN)	150
Table 5.12	APM parameters for WRI PWHS 16040 ($P_v = 0$ kN)	161
Table 5.13	APM parameters for WRI PWHS 16040 ($P_v = 3$ kN)	161
Table 5.14	APM parameters for WRI PWHS 16040 S ($P_v = 0$ kN)	164
Table 5.15	APM parameters for WRI PWHS 16040 S ($P_v = 2$ kN)	164
Table 5.16	APM parameters for WRI PWHS 16060 ($P_v = 0$ kN)	167
Table 5.17	APM parameters for WRI PWHS 16060 ($P_v = 2$ kN)	167
Table 5.18	ANEM parameters for RR-FRB ($P_v = 16.9$ kN)	170
Table 5.19	APM parameters for RR-FRB ($P_v = 16.9$ kN)	179
Table 6.1	NLTHAs results with $\Delta t = 0.005$ s Structure A with LRBS	208
Table 6.2	NLTHAs results with $\Delta t = 0.001$ s Structure A with LRBS	209
Table 6.3	NLTHAs results with $\Delta t = 0.005$ s Structure B with LRBS	219
Table 6.4	NLTHAs results with $\Delta t = 0.001$ s Structure B with LRBS	220
Table 6.5	NLTHAs results with $\Delta t = 0.005$ s Structure A with FPBS	232
Table 6.6	NLTHAs results with $\Delta t = 0.001$ s Structure A with FPBS	233
Table 6.7	NLTHAs results with $\Delta t = 0.005$ s Structure B with FPBS	242

List of Tables

Table 6.8	NLTHAs results with $\Delta t = 0.001$ s Structure B with FPBS	243
Table 7.1	BWM and NEM parameters	254
Table 7.2	NLTHAs results with $\Delta t = 0.005$ s	256
Table 7.3	NLTHAs results with $\Delta t = 0.001$ s	257

Chapter 1

Introduction

Seismic base isolation has become a widely accepted technique for the earthquake protection of buildings and bridges. The concept of base isolation is quite simple: the introduction of a flexible base isolation system between the foundation and the structure allows one to move the period of the latter away from the predominant period of the ground motion with the benefit of reducing floor accelerations, story shears and interstory drifts (Kelly 1997, Naeim and Kelly 1999).

The analysis of seismically base-isolated structures to determine deformations and forces induced by the ground excitation is an essential step in the design process.

A structural analysis procedure requires a discrete structural model of the actual structure, a representation of the earthquake ground motion and a method of analysis for assembling and solving the governing equations. Structural analysis procedures currently adopted for base-isolated structures are: Linear Static Procedure (LSP), Linear Dynamic Procedure (LDP), and Nonlinear Dynamic Procedure (NDP).

This thesis deals with the NDP which requires a discrete structural model having nonlinear elements able to simulate the nonlinear dynamic behavior displayed by seismic isolation devices due to the nonlinear material response and/or nonlinear geometry under large displacements, specific earthquake ground motion records, and a nonlinear response history analysis method.

The three-dimensional (3d) discrete structural model of an actual base-isolated structure, generally consisting of frame elements for modeling beams and columns, can be divided into two substructures, namely, the superstructure and the base isolation system. The former is usually modeled under the assumption that it deforms within the elastic range. This assumption is reasonable in the context of base isolation and has been adopted by several researchers (Tarics et al. 1984, Asher et al. 1990) to reduce the computation effort. In some cases, it may be necessary to consider the superstructure also to be inelastic, although this is not dealt with in the present study. The base isolation system consists of seismic isolation

bearings, called seismic isolators, and a full diaphragm above the seismic isolation devices that is generally introduced to distribute the lateral loads uniformly to each seismic isolator (Naeim 2001). The base isolation system can include linear and nonlinear isolation elements. Existing phenomenological models (Nagarajaiah et al. 1991, Kikuchi and Aiken 1997, Hwang et al. 2002, Tsai et al. 2003) and plasticity-based models (Way and Jeng 1989, Huang et al. 2000, Huang 2002) can be adopted to simulate the nonlinear dynamic behavior of seismic isolators.

As far as the nonlinear response history analysis method is concerned, a conventional non-partitioned solution approach, characterized by the use of an implicit single-step time integration method adopted with an iteration procedure, such as the Newton-Raphson, the modified Newton-Raphson, or the pseudo-force iteration method, is generally employed to solve the nonlinear dynamic equilibrium equations of base-isolated structures subjected to earthquake excitation (Wilson 2002).

Among conventional non-partitioned solution methods and nonlinear mathematical models, the solution algorithm and analytical model proposed by Nagarajaiah et al. (1991), both implemented in the computer program 3D-BASIS-ME-MB (Tsopelas et al. 2005), are presented in this dissertation because specifically developed for the nonlinear dynamic analysis of base-isolated structures with either elastomeric and/or sliding isolation systems. In this non-partitioned solution approach, the equations of motion are solved using the implicit unconditionally stable Newmark's constant average acceleration method with the nonlinear restoring forces of the seismic isolators being represented as pseudo-forces. An iterative procedure consisting of corrective pseudo-forces is employed within each time step until equilibrium is achieved. The analytical model, based on the set of two first order nonlinear ordinary differential equations proposed by Park et al. (1986), is able to represent the uniaxial and biaxial behavior of both elastomeric and sliding isolation bearings.

The solution of the nonlinear dynamic equilibrium equations using the above-described conventional implicit single-time step integration method and the use of the differential equation model can require significant computational effort (Vaiana et al. 2017a).

This thesis deals with the development of five mathematical models and a numerical time integration method for the nonlinear time history analysis of base-isolated structures with the aim of simulating the nonlinear dynamic behavior of seismic isolators at both small and large displacements and reducing numerical computations, making the nonlinear dynamic analysis almost as fast as a linear dynamic analysis.

1.1 Mathematical Models

Seismic devices generally exhibit symmetric softening force-displacement hysteresis loops within a relatively large displacements range, that is, under the design earthquake loading (Constantinou et al. 2007). At large displacements, several isolators, such as high damping rubber bearings and Wire Rope Isolators (WRIs), exhibit a hardening stiffness (Tsai et al. 2003, Vaiana et al. 2017c, 2017d), whereas others, such as unbonded elastomeric bearings with deformable reinforcing layers, display a softening behavior with a negative tangent stiffness (Spizzuoco et al. 2014).

The differential equation Bouc-Wen Model (BWM), developed by Bouc (1971) and then adopted by Wen (1976, 1980) for the study of the random vibration of hysteretic systems, has been adapted for modeling the uniaxial behavior of elastomeric bearings, sliding bearings, and WRIs within the relatively large displacements range (Constantinou et al. 1990, Nagarajaiah et al. 1991, Demetriades et al. 1993), and has been implemented in many computer programs, such as 3D-BASIS, SAP2000, and ETABS. Nevertheless, this model is unable to efficiently capture the behavior of seismic isolators at large displacements (Ni et al. 1999, Tsai et al. 2003). Furthermore, the use of such differential equation model increases the computational effort very significantly (Vaiana and Serino 2017c) because of the numerical solution of a first order nonlinear ordinary differential equation required at each time step of a nonlinear time history analysis.

In this dissertation, four one-dimensional (1d) mathematical models, namely, Nonlinear Exponential Model (NEM), Parallel Model (PM), Advanced Nonlinear Exponential Model (ANEM), and Advanced Parallel Model (APM), are proposed in order to reduce the number of model parameters to be identified from experimental tests and to avoid the numerical solution of the nonlinear differential equation required in the BWM. The NEM and the PM are able to predict the bilinear and the rigid-plastic behavior displayed by seismic isolators within the relatively large displacements range, whereas the ANEM and the APM can simulate the nonlinear dynamic response of seismic isolation devices having hardening or softening behavior at large displacements and can capture the smooth transition of the hysteresis loops from small to large displacements using only one set of model parameters evaluated from experimental hysteresis loops with the largest amplitude.

The PM and the APM are sufficiently versatile to be easily implemented in existing nonlinear finite element computer programs.

The proposed mathematical models have been validated by comparing the experimental hysteresis loops obtained from horizontal dynamic tests, performed at the Department of Industrial Engineering of the University of Naples Federico II on four WRIs and a Recycled Rubber-Fiber Reinforced Bearing (RR-FRB), with those predicted numerically.

In addition, a two-dimensional (2d) Parallel Model (2d PM), able to take into account the transverse biaxial interaction between the nonlinear hysteretic restoring forces within the relatively large displacements range, is also presented.

1.2 Numerical Method

The numerical solution of the nonlinear dynamic equilibrium equations of seismically base-isolated structures adopting a conventional non-partitioned solution approach, that is, an implicit single-step time integration method employed in conjunction with an iterative procedure, can require considerable computational effort (Vaiana et al. 2017a, 2017b).

In order to achieve a substantial reduction in computation, a partitioned solution approach (Felippa et al. 2001) can be used to perform the nonlinear dynamic analysis.

In the last 30 years, various authors (Hughes et Liu 1978, Belytschko et al. 1979, Wu and Smolinski 2000, Combescure and Gravouil 2002, Herry et al. 2002) developed several partitioned time integration methods allowing different time steps or time integration algorithms or both to be used in different spatial subdomains of the mesh.

In the context of seismically base-isolated structures, the above-mentioned approach can be easily employed being the decomposition of the discrete structural model of such structures driven by physical considerations: the base isolation system is much more flexible than the superstructure to decouple the latter from the earthquake ground motion.

In this dissertation, a Mixed Explicit-Implicit time integration Method (MEIM) is specifically proposed for the nonlinear dynamic analysis of base-isolated structures: at each time step of the analysis, the nonlinear response of the base isolation system is computed first using the explicit conditionally stable central difference method, then the implicit unconditionally stable Newmark's constant average acceleration method is employed to evaluate the superstructure linear response, with the remarkable benefit of avoiding the iterative procedure within each time step of a nonlinear time history analysis required by conventional non-partitioned solution approaches.

Since the MEIM is conditionally stable because of the use of the central difference method, a procedure to evaluate the critical time step is first developed for 2d base-isolated structures

and then extended to the 3d case.

The proposed numerical time integration method is adopted to analyze four different 3d base-isolated structures subjected to bidirectional earthquake excitation and the numerical results are compared with those obtained by using the solution algorithm proposed by Nagarajaiah et al. (1991) in order to demonstrate the accuracy and the computational efficiency of the proposed method.

1.3 Outline of the Dissertation

The dissertation is organized into eight chapters, whose contents are herein briefly described.

Chapter 1 illustrates the objective and scope of the study.

Chapter 2 deals with the modeling of seismically base-isolated structures: starting from the description of the 3d discrete structural model of such structures, the superstructure and the base isolation system modeling are presented and then the dynamic equilibrium equations are formulated.

In Chapter 3, two common types of seismic isolation devices, namely, elastomeric and sliding bearings, are described. Furthermore, the results of an extensive series of experimental tests, conducted at the Department of Industrial Engineering of the University of Naples Federico II on a RR-FRB and four WRIs, are presented.

Chapter 4 is concerned with the modeling of seismic isolators. After a detailed description of widely used differential equation models, namely, BWM, Modified Bouc-Wen Model (MBWM), and 2d Bouc-Wen Model (2d BWM), the proposed mathematical models, that is, NEM, ANEM, PM, APM, and 2d PM, are presented. The chapter concludes with comparisons between the described differential equation models and the proposed ones.

In order to demonstrate the validity of the proposed mathematical models, in Chapter 5, the results predicted numerically are compared to those obtained experimentally from horizontal dynamic tests performed on a RR-FRB and four WRIs, as described in Chapter 3.

Chapter 6 describes the conventional non-partitioned solution approach developed by Nagarajaiah et al. (1991) specifically for seismically base-isolated structures and presents the proposed partitioned solution approach. After the description of the MEIM, a procedure to evaluate the critical time step is illustrated and then four numerical applications are presented to demonstrate the accuracy and the computational efficiency of the proposed method.

Chapter 7 presents a numerical application in order to show the significant reduction of the computational effort due to the use of the MEIM and NEM.

In Chapter 8, conclusions are presented, as well as considerations and suggestions for further research and future developments.

Parts of this original research have been already published in the proceedings of international conferences or peer-reviewed journals. The experimental tests performed on WRIs, described in Chapter 3, have been presented in Vaiana et al. (2017c, 2017d), the mathematical models, described in Chapter 4 and verified in Chapter 5, have been presented in Vaiana et al. (2016, 2017a, 2017d) and in Vaiana and Serino (2017a, 2017b, 2017c), the proposed partitioned solution approach, described in Chapter 6, has been presented in Vaiana et al. (2017a, 2017b), whereas the content of Chapter 7 in Vaiana et al. (2017a).

Chapter 2

Modeling of Base-Isolated Structures

2.1 Introduction

The 3d discrete structural model of an actual base-isolated structure can be decomposed into two substructures: the superstructure and the base isolation system.

The base isolation system consists of seismic isolation bearings called seismic isolators and a full diaphragm above the seismic isolation devices which is generally introduced to distribute the lateral loads uniformly to each bearing (Naeim 2001). Introducing a flexible base isolation system between the foundation and the superstructure leads to decouple the latter from the earthquake ground motion.

Figure 2.1 shows the 3d discrete structural model of a two-story base-isolated structure.

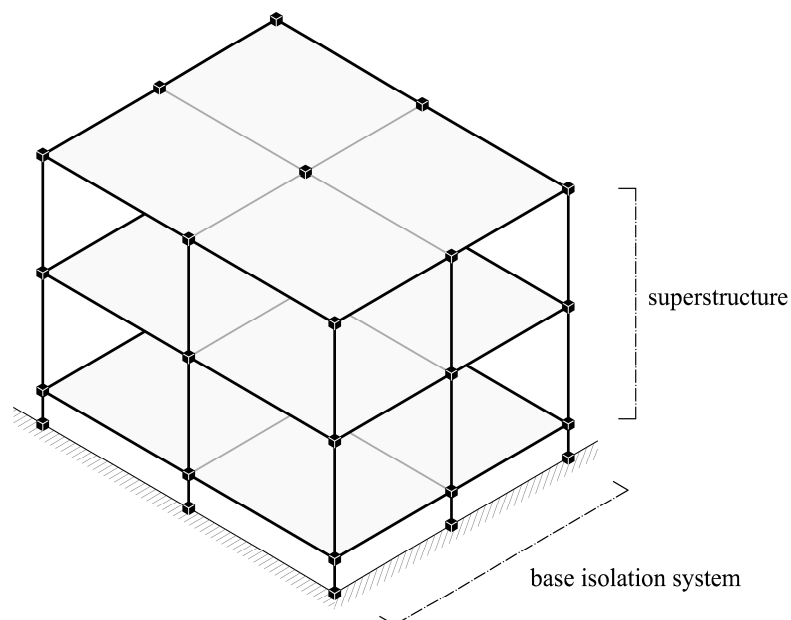


Figure 2.1. 3d discrete structural model of a two-story base-isolated structure.

In the following, the superstructure and the base isolation system modeling are presented and the dynamic equilibrium equations are formulated.

2.2 Modeling of the Superstructure

The geometry of the 3d discrete structural model of a base-isolated structure is defined in a global, right-handed Cartesian coordinate system, denoted with upper case letters X , Y , and Z , and attached to the center of mass of the base isolation system.

The superstructure is considered to remain elastic during the earthquake excitation because it is assumed that the introduction of a flexible base isolation system allows one to reduce the earthquake response in such a way that the superstructure deforms within the elastic range. Each superstructure floor diaphragm (or floor slab) is assumed to be infinitely rigid in its own plane, the columns are assumed to be axially inextensible and the beams are considered to be axially inextensible and flexurally rigid. These kinematics constraints, generally adopted in the literature (Chopra 2012) for beams and columns, are here assumed for simplicity and can be removed straightforwardly without any influence on the generality of the results presented in this work. Because of this structural idealization, the total number of a n -story superstructure degrees of freedom (dofs), denoted with nts , is equal to $3n$ and three dofs are attached to the i -th superstructure diaphragm reference point o_i belonging to the horizontal plane of the i -th floor diaphragm and vertically aligned to the global coordinate system origin O . The three dofs of the i -th superstructure diaphragm are the two horizontal translations $u_x^{(i)}$ and $u_y^{(i)}$ in the X and Y directions and the torsional rotation $u_r^{(i)}$ about the vertical axis Z . These three floor diaphragm displacements can be defined relative to the ground or relative to the base isolation system (Muscolino 1990). In this thesis, the former approach is selected so that the dynamic equilibrium equations of the 3d discrete structural model of an actual base-isolated structure are coupled in terms of elastic and viscous forces and decoupled in terms of inertial forces.

The superstructure displacement vector \mathbf{u}_s , having size $nts \times 1$, is defined by:

$$\mathbf{u}_s = \{ \mathbf{u}_1 \quad \cdots \quad \mathbf{u}_i \quad \cdots \quad \mathbf{u}_n \}^T, \quad (2.1)$$

where

$$\mathbf{u}_1 = \{ u_x^{(1)} \quad u_y^{(1)} \quad u_r^{(1)} \}^T, \quad (2.2)$$

$$\mathbf{u}_i = \{ u_x^{(i)} \quad u_y^{(i)} \quad u_r^{(i)} \}^T, \quad (2.3)$$

$$\mathbf{u}_n = \left\{ u_x^{(n)} \quad u_y^{(n)} \quad u_r^{(n)} \right\}^T, \quad (2.4)$$

are the displacement vectors of the first, i -th, and n -th superstructure floor diaphragm, respectively.

The superstructure diaphragm mass should include the contributions of the dead load and live load on the floor diaphragm and the contributions of the structural elements, such as columns and walls, and of the nonstructural elements, such as partition walls and architectural finishes, between floors (Chopra 2012).

The superstructure mass matrix \mathbf{m}_s is:

$$\mathbf{m}_s = \begin{bmatrix} \mathbf{m}_1 & \mathbf{0} & \mathbf{0} \\ \mathbf{0} & \mathbf{m}_2 & \mathbf{0} \\ & & \ddots \\ \mathbf{0} & \mathbf{0} & & \mathbf{m}_n \end{bmatrix}, \quad (2.5)$$

where the i -th superstructure diaphragm mass matrix \mathbf{m}_i is given by:

$$\mathbf{m}_i = \begin{bmatrix} m^{(i)} & 0 & -S_x^{(i)} \\ 0 & m^{(i)} & S_y^{(i)} \\ -S_x^{(i)} & S_y^{(i)} & I_O^{(i)} \end{bmatrix}, \quad (2.6)$$

in which, $m^{(i)}$ is the i -th diaphragm mass, $S_x^{(i)}$ and $S_y^{(i)}$ are the first moments of the i -th diaphragm mass about the global horizontal axes X and Y , respectively, and $I_O^{(i)}$ is the moment of inertia of the i -th diaphragm about the global vertical axis Z . If the mass center of the i -th floor diaphragm and the origin of the global coordinate system O are aligned vertically the superstructure diaphragm mass matrix is diagonal.

The superstructure stiffness matrix \mathbf{k}_s is:

$$\mathbf{k}_s = \begin{bmatrix} \mathbf{k}_1 + \mathbf{k}_2 & -\mathbf{k}_2 & & \mathbf{0} \\ -\mathbf{k}_2 & \mathbf{k}_2 + \mathbf{k}_3 & \ddots & \\ & \ddots & \ddots & -\mathbf{k}_n \\ \mathbf{0} & & -\mathbf{k}_n & \mathbf{k}_n \end{bmatrix}, \quad (2.7)$$

where the i -th superstructure story stiffness matrix \mathbf{k}_i is given by:

$$\mathbf{k}_i = \begin{bmatrix} k_{xx}^{(i)} & k_{xy}^{(i)} & -k_{xr}^{(i)} \\ k_{yx}^{(i)} & k_{yy}^{(i)} & k_{yr}^{(i)} \\ -k_{xr}^{(i)} & k_{yr}^{(i)} & k_{rr}^{(i)} \end{bmatrix}, \quad (2.8)$$

in which, $k_{xx}^{(i)}$, $k_{xy}^{(i)}$, and $k_{xr}^{(i)}$ are the resulting elastic forces in X direction of the i -th superstructure story due to unit translation in X and Y directions and unit torsional rotation of the i -th superstructure diaphragm about the vertical axis Z , respectively; $k_{yy}^{(i)}$, $k_{yx}^{(i)}$ and $k_{yr}^{(i)}$ are the resultants of the elastic forces in Y direction of the i -th superstructure story due to unit translation in Y and X directions and unit torsional rotation of the i -th superstructure diaphragm about the vertical axis Z , respectively; and $k_{rr}^{(i)}$ is the resultant of the elastic torsional moment of the i -th superstructure story due to unit torsional rotation of the i -th superstructure diaphragm about the vertical axis Z . The torsional stiffness of each individual resisting vertical element, that is, column or wall, is considered negligible (Jangid and Datta 1995).

Classical damping is an appropriate idealization if similar damping mechanisms are distributed throughout the superstructure. In order to construct a classical damping matrix from modal damping ratios the Rayleigh damping can be assumed allowing one to express the damping matrix in terms of the superstructure mass and stiffness matrices:

$$\mathbf{c}_s = \alpha_0 \mathbf{m}_s + \alpha_1 \mathbf{k}_s. \quad (2.9)$$

The Rayleigh damping coefficients α_0 and α_1 can be selected to match the desired damping ratio for two modes, oftentimes the two lowest, but not always (Bozorgnia and Bertero 2004). Denoting these modes as the f -th and the s -th, it is possible to write:

$$\begin{aligned} \alpha_0 + \alpha_1 \omega_f^2 &= 2 \xi_f \omega_f \\ \alpha_0 + \alpha_1 \omega_s^2 &= 2 \xi_s \omega_s \end{aligned} \quad (2.10)$$

With given damping ratios ξ_f and ξ_s these two equations can be solved for α_0 and α_1 .

2.3 Modeling of the Base Isolation System

The base isolation system diaphragm is assumed to be infinitely rigid in its own plane, the beams are considered to be axially inextensible and flexurally rigid and the seismic isolators are assumed to be infinitely rigid in the vertical direction. As a result of these kinematic constraints, the total number of the base isolation system dofs, denoted with ntb , is equal to 3. These three dofs, which are attached to the mass center of the base diaphragm and are defined relative to the ground, are the two horizontal translations $u_x^{(b)}$ and $u_y^{(b)}$ in the X and Y directions and the torsional rotation $u_r^{(b)}$ about the vertical axis Z .

The isolation system displacement vector \mathbf{u}_b , having size $ntb \times 1$, is:

$$\mathbf{u}_b = \left\{ u_x^{(b)} \quad u_y^{(b)} \quad u_r^{(b)} \right\}^T. \quad (2.11)$$

The base isolation system mass matrix \mathbf{m}_b is defined by:

$$\mathbf{m}_b = \begin{bmatrix} m^{(b)} & 0 & 0 \\ 0 & m^{(b)} & 0 \\ 0 & 0 & I_O^{(b)} \end{bmatrix}, \quad (2.12)$$

where $m^{(b)}$ is the diaphragm mass and $I_O^{(b)}$ is the moment of inertia of the diaphragm about the global vertical axis Z . The two first moments $S_x^{(b)}$ and $S_y^{(b)}$ of the base diaphragm mass about the global horizontal axes X and Y are equal to zero because the diaphragm mass center and the origin of the global coordinate system O are coincident.

The base isolation system can include linear isolation elements and nonlinear isolation elements. Considering the linear elements, that is, seismic isolators whose behavior can be modeled by a linear spring and a linear viscous damper in parallel, the base isolation system stiffness matrix \mathbf{k}_b is:

$$\mathbf{k}_b = \begin{bmatrix} k_{xx}^{(b)} & k_{xy}^{(b)} & -k_{xr}^{(b)} \\ k_{yx}^{(b)} & k_{yy}^{(b)} & k_{yr}^{(b)} \\ -k_{xr}^{(b)} & k_{yr}^{(b)} & k_{rr}^{(b)} \end{bmatrix}, \quad (2.13)$$

where $k_{xx}^{(b)}$, $k_{xy}^{(b)}$, and $k_{xr}^{(b)}$ are the resultants of the elastic forces in X direction of the linear elements due to unit translation in X and Y directions and unit torsional rotation of the base diaphragm about the vertical axis Z , respectively; $k_{yy}^{(b)}$, $k_{yx}^{(b)}$, and $k_{yr}^{(b)}$ are the resultants of the elastic forces in Y direction of the linear elements due to unit translation in Y and X directions and unit torsional rotation of the base diaphragm about the vertical axis Z , respectively; and $k_{rr}^{(b)}$ is the resultant elastic torsional moment of the linear elements due to unit torsional rotation of the base diaphragm about the vertical axis Z . The torsional stiffness of the seismic isolators is negligible and is not included (Kelly 1997).

The base isolation system viscous damping matrix \mathbf{c}_b is:

$$\mathbf{c}_b = \begin{bmatrix} c_{xx}^{(b)} & 0 & 0 \\ 0 & c_{yy}^{(b)} & 0 \\ 0 & 0 & c_{rr}^{(b)} \end{bmatrix}, \quad (2.14)$$

where $c_{xx}^{(b)}$ and $c_{yy}^{(b)}$ are the resultants of the viscous damping forces in X and Y directions, respectively, of the linear elements due to unit velocity of the base diaphragm in X and Y directions, and $c_{rr}^{(b)}$ is the resultant of the viscous damping torsional moment of the linear elements due to unit rotational velocity of the base diaphragm about the vertical axis Z . The off-diagonal terms of the base isolation system viscous damping matrix are neglected (Alhan and Gavin 2004).

As far as the nonlinear elements is concerned, the resultant nonlinear forces vector of the base isolation system \mathbf{f}_n is:

$$\mathbf{f}_n = \begin{Bmatrix} f_{nx} \\ f_{ny} \\ f_{nr} \end{Bmatrix}, \quad (2.15)$$

where f_{nx} , f_{ny} , and f_{nr} are the resultant nonlinear forces in X and Y directions and the resultant nonlinear torsional moment about the vertical axis Z of the nonlinear elements. The nonlinear behavior of each seismic isolator can be modeled using an explicit nonlinear force-displacement relation (Nagarajaiah et al. 1991).

2.4 Dynamic Equilibrium Equations

The equations of motion for the elastic superstructure are expressed in the following form:

$$\mathbf{m}_s \ddot{\mathbf{u}}_s + \mathbf{c}_s \dot{\mathbf{u}}_s + \mathbf{k}_s \mathbf{u}_s + \mathbf{c} \dot{\mathbf{u}}_b + \mathbf{k} \mathbf{u}_b = -\mathbf{m}_s \mathbf{r}_s \ddot{\mathbf{u}}_g, \quad (2.16)$$

with

$$\mathbf{c} = [-\mathbf{c}_1 \quad \mathbf{0}]^T, \quad (2.17)$$

$$\mathbf{k} = [-\mathbf{k}_1 \quad \mathbf{0}]^T, \quad (2.18)$$

$$\ddot{\mathbf{u}}_g = \{\ddot{u}_{gx} \quad \ddot{u}_{gy} \quad 0\}^T, \quad (2.19)$$

where \mathbf{m}_s is the superstructure mass matrix, \mathbf{c}_s the superstructure damping matrix, \mathbf{k}_s the superstructure stiffness matrix, and \mathbf{r}_s the superstructure earthquake influence matrix. Furthermore, \mathbf{u}_s , $\dot{\mathbf{u}}_s$, and $\ddot{\mathbf{u}}_s$ represent the floor displacement, velocity, and acceleration vectors relative to the ground, respectively, \mathbf{c}_1 and \mathbf{k}_1 the viscous damping and stiffness matrices of the superstructure first story, and $\ddot{\mathbf{u}}_g$ is the ground (or support) acceleration vector in which \ddot{u}_{gx} and \ddot{u}_{gy} are the X and Y ground acceleration components whereas the rotational component is neglected.

The equations of motion for the base are:

$$\mathbf{m}_b \ddot{\mathbf{u}}_b + (\mathbf{c}_b + \mathbf{c}_1) \dot{\mathbf{u}}_b + (\mathbf{k}_b + \mathbf{k}_1) \mathbf{u}_b + \mathbf{c}^T \dot{\mathbf{u}}_s + \mathbf{k}^T \mathbf{u}_s + \mathbf{f}_n = -\mathbf{m}_b \mathbf{r}_b \ddot{\mathbf{u}}_g, \quad (2.20)$$

where \mathbf{m}_b is the base isolation system mass matrix, \mathbf{c}_b the damping matrix of linear viscous isolation elements, \mathbf{k}_b the stiffness matrix of linear elastic isolation elements, \mathbf{f}_n the resultant nonlinear forces vector of nonlinear elements, and \mathbf{r}_b the base isolation system influence matrix. Furthermore, \mathbf{u}_b , $\dot{\mathbf{u}}_b$, and $\ddot{\mathbf{u}}_b$ represent the base isolation system displacement, velocity, and acceleration vectors relative to the ground, respectively.

Combining Equations (2.16) and (2.20), the following system of $3n + 3$ Ordinary Differential Equations (ODEs) of the second order in time, coupled in terms of elastic and viscous forces and decoupled in terms of inertial forces, is obtained:

$$\begin{bmatrix} \mathbf{m}_b & \mathbf{0}^T \\ \mathbf{0} & \mathbf{m}_s \end{bmatrix} \begin{Bmatrix} \ddot{\mathbf{u}}_b \\ \ddot{\mathbf{u}}_s \end{Bmatrix} + \begin{bmatrix} \mathbf{c}_b + \mathbf{c}_1 & \mathbf{c}^T \\ \mathbf{c} & \mathbf{c}_s \end{bmatrix} \begin{Bmatrix} \dot{\mathbf{u}}_b \\ \dot{\mathbf{u}}_s \end{Bmatrix} + \begin{bmatrix} \mathbf{k}_b + \mathbf{k}_1 & \mathbf{k}^T \\ \mathbf{k} & \mathbf{k}_s \end{bmatrix} \begin{Bmatrix} \mathbf{u}_b \\ \mathbf{u}_s \end{Bmatrix} + \begin{Bmatrix} \mathbf{f}_n \\ \mathbf{0} \end{Bmatrix} = - \begin{bmatrix} \mathbf{m}_b & \mathbf{0}^T \\ \mathbf{0} & \mathbf{m}_s \end{bmatrix} \begin{Bmatrix} \mathbf{r}_b \\ \mathbf{r}_s \end{Bmatrix} \ddot{\mathbf{u}}_g. \quad (2.21)$$

The dynamic equilibrium equations of the 3d discrete structural model of an actual base-isolated structure given in Equation (2.21) can be written in a more compacted form as follows:

$$\mathbf{m} \ddot{\mathbf{u}} + \mathbf{c} \dot{\mathbf{u}} + \mathbf{k} \mathbf{u} + \mathbf{f} = -\mathbf{m} \mathbf{r} \ddot{\mathbf{u}}_g, \quad (2.22)$$

where \mathbf{m} is the mass matrix, \mathbf{c} the damping matrix, \mathbf{k} the stiffness matrix, \mathbf{f} the nonlinear forces vector and \mathbf{r} the earthquake influence matrix of the seismically base-isolated structure. Furthermore, \mathbf{u} , $\dot{\mathbf{u}}$, and $\ddot{\mathbf{u}}$ represent the floor displacement, velocity, and acceleration vectors of the base-isolated structure relative to the ground.

The system of $3n + 3$ coupled ODEs is nonlinear because of the presence of the resultant nonlinear forces vector of the base isolation system \mathbf{f}_n , which could be function of both displacement and velocity vectors, according to the model adopted for each seismic isolator.

Chapter 3

Seismic Isolation Bearings

3.1 Introduction

Seismic isolation bearings are special devices able to provide flexibility and energy dissipation capacity in horizontal directions, sufficient vertical stiffness to resist service loading, rigidity under low levels of lateral loads due to wind or minor earthquakes, and recentering capability.

Seismic isolators can be divided into two main categories:

- elastomeric bearings;
- sliding bearings.

The former rely on the flexible properties of rubber to achieve isolation, whereas the latter allow one to achieve low horizontal stiffness through the action of sliding and to dissipate energy through the friction damping occurring at the sliding interface (Constantinou et al. 2007).

Metal devices, such as Wire Rope Isolators, currently used for the seismic protection of equipment in buildings (Demetriades et al. 1993), can be adopted with flat surface sliders when the complete recentering of the base-isolated structure is required and when the displacements of the base isolation system have to be reduced (Spizzuoco et al. 2016).

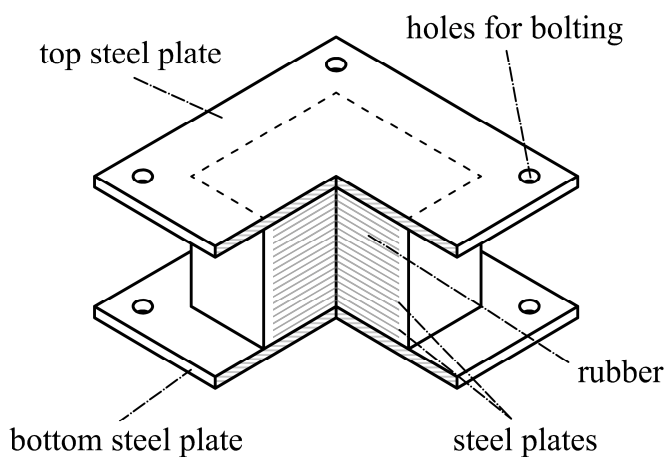
In the following, the two common types of seismic isolation devices, namely, elastomeric and sliding bearings, are described. Furthermore, the results of an extensive series of experimental tests, conducted at the Department of Industrial Engineering of the University of Naples Federico II on a Recycled Rubber-Fiber Reinforced Bearing and four Wire Rope Isolators, are presented.

3.2 Elastomeric Bearings

3.2.1 Introduction

Elastomeric bearings are seismic isolation devices made of alternate layers of rubber (5-20 mm thick) and thin reinforcing steel plates (2-3 mm thick). Two thick steel plates (25-30 mm) are bounded to the top and bottom surfaces of the bearing to facilitate its connection and a rubber cover is used to wrap the bearing in order to protect steel plates from corrosion. Elastomeric bearings can be square or circular, as shown in Figure 3.1.

(a)



(b)

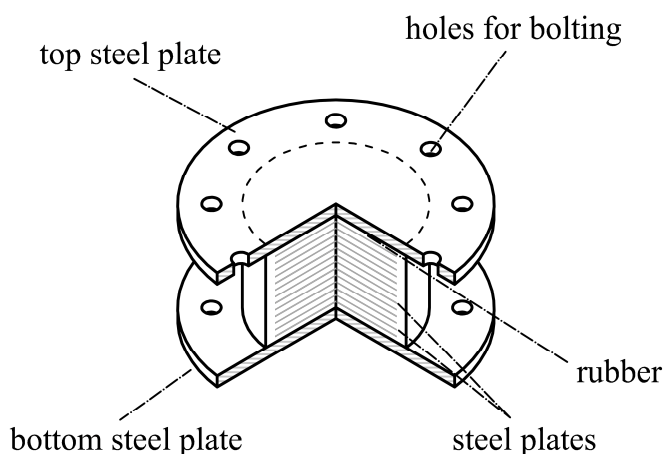


Figure 3.1. (a) Square and (b) circular elastomeric bearing.

Square elastomeric bearings are economical to manufacture, offer the advantage of simple connection configurations, and have compact geometry requiring a minimum of space for

installation: the space required for a square bearing is less than that for a circular bearing for the equivalent vertical load.

The rubber, a cross-linked polymer that can be produced in numerous compounds with different properties, is vulcanized and bounded to the steel in a single operation under heat and pressure in a mold. Vulcanization is the conversion of raw rubber by means of chemical crosslinking from a plastic state to an essentially elastic state (Hills, 1971).

The steel plates prevent bulging of the rubber and provide a vertical stiffness that is several hundred times the horizontal one without modifying the latter, which is controlled by the low shear modulus of the elastomer. The large vertical stiffness prevents undesirable rocking response of a base-isolated structure, reduces shear strain and creep deformations in the rubber, and increases the capacity of the bearing to carry axial load at large displacements.

Figure 3.2 illustrates the behavior of elastomeric bearings in horizontal and vertical directions.

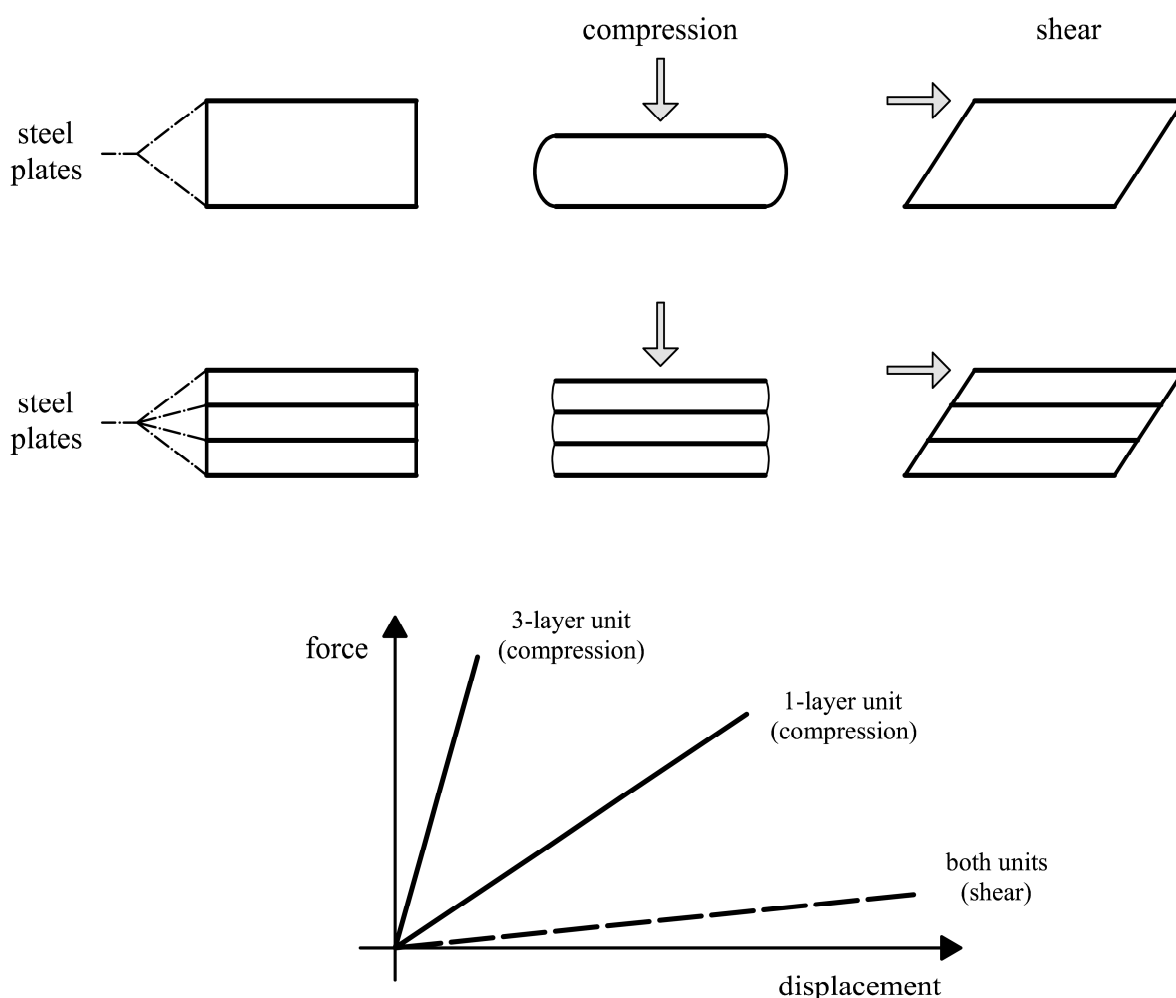
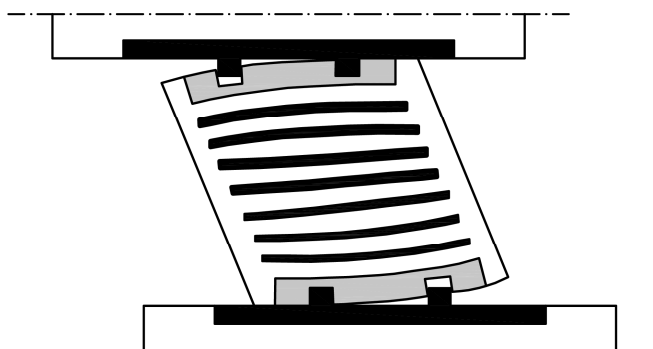


Figure 3.2. Behavior of elastomeric bearings in horizontal and vertical directions.

Elastomeric bearings can be installed dowelled or bolted, as shown in Figure 3.3. Dowels are used when tension in the bearing must be avoided. Bolted bearings are typically used nowadays because well fabricated elastomeric bearings have significant tensile strain capacity. In the undeformed state, when loaded only by vertical force, the buckling load of bearings installed in either configuration is theoretically the same. Under combined vertical load and lateral deformation, the two bearings have different instability limits.

(a)



(b)

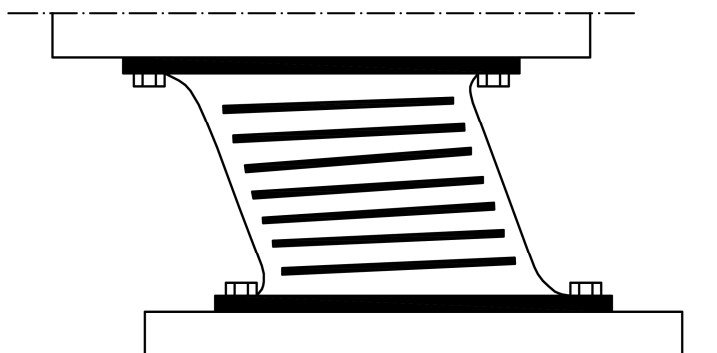


Figure 3.3. (a) Dowelled and (b) bolted elastomeric bearing.

Elastomeric bearings can be divided into three subcategories:

- Low Damping Rubber Bearings;
- High Damping Rubber Bearings;
- Lead Rubber Bearings.

3.2.2 Low Damping Rubber Bearings

Low Damping Rubber Bearings (LDRBs) are laminated elastomeric bearings made of natural rubber or synthetic rubber.

Generally, within a relatively large displacement range, that is, a rubber shear strain smaller than 75 %:

- low temperature has a substantial effect on both stiffness and damping, resulting in increases in both quantities. The percent increase is greater when the exposure to low temperature is longer;
- high temperature has an insignificant effect on stiffness and damping, with small reductions in stiffness and damping;
- there are no scragging effects;
- the frequency of motion has insignificant effect on the mechanical properties, thus, the behavior can be assumed to be rate independent;
- the equivalent viscous damping ratio is generally less than 5 %.

Figure 3.4 shows the typical symmetric softening force-displacement hysteresis loop displayed by LDRBs within a relatively large displacement range.

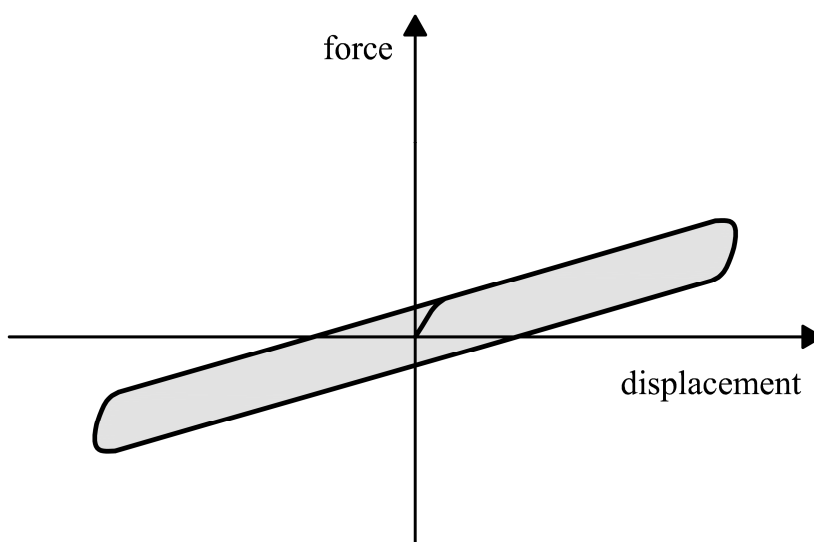


Figure 3.4. Typical hysteresis loop displayed by LDRBs at relatively large displacements.

Because of their low damping, LDRBs are normally used in conjunction with supplementary damping devices such as viscous dampers, steel bars, lead bars, and frictional devices.

3.2.3 High Damping Rubber Bearings

High Damping Rubber Bearings (HDRBs) are laminated elastomeric bearings with high inherent damping property obtained by adding extra fine carbons, oils, resins, or other proprietary fillers to the natural rubber compound.

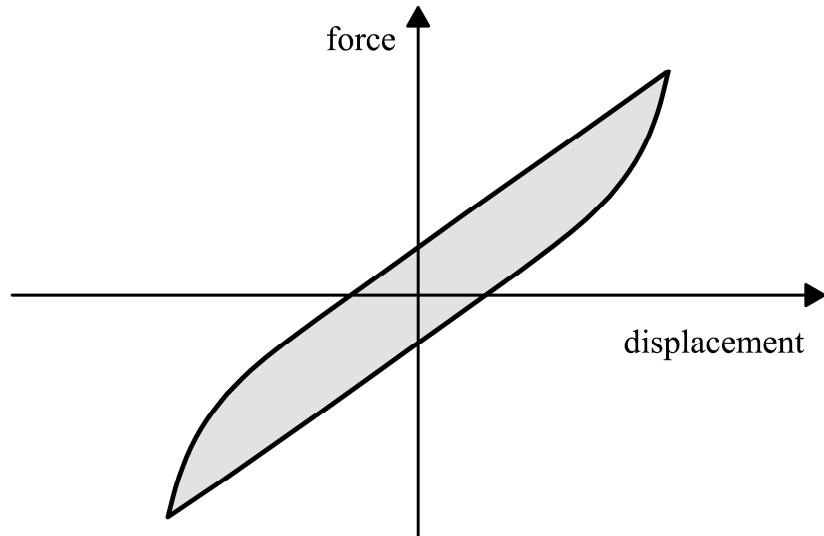
Generally, in HDRBs:

- an increase in the vertical load produces a reduction in the effective horizontal stiffness and an increase in the equivalent viscous damping ratio;
- an increase in the frequency of excitation results in modest increases in effective horizontal stiffness and equivalent viscous damping ratio;
- the effective stiffness and equivalent viscous damping ratio are relatively large at small shear strains (under 20 %). This is a desirable characteristic for minimizing the response under wind load and low level seismic load;
- the effective stiffness increases at large shear strains (above 150 %) because of the strain crystallization of the rubber matrix that is accompanied by an increase in the energy dissipation. This characteristic allows one to limit displacements under unanticipated input levels that exceed design levels;
- the equivalent viscous damping ratio range is generally between 5 % and 15 % at relatively large displacements, that is, shear strains around 100 %. Damping is neither viscous nor hysteretic, but somewhat in between;
- the maximum shear strain range is generally between 200 % and 350 %.

Figures 3.5a and 3.5b show the typical symmetric force-displacement hysteresis loop displayed by HDRBs at relatively large (shear strain between 20 % and 150 %) and large displacements (shear strain above 150 %), respectively. It is important to note that the shape of the hysteresis loops changes according to the displacements range: at relatively large displacements (Figure 3.5a), the hysteresis loops display a softening tangent stiffness whereas, at large displacements (Figure 3.5b), the device exhibits a hardening behavior.

HDRBs typically display higher characteristic strength and stiffness when tested for the first time. The properties under these conditions are generally termed *unscragged*. Subsequent testing under the same conditions results in stable but lower values of strength and stiffness, which are termed as *scragged* properties. Figure 3.6 shows the typical effects of scragging in a HDRB.

(a)



(b)

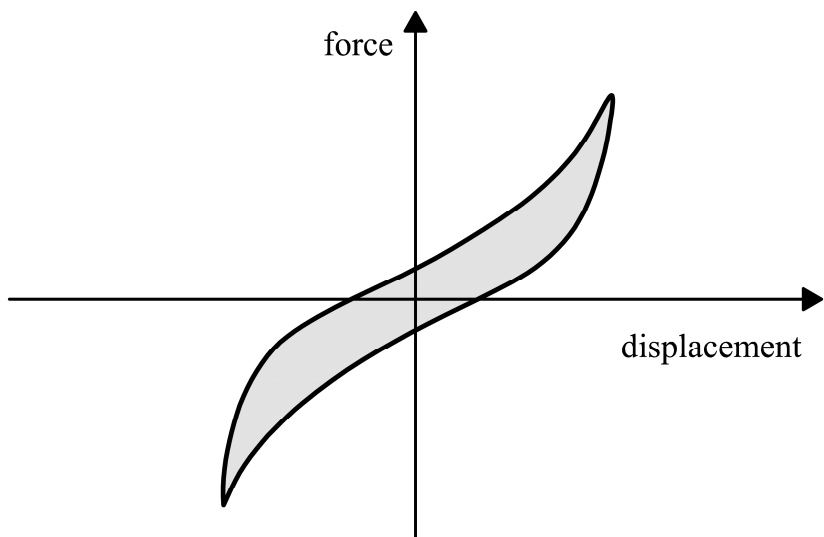


Figure 3.5. Typical hysteresis loop displayed by HDRBs at (a) relatively large and (b) large displacements.

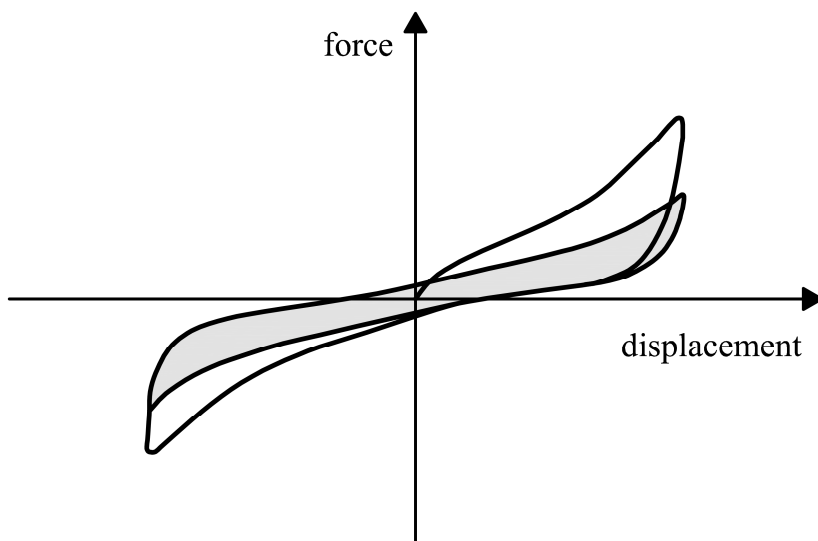
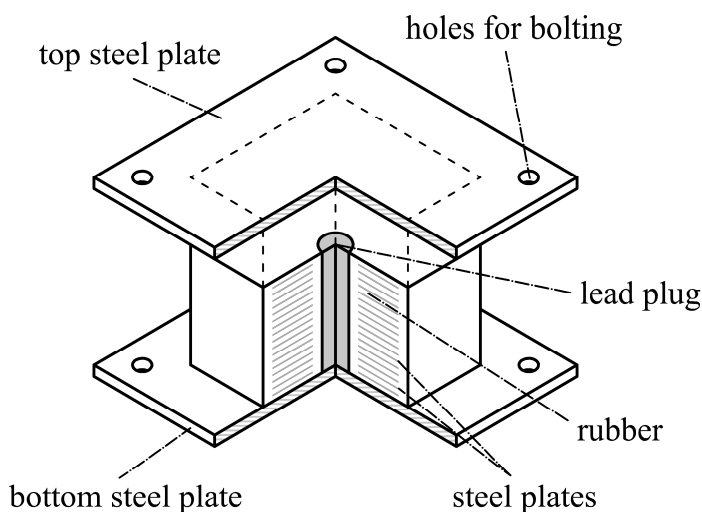


Figure 3.6. Typical effect of scragging in a HDRB.

3.2.4 Lead Rubber Bearings

Lead Rubber Bearings (LRBs) are laminated elastomeric bearings made of alternate layers of low damping natural rubber, reinforcing steel plates and a cylinder of lead inserted into a hole in the core of the bearing in order to increase the amount of dissipated energy. Figures 3.7a and 3.7b show a typical square and circular LRB, respectively.

(a)



(b)

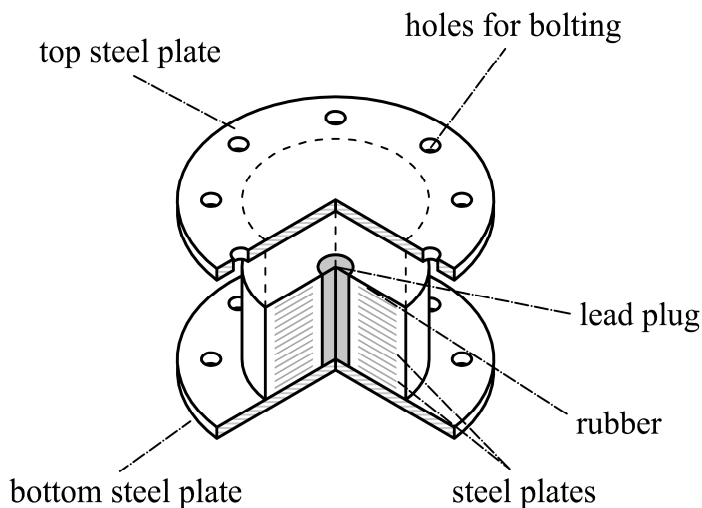


Figure 3.7. (a) Square and (b) circular LRB.

The lead must fit tightly in the elastomeric bearing, and this is achieved by making the lead plug slightly larger than the hole and forcing it in. The plug is typically cut longer than the height of the bearing so the core is compressed upon bolting the flange plates to the end

plates. The lead core expands laterally and wedges into the rubber layers between the steel plates. Under such confined conditions, the steel plates force the lead plug to deform in horizontal direction providing excellent energy dissipation capacity with a magnitude depending on the diameter of the lead plug. The lead in the bearing deforms physically at a relatively low stress of around 10 MPa.

LRBs have an initial high stiffness, which is about ten times the post-yield stiffness, before the yielding of the lead plug, and a low post-yield stiffness equal to the shear stiffness of the rubber.

Generally, in LRBs:

- temperature has a substantial effect on the effective stiffness and dissipated energy per cycle;
- the reduction in effective stiffness and dissipated energy with an increasing number of cycles depends on the heat generated in the lead core;
- the velocity of motion has a significant effect on the mechanical properties primarily because of the viscoelastic behavior of the rubber;
- the equivalent viscous damping ratio range is generally between 15 % and 35 %;
- the maximum shear strain range is generally between 125 % and 200 %.

Figure 3.8 shows the typical symmetric softening force-displacement hysteresis loop with bilinear characteristics displayed by LRBs at both small and large displacements.

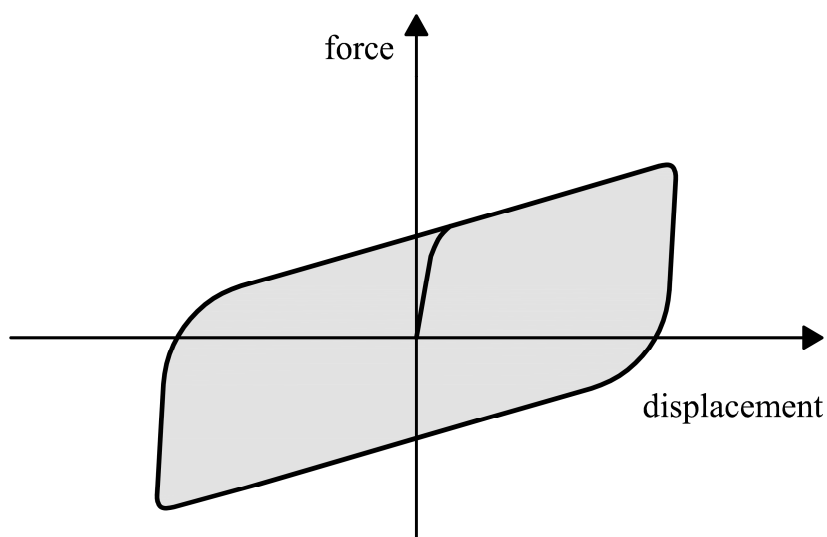


Figure 3.8. Typical hysteresis loop with bilinear characteristics displayed by LRBs at small and large displacements.

3.2.5 Unbonded Elastomeric Bearings with Deformable Reinforcing Layers

Bonded steel reinforced elastomeric bearings and unbonded elastomeric bearings having deformable reinforcing layers, such as Fiber Reinforced Bearings (FRBs), display a different deformed configuration when subjected to horizontal loads or displacements under the effect of the vertical load.

In conventional bonded elastomeric bearings (Figure 3.9a), the compression is carried through the overlap region between top and bottom surfaces, and the unbalanced moment is carried by tension stresses in the regions outside the overlap. Unbonded elastomeric bearings with deformable reinforcing layers show a rollover deformation, such as the one represented in Figure 3.9b, with portions of the isolator detaching from the structure (Kelly and Takhirov 2001, Kelly and Takhirov 2002, Kelly and Konstantinidis 2007, Toopchi-Nezhad et al. 2007, Mordini and Strauss 2008, Russo et al. 2008, Toopchi-Nezhad et al. 2008, Toopchi-Nezhad et al. 2009, Russo and Pauletta 2013). These portions are then substantially unstressed (Kelly and Konstantinidis 2007, Toopchi-Nezhad et al. 2011), hence no traction develops between the reinforcements and the elastomer. In this case, the moment created by the offset of the resultant compressive loads balances the moment created by the applied shear.

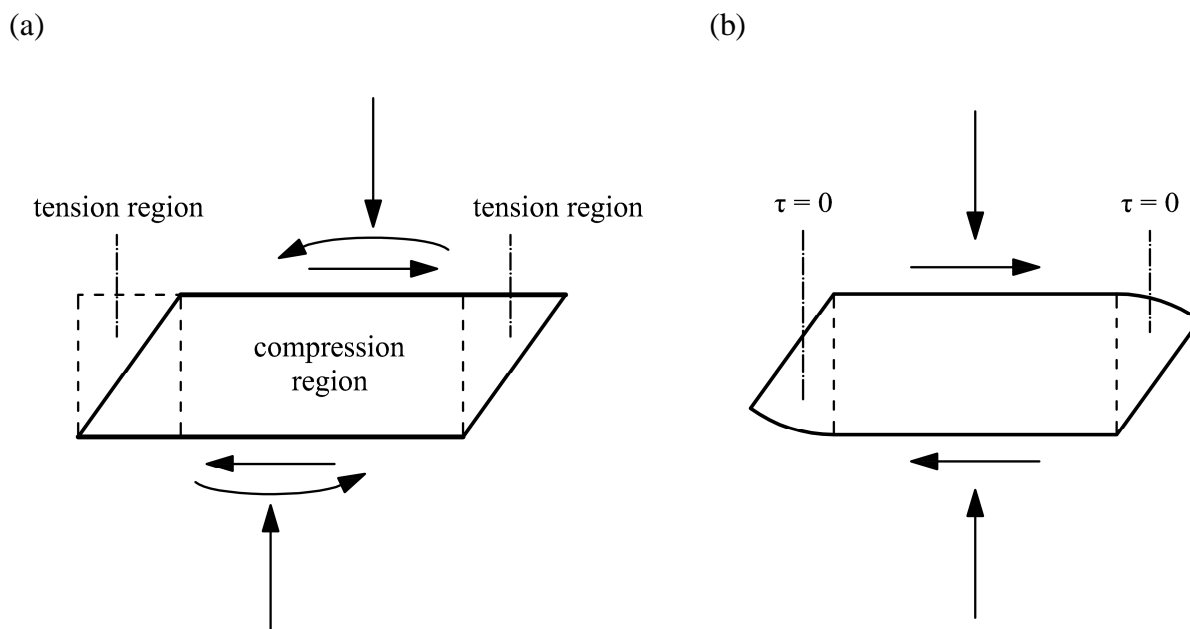


Figure 3.9. Deformed configuration of (a) bonded steel reinforced elastomeric bearing and (b) unbonded elastomeric bearing with deformable reinforcing layers loaded in compression and shear.

3.2.5.1 Recycled Rubber-Fiber Reinforced Bearings

3.2.5.1.1 Introduction

Steel reinforced elastomeric bearings are generally heavy and expensive. Most of their weight derives from two steel end plates and a consistent number of thin reinforcing steel plates used to achieve the desired vertical stiffness. Their high cost is due to a highly labor-intensive manufacturing process that ends with the vulcanization of the compounded rubber layers and the bonding of the steel reinforcements.

The manufacturing cost of FRBs is greater than that of traditional bearings, due to the major cost of the fibers. Anyhow, the costs connected with the labor involved in preparing the steel reinforcement (cutting, sandblasting, cleaning with acid, coating with bonding compound) are eliminated. Moreover, the absence of end plates for the anchorage to the structure and the substitution of the steel reinforcements with fiber ones reduces the isolator weight. Hence, being FRBs much lighter than the traditional ones and also less voluminous, transportation and installation are simpler and the relevant costs are lower. It results that the overall cost of a FRB is a little lower than the one of a traditional steel reinforced elastomeric bearing (Russo et al. 2013).

Spizzuoco et al. (2014) demonstrated that the use of recycled rubber, derived from used tires and rubber factory leftovers, represents an ideal possibility of a further significant costs reduction. The prototyping manufacturing of the proposed Recycled Rubber-Fiber Reinforced Bearings (RR-FRBs) was made by the Italian Company Isolgomma S.r.l. (Vicenza, Italy), specialized in the use of recycled rubber for the production of antivibrating mats for railway applications. The Company has computed for the prototype bearing a total cost of about ten Euros, whereas the market price of an equivalent traditional steel reinforced rubber isolator is ten times larger. Most of this difference is due to the costs of the natural rubber and the vulcanization process. The manufacturing of a FRB anyhow includes the latter two costs, while it reduces the installation cost due to the absence of the end plates. For this reason, the ratio between the cost of a FRB and the cost of an equivalent RR-FRB remains significant.

In the following, the experimental force-displacement hysteresis loops, obtained during cyclic tests conducted on a RR-FRB adopting a testing machine available at the Department of Industrial Engineering of the University of Naples Federico II, are presented.

3.2.5.1.2 Description of Tested Device

Figure 3.10 shows the tested RR-FRB, manufactured by Isolgamma S.r.l. (Vicenza, Italy), which is made of 12 layers of recycled rubber and 11 high strength quadri-directional carbon fiber fabric sheets used as reinforcing elements. The device is square in plan with dimensions 7 cm x 7 cm and has a total height of approximately 6.3 cm. The equivalent thickness of the carbon fiber layers is 0.007 cm. The shear modulus of the recycled rubber, under the applied vertical load $P_v = 16.9$ kN, is equal to 1 MPa at 100 % shear strain.



Figure 3.10. Tested RR-FRB.

3.2.5.1.3 Experimental Tests Results

The RR-FRB has been tested in unbounded configuration by imposing, in two different horizontal loading directions, namely, 0° and 45° directions (Figure 3.11), three cycles of harmonic displacement, having frequency $f = 0.87$ Hz, under the effect of a constant vertical pressure of 3.45 MPa, for eight different values of amplitude A , that is, 1 cm, 1.5 cm, 2 cm, 2.5 cm, 3 cm, 3.5 cm, 4 cm, and 4.5 cm.

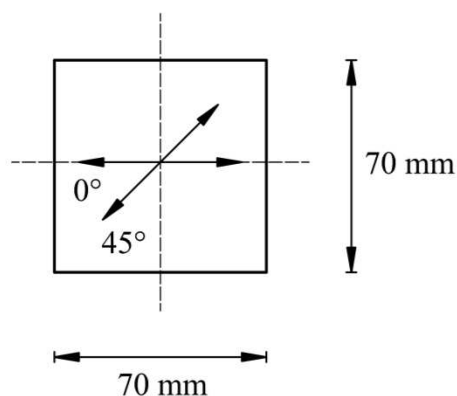
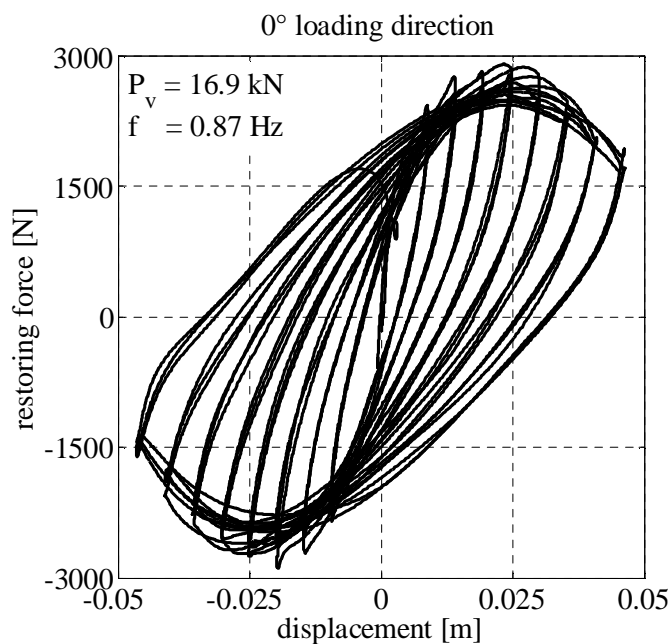


Figure 3.11. Loading directions.

Figures 3.12a and 3.12b show the experimental hysteresis loops obtained in 0° and 45° loading directions, respectively. According to the experimental tests results, the RR-FRB exhibits a softening behavior at relatively large displacements and a post-softening behavior at large displacements.

(a)



(b)

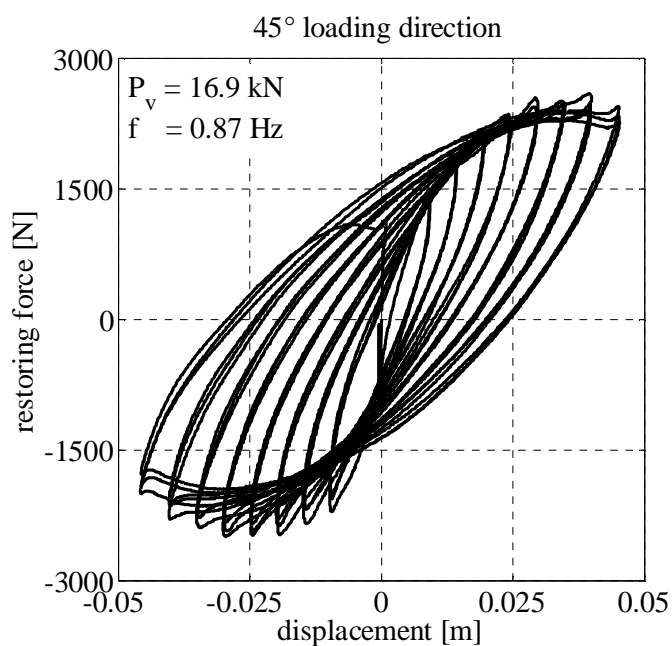


Figure 3.12. Experimental hysteresis loops of the tested RR-FRB obtained in (a) 0° and (b) 45° loading directions.

3.3 Sliding Bearings

3.3.1 Introduction

Sliding bearings are seismic isolation devices which allow one to achieve low horizontal stiffness through the action of sliding and to dissipate energy through the friction damping occurring at the sliding interface.

Sliding bearings can be divided into two subcategories:

- Flat Surface Sliding Bearings;
- Curved Surface Sliding Bearings.

3.3.2 Flat Surface Sliding Bearings

Figure 3.13 shows two different types of Flat Surface Sliding Bearings (FSSBs), namely, Pot and Disk FSSBs.

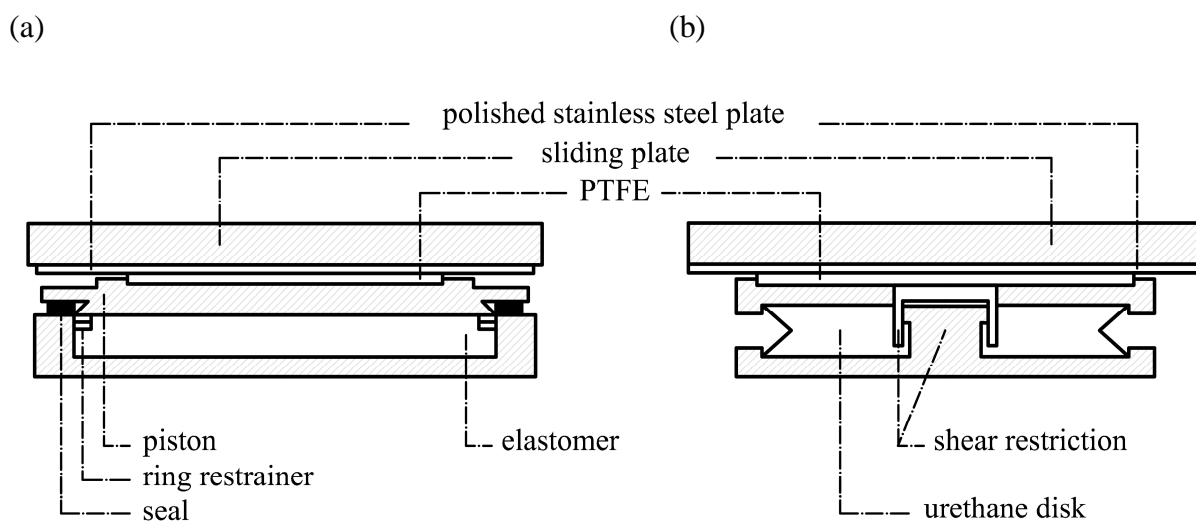


Figure 3.13. FSSBs: (a) Pot and (b) Disk FSSB.

Materials used for the sliding interface of these bearings are typically polished stainless steel in contact with unfilled or filled Polytetrafluoroethylene (PTFE or Teflon). To achieve significant energy dissipation capability, the PTFE needs to be unlubricated.

The frictional force F at the sliding interface of a FSSB can be described as:

$$F = \mu N, \tag{3.1}$$

where μ is the coefficient of friction and N is the normal load on the interface.

The static friction force is the maximum force that must be overcome to initiate macroscopic motion. This force is generally called breakaway friction force. Upon initiation of motion, the friction force generally drops, that is, the static friction force is typically higher than the sliding friction force, the latter being measured at a very low velocity of sliding, immediately following initiation of motion. Thus, it is important to distinguish between the static (or breakaway) coefficient of friction, μ_b , and the sliding coefficient of friction, μ_s .

The friction coefficient depends on several parameters such as the velocity of sliding, the normal load, and the temperature.

Figure 3.14 illustrates the dependency of the coefficient of friction of PTFE-polished stainless steel interface on the velocity of sliding and normal load. The behavior is characteristic of clean, unlubricated interfaces at normal ambient temperature, that is, around 20 °C. The static or breakaway value is shown at zero velocity of sliding. The sliding value is characterized by a low value immediately following initiation of sliding, $\mu_{s,min}$, and a progressively increasing value as the velocity increases. At large velocities, the sliding value attains a constant value, $\mu_{s,max}$. Increases in normal load result in reduction of the coefficient of friction; the percentage rate at which $\mu_{s,max}$ reduces diminishes at some limiting value of the normal load.

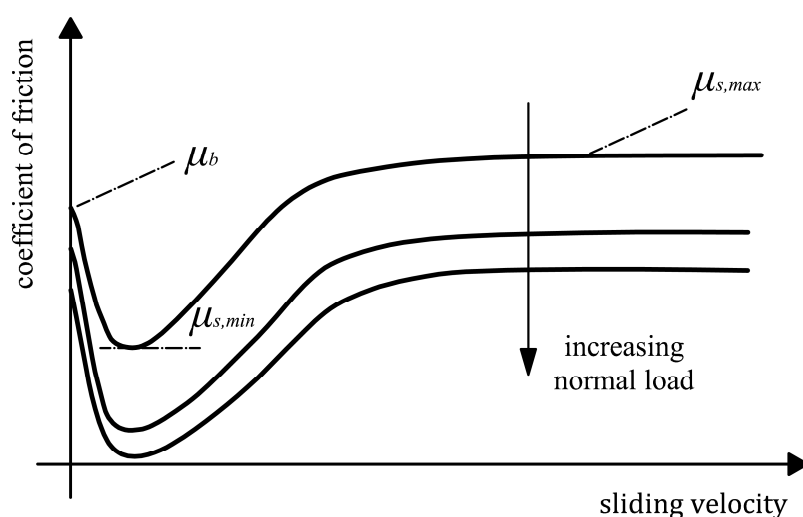


Figure 3.14. Dependency of friction coefficient of PTFE-polished stainless steel interface on sliding velocity and normal load.

Figure 3.15 illustrates the coefficient of friction as function of the sliding velocity for different values of temperature. It is evident that the temperature has a dramatic effect on the static and the very low velocity coefficients of friction, that is, μ_b and $\mu_{s,min}$.

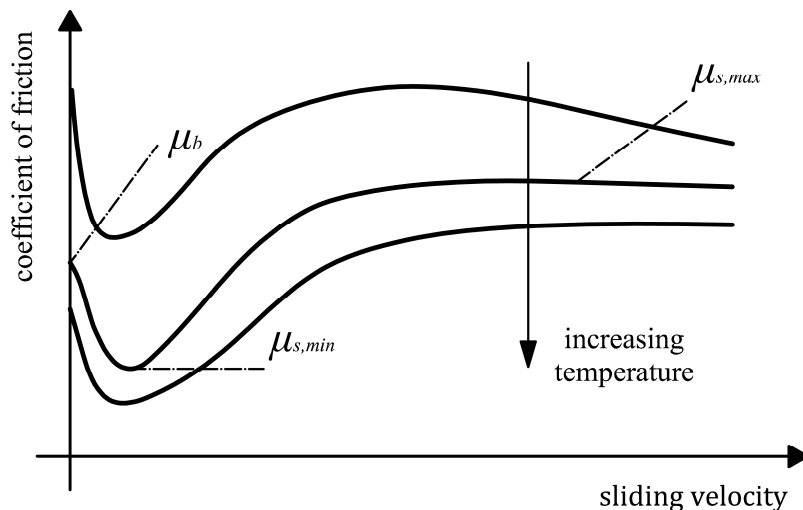


Figure 3.15. Dependency of friction coefficient of PTFE-polished stainless steel interface on sliding velocity and temperature.

Figure 3.16 shows the typical symmetric softening force-displacement hysteresis loop with rigid-plastic characteristics displayed by FSSBs.

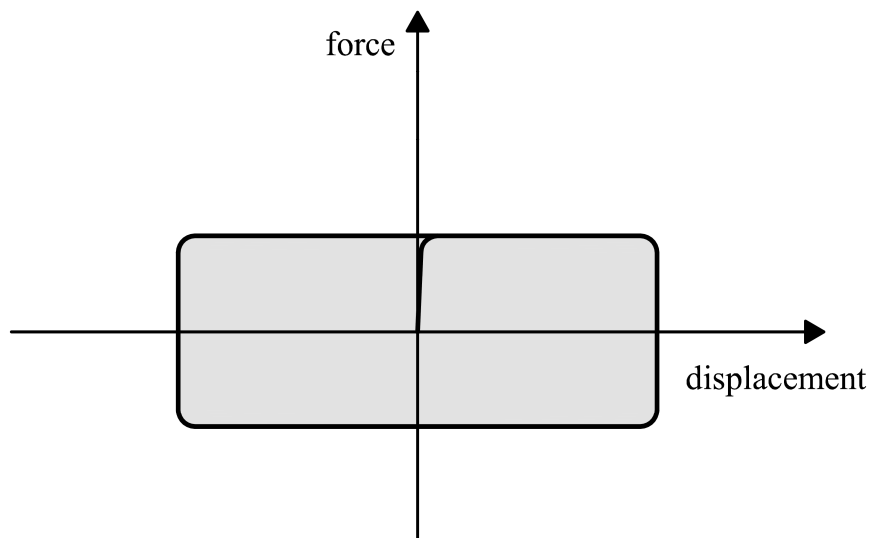


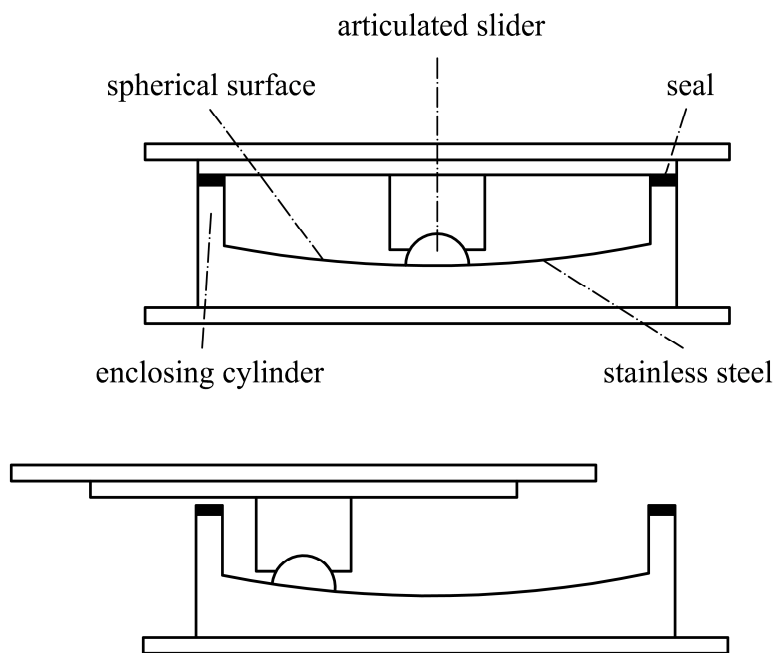
Figure 3.16. Typical hysteresis loop with rigid-plastic characteristics displayed by FSSBs.

FSSBs do not have the capability to return the structure to its initial position after an earthquake since they do not generate restoring forces. Thus, they have to be adopted in conjunction with recentering devices.

3.3.3 Curved Surface Sliding Bearings

Figure 3.17 shows two different types of Curved Surface Sliding Bearings (CSSBs), namely, Friction Pendulum Bearing (FPB) and Double Friction Pendulum Bearing (DFPB).

(a)



(b)

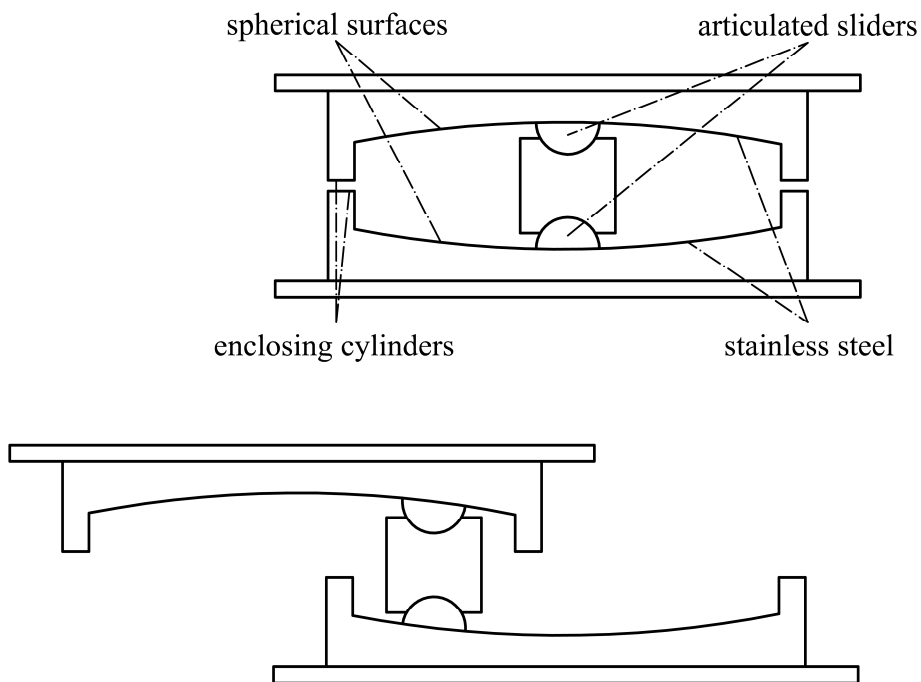


Figure 3.17. CSSBs: (a) FPB and (b) DFPB.

FPBs consist of an articulated slider that moves on a concave spherical surface. The slider is coated with a low-friction and high-pressure capacity composite material, typically PTFE, and the spherical surface is overlain by polished stainless steel. FPBs also include an enclosing cylinder that provides a lateral displacement restraint and protects the interior components from environmental contamination.

FPBs have an inherent ability to recenter the supported structure: as the slider moves along the spherical surface, it causes the supported structure to rise, developing a gravity restoring force that helps bring the structure back to its original position.

The force F required to impose a lateral displacement u in a FPB is given by:

$$F = \frac{N}{R}u + \mu N, \quad (3.2)$$

where N is the vertical load on the bearing, R is the effective radius of curvature of the sliding interface, and μ is the coefficient of sliding friction.

Figure 3.18 shows the typical symmetric softening hysteresis loop displayed by FPBs.

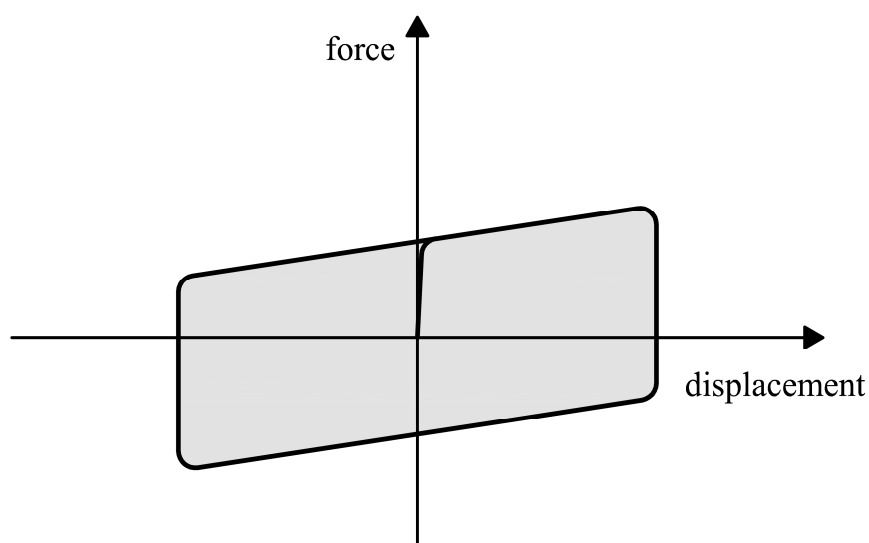


Figure 3.18. Typical hysteresis loop displayed by FPBs.

DFPBs consist of two facing concave stainless steel surfaces. The upper and lower concave surfaces have radii of curvature which can be different. The coefficients of friction of the concave surfaces can also be different. An articulated slider faced with a non-metallic sliding material separates the two surfaces. The articulation is necessary for the appropriate distribution of pressure on the sliding interface and to accommodate differential movements along the top and bottom sliding surfaces.

3.4 Metal Devices

3.4.1 Wire Rope Isolators

3.4.1.1 Introduction

Wire Rope Isolators (WRIs) are metal devices that have demonstrated to be effective in protecting sensitive equipment from shock and vibration and have been originally used in numerous military, electronic and air space applications (Tinker and Cutchins 1992). All the different types of WRIs, such as helical, arch or spherical devices, are made of two basic elements: a stainless steel cable and two aluminum alloy or steel retainer bars where the cable is embedded.

As far as the use of WRIs as seismic devices is concerned, Demetriades et al. (1993) showed that an isolation system including stiff WRIs can reduce the acceleration transmitted to light but costly equipment allowing very small displacements in contrast to the classical base isolation approach of increasing the fundamental natural period of the system. Serino et al. (1995a, 1995b) and Di Donna and Serino (2002) investigated the use of WRIs for the seismic protection of circuit breakers of a transformation open-air substation, thus concluding that these devices permit to reduce remarkably stresses in the porcelain insulators. Alessandri et al. (2015a, 2015b) also investigated the effectiveness of a base isolation system including adequately designed WRIs in reducing the seismic demand of a high voltage ceramic circuit breaker.

In the research literature there are no applications of WRIs in the seismic isolation of structures, such as new or existing buildings or bridges. Indeed, although WRIs are generally stiffer in the vertical direction than in the other two principal horizontal directions (Demetriades et al. 1993), namely, Roll and Shear directions, the value of the vertical load which can be supported by these metal devices is not high enough to allow their use for the seismic protection of structures. However, a shaking table experimental campaign, performed at the Department of Structures for Engineering and Architecture of the University of Naples Federico II (Italy) on a scaled structure mock-up, seismically isolated using four curved surface sliders and four WRIs, have shown that the latter can be strongly useful when the complete recentering of the base-isolated structure is required and when the displacements of the base isolation system have to be reduced (Spizzuoco et al. 2016).

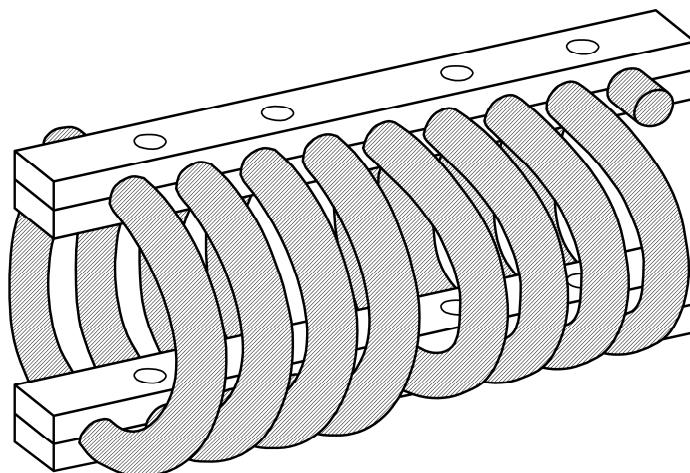
In order to allow the use of these metal devices with other different types of seismic isolators, such as sliding or elastomeric bearings, for the seismic protection of lightweight structures, an accurate characterization of their mechanical properties is required. The experimental studies described in Demetriades et al. (1993) and Alessandri et al. (2015a, 2015b) do not provide enough information to investigate the use of WRIs in a base isolation system of a seismically base-isolated structure. Indeed, their dynamic behavior in Roll and Shear directions and the influence of the vertical load have been studied only in the small displacements range.

To this end, an extensive series of dynamic tests was conducted at the Laboratory of the Department of Industrial Engineering of the University of Naples Federico II (Italy) on four different WRIs, by imposing cyclic sinusoidal displacements having different amplitudes and frequencies, under different values of the vertical load. More specifically, this experimental program was aimed at studying the influence of the displacement amplitude, frequency, vertical load, device geometrical characteristics and wire rope diameter on the dynamic behavior of the selected WRIs in the two principal horizontal directions. In addition, static tests were also carried out to evaluate the static to dynamic effective stiffness ratios for different values of displacement and applied vertical load.

3.4.1.2 Description of Tested Devices

The selected WRIs, manufactured by Powerflex S.r.l. (Limatola, Italy), are made of a wire rope wound in the form of a helix and two slotted metal retainer bars in which the cable is embedded, as shown in Figure 3.19a. The cross section of the wire rope, which is constructed by winding a number of strands around an inner core, is shown in Figure 3.19b. Each strand has an axial member around which the individual metal wires are wrapped. The rope of the tested devices is made of six strands, each having 25 steel wires, plus a central one with 49 wires. The material of the wires is American Iron and Steel Institute (AISI) Stainless Steel Type 316 whereas the material of the two metal bars is aluminum alloy.

(a)



(b)

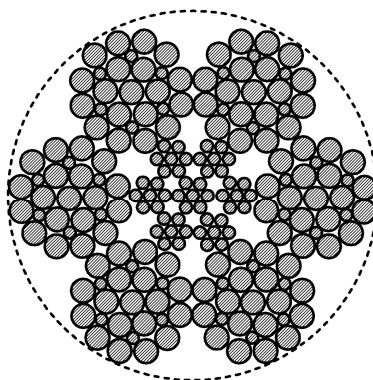


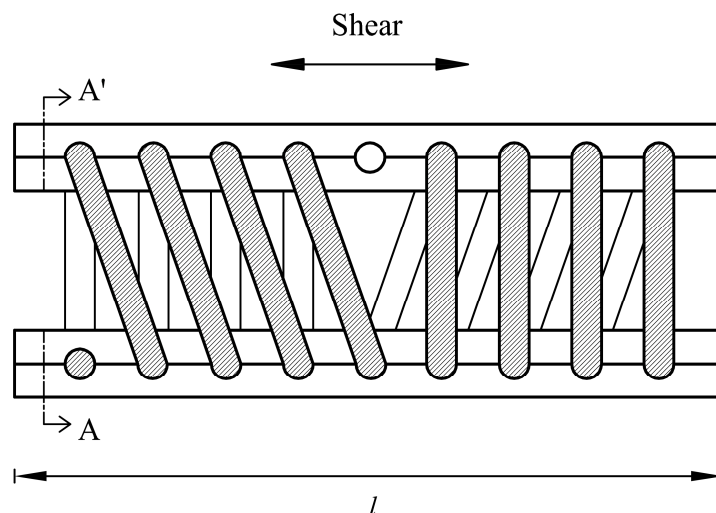
Figure 3.19. (a) WRI; and (b) wire rope cross section.

In order to study the influence of the height to width ratio, h/v , of the loop and the wire rope diameter, d_r , on the dynamic behavior of WRIs in the two principal horizontal directions, namely, Roll and Shear directions, four devices having 8 loops have been selected for experimental tests. Their geometrical characteristics are presented in Table 3.1 with reference to Figure 3.20.

Table 3.1. Geometrical characteristics of tested WRIs.

WRI	l [mm]	h [mm]	v [mm]	h/v	d_r [mm]
PWHS 16010	267	100	110	0.90	16
PWHS 16040	267	125	150	0.83	16
PWHS 16040 S	267	125	150	0.83	19
PWHS 16060	267	145	185	0.78	16

(a)



(b)

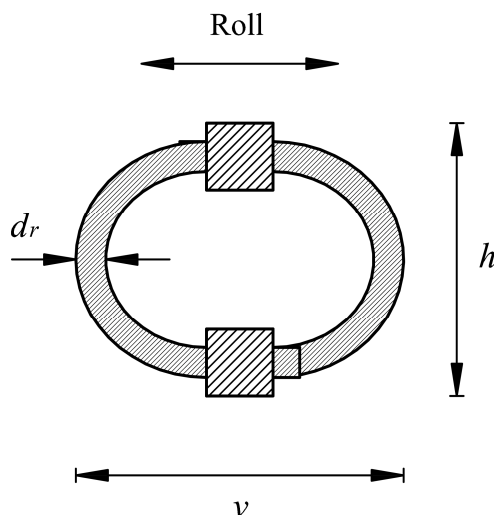


Figure 3.20. Schematic of WRIs PWHS 160: (a) lateral view; (b) section A-A'.

3.4.1.3 Experimental Study

The experimental campaign here presented was aimed at studying the influence of the displacement amplitude, frequency, vertical load, device geometrical characteristics and wire rope diameter on the dynamic behavior of WRIs in Roll and Shear directions. Since in a base-isolated structure the maximum vertical displacement of the base isolation system is considerably smaller than the horizontal one (Spizzuoco et al. 2016), only the dynamic behavior in the horizontal directions has been studied. Static tests have been also carried out to better investigate the static horizontal response of these devices in three displacements

ranges, under different values of applied vertical load. The experimental set-up and the dynamic and static tests are described in the following.

3.4.1.3.1 Experimental Set-up

The experimental investigation of the dynamic and static responses of WRIs in the two principal horizontal directions has been performed by adopting the testing machine (TM) available at the Laboratory of the Department of Industrial Engineering of the University of Naples Federico II (Pagano et al. 2014). As shown in Figure 3.21, the TM consists of two hydraulic actuators for loading in both horizontal and vertical directions, thus allowing one to impose horizontal displacement or load histories to the tested device with a constant vertical compression. Four guiding rollers, two on each side of the horizontal lower frame, prevent lateral movement of the TM basement. This equipment can be used as a 1d shaking table machine (Calabrese et al. 2013, Strano and Terzo 2014). The maximum vertical force, exerted by means of the vertical actuator and transferred through the horizontal upper plate, is equal to 190 kN. The horizontal hydraulic actuator, powered by a 75 kW AC electric motor, has a maximum stroke of ± 200 mm, a maximum force of 50 kN and a maximum speed of 2.2 m/s.

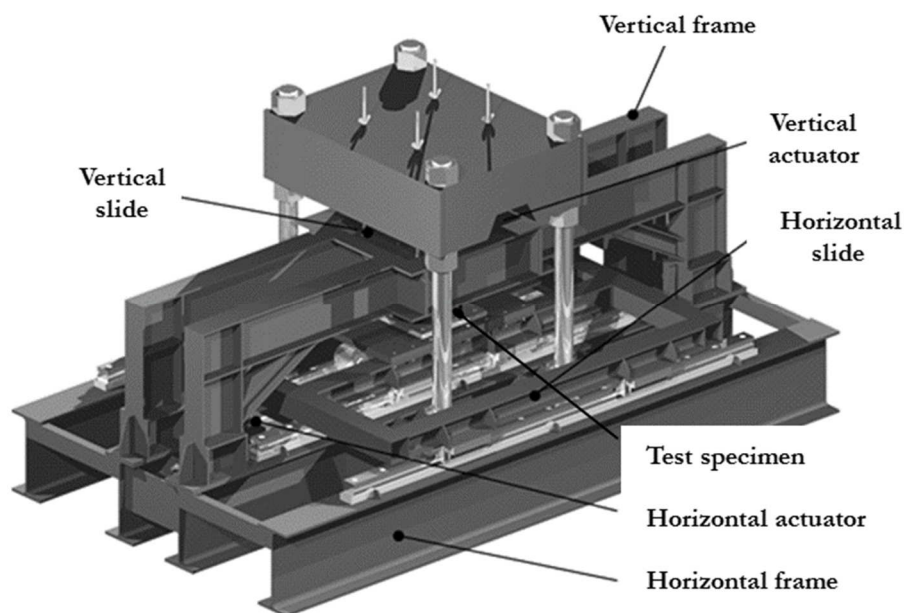
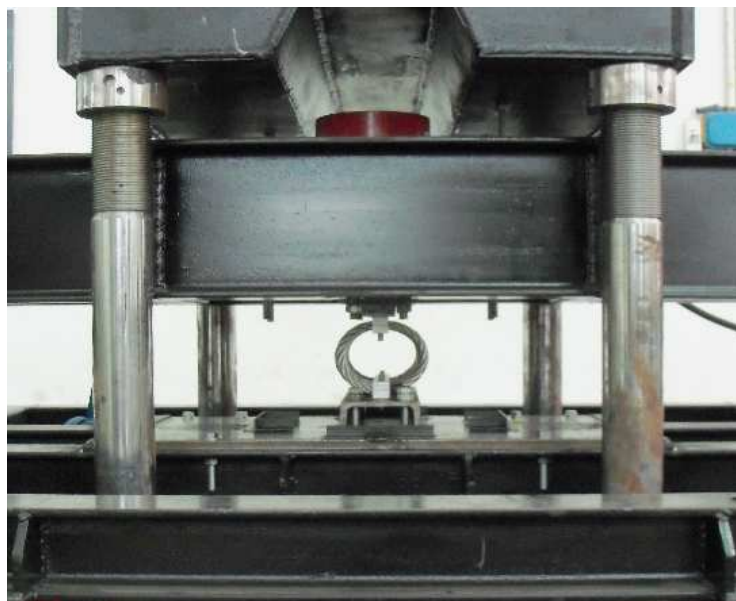


Figure 3.21. TM adopted to perform experimental tests.

The tested WRIs have been mounted by fixing their aluminum retainer bars to the upper and lower rigid steel plates. Figures 3.22a and 3.22b show WRI PWHS 16040 mounted in Roll and Shear directions, respectively.

(a)



(b)

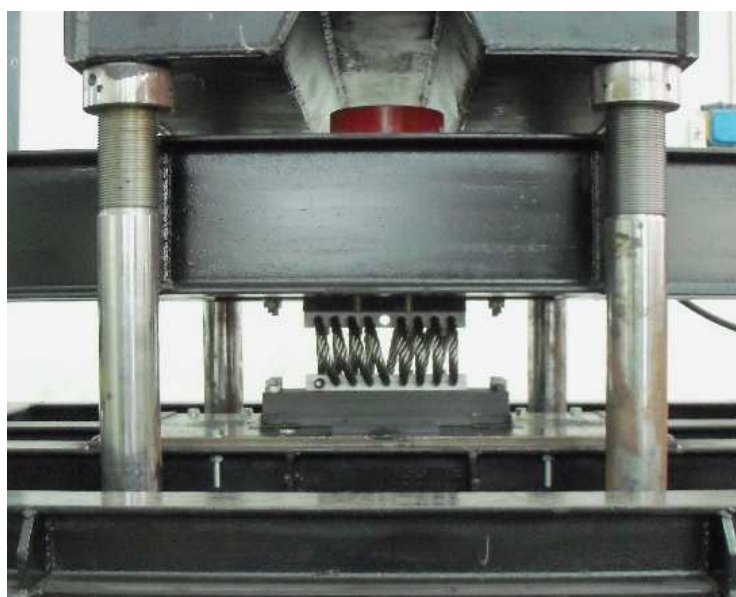


Figure 3.22. WRI PWHS 16040 mounted in: (a) Roll and (b) Shear directions.

The experimental apparatus has been instrumented in order to measure the time histories of the relative horizontal displacements between the lower and upper plates, the horizontal and vertical loads. All tests have been conducted at room temperature and the data was sampled at 250 Hz. Data acquisition and control of the hydraulic actuators have been carried out through a dedicated software package and a dSPACE DS1103 controller board (Pagano et al. 2013, Pagano et al. 2014).

3.4.1.3.2 Dynamic Tests

A large number of dynamic tests in Roll and Shear directions was conducted on the selected devices. Each test consisted in imposing five cycles of sinusoidal displacement having specified amplitude A and frequency f , under different values of vertical load P_v .

The dynamic response of WRIs has been analyzed in three displacements ranges, namely, small, relatively large and large displacements ranges. Three amplitude values have been chosen for each metal device, with the maximum value selected in order to avoid damages to the two aluminum alloy retainer bars during the experimental tests.

The influence of the frequency has been studied by imposing to WRI PWHS 16040 a sinusoidal motion with amplitude of 3 cm, without applying a vertical load. The frequency was assumed varying within the range $0.5 \div 2$ Hz.

The maximum value of the vertical load has been selected with the aim of obtaining a maximum vertical deflection less than one tenth of the device height h . The dynamic tests are listed in Table 3.2.

Table 3.2. Dynamic displacement-controlled tests in Roll and Shear directions.

WRI	no. of tests	vertical load [kN]	frequency [Hz]	amplitude [cm]
PWHS 16010	3+3	0	1	0.25, 0.5, 1
	3+3	2	1	0.25, 0.5, 1
PWHS 16040	3+3	0	1	1, 3, 6
	3+3	1.2	1	1, 3, 6
	3+3	2	1	1, 3, 6
	3+3	3	1	1, 3, 6
	4+4	0	0.5, 1, 1.5, 2	3
PWHS 16040 S	3+3	0	1	1, 3, 6
	3+3	2	1	1, 3, 6
PWHS 16060	3+3	0	1	1, 4, 8
	3+3	2	1	1, 4, 8

3.4.1.3.3 Static Tests

Static tests in Roll and Shear directions were also carried out to study the overall behavior of each WRI, that is, to estimate the effective horizontal stiffness by the secant line method and to evaluate the static to dynamic effective stiffness ratio for different values of maximum horizontal displacement and applied vertical load. In each static test, the horizontal

displacement has been increased linearly with a velocity of 0.5 mm/s. The static tests are listed in Table 3.3.

Table 3.3. Static displacement-controlled tests in Roll and Shear directions.

WRI	no. of tests	vertical load [kN]	max. displacement [cm]
PWHS 16010	2+2	0, 2	1
PWHS 16040	4+4	0, 1.2, 2, 3	6
PWHS 16040 S	2+2	0, 2	6
PWHS 16060	2+2	0, 2	8

3.4.1.4 Experimental Tests Results

In what follows, the results of the dynamic and static experimental tests are presented. The influence of the following parameters on the dynamic behavior of WRIs is described: (1) displacement amplitude, (2) frequency, (3) vertical load, (4) WRI geometrical characteristics and (5) wire rope diameter. Then, a comparison between the dynamic responses in Roll and Shear directions is presented, and finally the static behavior in both horizontal directions is analyzed.

Three parameters have been used to analyze the dynamic behavior of the tested WRIs in Roll and Shear directions: the average effective (or secant) stiffness $k_{eff,a}$, the average equivalent viscous damping ratio $\xi_{eq,a}$, and the average dissipated energy $E_{d,a}$, that is, the mean area computed on the experimental hysteresis loops.

The WRI effective stiffness, deduced by each cycle of harmonic motion, has been calculated by the formula:

$$k_{eff} = \frac{F_{max} - F_{min}}{u_{max} - u_{min}}, \quad (3.3)$$

where F_{max} and F_{min} are the forces recorded at the positive and negative maximum displacements u_{max} and u_{min} , respectively. This stiffness is interpreted as the overall stiffness of the device during one cycle of harmonic motion and is used to evaluate the elastic energy E_s . The average effective stiffness $k_{eff,a}$ has been calculated as mean value of those obtained from three of the five imposed cycles.

The equivalent viscous damping ratio of the device at each cycle has been evaluated as follows:

$$\xi_{eq} = \frac{E_d}{4 \pi E_s}, \quad (3.4)$$

where E_s is the restored elastic energy expressed as:

$$E_s = \frac{1}{2} k_{eff} u_a^2, \quad (3.5)$$

with u_a the average value of positive and negative maximum displacements given by:

$$u_a = \frac{u_{max} + |u_{min}|}{2}. \quad (3.6)$$

The average equivalent viscous damping ratio $\xi_{eq,a}$ has been calculated as mean value of those obtained from three of the five cycles of harmonic motion applied to the tested device.

A Matlab script was written to go through the experimental data file of a dynamic test, identify each force-displacement hysteresis loop and evaluate the mean value of each parameter, that is, $k_{eff,a}$, $\xi_{eq,a}$, and $E_{d,a}$.

As regards the static tests, the static effective (or secant) stiffness k_{eff}^{st} at displacement u^* has been estimated according to the secant line method as follows:

$$k_{eff}^{st} = \frac{F(u^*)}{u^*}, \quad (3.7)$$

where $F(u^*)$ is the recorded force corresponding to the applied displacement u^* .

3.4.1.4.1 Influence of Displacement Amplitude

The values of the average effective stiffness, equivalent viscous damping ratio and dissipated energy obtained from the dynamic tests performed along Roll and Shear directions on device PWHS 16040 are listed in Table 3.4; a sinusoidal motion, having frequency equal to 1 Hz, was applied in the two horizontal directions, without the effect of the vertical load, for three different values of amplitude.

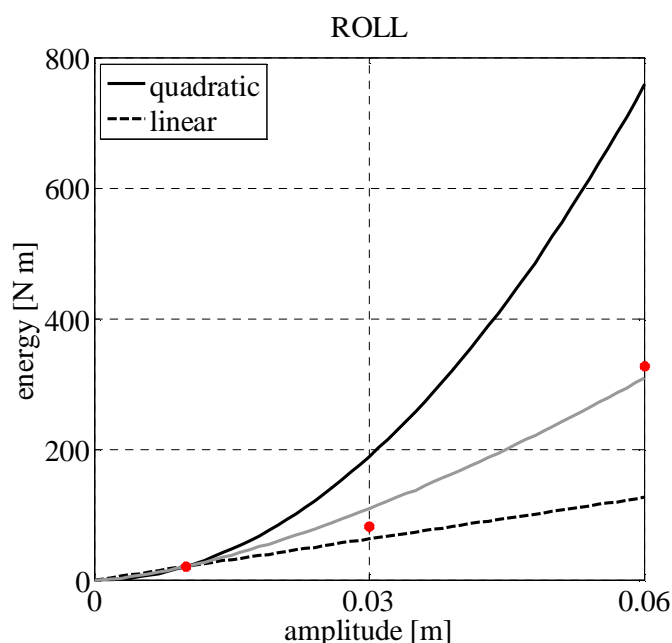
According to these results, the tested metal device is characterized by high effective stiffness and equivalent damping ratio in the range of small displacements. They decrease with increasing displacement amplitude in the relatively large displacements range, whereas, at larger displacements, the former increases dramatically and the latter continues to decrease.

Table 3.4. Influence of displacement amplitude | WRI PWHS 16040.

$f = 1 \text{ Hz}, P_v = 0 \text{ kN}$	amplitude [cm]	$k_{eff,a}$ [N/m]	$\xi_{eq,a}$ [%]	$E_{d,a}$ [N m]
Roll	1	131616.18	26.9	21.08
	3	96411.65	14.7	81.95
	6	172987.50	8.0	327.51
Shear	1	157702.20	21.5	20.02
	3	125189.71	13.8	99.76
	6	178735.04	9.8	413.25

In WRIs a significant proportion of energy is dissipated because of the interior rubbing and sliding friction between the intertwined strands (Demetriades et al. 1993, Piersol and Paez 2009). Table 3.4 shows that the amount of average dissipated energy increases with the displacement amplitude. In systems with viscous damping or rate-independent damping, the dissipated energy increases quadratically with displacement amplitude whereas, in a system with Coulomb damping, it is linear in displacement (Chopra 2012). In this case, the average dissipated energy is proportional to the displacement around the value of power 1.5 in Roll direction and 1.65 in Shear direction, as shown in Figure 3.23.

(a)



(b)

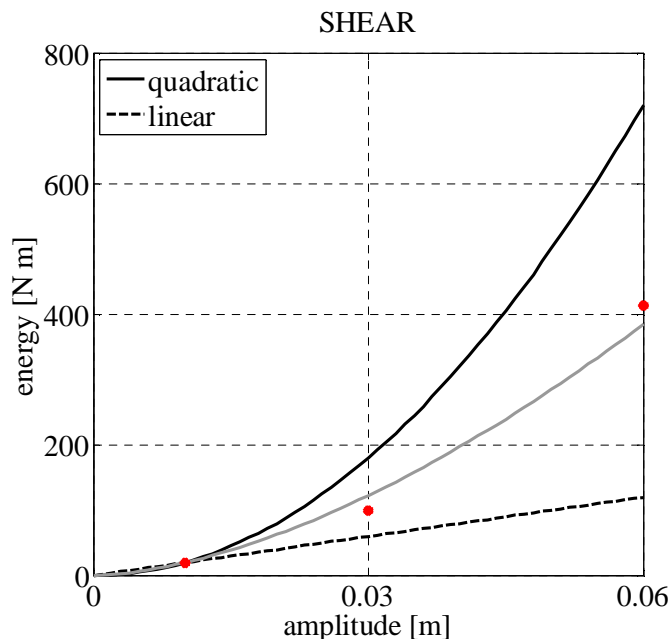
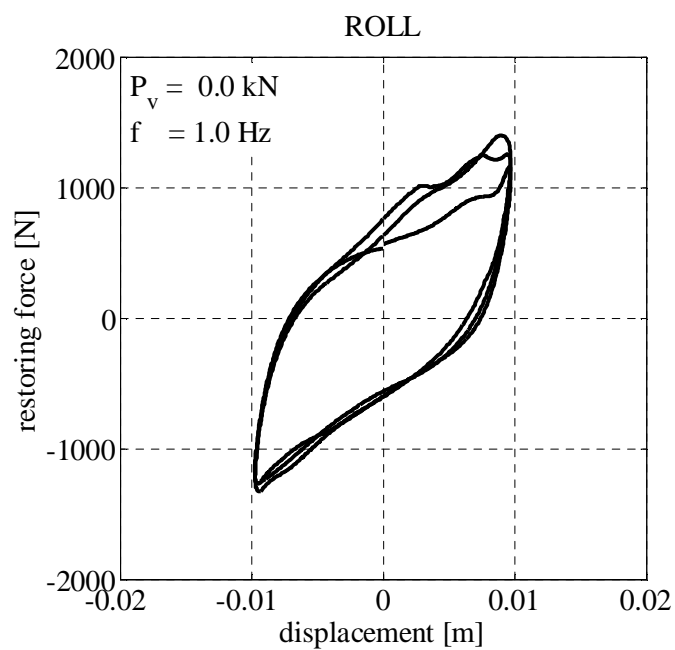


Figure 3.23. Average dissipated energy in WRI PWHS 16040 along (a) Roll and (b) Shear directions.

Figures 3.24, 3.25, and 3.26 show the symmetric force-displacement hysteresis loops obtained in the two horizontal directions for three different displacement amplitudes. It is worth to note that the shape of the hysteresis loops changes according to the displacements range: at small displacements, the hysteresis loops display a softening stiffness (Figure 3.24), whereas, in the relatively large displacements range, the device exhibits a hardening stiffness (Figure 3.25). When large horizontal displacements are applied, the metal device reaches the limit of deformation and a stronger nonlinear stiffening behavior can be observed (Figure 3.26). In spite of this, no damage to aluminum retainer bars was visible after the cyclic tests were completed.

Since the same dynamic behavior has been observed in the other three selected WRIs, their tests results are omitted.

(a)



(b)

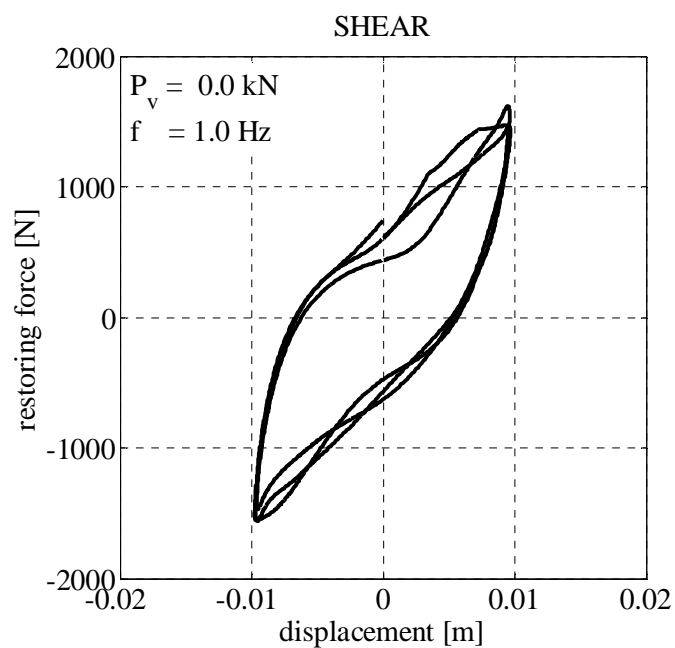
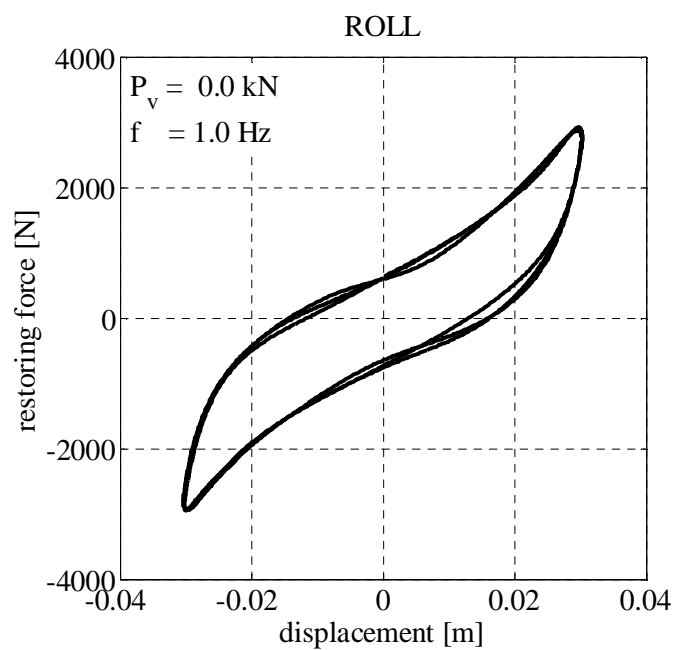


Figure 3.24. Experimental hysteresis loops of WRI PWHS 16040 obtained at small displacements in (a) Roll and (b) Shear directions.

(a)



(b)

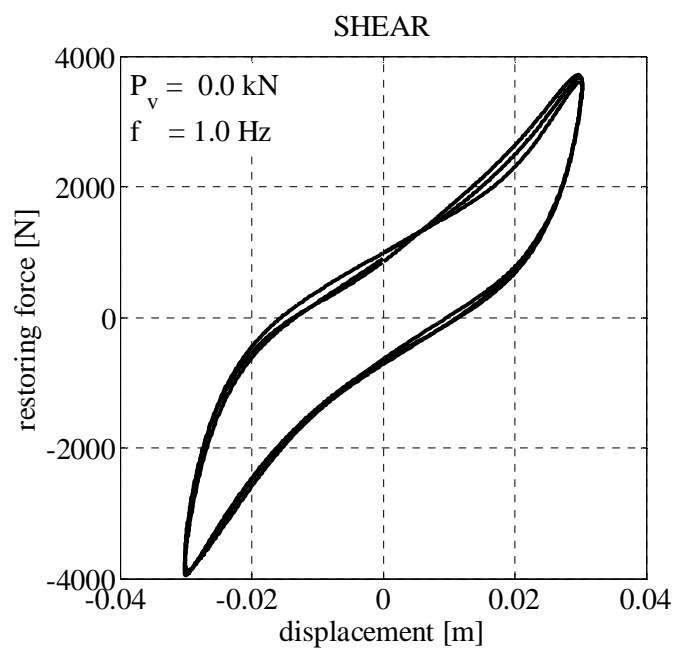
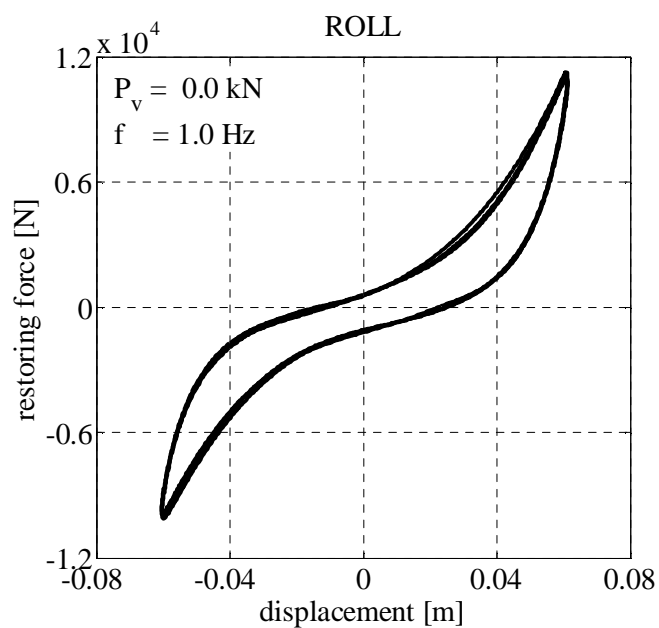


Figure 3.25. Experimental hysteresis loops of WRI PWHS 16040 obtained at relatively large displacements in (a) Roll and (b) Shear directions.

(a)



(b)

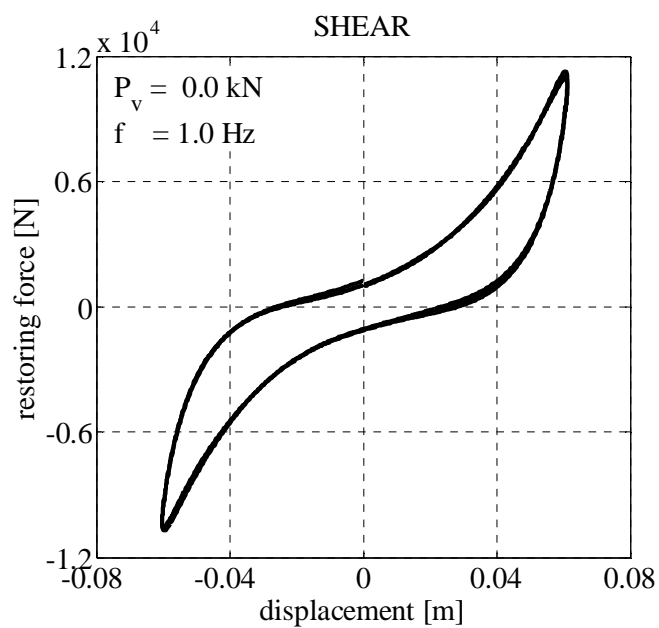


Figure 3.26. Experimental hysteresis loops of WRI PWHS 16040 obtained at large displacements in (a) Roll and (b) Shear directions.

3.4.1.4.2 Influence of Frequency

The experimental studies conducted on WRIs in the small displacements range by Demetriades et al. (1993) and Alessandri et al. (2015b) show the rate independent nature of these metal devices.

Interesting results have been obtained by studying the influence of the frequency on the dynamic behavior of the selected WRIs in the relatively large displacements range. Table 3.5 shows the dynamic tests results of WRI PWHS 16040 in Roll and Shear directions: the metal device was subjected to a harmonic sinusoidal motion having amplitude equal to 3 cm, without the effect of the vertical load, for different frequency values.

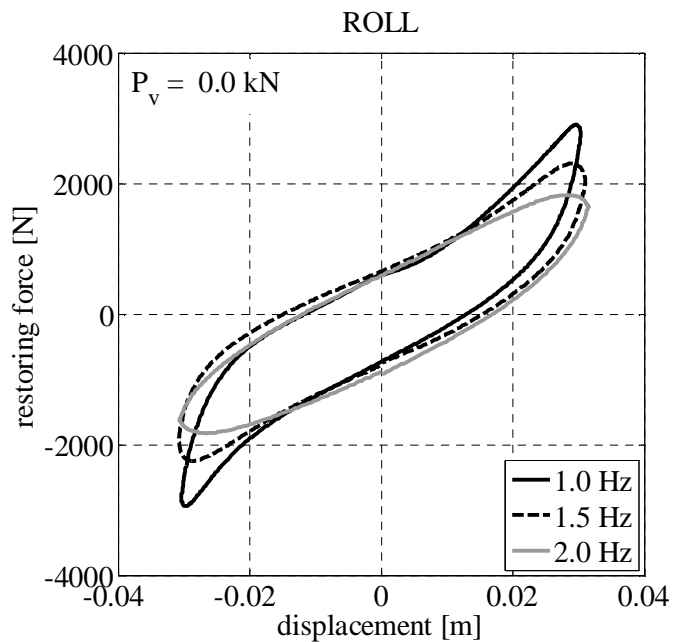
It can be observed that an increase in the frequency determines a decrease in the average effective stiffness, whereas the average equivalent damping ratio increases.

Table 3.5. Influence of frequency | WRI PWHS 16040.

$A = 3 \text{ cm}, P_v = 0 \text{ kN}$	frequency [Hz]	$k_{eff,a}$ [N/m]	$\xi_{eq,a}$ [%]	$E_{d,a}$ [N m]
Roll	0.5	91060.00	14.7	74.62
	1	96411.65	14.7	81.95
	1.5	73871.54	17.8	79.60
	2	57498.65	22.1	79.71
Shear	0.5	117302.66	13.8	90.09
	1	125189.71	13.8	99.76
	1.5	98304.42	19.1	113.31
	2	77313.19	20.3	98.35

Figures 3.27a and 3.27b shows the force-displacement hysteresis loops of the tested metal device, obtained in Roll and Shear directions. It is evident that, in the relatively large displacements range, a stronger hardening dynamic behavior is obtained at lower frequencies.

(a)



(b)

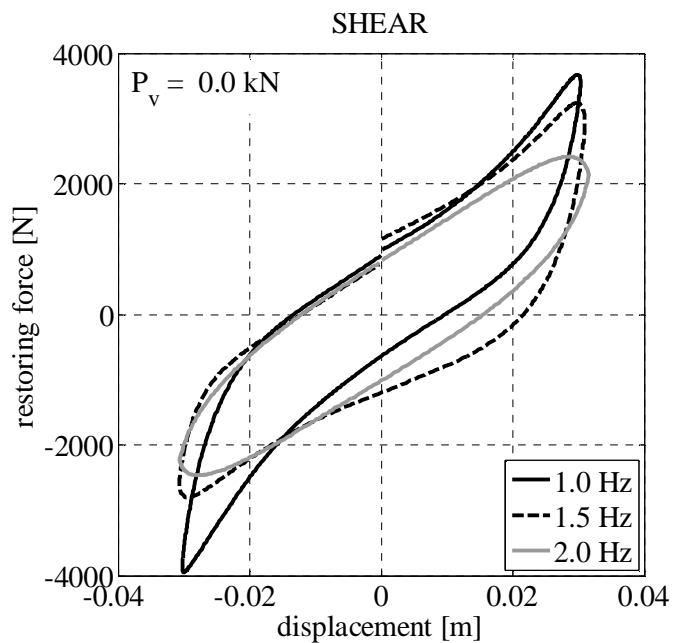


Figure 3.27. Influence of frequency on WRI PWHS 16040 hysteresis loops obtained in (a) Roll and (b) Shear directions.

3.4.1.4.3 Influence of Vertical Load

WRIs have flexibility in all directions, that is, horizontal and vertical directions. The vertical deflection of these metal devices depends on the height to width ratio h/v , and on the wire rope diameter d_r . Table 3.6 shows the vertical strain of each tested device, due to a vertical load equal to 2 kN, evaluated as:

$$\varepsilon = \frac{h' - h}{h}, \quad (3.8)$$

where h' is the device height after the vertical deformation. It can be observed that the higher is the device height to width ratio (see Table 3.1) the larger is the vertical deflection. By the comparison between the vertical strain values of WRI PWHS 16040 and WRI PWHS 16040 S, it can be deduced that the use of a larger wire rope diameter produces a reduction of the vertical deflection.

Table 3.6. Vertical strain of tested WRIs due to vertical load.

vertical load [kN]	PWHS 16010	PWHS 16040	PWHS 16040 S	PWHS 16060
2	-7.0 %	-5.6 %	-2.4 %	-4.8 %

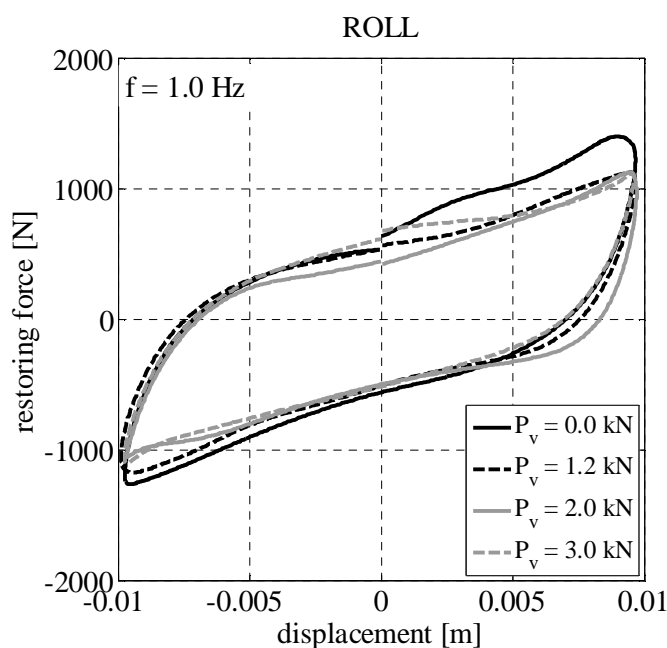
As far as the effect of the vertical load on the dynamic behavior of WRI PWHS 16040 is concerned, Table 3.7 shows the results obtained when a sinusoidal harmonic motion with amplitude equal to 3 cm and frequency of 1 Hz is applied in both the horizontal directions. An examination of these results reveals a reduction in the average effective stiffness due to the increase of the vertical load. For instance, if a vertical load equal to 3 kN is applied, the value of the vertical strain is -8.8 % and the percentage reduction in the average effective stiffness is 34.57 % in Roll direction and 43.55 % in Shear direction. In addition, Table 3.7 also shows that an increase in the vertical load produces a slight increase in the average equivalent viscous damping ratio and a reduction in the amount of dissipated energy. Therefore, it is important to point out that the application of a vertical load allows one to have a more flexible device with higher equivalent viscous damping ratio.

Table 3.7. Influence of vertical load | WRI PWHS 16040.

$A = 3 \text{ cm}, f = 1 \text{ Hz}$	vertical load [kN]	$k_{eff,a}$ [N/m]	$\xi_{eq,a}$ [%]	$E_{d,a}$ [N m]
Roll	0	96411.65	14.7	81.95
	1.2	84587.06	14.9	73.52
	2	73800.30	17.5	75.22
	3	63085.90	18.8	68.69
Shear	0	125189.71	13.8	99.76
	1.2	120047.68	12.3	85.44
	2	82622.23	14.5	69.29
	3	70673.76	15.7	64.16

Figures 3.28, 3.29, and 3.30 show the symmetric force-displacement hysteresis loops obtained in Roll and Shear directions under the effect of different values of vertical load at small (Figure 3.28), relatively large (Figure 3.29), and large displacements (Figure 3.30). It can be observed that in the small and relatively large displacements ranges, WRI PWHS 16040 displays a weaker hardening behavior if a larger vertical load is applied, whereas, at large displacements, the applied vertical load affects much less the dynamic response of the metal device. Indeed, a percentage reduction of 10.76 % in Roll direction and 6.12 % in Shear direction is recorded in the average effective stiffness of WRI PWHS 16040, subjected to a sinusoidal harmonic motion having amplitude of 6 cm and frequency equal to 1 Hz, under the effect of a vertical load of 3 kN. These two percentage values are then smaller than the previous values evaluated considering an amplitude of 3 cm and the same values of frequency and vertical load.

(a)



(b)

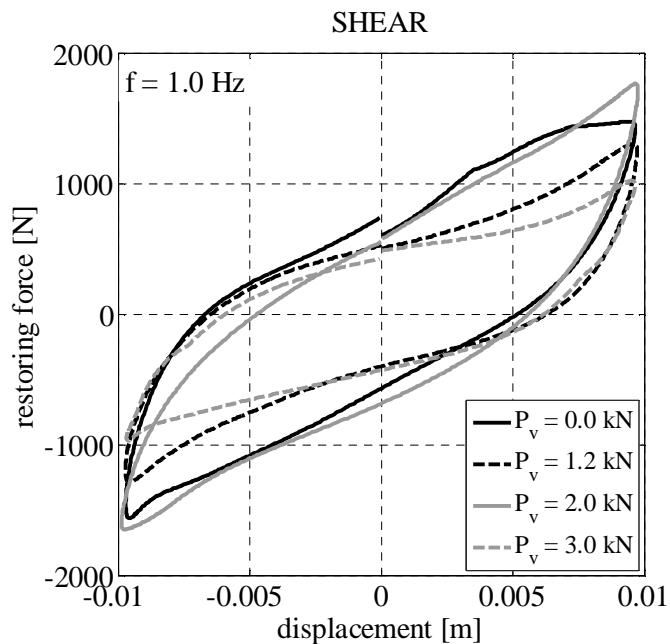
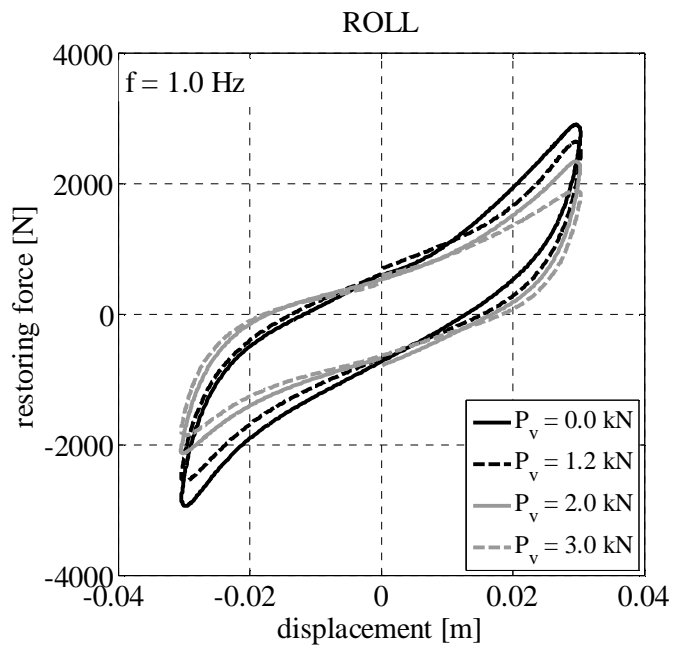


Figure 3.28. Influence of vertical load on WRI PWHS 16040 hysteresis loops obtained at small displacements in (a) Roll and (b) Shear directions.

(a)



(b)

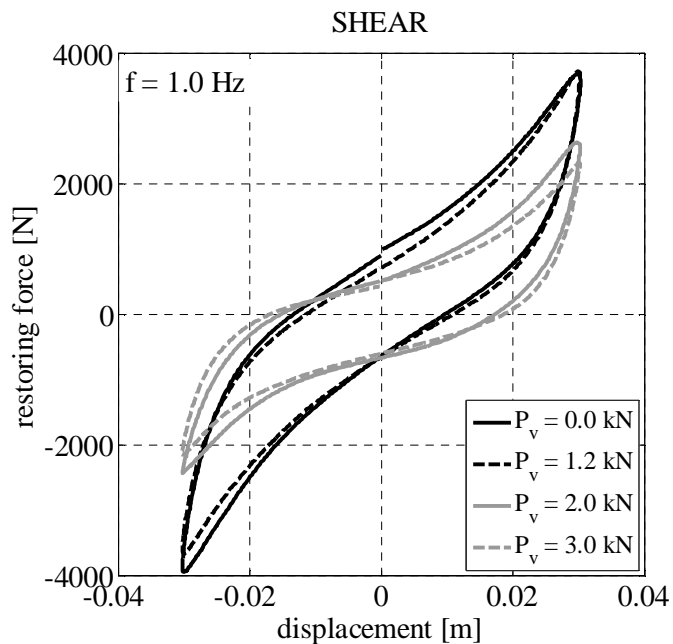
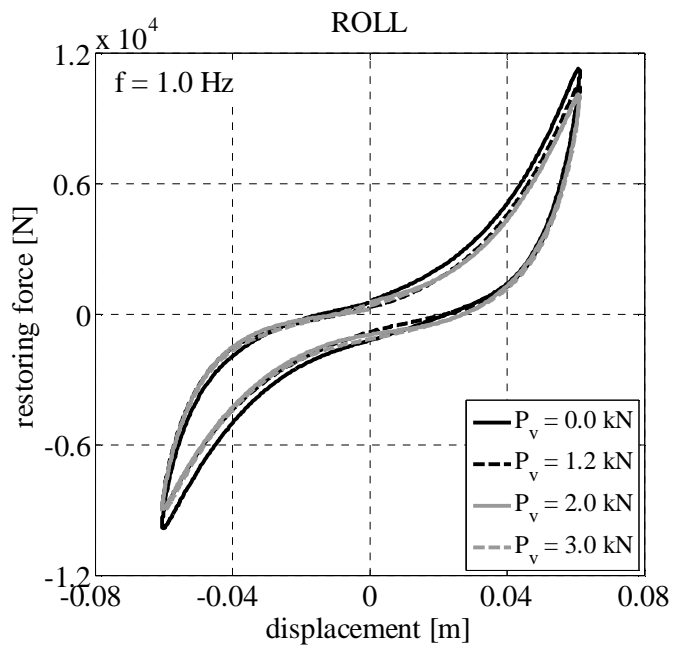


Figure 3.29. Influence of vertical load on WRI PWHS 16040 hysteresis loops obtained at relatively large displacements in (a) Roll and (b) Shear directions.

(a)



(b)

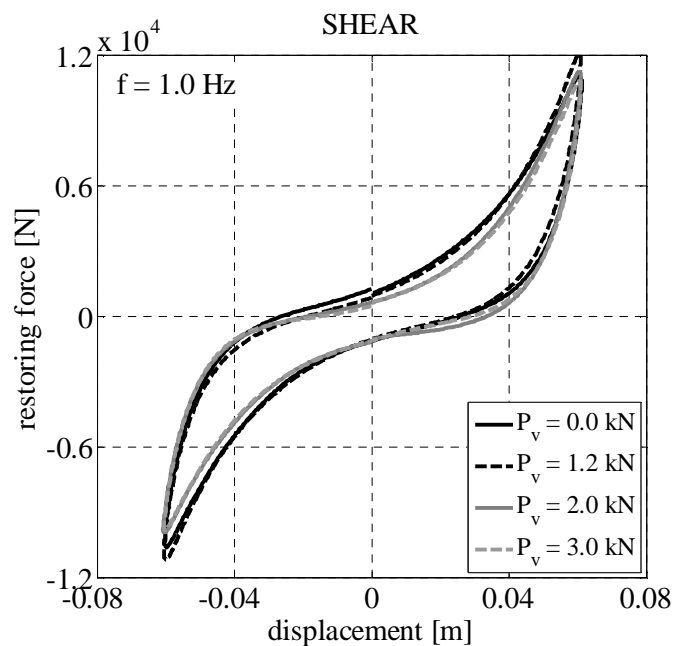


Figure 3.30. Influence of vertical load on WRI PWHS 16040 hysteresis loops obtained at large displacements in (a) Roll and (b) Shear directions.

The dynamic tests results of WRI PWHS 16040, obtained for $A = 6$ cm and $f = 1$ Hz, under the effect of the four different values of applied vertical load, are omitted for brevity.

Table 3.8 shows the results of the dynamic tests performed in Roll direction on WRI PWHS 16060, which is the most flexible device tested in the present experimental campaign. In this case, the vertical load acting on the device affects its dynamic response also when large displacements are applied. Indeed, the percentage reduction in the average effective stiffness is equal to 46.06 %, for $A = 4$ cm, and to 38.54 %, for $A = 8$ cm. In addition, the increase in the vertical load produces a slight increase in the average equivalent viscous damping ratio and a reduction in the dissipated energy amount.

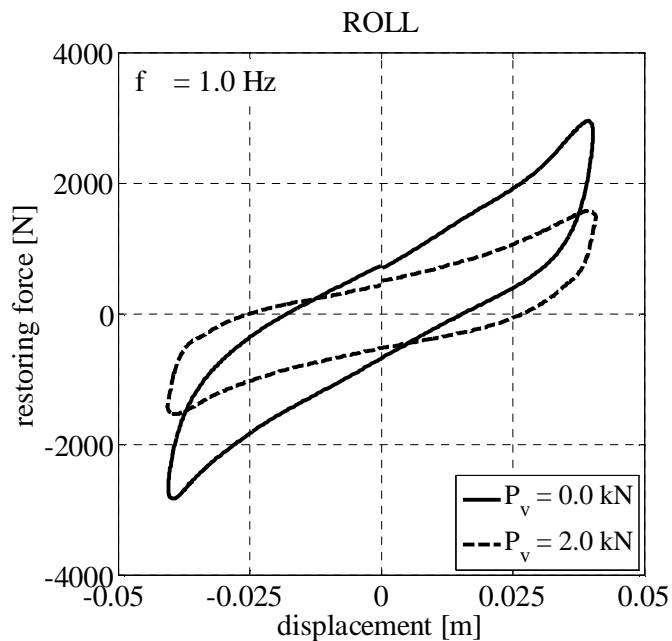
Table 3.8. Influence of vertical load | WRI PWHS 16060 (Roll direction).

$f = 1$ Hz	vertical load [kN]	$k_{eff,a}$ [N/m]	$\xi_{eq,a}$ [%]	$E_{d,a}$ [N m]
$A = 4$ cm	0	70499.96	16.1	116.78
	2	38022.41	20.2	80.18
$A = 8$ cm	0	79777.85	10.3	306.90
	2	49026.77	11.7	233.28

Figures 3.31a and 3.31b show the force-displacement hysteresis loops of WRI PWHS 16060, obtained for a frequency of 1 Hz and an amplitude equal to 4 and 8 cm, respectively. The comparison of Figure 3.30a with Figure 3.31b confirms that, when the metal device is more

flexible, the dynamic response at large displacements is more affected by the vertical load magnitude.

(a)



(b)

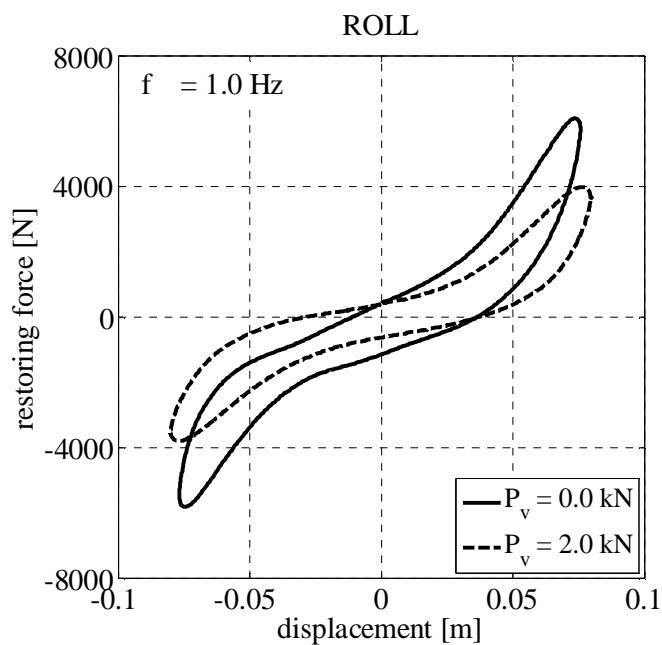


Figure 3.31. Influence of vertical load on WRI PWHS 16060 hysteresis loops obtained in Roll direction for (a) $A = 4$ cm and (b) $A = 8$ cm.

3.4.1.4.4 Influence of WRI Geometrical Characteristics

In the following, the influence of the height to width ratio on the dynamic behavior of the tested devices in the horizontal directions is described.

As shown in Table 3.1, WRIs PWHS 16010, 16040, and 16060 have the same length $l = 267$ mm, the same wire rope diameter $d_r = 16$ mm, but different height to width ratio h/v .

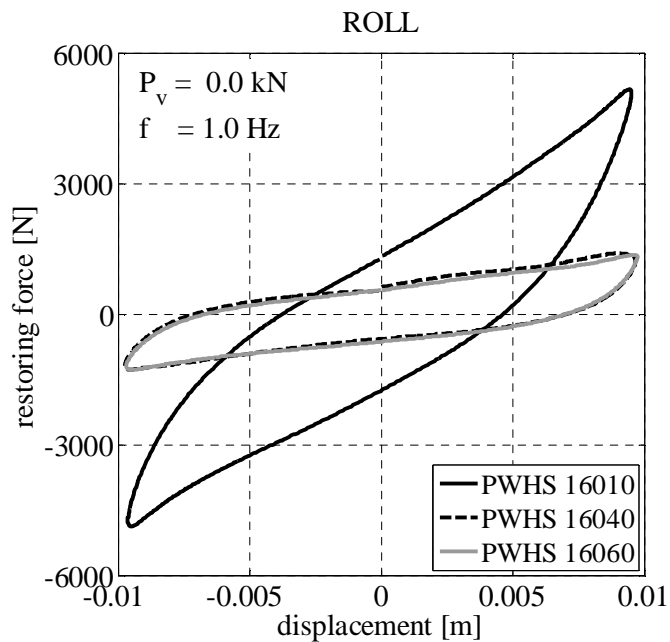
According to dynamic tests results listed in Table 3.9, the higher is the height to width ratio the stiffer is the metal device. For instance, the percentage reduction of WRI PWHS 16060 average effective stiffness, evaluated with respect to the WRI PWHS 16010 one, is 74.13 %, in Roll direction, and 79.88 %, in Shear direction. In addition, lower values of the height to width ratio allow one to have a larger average equivalent viscous damping ratio: the percentage increase of WRI PWHS 16060 equivalent viscous damping ratio, evaluated with respect to the WRI PWHS 16010 one, is 55.90 % and 78.62 % in Roll and Shear directions, respectively.

Table 3.9. Influence of WRI geometrical characteristics.

$A = 1 \text{ cm}, f = 1 \text{ Hz}, P_v = 0 \text{ kN}$	h/v	$k_{eff,a}$ [N/m]	$\xi_{eq,a}$ [%]	$E_{d,a}$ [N m]
Roll	0.90	527396.99	16.1	49.03
	0.83	131616.18	26.9	21.08
	0.78	136390.97	25.1	20.45
Shear	0.90	530276.67	13.1	40.30
	0.83	157702.20	21.5	20.02
	0.78	106653.68	23.4	14.91

Figure 3.32 shows the force-displacement hysteresis loops of the three devices, obtained imposing a cyclic sinusoidal motion of 1 cm amplitude and 1 Hz frequency, without applying the vertical load. It can be observed that the two WRIs having an higher height to width ratio display a softening force-displacement loop, whereas the third one has a hardening behavior. It is clear that smaller displacements have to be imposed to the latter device in order to avoid damages during the dynamic tests. In other words, the geometrical characteristic here investigated influences strongly the device capacity to undergo large deformations.

(a)



(b)

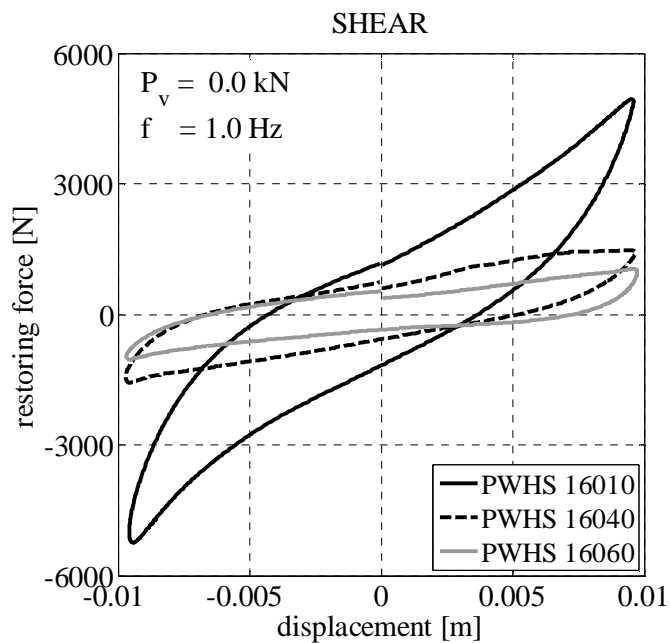


Figure 3.32. Influence of WRI geometrical characteristics on hysteresis loops obtained in (a) Roll and (b) Shear directions.

The influence of the height to width ratio has been investigated also under the effect of a vertical load equal to 2 kN. Since the same dynamic behavior has been observed in both two horizontal directions, these results are omitted for brevity.

3.4.1.4.5 Influence of Wire Rope Diameter

In order to study the influence of the wire rope diameter on the dynamic behavior of the tested WRIs, a special device, namely, WRI PWHS 16040 S, has been manufactured by Powerflex S.r.l. This device has the same geometrical characteristics of WRI PWHS 16040 but it has a wire rope with a diameter equal to 19 mm instead of 16 mm. As for WRI PWHS 16040, the rope of the special device is made of six strands having 25 steel wires plus a central one with 49 wires. The material of the wires is American Iron and Steel Institute (AISI) Stainless Steel Type 316.

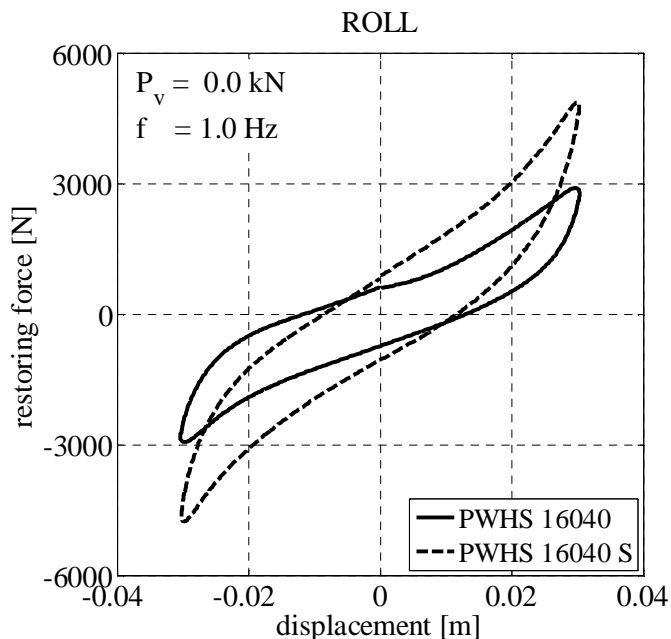
Table 3.10 shows the dynamic tests results in Roll direction, obtained for three different displacement amplitudes by imposing a sinusoidal harmonic motion having frequency equal to 1 Hz, without the effect of the vertical load. The use of a wire rope with a larger diameter allows one to have a stiffer device; indeed, the percentage increase of WRI PWHS 16040 S average effective stiffness, evaluated with respect to the WRI PWHS 16040 one, is 59.44 %, 62.08 % and 5.40 %, for $A = 1$ cm, $A = 3$ cm, and $A = 6$ cm, respectively. If it is observed that the average equivalent damping ratio values of the two tested WRIs, obtained for $A = 6$ cm, are very close to each other, it can be concluded that the wire rope diameter slightly influences the dynamic behavior of WRIs in the large displacements range in terms of effective stiffness and equivalent viscous damping ratio.

Table 3.10. Influence of wire rope diameter (Roll direction).

$f = 1$ Hz, $P_v = 0$ kN	amplitude [cm]	$k_{eff,a}$ [N/m]	$\xi_{eq,a}$ [%]	$E_{d,a}$ [N m]
PWHS 16040	1	131616.18	26.9	21.08
	3	96411.65	14.7	81.95
	6	172987.50	8.00	327.51
PWHS 16040 S	1	209857.05	22.8	28.66
	3	156260.94	12.2	110.17
	6	182336.81	7.90	340.97

Figures 3.33a and 3.33b show the force-displacement hysteresis loops of the two metal devices, obtained for a frequency of 1 Hz and an amplitude equal to 3 and 6 cm, respectively, without applying the vertical load. It is evident that, in both displacements ranges, the tested WRIs display a hardening behavior, and that, at large displacements, the force-displacement loops are very similar to each other.

(a)



(b)

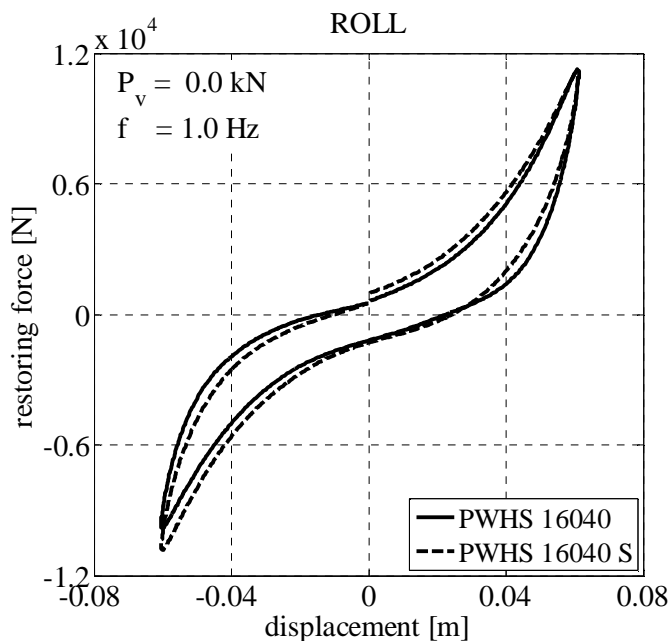


Figure 3.33. Influence of wire rope diameter on hysteresis loops obtained in Roll direction for: (a) $A = 3 \text{ cm}$ and (b) $A = 6 \text{ cm}$.

The influence of the wire rope diameter has been investigated in both two horizontal directions also under the effect of a vertical load equal to 2 kN and the same dynamic behavior has been observed.

3.4.1.4.6 Comparison between Roll and Shear Dynamic Responses

WRIs exhibit a similar symmetric hysteresis behavior in Roll and Shear directions. Table 3.11 shows the Roll to Shear average effective stiffness, equivalent viscous damping ratio and dissipated energy ratios, evaluated for WRIs PWHS 16010, 16040, and 16060, subjected to a sinusoidal harmonic motion having frequency of 1 Hz, without the effect of the vertical load. It can be observed that the first and third devices are stiffer in Roll direction whereas the second one displays a stiffer dynamic behavior in the other horizontal direction. In addition, it is clear that all tested metal devices have a higher average equivalent viscous damping ratio in Roll direction.

Table 3.11. Comparison between Roll and Shear dynamic responses.

$f = 1 \text{ Hz}, P_v = 0 \text{ kN}$	amplitude [cm]	$k_{eff,a}^R / k_{eff,a}^S$	$\xi_{eq,a}^R / \xi_{eq,a}^S$	$E_{d,a}^R / E_{d,a}^S$
WRI PWHS 16010	0.25	1.50	1.09	1.58
	0.50	1.22	1.16	1.39
	1	0.99	1.22	1.21
WRI PWHS 16040	1	0.83	1.25	1.05
	3	0.77	1.06	0.82
	6	0.96	0.81	0.79
WRI PWHS 16060	1	1.27	1.07	1.37
	4	1.12	1.53	1.71
	8	0.70	1.14	0.78

3.4.1.4.7 Static Behavior

Static tests in both two horizontal directions were carried out, following the scheme listed in Table 3.3, by applying a horizontal displacement which was increased linearly with a velocity of 0.5 mm/s up to a maximum value selected according to the each device properties.

Table 3.12 shows the static effective stiffnesses k_{eff}^{st} , evaluated using the secant line method, and the static to dynamic effective stiffness ratios $k_{ratio} = k_{eff}^{st} / k_{eff}^{dy}$, for WRI PWHS 16040. It can be observed that the static to dynamic effective stiffness ratio tends to 1 for large displacement values. Moreover, in the relatively large displacements range, the lower k_{ratio} value is obtained considering the average dynamic effective stiffness evaluated for a frequency of 1 Hz.

Table 3.12. Static tests results | WRI PWHS 16040.

$P_v = 0$ kN	amplitude [cm]	k_{eff}^{st} [N/m]	k_{ratio} (1 Hz)	k_{ratio} (0.5 Hz)	k_{ratio} (1.5 Hz)	k_{ratio} (2 Hz)
Roll	1	223224.67	1.69	-	-	-
	3	142044.04	1.47	1.55	1.92	2.47
	6	174274.07	1.00	-	-	-
Shear	1	264560.06	1.67	-	-	-
	3	163781.51	1.30	1.39	1.66	2.11
	6	196837.06	1.10	-	-	-

Testing WRI PWHS 16040 under the effect of different vertical loads, that is, 1.2 kN, 2 kN, and 3 kN, the same static behavior can be observed.

Figure 3.34 shows the force-displacement curves obtained for different vertical load values during the static tests in Roll direction, whereas Figure 3.35 shows the deformed shape of the metal device displayed in Roll direction for an amplitude of 6 cm when no vertical load is applied.

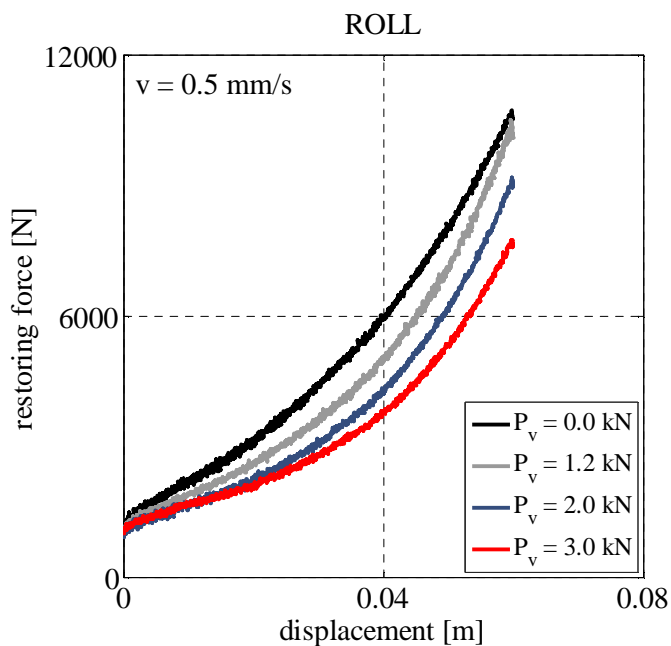


Figure 3.34. Force-displacement curves obtained for different vertical load values during static tests in Roll direction.

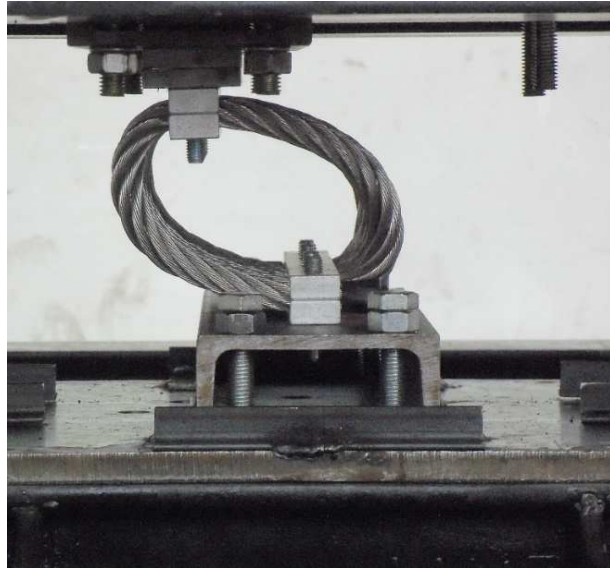


Figure 3.35. WRI PWHS 16040 deformed shape displayed in Roll direction for $A = 6$ cm and $P_v = 0$ kN.

Since the other three tested WRIs display a similar static response, these results are omitted for brevity.

Chapter 4

Mathematical Modeling of Seismic Isolators

4.1 Introduction

Chapter 4 is concerned with the mathematical modeling of seismic isolation bearings and is organized into three parts.

The first part presents three Differential Equation Models (DEMs). First, the widely used Bouc-Wen Model (BWM), which has been adapted for modeling the uniaxial behavior of elastomeric bearings, sliding bearings, and wire rope isolators (Constantinou et al. 1990, Nagarajaiah et al. 1991, Demetriades et al. 1993) and implemented in many computer programs, such as 3D-BASIS, SAP2000, and ETABS, is described. Then, an improved version of the BWM, namely, Modified Bouc-Wen Model (MBWM), able to simulate the increase or decrease of the tangent stiffness at large displacements, and the 2d Bouc-Wen Model (2d BWM), developed by Park et al. (1986) and then adapted for modeling the biaxial behavior of elastomeric and sliding bearings (Constantinou et al. 1990, Nagarajaiah et al. 1991), are presented.

The second part presents five proposed mathematical models: two uniaxial models able to predict the dynamic behavior of seismic isolators within a relatively large displacements range, namely, Nonlinear Exponential Model (NEM) and Parallel Model (PM), two uniaxial models able to simulate the post-hardening or post-softening behavior at large displacements, namely, Advanced Nonlinear Exponential Model (ANEM) and Advanced Parallel Model (APM), which are an improved version of the NEM and PM, respectively, and one biaxial model able to take into account the biaxial interaction between the restoring forces along two orthogonal horizontal directions within the relatively large displacements range, namely, 2d Parallel Model (2d PM).

In the third part, the force-displacement hysteresis loops simulated adopting the described DEMs are compared to those obtained adopting the proposed ones.

4.2 Differential Equation Models

4.2.1 Uniaxial Models

In the following, two uniaxial DEMs are described. The former is able to simulate symmetric softening hysteresis loops with bilinear or rigid-plastic characteristics, the latter symmetric hysteresis loops with post-hardening or post-softening characteristics.

4.2.1.1 Bouc-Wen Model

According to this DEM, the restoring force $z(u)$ of a hysteretic system can be obtained by solving the following first order nonlinear ordinary differential equation, proposed by Wen (1976, 1980):

$$\dot{z} = A \dot{u} - \beta |\dot{u}| z^n - \gamma \dot{u} |z|^n, \quad \text{for } n \text{ odd} \quad (4.1)$$

$$\dot{z} = A \dot{u} - \beta |\dot{u}| z^{n-1} |z| - \gamma \dot{u} z^n, \quad \text{for } n \text{ even} \quad (4.2)$$

with n a positive integer number, and A , β , and γ real constants. Equations (4.1) and (4.2) can be written in a more compacted form, valid for n odd or even, as follows:

$$\dot{z} = A \dot{u} - \beta |\dot{u}| z |z|^{n-1} - \gamma \dot{u} |z|^n. \quad (4.3)$$

Constantinou and Adnane (1987) have shown that, for $A = 1$ and $\beta + \gamma = 1$, the model given by Equation (4.3) collapses to the model of viscoplasticity proposed by Ozdemir (1976).

In order to evaluate the tangent stiffness of the restoring force $z(u)$, Equation (4.3) can be rewritten as follows:

$$\frac{dz}{dt} = A \frac{du}{dt} - \beta \left| \frac{du}{dt} \right| z |z|^{n-1} - \gamma \frac{du}{dt} |z|^n. \quad (4.4)$$

Then, multiplying both sides of Equation (4.4) by $dt > 0$:

$$dz = A du - \beta |du| z |z|^{n-1} - \gamma du |z|^n, \quad (4.5)$$

and dividing Equation (4.5) by du , leads to:

$$\frac{dz}{du} = A - \beta \operatorname{sgn}(du) z |z|^{n-1} - \gamma |z|^n. \tag{4.6}$$

Table 4.1 gives the different expressions of the tangent stiffness obtained for n odd or even, according to the signs of the velocity \dot{u} and restoring force z .

Table 4.1. Tangent stiffness of the restoring force in the BWM.

$\frac{dz}{du}$	n odd		n even	
	$z < 0$	$z > 0$	$z < 0$	$z > 0$
$\dot{u} > 0$	$A - (\beta - \gamma) z^n$ (portion I)	$A - (\beta + \gamma) z^n$ (portion II)	$A + (\beta - \gamma) z^n$ (portion I)	$A - (\beta + \gamma) z^n$ (portion II)
$\dot{u} < 0$	$A + (\beta + \gamma) z^n$ (portion IV)	$A + (\beta - \gamma) z^n$ (portion III)	$A - (\beta + \gamma) z^n$ (portion IV)	$A + (\beta - \gamma) z^n$ (portion III)

Figure 4.1 shows a generic force-displacement hysteresis loop simulated adopting the BWM and obtained by applying to a hysteretic system a harmonic displacement having amplitude u_0 or a harmonic force with amplitude z_0 .

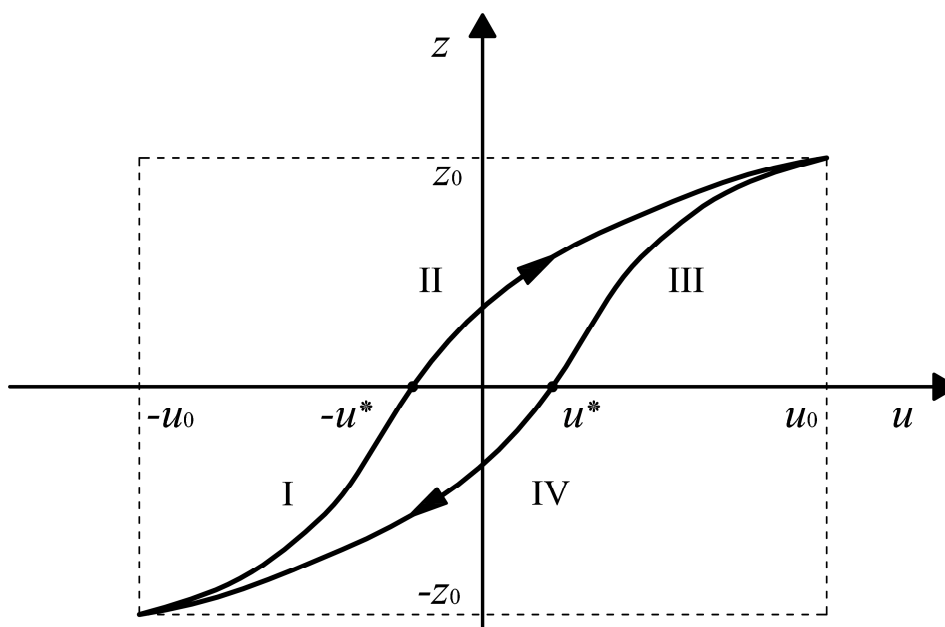


Figure 4.1. Generic hysteresis loop obtained with the BWM.

It can be observed that the hysteresis loop can be decomposed into four different portions, namely, portions I, II, III, and IV. According to Table 4.1, and as shown in Figure 4.1, for

both n odd and even, the tangent stiffness of the loading curve evaluated in $(-u_0, -z_0)$ is equal to the tangent stiffness of the unloading curve evaluated in (u_0, z_0) . Since it happens for each pair of points $(-u, -z)$ and (u, z) belonging to the two portions, that is, portion I and III, it can be concluded that the latter are symmetric with respect to the origin. The same is true for portions II and IV, thus the shape of the hysteresis loop can be studied by considering only portions I and II.

It can be shown that:

$$u_0 = \frac{1}{2} \left[\int_{-z_0}^0 \frac{dz}{A - (\beta - \gamma) z^n} + \int_0^{z_0} \frac{dz}{A - (\beta + \gamma) z^n} \right], \quad \text{for } n \text{ odd} \quad (4.7)$$

$$u_0 = \frac{1}{2} \left[\int_{-z_0}^0 \frac{dz}{A + (\beta - \gamma) z^n} + \int_0^{z_0} \frac{dz}{A - (\beta + \gamma) z^n} \right], \quad \text{for } n \text{ even} \quad (4.8)$$

whereas u^* can be evaluated as:

$$u^* = \frac{1}{2} \left[\int_0^{z_0} \frac{dz}{A - (\beta + \gamma) z^n} - \int_{-z_0}^0 \frac{dz}{A - (\beta - \gamma) z^n} \right], \quad \text{for } n \text{ odd} \quad (4.9)$$

$$u^* = \frac{1}{2} \left[\int_0^{z_0} \frac{dz}{A - (\beta + \gamma) z^n} - \int_{-z_0}^0 \frac{dz}{A + (\beta - \gamma) z^n} \right]. \quad \text{for } n \text{ even} \quad (4.10)$$

Finally, the area of the hysteresis loop, that is, the dissipated energy, is given by:

$$E_d = 2 \left[\int_{-z_0}^0 \frac{z}{A - (\beta - \gamma) z^n} dz + \int_0^{z_0} \frac{z}{A - (\beta + \gamma) z^n} dz \right], \quad \text{for } n \text{ odd} \quad (4.11)$$

$$E_d = 2 \left[\int_{-z_0}^0 \frac{z}{A + (\beta - \gamma) z^n} dz + \int_0^{z_0} \frac{z}{A - (\beta + \gamma) z^n} dz \right]. \quad \text{for } n \text{ even} \quad (4.12)$$

The parameter A represents the tangent to both the loading and unloading curves at their intersection with u -axis ($z = 0$).

The two parameters β and γ define the shape of the hysteresis loop and can assume positive or negative values. In order to understand how the shape of the force-displacement loop varies according to the values of the latter parameters, it is possible to analyze the variation of the

tangent stiffness which is determined by the sign of the quantity $\beta - \gamma$ in the portions I and III, and of the quantity $\beta + \gamma$ in portions II and IV.

Considering portion I and moving from point $(-u_0, -z_0)$ to point $(-u^*, 0)$, Table 4.1 reveals that the tangent stiffness:

- decreases from the value $A + (\beta - \gamma) z_0^n > A$ to value A , for $\beta - \gamma > 0$;
- is constant and equal to A for $\beta - \gamma = 0$;
- increases from the value $A + (\beta - \gamma) z_0^n < A$ to the value A , for $\beta - \gamma < 0$; in this case, in order to have a positive tangent stiffness, that is, $dz/du > 0$, $z_0 < \sqrt[n]{-A/(\beta - \gamma)}$.

Considering portion II and moving from point $(-u^*, 0)$ to point (u_0, z_0) , Table 4.1 reveals that the tangent stiffness:

- decreases from the value A to value $A - (\beta + \gamma) z_0^n < A$, for $\beta + \gamma > 0$, and $z_0 < \sqrt[n]{A/(\beta + \gamma)}$;
- is constant and equal to A for $\beta + \gamma = 0$;
- increases from the value A to the value $A - (\beta + \gamma) z_0^n > A$, for $\beta + \gamma < 0$.

In softening force-displacement hysteresis loops, the parameter n defines the sharpness of the transition from the linear to nonlinear range with the hysteresis approaching bilinear behavior as n approaches ∞ , as shown in Figure 4.2.

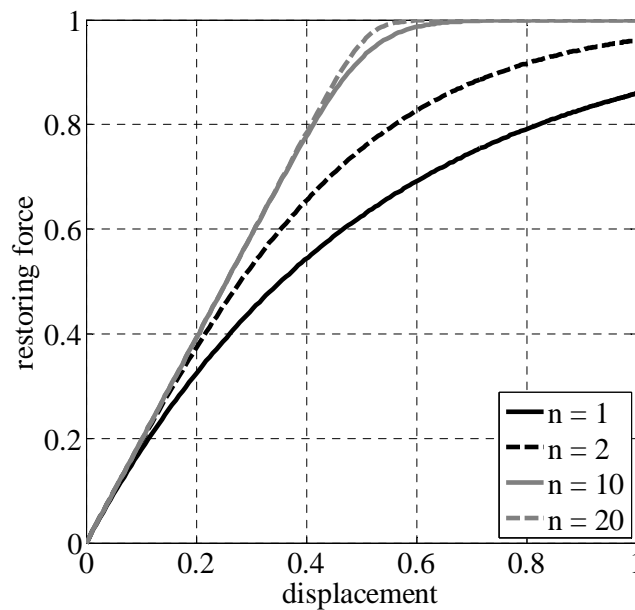


Figure 4.2. Influence of parameter n on the hysteresis loop shape in the BWM ($A = 1$, $\beta = \gamma = 0.5$).

Equation (4.3) is generally solved numerically by adopting the Runge-Kutta method (Rosenbrock 1963). In fact, explicit expressions for z are possible only for $n = 1$ or $n = 2$.

If $n = 1$, it can be shown that:

$$z_{\text{I}}(u) = \frac{A}{\beta - \gamma} - \left(z_0 + \frac{A}{\beta - \gamma} \right) e^{-(\beta - \gamma)(u + u_0)}, \quad \text{for portion I} \quad (4.13)$$

$$z_{\text{II}}(u) = \frac{A}{\beta + \gamma} \left[1 - e^{-(\beta + \gamma)(u^* + u)} \right], \quad \text{for portion II} \quad (4.14)$$

$$z_{\text{III}}(u) = -\frac{A}{\beta - \gamma} + \left(z_0 + \frac{A}{\beta - \gamma} \right) e^{-(\beta - \gamma)(u_0 - u)}, \quad \text{for portion III} \quad (4.15)$$

$$z_{\text{IV}}(u) = -\frac{A}{\beta + \gamma} \left[1 - e^{-(\beta + \gamma)(u^* - u)} \right], \quad \text{for portion IV} \quad (4.16)$$

with

$$u_0 = \frac{1}{2} \left\{ \frac{1}{\beta - \gamma} \log \left[\frac{A + (\beta - \gamma) z_0}{A} \right] + \frac{1}{\beta + \gamma} \log \left[\frac{A}{A - (\beta + \gamma) z_0} \right] \right\}, \quad (4.17)$$

and

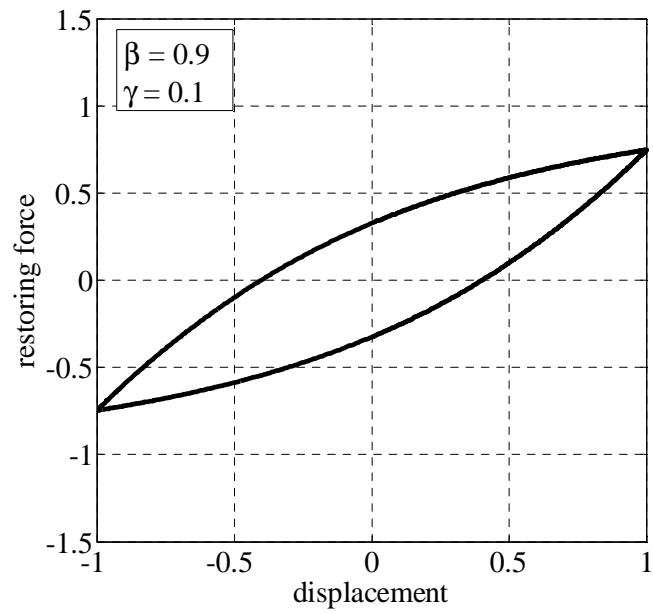
$$u^* = \frac{1}{2} \left\{ \frac{1}{\beta + \gamma} \log \left[\frac{A}{A - (\beta + \gamma) z_0} \right] - \frac{1}{\beta - \gamma} \log \left[\frac{A + (\beta - \gamma) z_0}{A} \right] \right\}. \quad (4.18)$$

In this case, the energy dissipated in one cycle is given by:

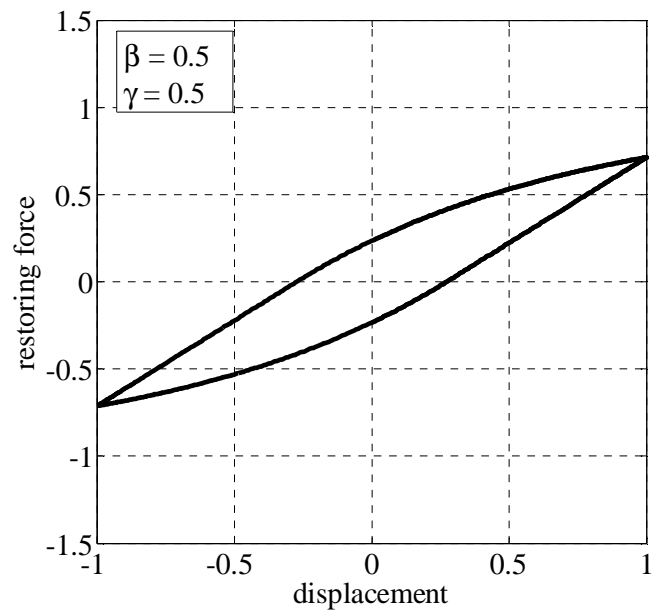
$$E_d = 2 \left\{ \frac{A}{(\beta - \gamma)^2} \log \left[\frac{A + (\beta - \gamma) z_0}{A} \right] + \frac{A}{(\beta + \gamma)^2} \log \left[\frac{A}{A - (\beta + \gamma) z_0} \right] - \frac{2\beta z_0}{\beta^2 - \gamma^2} \right\}. \quad (4.19)$$

Figure 4.3 shows the force-displacement hysteresis loop obtained for $n = 1$, $A = 1$, and for different values of the pairs of parameters β and γ .

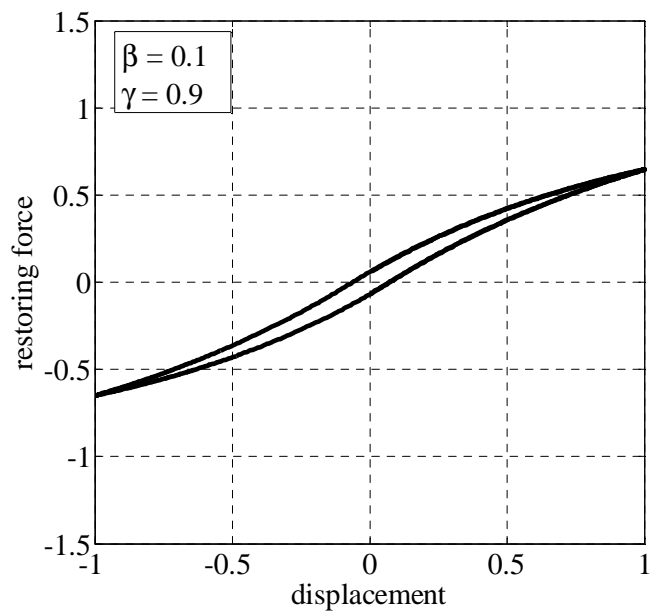
(a)



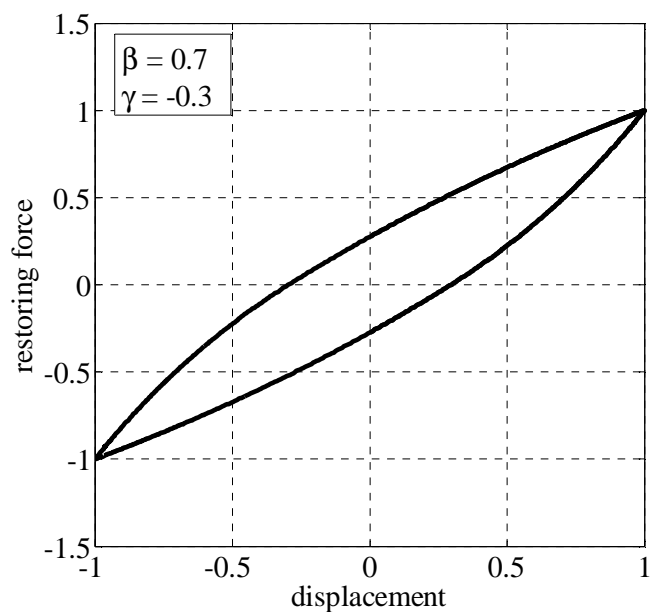
(b)



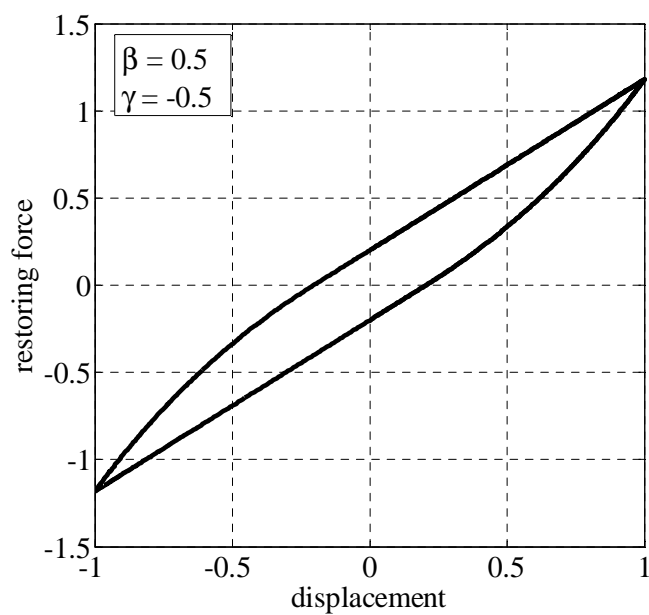
(c)



(d)



(e)



(f)

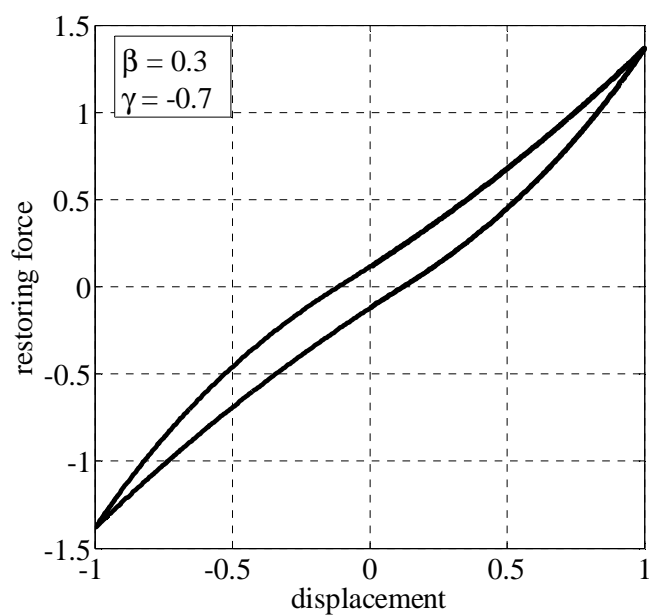


Figure 4.3. Hysteresis loops obtained with the BWM for different values of pairs of parameters β and γ ($A = 1, n = 1$).

If $n = 2$, for portion I:

$$z_I(u) = \sqrt{\frac{A}{\beta - \gamma}} \tan \left[\sqrt{A(\beta - \gamma)} (u + u_0) - \arctan \left(\sqrt{\frac{\beta - \gamma}{A}} z_0 \right) \right], \quad \text{if } \beta - \gamma > 0 \quad (4.20)$$

$$z_I(u) = A(u + u_0) - z_0, \quad \text{if } \beta - \gamma = 0 \quad (4.21)$$

$$z_I(u) = \sqrt{\frac{A}{\beta - \gamma}} \frac{(\sqrt{A} - \sqrt{\beta - \gamma} z_0) e^{2\sqrt{A(\beta - \gamma)}(u + u_0)} - (\sqrt{A} + \sqrt{\beta - \gamma} z_0)}{(\sqrt{A} - \sqrt{\beta - \gamma} z_0) e^{2\sqrt{A(\beta - \gamma)}(u + u_0)} + (\sqrt{A} + \sqrt{\beta - \gamma} z_0)}, \quad \text{if } \beta - \gamma < 0 \quad (4.22)$$

whereas, for portion II:

$$z_{II}(u) = \sqrt{\frac{A}{\beta + \gamma}} \frac{e^{2\sqrt{A(\beta + \gamma)}(u^* + u)} - 1}{e^{2\sqrt{A(\beta + \gamma)}(u^* + u)} + 1}, \quad \text{if } \beta + \gamma > 0 \quad (4.23)$$

$$z_{II}(u) = A(u^* + u), \quad \text{if } \beta + \gamma = 0 \quad (4.24)$$

$$z_{II}(u) = \sqrt{\frac{-A}{\beta + \gamma}} \tan \left[\sqrt{-A(\beta + \gamma)} (u^* + u) \right], \quad \text{if } \beta + \gamma < 0 \quad (4.25)$$

with

$$u_0 = \frac{1}{2} \left[\int_{-z_0}^0 \frac{dz}{A + (\beta - \gamma) z^2} + \int_0^{z_0} \frac{dz}{A - (\beta + \gamma) z^2} \right], \quad (4.26)$$

and

$$u^* = \frac{1}{2} \left[\int_0^{z_0} \frac{dz}{A - (\beta + \gamma) z^2} - \int_{-z_0}^0 \frac{dz}{A + (\beta - \gamma) z^2} \right], \quad (4.27)$$

taking into account that:

$$\int_{-z_0}^0 \frac{dz}{A + (\beta - \gamma) z^2} = \frac{1}{\sqrt{A(\beta - \gamma)}} \arctan \left(\sqrt{\frac{\beta - \gamma}{A}} z_0 \right), \quad \text{if } \beta - \gamma > 0 \quad (4.28)$$

$$\int_{-z_0}^0 \frac{dz}{A + (\beta - \gamma) z^2} = \frac{z_0}{A}, \quad \text{if } \beta - \gamma = 0 \quad (4.29)$$

$$\int_{-z_0}^0 \frac{dz}{A + (\beta - \gamma) z^2} = \frac{1}{2\sqrt{A(\beta - \gamma)}} \log \left(\frac{\sqrt{A} + \sqrt{\beta - \gamma} z_0}{\sqrt{A} - \sqrt{\beta - \gamma} z_0} \right), \quad \text{if } \beta - \gamma < 0 \quad (4.30)$$

$$\int_0^{z_0} \frac{dz}{A - (\beta + \gamma) z^2} = \frac{1}{2\sqrt{A(\beta + \gamma)}} \log \left(\frac{\sqrt{A} + \sqrt{\beta + \gamma} z_0}{\sqrt{A} - \sqrt{\beta + \gamma} z_0} \right), \quad \text{if } \beta + \gamma > 0 \quad (4.31)$$

$$\int_0^{z_0} \frac{dz}{A - (\beta + \gamma) z^2} = \frac{z_0}{A}, \quad \text{if } \beta + \gamma = 0 \quad (4.32)$$

$$\int_0^{z_0} \frac{dz}{A - (\beta + \gamma) z^2} = \frac{1}{\sqrt{-A(\beta + \gamma)}} \arctan \left(\sqrt{\frac{\beta + \gamma}{-A}} z_0 \right). \quad \text{if } \beta + \gamma < 0 \quad (4.33)$$

For portions III and IV:

$$z_{\text{III}}(u) = -z_{\text{I}}(-u), \quad (4.34)$$

$$z_{\text{IV}}(u) = -z_{\text{II}}(-u). \quad (4.35)$$

In this case, the energy dissipated in one cycle is given by:

$$E_d = 2 \left[\int_{-z_0}^0 \frac{z}{A + (\beta - \gamma) z^2} dz + \int_0^{z_0} \frac{z}{A - (\beta + \gamma) z^2} dz \right], \quad (4.36)$$

in which

$$\int_{-z_0}^0 \frac{z}{A + (\beta - \gamma) z^2} dz = \frac{1}{2(\beta - \gamma)} \log \left[\frac{A}{A + (\beta - \gamma) z_0^2} \right], \quad \text{if } \beta - \gamma \neq 0 \quad (4.37)$$

$$\int_{-z_0}^0 \frac{z}{A + (\beta - \gamma) z^2} dz = \frac{z_0^2}{2A}, \quad \text{if } \beta - \gamma = 0 \quad (4.38)$$

$$\int_0^{z_0} \frac{z}{A - (\beta + \gamma) z^2} dz = \frac{1}{2(\beta + \gamma)} \log \left[\frac{A}{A - (\beta + \gamma) z_0^2} \right], \quad \text{if } \beta + \gamma \neq 0 \quad (4.39)$$

$$\int_0^{z_0} \frac{z}{A - (\beta + \gamma) z^2} dz = \frac{z_0^2}{2A}. \quad \text{if } \beta + \gamma = 0 \quad (4.40)$$

Nagarajaiah et al. (1991) have adapted the above described uniaxial DEM for simulating the dynamic behavior of elastomeric bearings, such as high damping rubber bearings and lead rubber bearings.

For an elastomeric bearing, the nonlinear restoring force can be evaluated by using the following equation:

$$f(u) = f_e(u) + f_h(u), \quad (4.41)$$

in which $f_e(u)$ is a linear elastic force evaluated as:

$$f_e(u) = \alpha \frac{f_y}{u_y} u, \quad (4.42)$$

and $f_h(u)$ is a nonlinear hysteretic force defined as:

$$f_h(u) = (1 - \alpha) \frac{f_y}{u_y} z(u), \quad (4.43)$$

where α is the post-yield to pre-yield stiffness ratio, f_y is the yield force, and u_y is the yield displacement. The function z , which is obtained by solving Equation (4.3), has the unit of displacement.

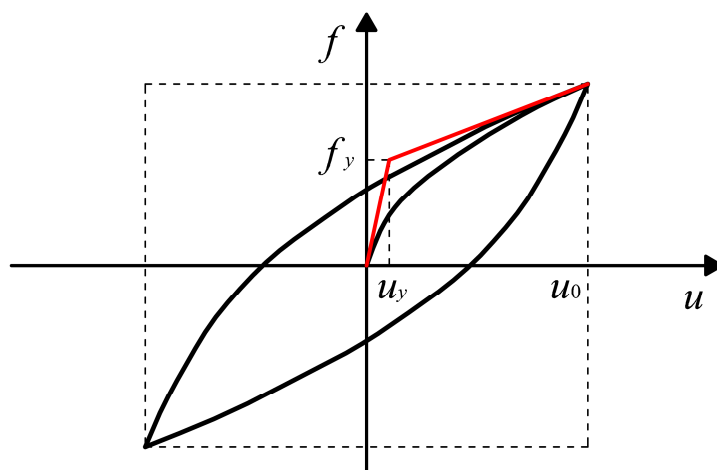
Nagarajaiah et al. (1991) suggests the following values for the model parameters:

$$A = 1, \beta = \frac{0.9}{u_y^2}, \gamma = \frac{0.1}{u_y^2}, \text{ and } n = 2.$$

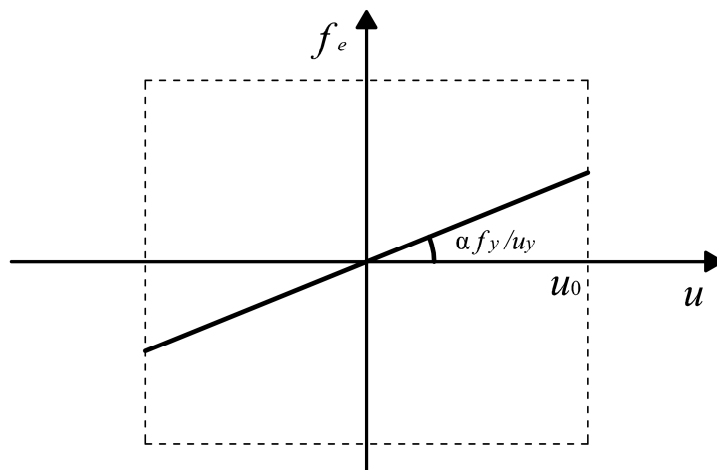
Figure 4.4 shows the total nonlinear restoring force given by Equation (4.41) and its two components, obtained by Equations (4.42) and (4.43), respectively.

The above-described model has been also adopted by Demetriades et al. (1993) to simulate the dynamic behavior of wire rope isolators in Roll and Shear directions.

(a)



(b)



(c)

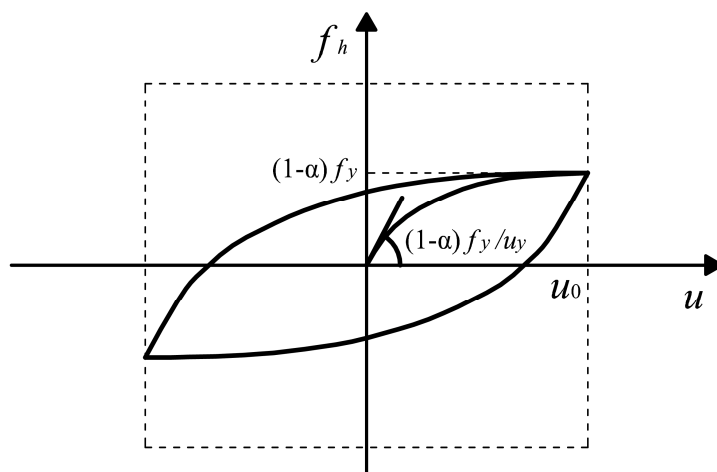


Figure 4.4. (a) Total nonlinear restoring force and its two components: (b) linear elastic force and (c) nonlinear hysteretic force.

Constantinou et al. (1990) have adapted the BWM for modeling sliding bearings, such as friction pendulum bearings and flat sliding bearings.

For a friction pendulum bearing, the nonlinear restoring force can be obtained as:

$$f(u) = f_e(u) + f_h(u), \quad (4.44)$$

in which $f_e(u)$ is a linear elastic force evaluated as:

$$f_e(u) = \frac{N}{R} u, \quad (4.45)$$

and $f_h(u)$ is a nonlinear hysteretic force defined as:

$$f_h(u) = \frac{\mu N}{u_y} z(u), \quad (4.46)$$

where N is the vertical load carried by the seismic isolator, R is the radius of curvature of the spherical concave surface of the bearing, μ is the sliding friction coefficient, which depends on the value of bearing pressure and the instantaneous velocity of sliding \dot{u} .

For a flat sliding bearing, Equation (4.44) becomes:

$$f(u) = f_h(u), \quad (4.47)$$

where $f_h(u)$ is the nonlinear hysteretic force given by Equation (4.46).

The coefficient of sliding friction is modeled by the following equation suggested by Constantinou et al. (1990):

$$\mu = \mu_{s,max} - (\mu_{s,max} - \mu_{s,min}) e^{-a|\dot{u}|}, \quad (4.48)$$

in which, $\mu_{s,max}$ is the maximum value of the coefficient of friction, $\mu_{s,min}$ is its minimum value (at $\dot{u} = 0$), and a is a parameter which controls the variation of the coefficient of friction with the velocity. Values of parameters $\mu_{s,max}$, $\mu_{s,min}$, and a for interfaces used in sliding bearings have been reported in Constantinou et al. (1990) and Mokha et al. (1991). In general, the latter parameters are functions of bearing pressure.

4.2.1.2 Modified Bouc-Wen Model

Since the BWM is not able to reproduce the hysteretic behavior with post-hardening, displayed by high damping rubber bearings and wire rope isolators at large displacements (Ni et al. 1999, Tsai et al. 2003), or the hysteretic behavior with post-softening, displayed by unbounded elastomeric bearings with deformable reinforcing layers (Spizzuoco et al. 2014), in the following, an improved version of such model is described.

As proposed by Ni et al. (1999), in order to predict the increase or decrease of the tangent stiffness at large displacements, the symmetric softening nonlinear hysteretic force described by the BWM can be modulated with a nonhysteretic term as follows:

$$f(u) = f_1(u) \cdot f_2(u), \tag{4.49}$$

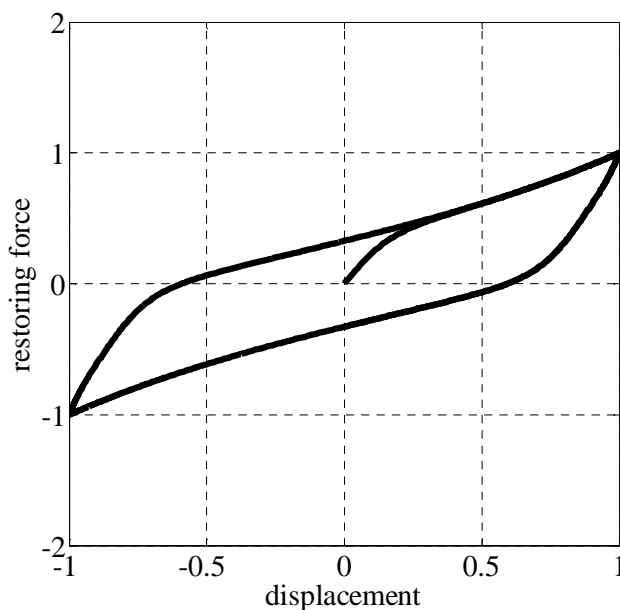
in which $f_1(u)$ is the nonlinear elastic modulation function given by:

$$f_1(u) = 1 + c_1 u^2 + c_2 \operatorname{sgn}(u) u^3, \tag{4.50}$$

where c_1 and c_2 are the two coefficients of the proposed even function, whereas $f_2(u)$ is the symmetric softening nonlinear hysteretic force given by Equation (4.41).

Figures 4.5a and 4.5b show the total nonlinear restoring force, given by Equation (4.49), in the case of post-hardening and post-softening behavior, respectively.

(a)



(b)

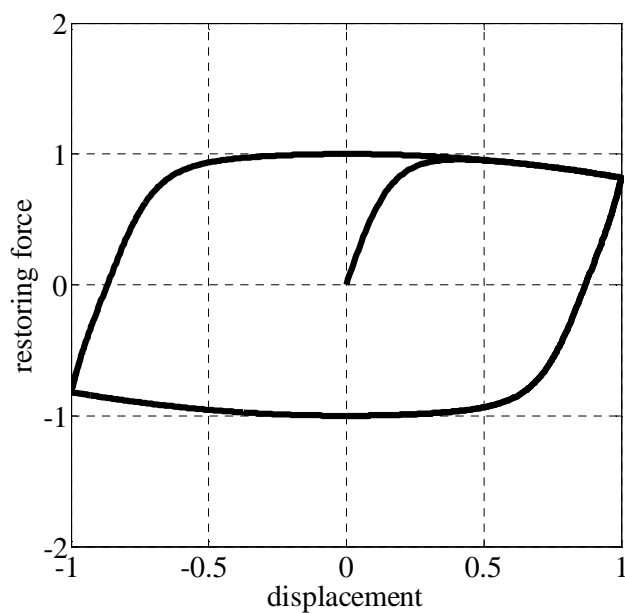


Figure 4.5. Total restoring force with (a) post-hardening and (b) post-softening characteristics at large displacements simulated by adopting the MBWM.

4.2.2 Biaxial Models

In what follows, a DEM able to simulate symmetric softening hysteresis loops with bilinear or rigid-plastic characteristics, taking into account the biaxial interaction between the restoring forces in two orthogonal horizontal directions, is described.

4.2.2.1 2d Bouc-Wen Model

The DEM for the biaxial behavior developed by Park et al. (1986) is an extension of the model introduced by Wen (1976, 1980) for uniaxial behavior. According to the former model, the isotropic hysteretic restoring forces in the x and y directions, that is, $z_x(u)$ and $z_y(u)$, can be obtained by solving the following coupled first order nonlinear ordinary differential equations:

$$\dot{z}_x = A \dot{u}_x - \beta |\dot{u}_x z_x| z_x - \gamma \dot{u}_x z_x^2 - \beta |\dot{u}_y z_y| z_x - \gamma \dot{u}_y z_x z_y, \quad (4.51)$$

$$\dot{z}_y = A \dot{u}_y - \beta |\dot{u}_y z_y| z_y - \gamma \dot{u}_y z_y^2 - \beta |\dot{u}_x z_x| z_y - \gamma \dot{u}_x z_x z_y. \quad (4.52)$$

The hysteretic behavior prescribed by Equations (4.51) and (4.52) can be illustrated by a simple displacement path as the one shown in Figure 4.6.

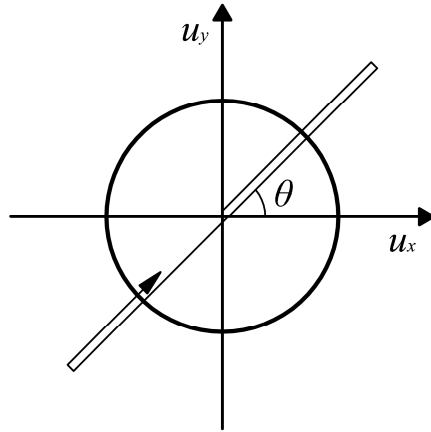


Figure 4.6. Linear displacement path.

In this case, the variables in Equations (4.51) and (4.52) are expressed as:

$$z_x = z \cos \vartheta, \quad z_y = z \sin \vartheta, \quad u_x = u \cos \vartheta, \quad u_y = u \sin \vartheta, \quad (4.53)$$

in which u and z are the uniaxial displacement and hysteretic restoring force, respectively. Substituting Equation (4.53) into Equations (4.51) and (4.52), it may be shown that the latter reduce to the following form:

$$\dot{z} = A\dot{u} - \beta|\dot{u}z|z - \gamma\dot{u}z^2, \tag{4.54}$$

which is the nonlinear ordinary differential equation proposed by Wen (1976, 1980) for $n = 2$. The total hysteretic restoring force along the displacement path of Figure 4.6 is illustrated in Figure 4.7.

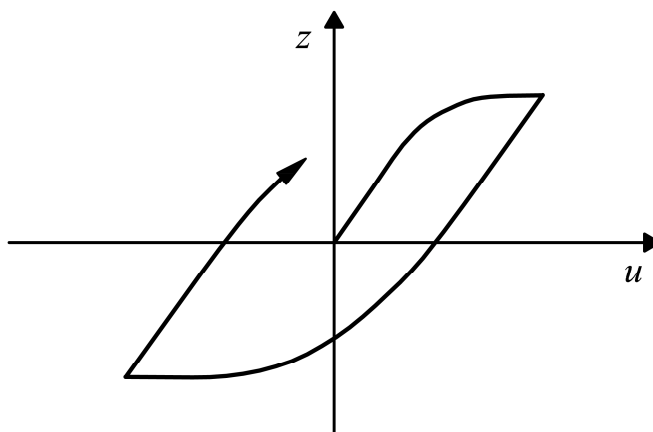


Figure 4.7. Hysteretic behavior under linear path.

The same is true for any value of ϑ therefore the restoring force is isotropic.

Nagarajaiah et al. (1991) have adapted the model for biaxial behavior to predict the dynamic response of elastomeric bearings.

For an elastomeric bearing, the nonlinear restoring forces along the orthogonal directions x and y can be described by the following equations:

$$f_x = \alpha \frac{F_y}{y} u_x + (1 - \alpha) \frac{F_y}{y} z_x, \tag{4.55}$$

$$f_y = \alpha \frac{F_y}{y} u_y + (1 - \alpha) \frac{F_y}{y} z_y, \tag{4.56}$$

where α is the post-yield to the pre-yield stiffness ratio, F_y is the yield force, y is the yield displacement, u_x and u_y represent the displacements of the isolation device in the x and y directions, respectively. The functions z_x and z_y , obtained by solving Equations (4.51) and (4.52), respectively, have the unit of displacement and account for the direction and biaxial

interaction of hysteresis forces. To account for the effects of axial load, α , F_y , and y have to be adjusted based on experimental results (Built 1982).

Nagarajaiah et al. (1991) suggests the following values for the model parameters:

$$A = 1, \beta = \frac{0.9}{y^2}, \text{ and } \gamma = \frac{0.1}{y^2}.$$

Constantinou et al. (1990) have adapted the DEM for the biaxial behavior developed by Park et al. (1986) for modeling sliding bearings, such as friction pendulum bearings and flat sliding bearings.

For a friction pendulum bearing, the nonlinear restoring forces along the orthogonal directions x and y are described by the following equations:

$$f_x = \frac{N}{R} u_x + \frac{\mu N}{y} z_x(u), \quad (4.57)$$

$$f_y = \frac{N}{R} u_y + \frac{\mu N}{y} z_y(u), \quad (4.58)$$

where N is the vertical load carried by the bearing, R is the radius of curvature of the spherical concave surface of the bearing, and μ is the sliding friction coefficient which depends on the value of bearing pressure and on the instantaneous velocity of sliding \dot{u} , given by:

$$\dot{u} = \sqrt{\dot{u}_x^2 + \dot{u}_y^2}. \quad (4.59)$$

The functions z_x and z_y , obtained by solving Equations (4.51) and (4.52), respectively, have the unit of displacement and account for the direction and biaxial interaction of hysteresis forces.

For a flat sliding bearing, the nonlinear restoring forces along the two orthogonal directions x and y are given by:

$$f_x = \frac{\mu N}{y} z_x(u), \quad (4.60)$$

$$f_y = \frac{\mu N}{y} z_y(u). \quad (4.61)$$

4.3 Proposed Mathematical Models

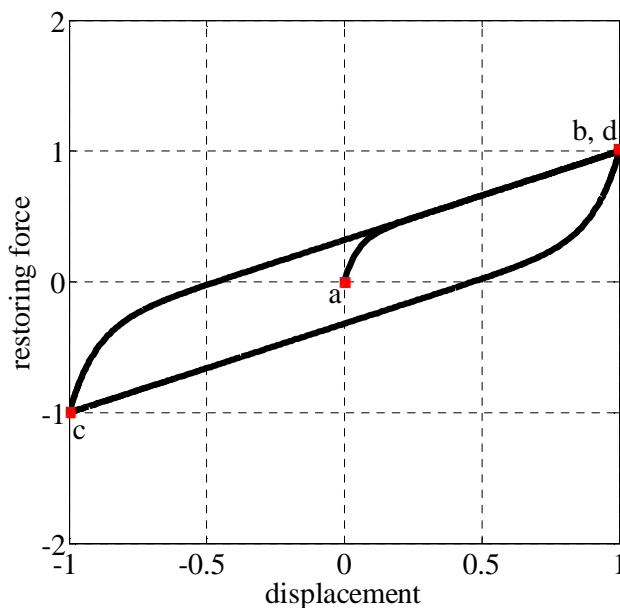
In the following, four uniaxial mathematical models, namely, Nonlinear Exponential Model (NEM), Advanced Nonlinear Exponential Model (ANEM), Parallel Model (PM), and Advanced Parallel Model (APM), and one biaxial mathematical model, namely, 2d Parallel Model (2d PM), are presented. The ANEM and the APM are an improved version of the NEM and PM, respectively.

4.3.1 Uniaxial Models

4.3.1.1 Nonlinear Exponential Model

Figure 4.8a shows the normalized symmetric softening force-displacement hysteresis loop with bilinear characteristics typical of elastomeric bearings, such as high damping rubber bearings and lead rubber bearings, and metal devices, such as wire rope isolators, whereas Figure 4.8b presents the normalized symmetric softening force-displacement loop having rigid-plastic characteristics generally displayed by sliding bearings, such as flat sliding bearings. Each hysteresis loop can be decomposed into three curves: the first loading curve (portion a-b), namely, virgin curve, the unloading curve (portion b-c), and the loading curve (portion c-d).

(a)



(b)

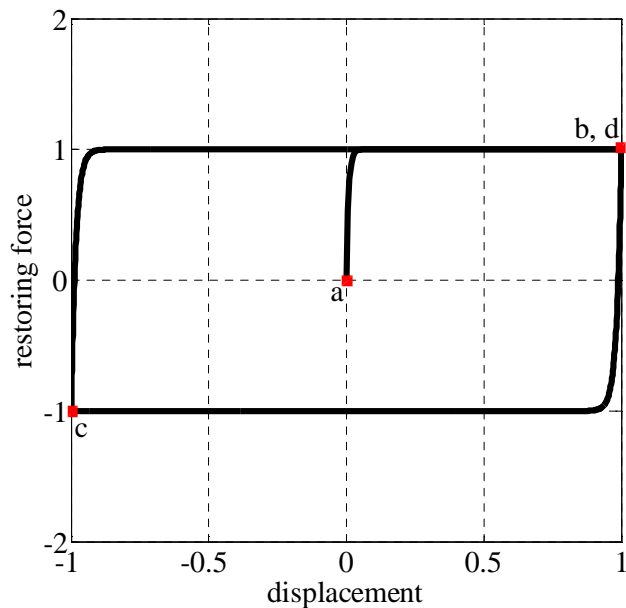
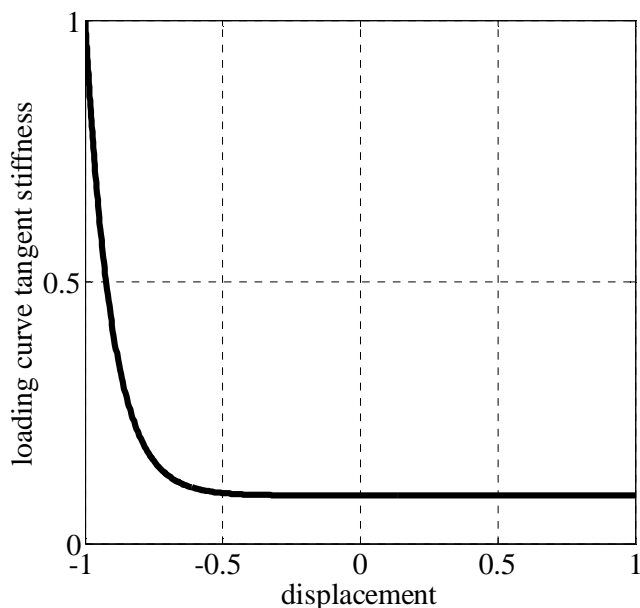


Figure 4.8. Normalized hysteresis loop with (a) bilinear and (b) rigid-plastic characteristics.

The loading curve tangent stiffness of the two normalized hysteresis loops shown in Figure 4.8 is plotted in Figure 4.9 as function of the horizontal displacement. Since the tangent stiffness functions of the loading and unloading curves are antisymmetric, only the former has been plotted. It can be observed that, in both two cases, the tangent horizontal stiffness exponentially decreases with increasing displacement.

(a)



(b)

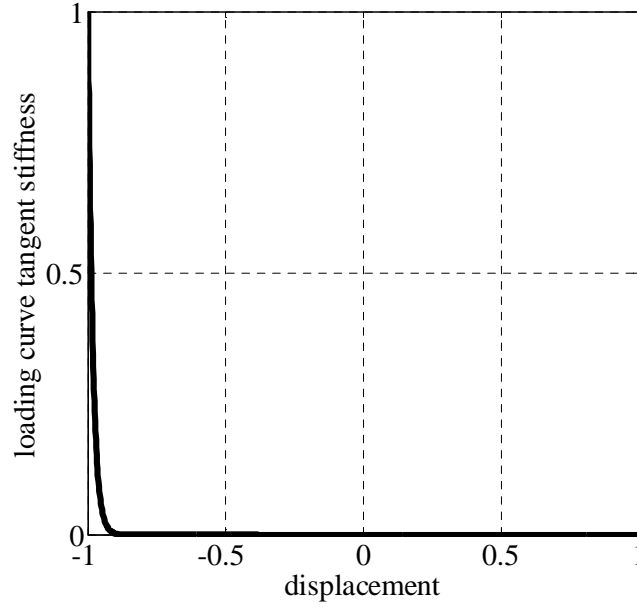


Figure 4.9. Tangent stiffness variation of the loading curve with (a) bilinear and (b) rigid-plastic characteristics.

The tangent stiffness $k_t(u)$ can be expressed by the following two mathematical expressions, valid for a loading and an unloading curve, respectively:

$$k_t(u) = k_2 + (k_1 - k_2) e^{-a(u - u_{min})}, \quad (\dot{u} > 0) \quad (4.62)$$

$$k_t(u) = k_2 + (k_1 - k_2) e^{-a(u_{max} - u)}, \quad (\dot{u} < 0) \quad (4.63)$$

where k_1 and k_2 are the initial and the asymptotic values of the tangent stiffness, u_{max} and u_{min} are the horizontal displacement values at the most recent point of unloading and loading, respectively, and a is a parameter that defines the transition from k_1 to k_2 .

Integrating Equations (4.62) and (4.63):

$$\int_{u_{min}}^u [k_2 + (k_1 - k_2) e^{-a(u - u_{min})}] du, \quad (\dot{u} > 0) \quad (4.64)$$

$$\int_{u_{max}}^u [k_2 + (k_1 - k_2) e^{-a(u_{max} - u)}] du, \quad (\dot{u} < 0) \quad (4.65)$$

the following nonlinear hysteretic restoring force is obtained:

$$f_h(u) = f_h(u_{min}) + k_2(u - u_{min}) - \frac{b}{a} \left[e^{-a(u - u_{min})} - 1 \right], \quad (\dot{u} > 0) \quad (4.66)$$

$$f_h(u) = f_h(u_{max}) - k_2(u_{max} - u) + \frac{b}{a} \left[e^{-a(u_{max} - u)} - 1 \right], \quad (\dot{u} < 0) \quad (4.67)$$

Equations (4.66) and (4.67) can be written in a more compacted form as follows:

$$f_h(u) = f_{lr} + k_2(u - u_{lr}) - \text{sgn}(\dot{u}) \frac{b}{a} \left[e^{-\text{sgn}(\dot{u})a(u - u_{lr})} - 1 \right], \quad (4.68)$$

where (u_{lr}, f_{lr}) is the most recent point of load reversal.

According to Masing's rule, the virgin curve can be obtained applying a similitude transformation of ratio 0.5 to the generic loading or unloading curve of the nonlinear restoring force $f_h(u)$. This means that for a given u on the virgin curve, where u is computed starting from zero, the corresponding tangent stiffness $k_t(u)$ must be equal to the one obtained from the generic loading or unloading curve for a value of $2u$. For this reason, if the initial displacement of the bearing is equal to zero, the virgin curve can be evaluated using the following expressions, valid for a loading and an unloading curve, respectively:

$$f_h(u) = k_2 u - \frac{b}{2a} \left[e^{-2au} - 1 \right], \quad (\dot{u} > 0) \quad (4.69)$$

$$f_h(u) = k_2 u + \frac{b}{2a} \left[e^{2au} - 1 \right], \quad (\dot{u} < 0) \quad (4.70)$$

Equations (4.69) and (4.70) can be written in a more compacted form as follows:

$$f_h(u) = k_2 u - \text{sgn}(\dot{u}) \frac{b}{2a} \left[e^{-\text{sgn}(\dot{u})2au} - 1 \right]. \quad (4.71)$$

The area within a force-displacement hysteresis loop, that is, the value of the dissipated energy in one cycle of motion, can be evaluated as:

$$E_d = \int_{u_{min}}^{u_{max}} f_h(u_{min}) + k_2(u - u_{min}) - \frac{b}{a} \left[e^{-a(u - u_{min})} - 1 \right] du - \int_{u_{min}}^{u_{max}} f_h(u_{max}) - k_2(u_{max} - u) + \frac{b}{a} \left[e^{-a(u_{max} - u)} - 1 \right] du, \quad (4.72)$$

which gives:

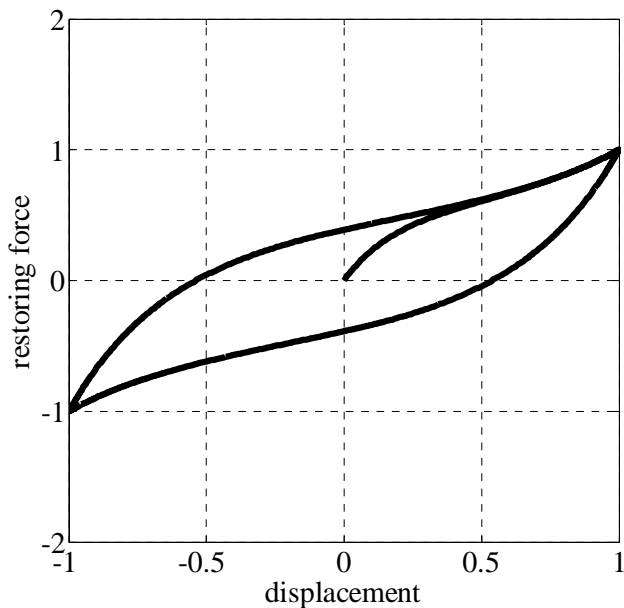
$$E_d = 4k_2 u_{max}^2 + \frac{2b}{a^2} [e^{-2a u_{max}} - 1] + \frac{4b}{a} u_{max} - 4f_h(u_{max}) u_{max}. \quad (4.73)$$

It is worth to notice that the proposed analytical model requires the evaluation of only 3 parameters, that is, k_1 , k_2 , and a , whereas in the widely used uniaxial differential equation BWM (Bouc 1971, Wen 1976, 1980) the number of parameters to be identified is equal to 7 for both elastomeric and sliding bearings (Constantinou et al. 1990, Nagarajaiah et al. 1991) and wire rope isolators (Demetriades et al. 1993). In addition, the presented model allows one to reduce the computational effort of a nonlinear time history analysis by avoiding, for each time step, the numerical solution of the first order nonlinear ordinary differential equation required by the BWM to evaluate the hysteretic variable.

4.3.1.2 Advanced Nonlinear Exponential Model

Figure 4.10a shows the typical normalized symmetric force-displacement hysteresis loop displayed by seismic isolators having post-hardening behavior at large displacements, such as high damping rubber bearings and wire rope isolators, whereas Figure 4.10b shows the typical normalized symmetric force-displacement loop of seismic isolators with post-softening behavior at large displacements, such as unbounded recycled rubber-fiber reinforced bearings.

(a)



(b)

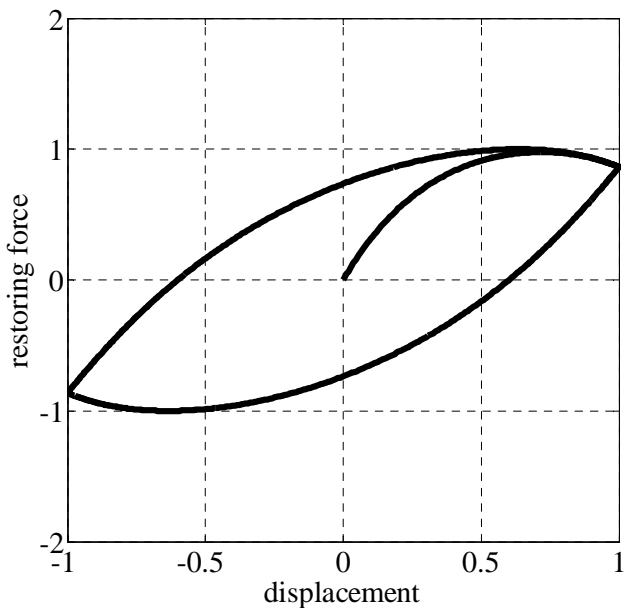
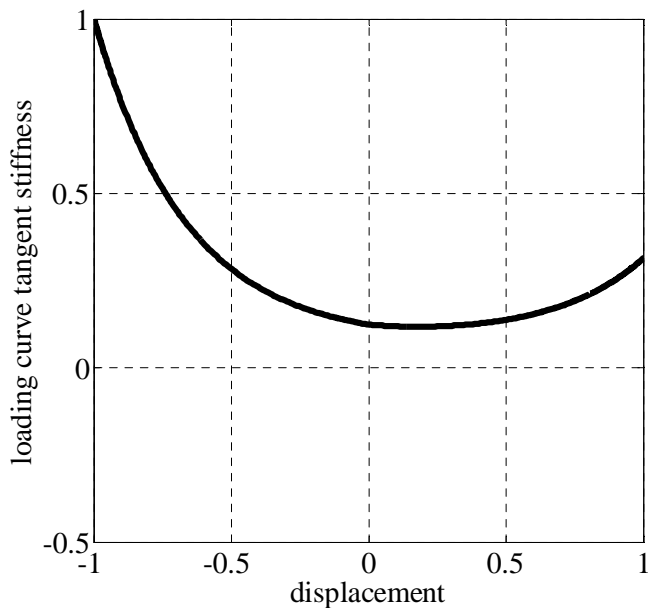


Figure 4.10. Normalized hysteresis loop with (a) post-hardening and (b) post-softening characteristics.

The loading curve tangent stiffness of the two normalized hysteresis loops shown in Figure 4.10 is plotted in Figure 4.11 as function of the horizontal displacement. Since the tangent stiffness functions of the loading and unloading curves are antisymmetric, only the former has been plotted.

(a)



(b)

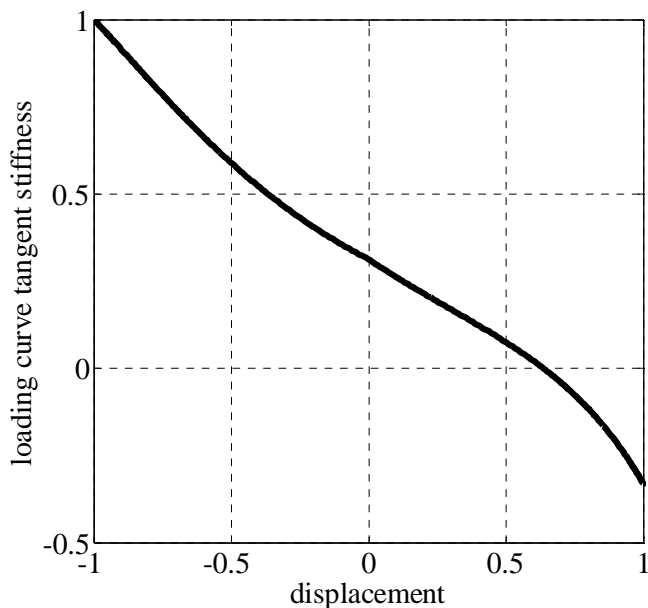


Figure 4.11. Tangent stiffness variation of the loading curve with (a) post-hardening and (b) post-softening characteristics.

The increase or decrease of the tangent stiffness can be simulated by connecting in parallel to the proposed NEM, a nonlinear elastic spring having a tangent stiffness function given by the following mathematical expression:

$$k_t(u) = c (e^{d \cdot u} - 1), \quad (u > 0) \quad (4.74)$$

$$k_t(u) = c (e^{-d \cdot u} - 1), \quad (u < 0) \quad (4.75)$$

where c and d are two parameters of the proposed exponential function.

Integrating Equations (4.74) and (4.75):

$$\int_0^u [c (e^{d \cdot u} - 1)] du, \quad (u > 0) \quad (4.76)$$

$$\int_0^u [c (e^{-d \cdot u} - 1)] du, \quad (u < 0) \quad (4.77)$$

the following nonlinear elastic restoring force is obtained:

$$f_e(u) = -c u + \frac{c}{d} (e^{d \cdot u} - 1), \quad (u > 0) \quad (4.78)$$

$$f_e(u) = -c u - \frac{c}{d} (e^{-d \cdot u} - 1). \quad (u < 0) \quad (4.79)$$

Equations (4.78) and (4.79) can be written in a more compacted form as follows:

$$f_e(u) = -c u + \text{sgn}(u) \frac{c}{d} [e^{\text{sgn}(u)d u} - 1]. \quad (4.80)$$

Hence, the nonlinear total restoring force of a seismic device is:

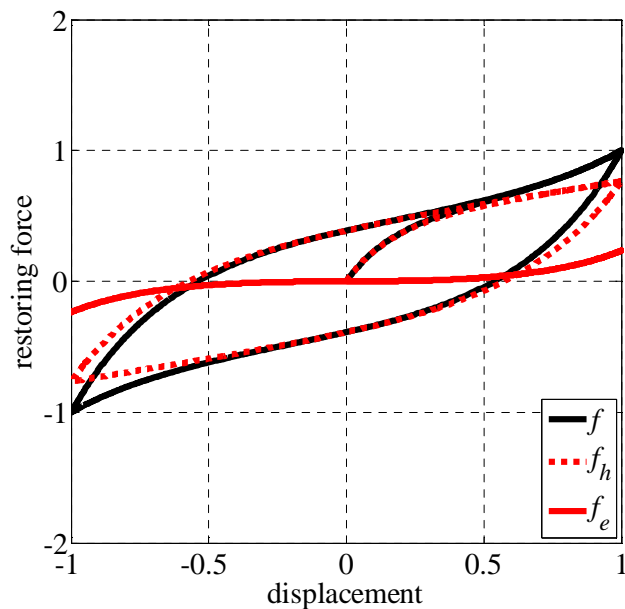
$$f(u) = f_h(u) + f_e(u), \quad (4.81)$$

where $f_h(u)$ is given by Equation (4.68).

Figures 4.12a and 4.12b show the two components of the nonlinear total restoring force $f(u)$ at large displacements, namely, the nonlinear hysteretic force $f_h(u)$ and the nonlinear elastic

force $f_e(u)$, in the case of force-displacement loop with post-hardening and post-softening characteristics, respectively.

(a)



(b)

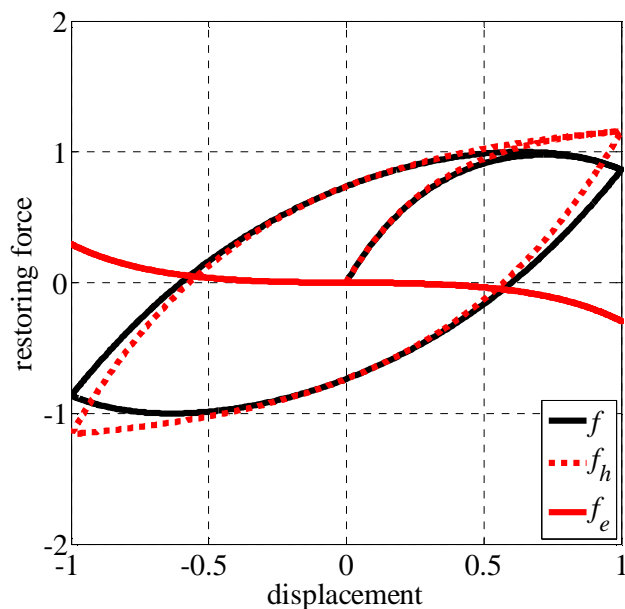


Figure 4.12. Total restoring force components for hysteresis loop with (a) post-hardening and (b) post-softening characteristics.

Figure 4.13 shows the mechanical model postulated to represent the 1d dynamic response of seismic isolators with hardening or softening behavior at large displacements. The model comprises a uniaxial Nonlinear Hysteretic Spring (NHS) and a uniaxial Nonlinear Elastic Spring (NES) in parallel and two rigid columns representing the height h of the bearing.

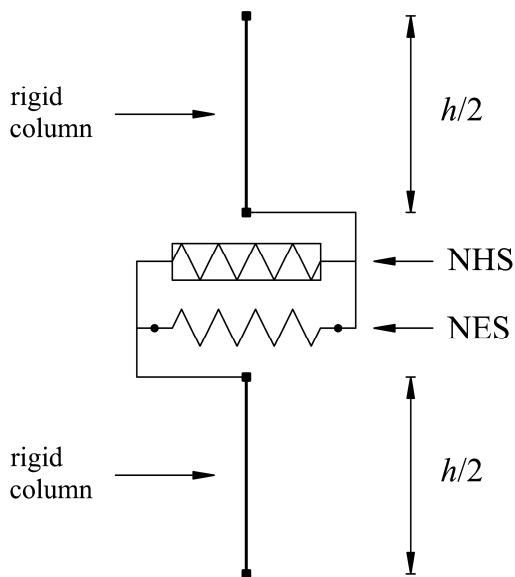


Figure 4.13. 1d mechanical model.

As it will be shown in Chapter 5, the mathematical model expressed by Equation (4.81) can capture the smooth transition of the hysteresis loops from the small to large horizontal displacement levels by using the same set of 5 parameters, that is, k_1 , k_2 , a , c , and d , identified from the experimental loops with the largest amplitude. Finally, it has to be noted that the axial load effects in the isolator device can be accounted for by adjusting the appropriate model parameters.

4.3.1.3 Parallel Model

In this section, a 1d PM is proposed to reproduce the dynamic behavior of seismic isolators having a continuously decreasing tangent stiffness, generally displayed within the relatively large displacements range.

4.3.1.3.1 Parallel Modeling of Inelastic Material Behavior

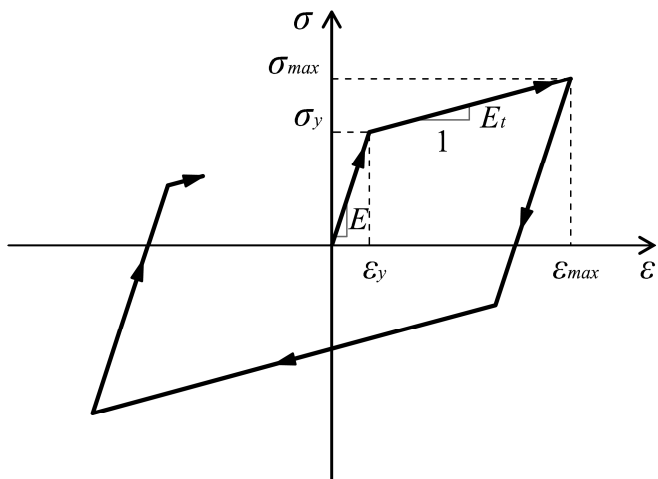
Hysteretic curves with continuously decreasing tangent stiffness can be easily discretized using the parallel modeling concept. The basic idea is to consider purely elastic elements and elastic-perfectly plastic elements connected in parallel, all having the same deformation but each carrying a different force. The total force acting on the parallel assemblage is then obtained by summing the forces acting on each element.

Parallel modeling has been already used in the past for representing the mechanical behavior of inelastic materials. The idea of effective stress introduced by Terzaghi to describe the behavior of wet soils is essentially a parallel model, as water and soil fabric both carry the total stress. The concept was first formalized by Mroz (1963) in treating nonassociated flow plasticity and then used by Owen et al. (1974) and Pande et al. (1977) to achieve a better representation of actual material behavior through a number of overlays of simple models. Nelson and Dorfmann (1995) have used parallel mathematical models in incremental elastoplasticity to represent strain hardening in metals and to develop models of frictional materials such as soils, rock and concrete.

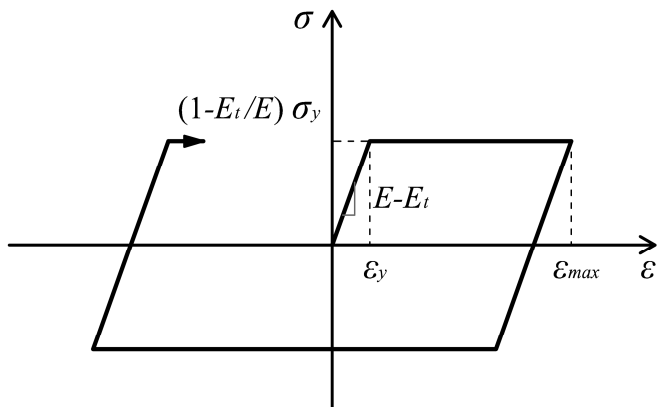
In what follows, the parallel modeling concept is first presented through a simple 1d example. Figure 4.14a shows the 1d stress-strain curve of a work hardening material which is elastic with Young's modulus E up to a yield stress σ_y and presents a tangent stiffness $E_t < E$ above the yield stress. The material is assumed to have the same yield stress in compression as in tension and to exhibit kinematic hardening, that is, the difference between the stresses which limit the elastic range remains constant during cyclic loading. A mathematical representation of the elasto-plastic response of the material is shown in the schematic diagram of Figure 4.14d, where an elastic element with Young's modulus E_t (Figure 4.14c) is connected in parallel to an elastic-perfectly plastic element having elastic stiffness $E - E_t$ and a yield stress $(1 - E_t/E)\sigma_y$ (Figure 4.14b). The parallel model does not only reproduce the stress-strain

curve during the loading, but also the behavior during unloading and cyclic loops as well as kinematic hardening.

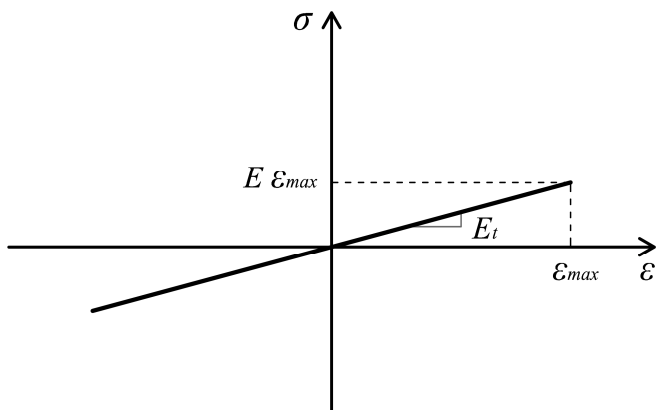
(a)



(b)



(c)



(d)

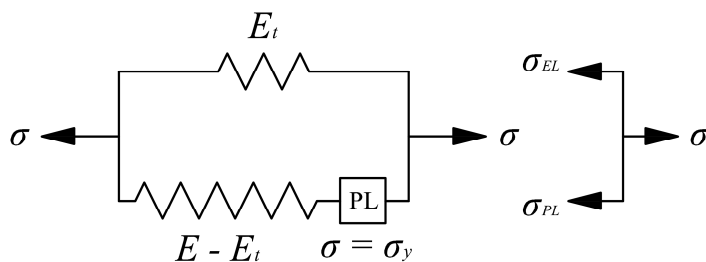


Figure 4.14. Parallel modeling of a 1d stress-strain curve for a work hardening material (two elements case).

The previous simple two-element model can be easily generalized to the case of a multilinear 1d stress-strain curve, using one elastic element and a finite number of elastic-perfectly plastic elements connected in parallel. As shown in Figure 4.15 for the case of four constitutive elements, the initial stiffness of the parallel assemblage is the sum of the elastic stiffness of each element. As the carried load increases, each of the elasto-plastic elements yields and the total stiffness correspondingly decreases.

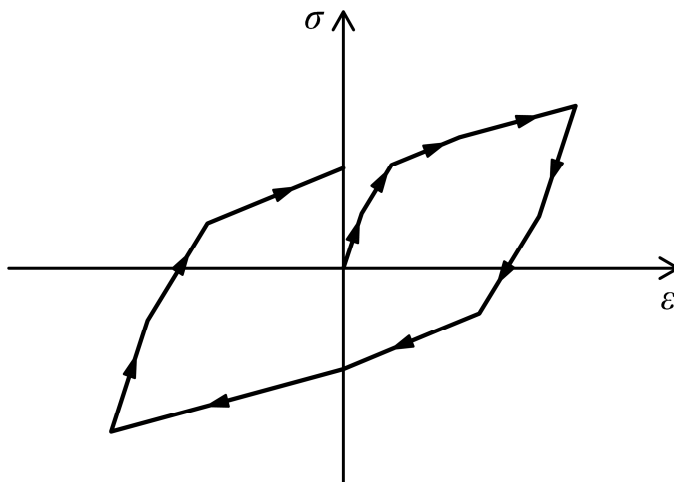


Figure 4.15. Parallel modeling of a 1d stress-strain curve for a work hardening material (four elements case).

It is easy to understand that 1d curves with continuously decreasing stiffness, like those exhibited by isolation bearings, can be effectively approximated through parallel modeling using a sufficiently high number of constitutive elements.

4.3.1.3.2 Application of Parallel Modeling to Seismic Isolators

The continuously decreasing tangent stiffness, generally displayed by seismic isolators within the relatively large displacements range, can be expressed by the following two mathematical expressions, valid for a loading and an unloading curve, respectively:

$$k_{t1}(u) = k_{\infty} + (k_0 - k_{\infty}) e^{-c_1(u - u_{min})}, \quad (\dot{u} > 0) \quad (4.82)$$

$$k_{t1}(u) = k_{\infty} + (k_0 - k_{\infty}) e^{-c_1(u_{max} - u)}, \quad (\dot{u} < 0) \quad (4.83)$$

where k_0 and k_{∞} are the initial and the asymptotic values of the tangent stiffness, u_{max} and u_{min} are the displacement values at the most recent point of unloading and loading, respectively, and c_1 is a parameter that defines the transition from k_0 to k_{∞} .

Equations (4.82) and (4.83) can be written in a more compacted form, valid for a generic loading or unloading curve obtained during cyclic testing on a single seismic isolation device:

$$k_{t1}(u) = k_{\infty} + a e^{-c_1 u}, \quad (4.84)$$

where $a = k_0 - k_{\infty}$ and u is evaluated starting from the latest point of unloading or reloading.

Figure 4.16 shows a plot of the tangent stiffness function $k_{t1}(u)$ given by Equation (4.84).

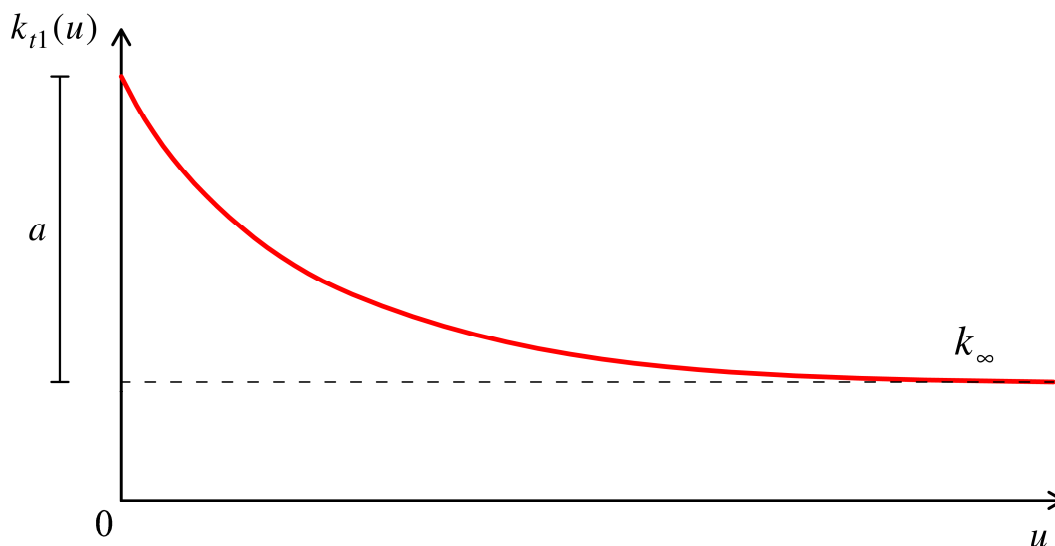


Figure 4.16. Plot of the tangent stiffness function $k_{t1}(u)$.

The proposed continuously decreasing tangent stiffness function can be approximated through a piecewise constant function with $N+1$ equally spaced decreasing values of $k_{t1}(u)$, as shown in Figure 4.17.

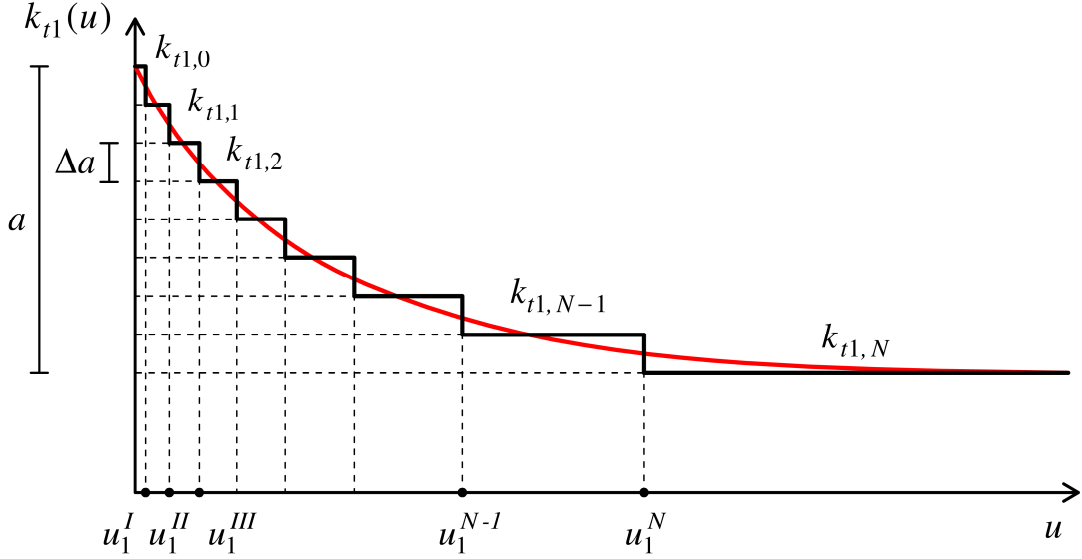


Figure 4.17. Continuous and discretized tangent stiffness function $k_{t1}(u)$.

Assuming $\Delta a = a/N$, the discretized tangent stiffness values are:

$$k_{t1,0} = k_{\infty} + a, \quad (4.85)$$

$$k_{t1,1} = k_{\infty} + (N - 1) \Delta a, \quad (4.86)$$

$$k_{t1,2} = k_{\infty} + (N - 2) \Delta a, \quad (4.87)$$

$$\dots, \quad (4.88)$$

$$k_{t1,N-1} = k_{\infty} + \Delta a, \quad (4.89)$$

$$k_{t1,N} = k_{\infty}, \quad (4.90)$$

and the corresponding values of the displacements are obtained by solving Equation (4.84) with respect to u :

$$u_{1,j} = -\frac{1}{c_1} \log \left(\frac{k_{t1,j} - k_{\infty}}{a} \right) \quad j = 0, 1, 2, \dots, N - 1. \quad (4.91)$$

Thus, the expression of the tangent stiffness $k_{t1}(u)$ can be approximated through the piecewise constant function given by:

$$u \leq u_1^I \rightarrow k_{t1}(u) = k_{t1,0} = k_\infty + a, \quad (4.92)$$

$$u_1^I \leq u < u_1^{II} \rightarrow k_{t1}(u) = k_{t1,1}, \quad (4.93)$$

$$u_1^{II} \leq u < u_1^{III} \rightarrow k_{t1}(u) = k_{t1,2}, \quad (4.94)$$

$$\dots, \quad (4.95)$$

$$u_1^{N-1} \leq u < u_1^N \rightarrow k_{t1}(u) = k_{t1,N-1}, \quad (4.96)$$

$$u \geq u_1^N \rightarrow k_{t1}(u) = k_{t1,N} = k_\infty, \quad (4.97)$$

where the limit displacement values u_1^i are:

$$u_1^I = \frac{u_{1,0} + u_{1,1}}{2}, \quad (4.98)$$

$$u_1^{II} = \frac{u_{1,1} + u_{1,2}}{2}, \quad (4.99)$$

$$\dots, \quad (4.100)$$

$$u_1^{N-1} = \frac{u_{1,N-2} + u_{1,N-1}}{2}, \quad (4.101)$$

$$u_1^N = \alpha u_{1,N-1}, \quad (4.102)$$

and α is an appropriate constant.

The above-described discretization of the tangent stiffness function $k_{t1}(u)$ allows one to simulate the dynamic behavior of seismic isolators within the relatively large displacements range by adopting a parallel assemblage made of one 1d elastic element, having stiffness $k_{el} = k_\infty$, and N 1d elastic-perfectly plastic elements, having stiffness $k_{ep,i} = \Delta a$, when in the elastic state, and yielding displacement u_1^i , for $i = I, II, \dots, N$. Thus, the nonlinear hysteretic

restoring force of the seismic isolation device can be obtained by summing the forces acting on each element. More specifically, the generic loading curve can be evaluated as:

$$f_1(u) = f_1(u_{min}) + f_e(u - u_{min}) + f_{ep,tot}(u - u_{min}), \quad (\dot{u} > 0) \quad (4.103)$$

where the restoring force of the 1d elastic element is given by:

$$f_e(u - u_{min}) = k_\infty(u - u_{min}), \quad (4.104)$$

whereas the total restoring force of the N 1d elastic-perfectly plastic elements is obtained as:

$$f_{ep,tot}(u - u_{min}) = \sum_{i=1}^N f_{ep,i}(u - u_{min}), \quad (4.105)$$

in which the restoring force of the i -th 1d elastic-perfectly plastic element is evaluated as:

$$f_{ep,i}(u - u_{min}) = \begin{cases} \Delta a (u - u_{min}) & \text{if } (u - u_{min}) < u_1^i \\ \Delta a u_1^i & \text{if } (u - u_{min}) > u_1^i \end{cases} \quad (4.106)$$

The generic unloading curve is given by:

$$f_1(u) = f_1(u_{max}) - f_e(u_{max} - u) - f_{ep,tot}(u_{max} - u), \quad (\dot{u} < 0) \quad (4.107)$$

with the restoring force of the 1d elastic element given by:

$$f_e(u_{max} - u) = k_\infty(u_{max} - u), \quad (4.108)$$

and the total restoring force of the N 1d elastic-perfectly plastic elements obtained as:

$$f_{ep,tot}(u_{max} - u) = \sum_{i=1}^N f_{ep,i}(u_{max} - u), \quad (4.109)$$

where the restoring force of the i -th 1d elastic-perfectly plastic element is evaluated as:

$$f_{ep,i}(u_{max} - u) = \begin{cases} \Delta a (u_{max} - u) & \text{if } (u_{max} - u) < u_1^i \\ \Delta a u_1^i & \text{if } (u_{max} - u) > u_1^i \end{cases} \quad (4.110)$$

Equations (4.103) and (4.107) can be written in a more compacted form, valid for a generic loading or unloading curve:

$$f_1(u) = f_1(u_{lr}) + \text{sgn}(\dot{u}) f_e [\text{sgn}(\dot{u})(u - u_{lr})] + \text{sgn}(\dot{u}) f_{ep, \text{tot}} [\text{sgn}(\dot{u})(u - u_{lr})], \quad (4.111)$$

in which:

$$f_e [\text{sgn}(\dot{u})(u - u_{lr})] = k_\infty \text{sgn}(\dot{u})(u - u_{lr}), \quad (4.112)$$

$$f_{ep, \text{tot}} [\text{sgn}(\dot{u})(u - u_{lr})] = \sum_{i=1}^N f_{ep, i} [\text{sgn}(\dot{u})(u - u_{lr})], \quad (4.113)$$

$$f_{ep, i} [\text{sgn}(\dot{u})(u - u_{lr})] = \begin{cases} \Delta a \text{sgn}(\dot{u})(u - u_{lr}) & \text{if } [\text{sgn}(\dot{u})(u - u_{lr})] < u_1^i \\ \Delta a u_1^i & \text{if } [\text{sgn}(\dot{u})(u - u_{lr})] > u_1^i \end{cases}, \quad (4.114)$$

and u_{lr} is the value of the displacement at the latest point of unloading or reloading, that is, u_{max} and u_{min} , respectively.

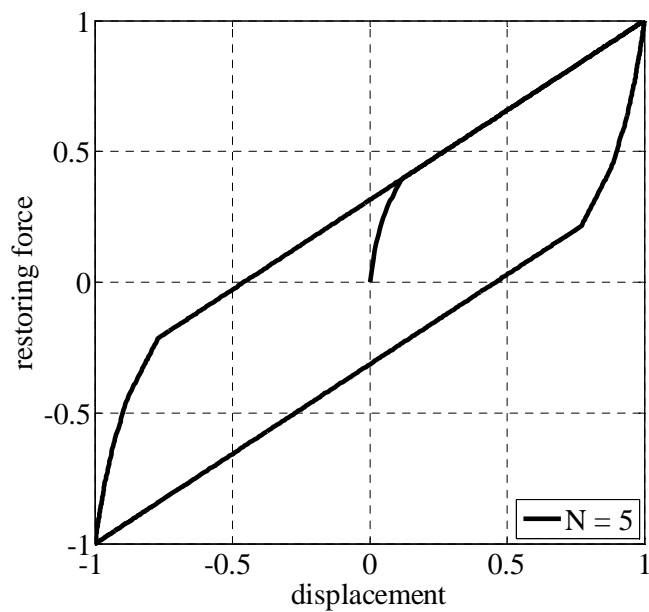
According to Masing's rule, the first loading curve, namely virgin curve, can be obtained from the generic loading curve from a similitude transformation of ratio 0.5. This means that for a given u on the virgin curve, where u is computed starting from zero, the corresponding tangent stiffness must be equal to the one obtained from the generic loading curve for a value of $2u$. Thus, in order to obtain the tangent stiffness for the virgin curve, it is just necessary to substitute c_1 with $2c_1$ in Equation (4.84):

$$k_{t1}(u) = k_\infty + a e^{-2c_1 u}. \quad (4.115)$$

Figures 4.18 and 4.19 show the nonlinear hysteretic force $f_1(u)$ having bilinear and rigid-plastic characteristics, respectively, simulated adopting 5 and 50 1d elastic-perfectly plastic elements, that is, $N = 5$ and $N = 50$.

It is worth to notice that the proposed mathematical model requires the evaluation of only 3 parameters, that is, k_0 , k_∞ , and c_1 , whereas in the widely used uniaxial differential equation BWM (Bouc 1971, Wen 1976, 1980) the number of parameters to be identified is equal to 7 for both elastomeric and sliding bearings (Constantinou et al. 1990, Nagarajaiah et al. 1991) and wire rope isolators (Demetriades et al. 1993). In addition, the presented model allows one to reduce the computational effort of a nonlinear time history analysis by avoiding, for each time step, the numerical solution of the first order nonlinear ordinary differential equation required by the BWM to evaluate the hysteretic variable.

(a)



(b)

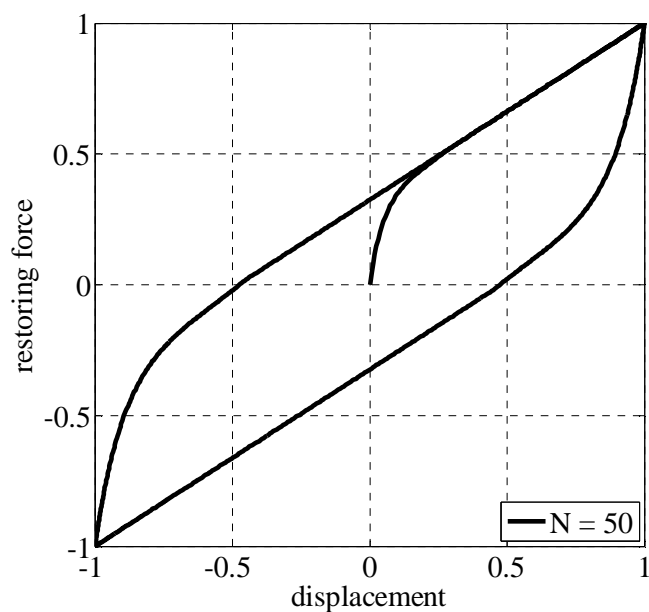
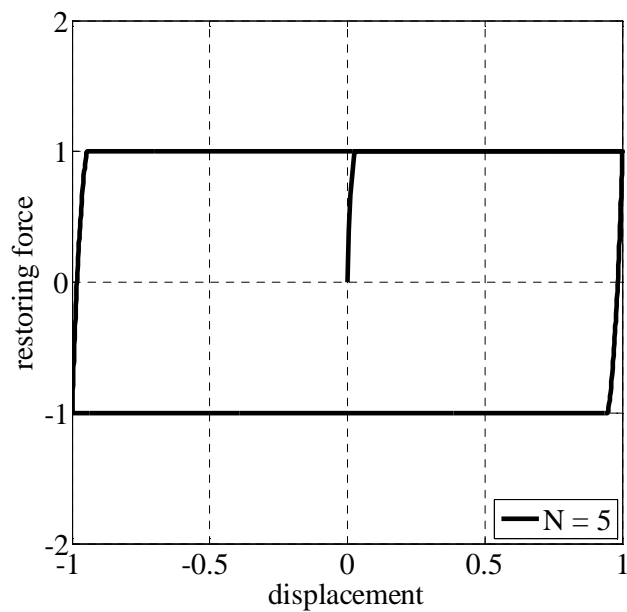


Figure 4.18. Nonlinear hysteretic force $f_1(u)$ having bilinear characteristics simulated adopting (a) $N=5$ and (b) $N=50$.

(a)



(b)

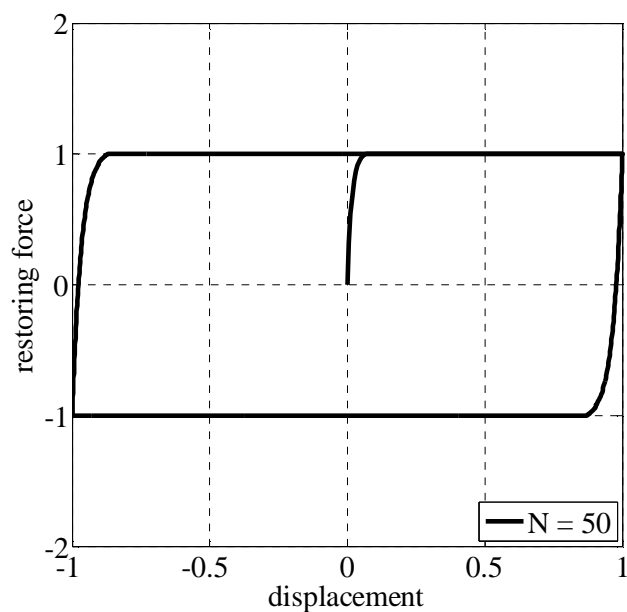


Figure 4.19. Nonlinear hysteretic force $f_1(u)$ having rigid-plastic characteristics simulated adopting (a) $N = 5$ and (b) $N = 50$.

4.3.1.4 Advanced Parallel Model

In the following, the proposed 1d PM is modified in order to reproduce the dynamic response of seismic isolators with post-hardening or post-softening behavior at large displacements.

The increase or decrease of the tangent stiffness displayed at large displacements can be obtained by summing the following mathematical expressions to Equation (4.84):

$$k_{t2}(u) = -c_2 + c_2 e^{c_3 u}, \quad (u > 0) \quad (4.116)$$

$$k_{t2}(u) = -c_2 + c_2 e^{-c_3 u}, \quad (u < 0) \quad (4.117)$$

where c_2 and c_3 are two parameters of the proposed exponential function.

Equations (4.116) and (4.117) can be written in a more compacted form, valid for positive or negative displacement values:

$$k_{t2}(u) = -c_2 + c_2 e^{\text{sgn}(u)c_3 u}. \quad (4.118)$$

Figure 4.20 shows a plot of the tangent stiffness function $k_{t2}(u)$, given by Equation (4.118), obtained for positive values of the parameters c_2 and c_3 .

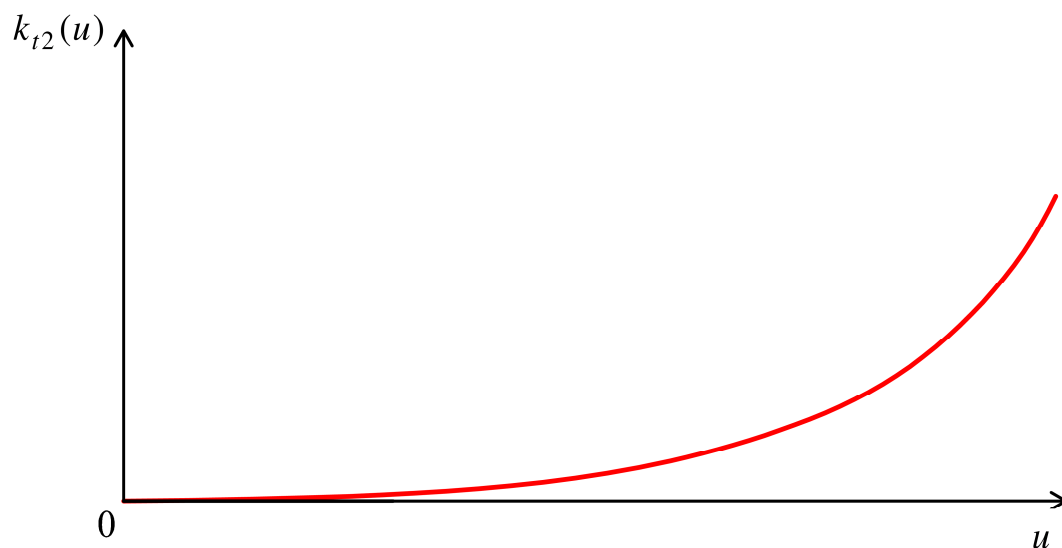


Figure 4.20. Plot of the tangent stiffness function $k_{t2}(u)$ obtained for $c_2 > 0$ and $c_3 > 0$.

The proposed continuously increasing or decreasing tangent stiffness function given by Equation (4.118) can be approximated through a piecewise constant function with M equally spaced increasing or decreasing values of $k_{t2}(u)$. Figure 4.21 shows the continuous and discretized increasing tangent stiffness function obtained for positive values of c_2 and c_3 .

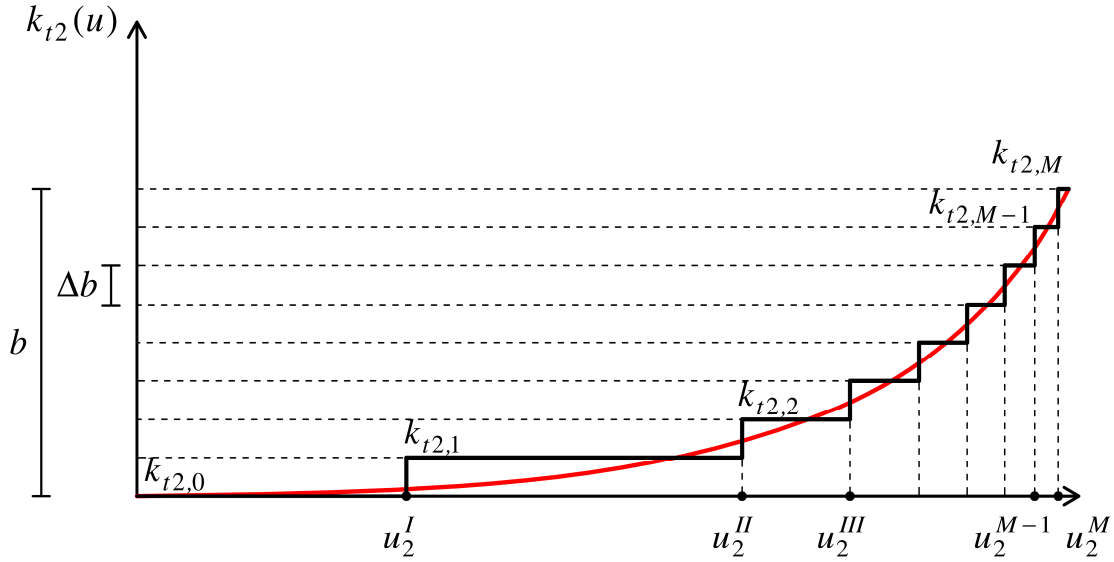


Figure 4.21. Continuous and discretized increasing tangent stiffness function $k_{t2}(u)$ obtained for $c_2 > 0$ and $c_3 > 0$.

Assuming $\Delta b = b/M$, the discretized tangent stiffness values are:

$$k_{t2,0} = 0, \quad (4.119)$$

$$k_{t2,1} = \Delta b, \quad (4.120)$$

$$k_{t2,2} = 2 \Delta b, \quad (4.121)$$

$$\dots, \quad (4.122)$$

$$k_{t2,M-1} = (M - 1) \Delta b, \quad (4.123)$$

$$k_{t2,M} = M \Delta b = b, \quad (4.124)$$

and the corresponding values of the displacements are obtained by solving Equation (4.118) with respect to u :

$$u_{2,j} = \frac{1}{c_3} \log \left(\frac{k_{t2,j} + c_2}{c_2} \right) \quad j = 0, 1, 2, \dots, M. \quad (4.125)$$

Thus, the expression of the tangent stiffness $k_{t2}(u)$ can be approximated through the piecewise constant function given by:

$$u \leq u_2^I \rightarrow k_{t2}(u) = k_{t2,0}, \quad (4.126)$$

$$u_2^I \leq u < u_2^{II} \rightarrow k_{t2}(u) = k_{t2,1}, \quad (4.127)$$

$$u_2^{II} \leq u < u_2^{III} \rightarrow k_{t2}(u) = k_{t2,2}, \quad (4.128)$$

$$\dots, \quad (4.129)$$

$$u_2^{M-1} \leq u < u_2^M \rightarrow k_{t2}(u) = k_{t2,M-1}, \quad (4.130)$$

$$u \geq u_2^M \rightarrow k_{t2}(u) = k_{t2,M} = b, \quad (4.131)$$

where the limit displacement values u_2^i are:

$$u_2^I = \frac{u_{2,0} + u_{2,1}}{2}, \quad (4.132)$$

$$u_2^{II} = \frac{u_{2,1} + u_{2,2}}{2}, \quad (4.133)$$

$$\dots, \quad (4.134)$$

$$u_2^{M-1} = \frac{u_{2,M-2} + u_{2,M-1}}{2}, \quad (4.135)$$

$$u_2^M = \frac{u_{2,M-1} + u_{2,M}}{2}. \quad (4.136)$$

The above-described discretization of the tangent stiffness function $k_{t2}(u)$ allows one to obtain a nonlinear elastic force by adopting a parallel assemblage made of M 1d linear elastic gap elements, having stiffness $k_{eg,i} = \Delta b$ and gap length equal to u_2^i , for $i = I, II, \dots, M$. More specifically, the nonlinear elastic force can be evaluated as:

$$f_2(u) = f_{ge,tot}(u), \quad (4.137)$$

where the total restoring force of the M 1d linear elastic gap elements is given by:

$$f_{ge,tot}(u) = \sum_{i=1}^M f_{ge,i}(u), \quad (4.138)$$

in which the restoring force of the i -th 1d gap element is evaluated as:

$$f_{ge,i}(u) = \begin{cases} 0 & \text{if } |u| < u_2^i \\ \Delta b [u - \text{sgn}(u) u_2^i] & \text{if } |u| > u_2^i \end{cases}. \quad (4.139)$$

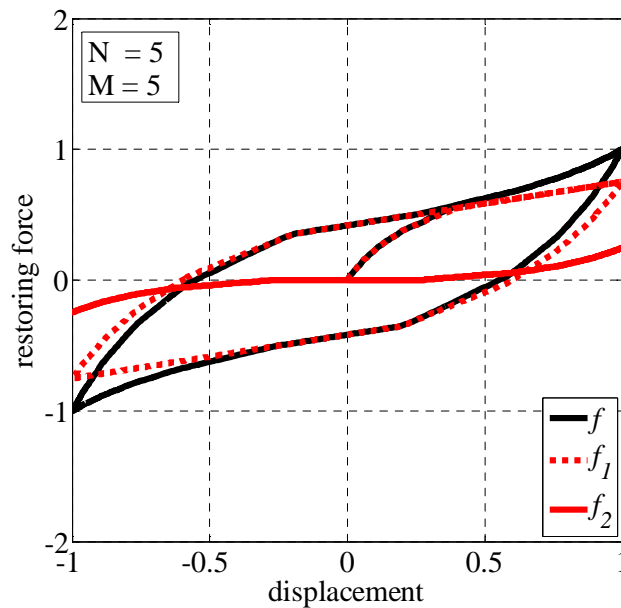
Hence, the nonlinear total restoring force of a seismic device can be calculated as:

$$f(u) = f_1(u) + f_2(u), \quad (4.140)$$

where $f_1(u)$ is given by Equation (4.111).

Figures 4.22a and 4.22b show the two components of the nonlinear total restoring force $f(u)$ at large displacements, namely, the nonlinear hysteretic force $f_1(u)$ and the nonlinear elastic force $f_2(u)$, in the case of force-displacement loop with post-hardening and post-softening characteristics, respectively, obtained adopting one 1d elastic element, 5 1d elastic-perfectly plastic elements, and 5 1d linear elastic gap elements, that is, $N = 5$ and $M = 5$.

(a)



(b)

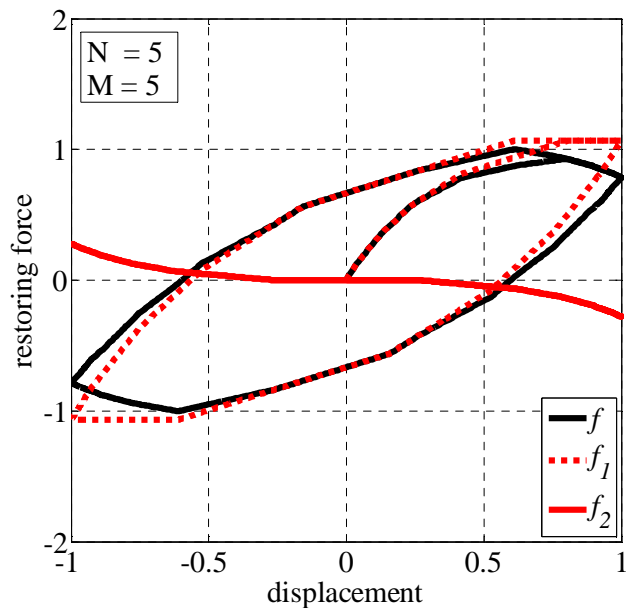
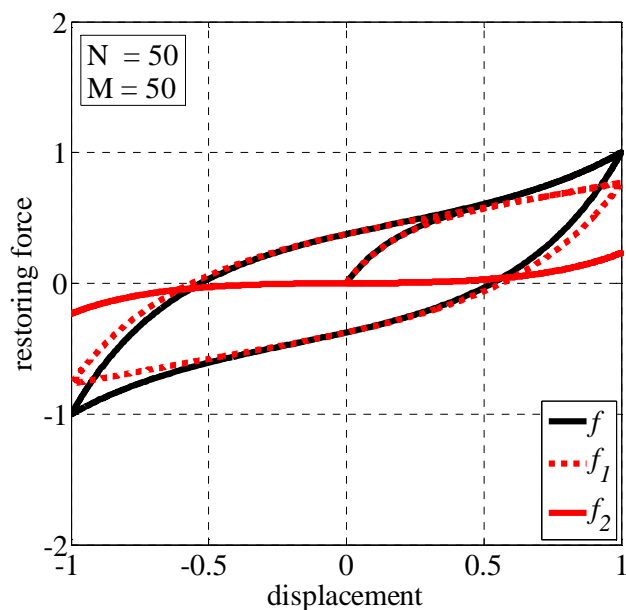


Figure 4.22. Total restoring force components for hysteresis loop with (a) post-hardening and (b) post-softening characteristics ($N = 5, M = 5$).

Figures 4.23a and 4.23b show the two components of the nonlinear total restoring force $f(u)$ at large displacements in the case of force-displacement loop with post-hardening and post-softening characteristics, respectively, obtained adopting one 1d elastic element, 50 1d elastic-perfectly plastic elements, and 50 1d linear elastic gap elements, that is, $N = 50$ and $M = 50$.

(a)



(b)

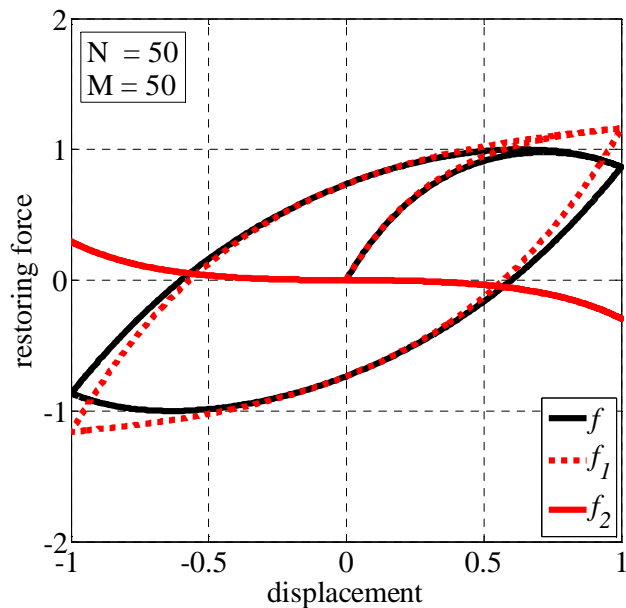


Figure 4.23. Total restoring force components for hysteresis loop with (a) post-hardening and (b) post-softening characteristics ($N = 50, M = 50$).

As it will be shown in Chapter 5, the mathematical model expressed by Equation (4.140) can capture the smooth transition of the hysteresis loops from the small to large horizontal displacement levels by using the same set of 5 parameters, that is, $k_0, k_\infty, c_1, c_2,$ and c_3 , identified from the experimental loops with the largest amplitude. Finally, it has to be noted that the axial load effects in the isolator device can be accounted for by adjusting the appropriate model parameters.

4.3.2 Biaxial Model

4.3.2.1 2d Parallel Model

In what follows, the parallel modeling of the inelastic material behavior is extended to the 3d case and the proposed PM is improved in order to represent the coupling of the nonlinear restoring forces along two orthogonal horizontal directions.

4.3.2.1.1 Parallel Modeling of Inelastic Material Behavior

The parallel modeling concept presented in 4.3.1.3.1 using a 1d representation can be extended to 2d or 3d without difficulty.

By considering the case of N elastic-perfectly plastic 3d elements and one elastic element connected in parallel, at each step of an incremental elasto-plastic analysis, all the elements have the same incremental strain tensor components:

$$d\boldsymbol{\varepsilon}_{ij} = d\boldsymbol{\varepsilon}_{ij}^I = d\boldsymbol{\varepsilon}_{ij}^{II} = \dots = d\boldsymbol{\varepsilon}_{ij}^N = d\boldsymbol{\varepsilon}_{ij}^{el}, \quad (4.141)$$

whereas the increments of stress tensor components carried by each element are summed together to obtain the total incremental stress tensor components:

$$d\boldsymbol{\sigma}_{ij} = d\boldsymbol{\sigma}_{ij}^I + d\boldsymbol{\sigma}_{ij}^{II} + \dots + d\boldsymbol{\sigma}_{ij}^N + d\boldsymbol{\sigma}_{ij}^{el}. \quad (4.142)$$

In the above, the total incremental strain and stress tensor components are indicated without apex, whereas the apices I, II, \dots, N refer to each elastic-perfectly plastic element and the apex el to the elastic element.

Denoting with $[C^{el}]$ the symmetric positive definite 6x6 stiffness matrix of the elastic element and with $\{d\boldsymbol{\sigma}^{el}\}$ and $\{d\boldsymbol{\varepsilon}^{el}\}$ the corresponding 6x1 vectors of incremental stress and incremental strain components, respectively, we have:

$$\{d\boldsymbol{\sigma}^{el}\} = [C^{el}] \{d\boldsymbol{\varepsilon}^{el}\}. \quad (4.143)$$

Regarding the K -th elastic-perfectly plastic element, its behavior is assumed to depend on the state of stress only, represented by the 6x1 vector $\{\boldsymbol{\sigma}^K\}$ of the stress tensor components, and

is determined by the value assumed by a scalar yield function $f(\sigma^K)$. If $f(\sigma^K) < 0$, the behavior is elastic:

$$\{d\sigma^K\} = [C^K] \{d\epsilon^K\}, \quad (4.144)$$

where $[C^K]$ is the element stiffness matrix in the elastic state. When $f(\sigma^K) = 0$, the plasticity mechanism becomes active and an incremental plastic flow, denoted by $\{d\epsilon^{K,pl}\}$, may occur, which in that case is added to the incremental elastic strain vector. In other words:

$$\{d\epsilon^K\} = \{d\epsilon^{K,el}\} + \{d\epsilon^{K,pl}\}, \quad (4.145)$$

where

$$\{d\epsilon^{K,el}\} = [C^K]^{-1} \{d\sigma^K\}. \quad (4.146)$$

Plastic flow occurs when $f(\sigma^K) = 0$ and the incremental stress vector $\{d\sigma^K\}$ lies in the tangent plane to the yield surface. Mathematically this is expressed by:

$$\{\nabla f\}^T \{d\sigma^K\} = 0, \quad (4.147)$$

with $\{\nabla f\}$ the 6x1 gradient vector of the yield function. In this way, for an infinitesimal $\{d\sigma^K\}$, the state of stress $\{\sigma^K + d\sigma^K\}$ is still represented by a point on the yield surface, as:

$$f(\sigma^K + d\sigma^K) = f(\sigma^K) + \{\nabla f\}^T \{d\sigma^K\} = 0. \quad (4.148)$$

When $f(\sigma^K) = 0$ and $\{\nabla f\}^T \{d\sigma^K\} < 0$, the behavior is elastic and Equation (4.144) is valid, whereas $f(\sigma^K) = 0$ and $\{\nabla f\}^T \{d\sigma^K\} > 0$ is not permitted because this would imply a change of the yield surface, which is not allowed due to the hypothesis of perfect plasticity. Assuming an associated plasticity law, the incremental plastic flow is given by:

$$\{d\epsilon^{K,pl}\} = d\lambda \{\nabla f\}, \quad (4.149)$$

where $d\lambda$ is an undetermined positive quantity. In other words, the plastic strain incremental vector is always perpendicular to the yield surface.

According to Equations (4.145), (4.146), and (4.149) we have:

$$\{d\boldsymbol{\varepsilon}^K\} = \{d\boldsymbol{\varepsilon}^{K,el}\} + \{d\boldsymbol{\varepsilon}^{K,pl}\} = [C^K]^{-1} \{d\boldsymbol{\sigma}^K\} + d\lambda \{\nabla f\}, \quad (4.150)$$

which can be rearranged by solving with respect to $\{d\boldsymbol{\sigma}^K\}$:

$$\{d\boldsymbol{\sigma}^K\} = [C^K] \{d\boldsymbol{\varepsilon}^K\} - d\lambda [C^K] \{\nabla f\}. \quad (4.151)$$

Once $\{d\boldsymbol{\varepsilon}^K\}$ is known, the value of $d\lambda$ can be determined from Equation (4.147):

$$\{\nabla f\}^T \{d\boldsymbol{\sigma}^K\} = \{\nabla f\}^T ([C^K] \{d\boldsymbol{\varepsilon}^K\} - d\lambda [C^K] \{\nabla f\}) = 0, \quad (4.152)$$

which gives:

$$d\lambda = \frac{\{\nabla f\}^T [C^K] \{d\boldsymbol{\varepsilon}^K\}}{\{\nabla f\}^T [C^K] \{\nabla f\}}. \quad (4.153)$$

It can be noted that, when plastic flow occurs, it is possible to define a tangent elasto-plastic stiffness matrix $[C^{K,ep}]$ such that:

$$\{d\boldsymbol{\sigma}^K\} = [C^{K,ep}] \{d\boldsymbol{\varepsilon}^K\}, \quad (4.154)$$

obtained from Equations (4.151) and (4.153) and equal to:

$$[C^{K,ep}] = [C^K] - \frac{[C^K] \{\nabla f\} \{\nabla f\}^T [C^K]}{\{\nabla f\}^T [C^K] \{\nabla f\}}. \quad (4.155)$$

In summary, for a given incremental strain vector $\{d\boldsymbol{\varepsilon}\}$, it is possible to compute the corresponding incremental stress vector for all the elements of the parallel assemblage. This is given by Equation (4.143) or (4.144), respectively, if the element is elastic or is elasto-plastic with an elastic response, or by Equation (4.154), when the element is elasto-plastic and plastic flow is occurring.

4.3.2.1.2 Application of Parallel Modeling to Seismic Isolators

In what follows, the presented 1d PM is extended to the 2d case to take into account the transverse biaxial interaction between the nonlinear hysteretic restoring forces along the orthogonal directions x and y , namely, $f_x(u_x)$ and $f_y(u_y)$.

The discretization of the tangent stiffness function k_{t1} , described in 4.3.1.3.2, allows one to simulate the 2d dynamic behavior of seismic isolation devices within the relatively large displacements range by adopting a parallel assemblage made of one elastic element, having stiffness $k_{el} = k_{\infty}$, and N 2d elastic-perfectly plastic elements, having stiffness $k_{ep,i} = \Delta a$, when in the elastic state, and yielding function $f_x^2 + f_y^2 - (\Delta a u_1^i)^2$, for $i = I, II, \dots, N$.

The nonlinear hysteretic restoring forces of the seismic isolator can be obtained by summing the forces acting on each element. More specifically, the generic loading curves along x and y directions can be evaluated as:

$$\begin{Bmatrix} f_x(u_x) \\ f_y(u_y) \end{Bmatrix} = \begin{Bmatrix} f_x(u_{x\min}) \\ f_y(u_{y\min}) \end{Bmatrix} + \begin{Bmatrix} f_{ex}(u_x - u_{x\min}) \\ f_{ey}(u_y - u_{y\min}) \end{Bmatrix} + \begin{Bmatrix} f_{ep,tot\ x}(u_x - u_{x\min}) \\ f_{ep,tot\ y}(u_y - u_{y\min}) \end{Bmatrix}, \quad (4.156)$$

where the restoring forces of the elastic element are given by:

$$f_{ex}(u_x - u_{x\min}) = k_{\infty} (u_x - u_{x\min}), \quad (4.157)$$

$$f_{ey}(u_y - u_{y\min}) = k_{\infty} (u_y - u_{y\min}), \quad (4.158)$$

whereas the total restoring forces of the N 2d elastic-perfectly plastic elements are:

$$f_{ep,tot\ x}(u_x - u_{x\min}) = \sum_{i=I}^N f_{ep\ x,i}(u_x - u_{x\min}), \quad (4.159)$$

$$f_{ep,tot\ y}(u_y - u_{y\min}) = \sum_{i=I}^N f_{ep\ y,i}(u_y - u_{y\min}), \quad (4.160)$$

in which the restoring forces of the i -th 2d elastic-perfectly plastic element are evaluated as:

$$f_{ep\ x,i}(u_x - u_{x\min}) = \begin{cases} \Delta a (u_x - u_{x\min}) & \text{if } f_x^2 + f_y^2 - (\Delta a u_1^i)^2 < 0 \\ \Delta a u_1^i & \text{if } f_x^2 + f_y^2 - (\Delta a u_1^i)^2 = 0 \end{cases}, \quad (4.161)$$

$$f_{ep,y,i}(u_y - u_{ymin}) = \begin{cases} \Delta a (u_y - u_{ymin}) & \text{if } f_x^2 + f_y^2 - (\Delta a u_1^i)^2 < 0 \\ \Delta a u_1^i & \text{if } f_x^2 + f_y^2 - (\Delta a u_1^i)^2 = 0 \end{cases} \quad (4.162)$$

The generic unloading curves along x and y directions can be evaluated as:

$$\begin{cases} f_x(u_x) \\ f_y(u_y) \end{cases} = \begin{cases} f_x(u_{xmax}) \\ f_y(u_{ymax}) \end{cases} - \begin{cases} f_{ex}(u_{xmax} - u_x) \\ f_{ey}(u_{ymax} - u_y) \end{cases} - \begin{cases} f_{ep,totx}(u_{xmax} - u_x) \\ f_{ep,toty}(u_{ymax} - u_y) \end{cases}, \quad (4.163)$$

where the restoring forces of the elastic element are given by:

$$f_{ex}(u_{xmax} - u_x) = k_\infty (u_{xmax} - u_x), \quad (4.164)$$

$$f_{ey}(u_{ymax} - u_y) = k_\infty (u_{ymax} - u_y), \quad (4.165)$$

whereas the total restoring forces of the N 2d elastic-perfectly plastic elements are:

$$f_{ep,totx}(u_{xmax} - u_x) = \sum_{i=1}^N f_{ep,x,i}(u_{xmax} - u_x), \quad (4.166)$$

$$f_{ep,toty}(u_{ymax} - u_y) = \sum_{i=1}^N f_{ep,y,i}(u_{ymax} - u_y), \quad (4.167)$$

in which the restoring forces of the i -th 2d elastic-perfectly plastic element are evaluated as:

$$f_{ep,x,i}(u_{xmax} - u_x) = \begin{cases} \Delta a (u_{xmax} - u_x) & \text{if } f_x^2 + f_y^2 - (\Delta a u_1^i)^2 < 0 \\ \Delta a u_1^i & \text{if } f_x^2 + f_y^2 - (\Delta a u_1^i)^2 = 0 \end{cases}, \quad (4.168)$$

$$f_{ep,y,i}(u_{ymax} - u_y) = \begin{cases} \Delta a (u_{ymax} - u_y) & \text{if } f_x^2 + f_y^2 - (\Delta a u_1^i)^2 < 0 \\ \Delta a u_1^i & \text{if } f_x^2 + f_y^2 - (\Delta a u_1^i)^2 = 0 \end{cases}. \quad (4.169)$$

Equations (4.156) and (4.163) can be written in a more compacted form, valid for a generic loading or unloading curve:

$$\begin{cases} f_x(u_x) \\ f_y(u_y) \end{cases} = \begin{cases} f_x(u_{xlr}) \\ f_y(u_{ylr}) \end{cases} + \begin{cases} f_{ex}(u_x - u_{xlr}) \\ f_{ey}(u_y - u_{ylr}) \end{cases} + \begin{cases} \text{sgn}(\dot{u}_x) f_{ep,totx}[\text{sgn}(\dot{u}_x)(u_x - u_{xlr})] \\ \text{sgn}(\dot{u}_y) f_{ep,toty}[\text{sgn}(\dot{u}_y)(u_y - u_{ylr})] \end{cases}, \quad (4.170)$$

in which:

$$f_{ex}(u_x - u_{xlr}) = k_\infty (u_x - u_{xlr}), \quad (4.171)$$

$$f_{ey}(u_y - u_{y lr}) = k_{\infty} (u_y - u_{y lr}), \quad (4.172)$$

$$f_{ep, tot x} [\text{sgn}(\dot{u}_x)(u_x - u_{x lr})] = \sum_{i=1}^N f_{ep x, i} [\text{sgn}(\dot{u}_x)(u_x - u_{x lr})], \quad (4.173)$$

$$f_{ep, tot y} [\text{sgn}(\dot{u}_y)(u_y - u_{y lr})] = \sum_{i=1}^N f_{ep y, i} [\text{sgn}(\dot{u}_y)(u_y - u_{y lr})], \quad (4.174)$$

$$f_{ep x, i} [\text{sgn}(\dot{u}_x)(u_x - u_{x lr})] = \begin{cases} \Delta a \text{sgn}(\dot{u}_x)(u_x - u_{x lr}) & \text{if } f_x^2 + f_y^2 - (\Delta a u_1^i)^2 < 0 \\ \Delta a u_1^i & \text{if } f_x^2 + f_y^2 - (\Delta a u_1^i)^2 = 0 \end{cases}, \quad (4.175)$$

$$f_{ep y, i} [\text{sgn}(\dot{u}_y)(u_y - u_{y lr})] = \begin{cases} \Delta a \text{sgn}(\dot{u}_y)(u_y - u_{y lr}) & \text{if } f_x^2 + f_y^2 - (\Delta a u_1^i)^2 < 0 \\ \Delta a u_1^i & \text{if } f_x^2 + f_y^2 - (\Delta a u_1^i)^2 = 0 \end{cases}, \quad (4.176)$$

where $u_{x lr}$ and $u_{y lr}$ are the values of the displacement along x and y directions, respectively, at the latest point of unloading or reloading.

According to Masing's rule, the first loading curve, namely virgin curve, can be obtained from the generic loading curve from a similitude transformation of ratio 0.5. This means that for a given u on the virgin curve, where u is computed starting from zero, the corresponding tangent stiffness must be equal to the one obtained from the generic loading curve for a value of $2u$. Thus, in order to obtain the tangent stiffness for the virgin curve, it is just necessary to substitute c_1 with $2c_1$ in Equation (4.84).

4.4 Comparisons between DEMs and Proposed Mathematical Models

4.4.1 Comparison between BWM and NEM

Figure 4.24 shows a symmetric softening force-displacement hysteresis loop with bilinear characteristics, typical of elastomeric bearings, such as high damping rubber bearings and lead rubber bearings, and metal devices, such as wire rope isolators, simulated using the differential equation BWM and the proposed NEM. The values of the parameters adopted in the two analytical models are listed in Table 4.2.

Table 4.2. BWM and NEM parameters | Hysteresis loop with bilinear characteristics.

BWM	f_y [N]	u_y [m]	α	A	β	γ	n
	45400.29	0.0171	0.10	1	0.5	0.5	2
NEM	k_1 [N/m]	k_2 [N/m]	a				
	4513479	265498	50				

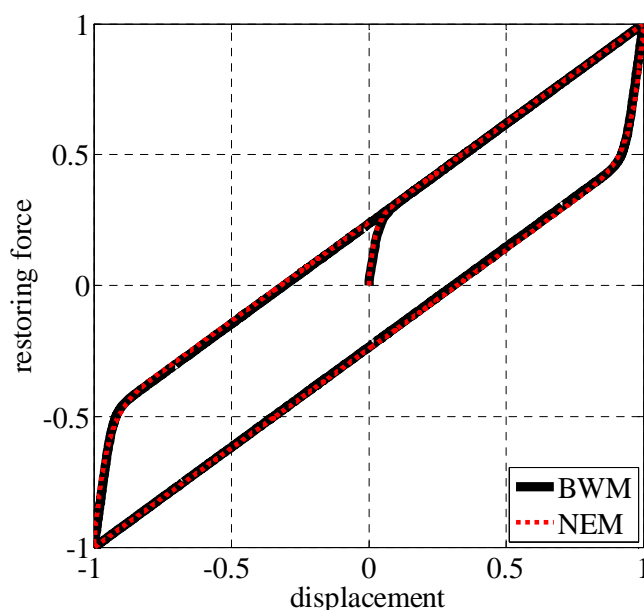


Figure 4.24. Symmetric softening hysteresis loop with bilinear characteristics simulated adopting the BWM and the proposed NEM.

Figure 4.25 presents a symmetric softening force-displacement hysteresis loop having bilinear characteristics and a very high value of the initial stiffness, generally displayed by friction

pendulum bearings, simulated using the BWM and the proposed NEM. The adopted models parameters are listed in Table 4.3.

Table 4.3. BWM and NEM parameters | Loop with bilinear characteristics and high initial stiffness.

BWM	N [N]	R [m]	u_y [m]	μ	A	β	γ	n
	265976	1.5522	0.0001	0.06	1	0.5	0.5	2
NEM	k_1 [N/m]	k_2 [N/m]	a					
	28756272	171354	850					

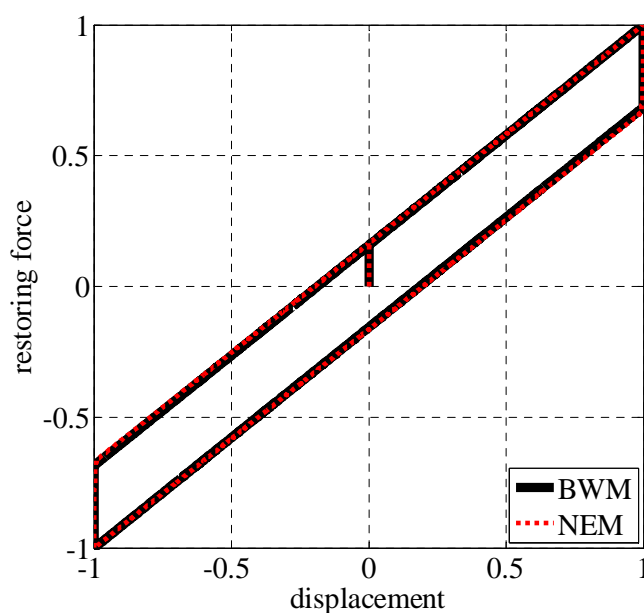


Figure 4.25. Symmetric softening hysteresis loop with bilinear characteristics and very high initial stiffness simulated adopting the BWM and the proposed NEM.

Figure 4.26 shows a symmetric softening force-displacement hysteresis loop having rigid-plastic characteristics, generally displayed by flat sliding bearings, simulated using the BWM and the proposed analytical model. The parameters adopted in the two models are listed in Table 4.4.

Table 4.4. BWM and NEM parameters | Hysteresis loop with rigid-plastic characteristics.

BWM	N [N]	u_y [m]	μ	A	β	γ	n
	265976	0.0001	0.06	1	0.5	0.5	2
NEM	k_1 [N/m]	k_2 [N/m]	a				
	14362714	0	850				

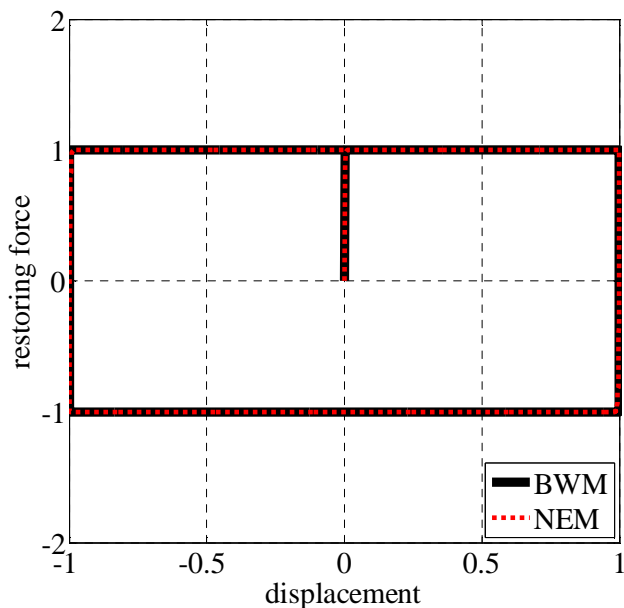


Figure 4.26. Symmetric softening hysteresis loop with rigid-plastic characteristics simulated adopting the BWM and the proposed NEM.

The theoretical force-displacement hysteresis loops produced by use of the BWM and NEM have been obtained, as done in experimental tests, by applying a sinusoidal harmonic displacement having amplitude equal to 0.50 m and frequency of 0.40 Hz.

It is worth to notice that the proposed analytical model requires the evaluation of only 3 parameters whereas in the BWM the number of parameters to be identified is equal to 7 for elastomeric bearings, flat sliding bearings, and wire rope isolators, and equal to 8 for friction pendulum bearings. In addition, it has to be noted that the proposed analytical model allows one to reduce the computational effort of a nonlinear time history analysis by avoiding, for each time step, the numerical solution of the first order nonlinear ordinary differential equation required by the BWM.

4.4.2 Comparison between BWM and PM

Figure 4.27 shows a symmetric softening force-displacement hysteresis loop with bilinear characteristics, typical of elastomeric bearings, such as high damping rubber bearings and lead rubber bearings, and metal devices, such as wire rope isolators, simulated using the BWM and the proposed PM. The values of the parameters adopted in the two models are listed in Table 4.5. In the PM, 50 1d elastic-perfectly plastic elements have been used, that is, $N = 50$.

Table 4.5. BWM and PM parameters | Hysteresis loop with bilinear characteristics.

BWM	f_y [N]	u_y [m]	α	A	β	γ	n
	45400.29	0.0171	0.10	1	0.5	0.5	2
PM	k_0 [N/m]	k_∞ [N/m]	c_1				
	4513479	265498	50				

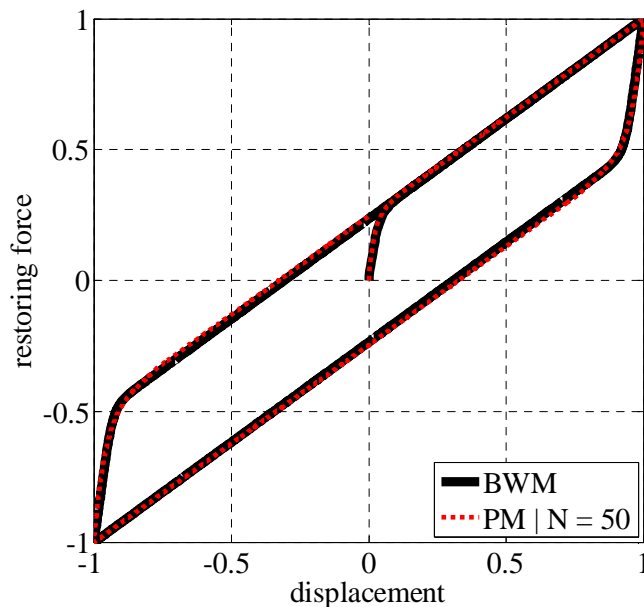
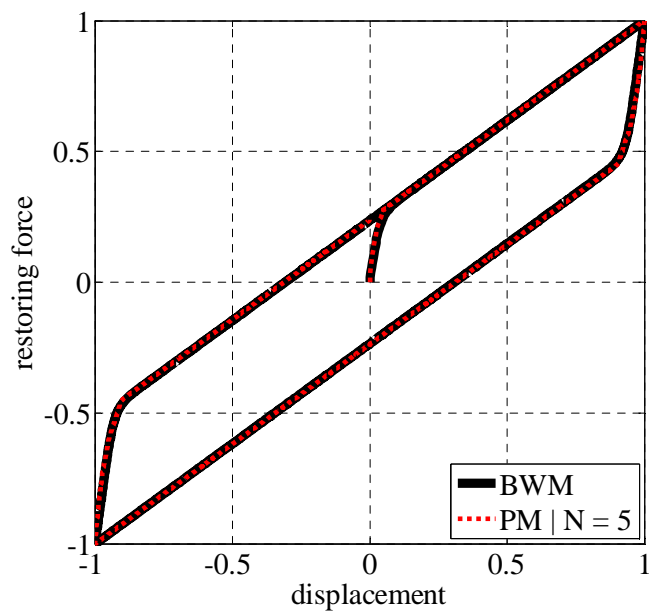


Figure 4.27. Symmetric softening hysteresis loop with bilinear characteristics simulated adopting the BWM and the proposed PM with $N = 50$.

Figures 4.28a and 4.28b show the same force-displacement hysteresis loop simulated adopting 5 and 100 1d elastic-perfectly plastic elements, respectively, in the proposed PM.

(a)



(b)

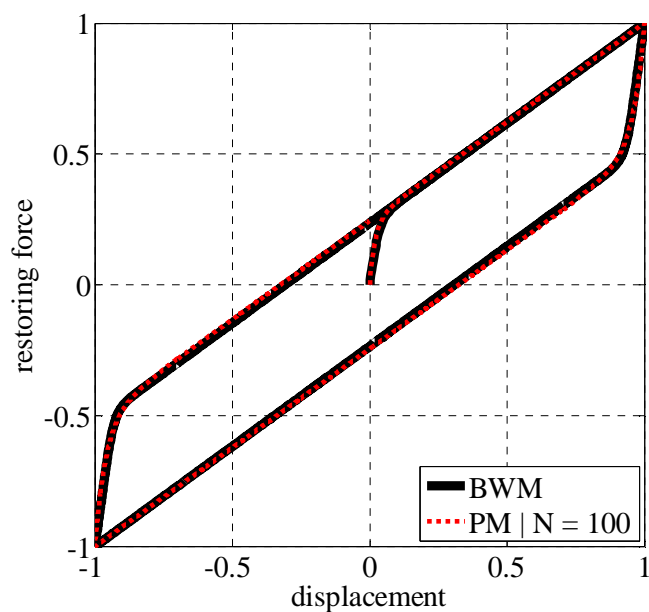


Figure 4.28. Symmetric softening hysteresis loop with bilinear characteristics simulated adopting the BWM and the proposed PM with (a) $N = 5$ and (b) $N = 100$.

Figure 4.29 presents a symmetric softening force-displacement hysteresis loop having bilinear characteristics and a very high value of the initial stiffness, generally displayed by friction pendulum bearings, simulated using the BWM and the proposed PM. The adopted models parameters are listed in Table 4.6. In the PM, 50 1d elastic-perfectly plastic elements have been used, that is, $N = 50$.

Table 4.6. BWM and PM parameters | Loop with bilinear characteristics and high initial stiffness.

BWM	N [N]	R [m]	u_y [m]	μ	A	β	γ	n
	265976	1.5522	0.0001	0.06	1	0.5	0.5	2
PM	k_0 [N/m]	k_∞ [N/m]	c_1					
	28756272	171354	850					

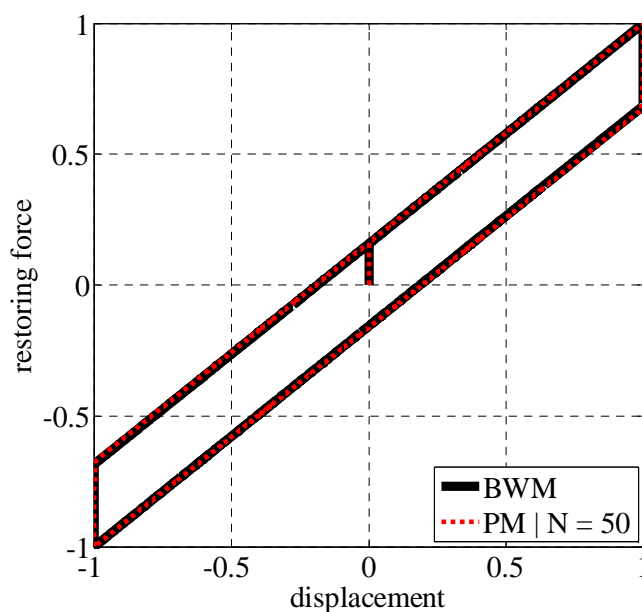
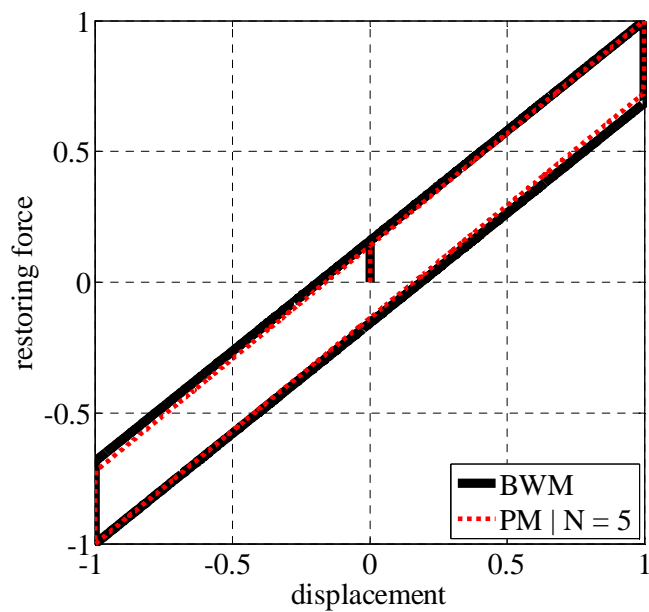


Figure 4.29. Symmetric softening hysteresis loop with bilinear characteristics and very high initial stiffness simulated adopting the BWM and the proposed PM with $N = 50$.

Figures 4.30a and 4.30b show the same force-displacement hysteresis loop simulated adopting 5 and 100 1d elastic-perfectly plastic elements, respectively, in the proposed PM.

(a)



(b)

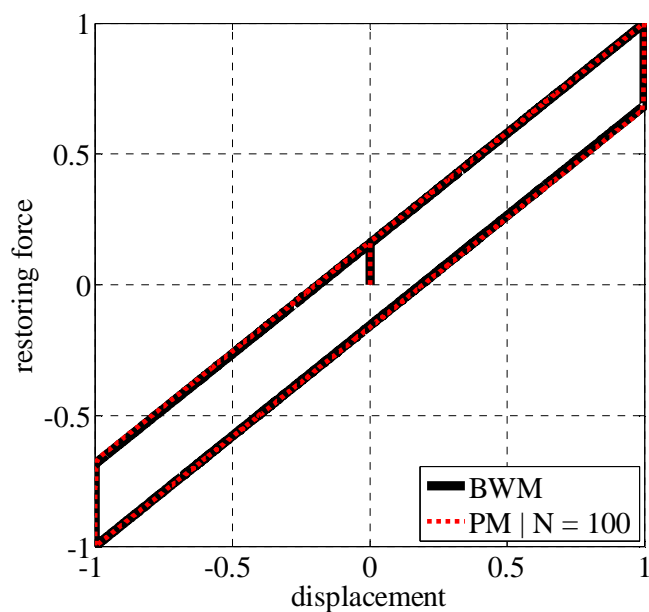


Figure 4.30. Symmetric softening hysteresis loop with bilinear characteristics and very high initial stiffness simulated adopting the BWM and the proposed PM with (a) $N = 5$ and (b) $N = 100$.

Figure 4.31 shows a symmetric softening force-displacement hysteresis loop having rigid-plastic characteristics, generally displayed by flat sliding bearings, simulated using the BWM and the proposed mathematical model. The parameters adopted in the two models are listed in Table 4.7. In the PM, 50 1d elastic-perfectly plastic elements have been used, that is, $N = 50$.

Table 4.7. BWM and PM parameters | Hysteresis loop with rigid-plastic characteristics.

BWM	N [N]	u_y [m]	α	A	β	γ	n
	265976	0.0001	0.06	1	0.5	0.5	2
PM	k_0 [N/m]	k_∞ [N/m]	c_1				
	14362714	0	850				

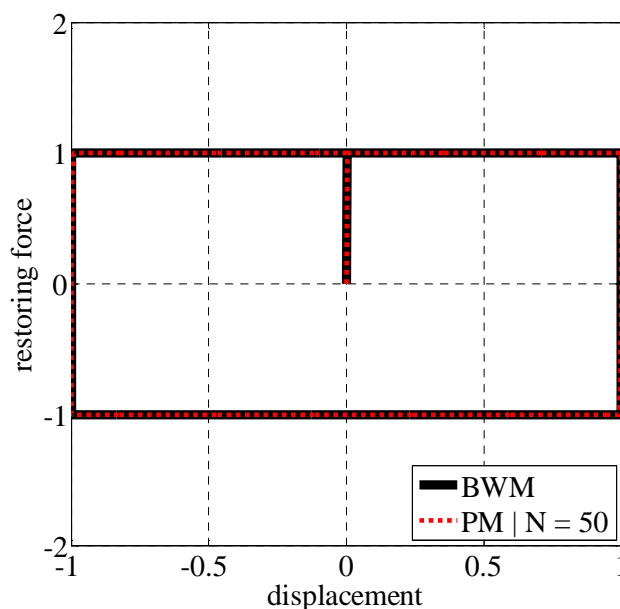
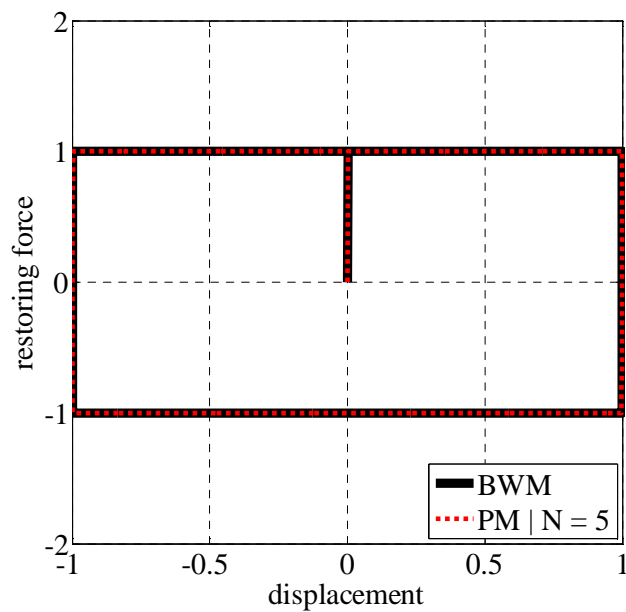


Figure 4.31. Symmetric softening hysteresis loop with rigid-plastic characteristics simulated adopting the BWM and the proposed PM with $N = 50$.

Figures 4.32a and 4.32b show the same force-displacement hysteresis loop simulated adopting 5 and 100 1d elastic-perfectly plastic elements, respectively, in the proposed PM.

(a)



(b)

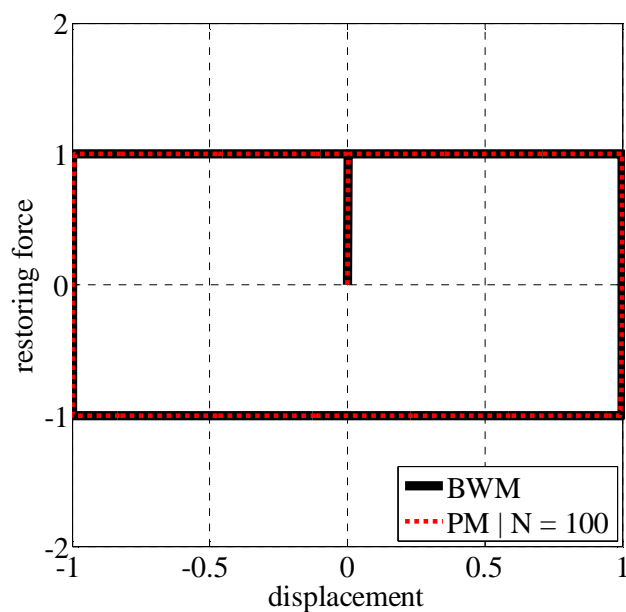


Figure 4.32. Symmetric softening hysteresis loop with rigid-plastic characteristics simulated adopting the BWM and the proposed PM with (a) $N = 5$ and (b) $N = 100$.

The theoretical force-displacement hysteresis loops produced by use of the BWM and PM have been obtained, as done in experimental tests, by applying a sinusoidal harmonic displacement having amplitude equal to 0.50 m and frequency of 0.40 Hz.

It is worth to observe that the proposed mathematical model requires the evaluation of only 3 parameters whereas in the BWM the number of parameters to be identified is equal to 7 for elastomeric bearings, flat sliding bearings, and wire rope isolators, and equal to 8 for friction pendulum bearings. In addition, it has to be noted that the proposed mathematical model allows one to reduce the computational effort of a nonlinear time history analysis by avoiding, for each time step, the numerical solution of the first order nonlinear ordinary differential equation required by the BWM.

4.4.3 Comparison between MBWM and ANEM

Figure 4.33 shows a symmetric force-displacement hysteresis loop, displayed by seismic isolators having post-hardening behavior at large displacements, such as high damping rubber bearings and wire rope isolators, simulated using the MBWM and the proposed ANEM. The values of the parameters adopted in the two analytical models are listed in Table 4.8.

Table 4.8. MBWM and ANEM parameters | Hysteresis loop with post-hardening characteristics.

MBWM	f_y [N]	u_y [m]	α	A	β	γ	n	c_1	c_2
	2025	0.0015	0.2407	1	0.9	0.1	2	1300	500
ANEM	k_1 [N/m]	k_2 [N/m]	a	c [N/m]	d				
	780000	81000	784.8	140000	36.75				

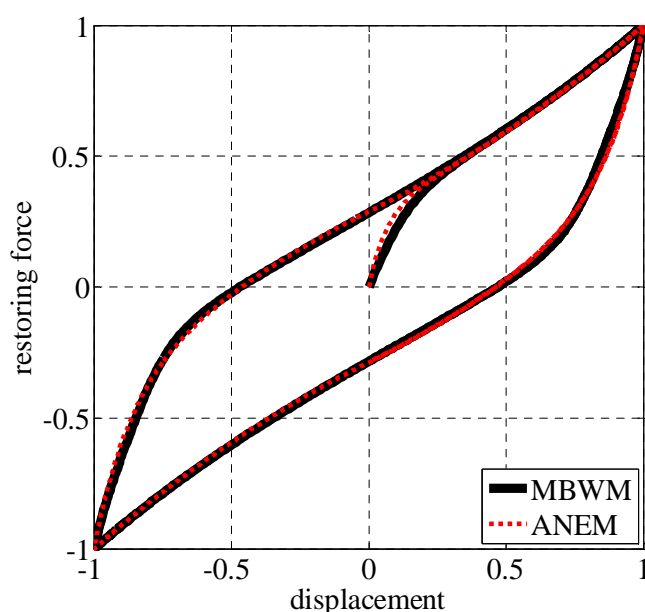


Figure 4.33. Symmetric hysteresis loop with post-hardening characteristics simulated adopting the MBWM and the proposed ANEM.

Figure 4.34 shows a symmetric force-displacement hysteresis loop, displayed by seismic isolators having post-softening behavior at large displacements, such as unbounded elastomeric bearings with deformable reinforcing layers, simulated using the MBWM and the proposed ANEM. The values of the parameters adopted in the two analytical models are listed in Table 4.9.

Table 4.9. MBWM and ANEM parameters | Hysteresis loop with post-softening characteristics.

MBWM	f_y [N]	u_y [m]	α	A	β	γ	n	c_1	c_2
	2025	0.0015	0.0481	1	0.9	0.1	2	-3000	500
ANEM	k_1 [N/m]	k_2 [N/m]	a	c [N/m]	d				
	2025000	64989	500	-1875000	8				

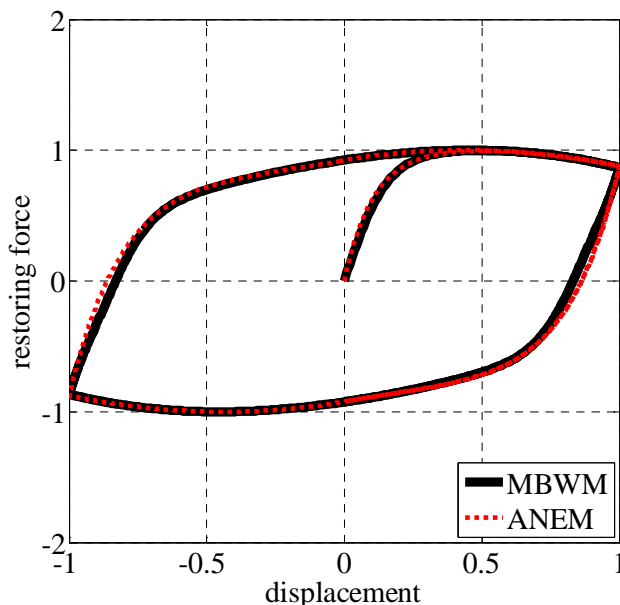


Figure 4.34. Symmetric hysteresis loop with post-softening characteristics simulated adopting the MBWM and the proposed ANEM.

The theoretical force-displacement hysteresis loops produced by use of the MBWM and the ANEM have been obtained, as done in experimental tests, by applying a sinusoidal harmonic displacement having amplitude equal to 0.01 m and frequency of 1 Hz.

It is important to notice that the proposed ANEM requires the evaluation of only five parameters whereas in the improved BWM the number of parameters to be identified is equal to nine. In addition, the proposed model allows one to reduce the computational effort of nonlinear time history analyses by avoiding, for each time step, the numerical solution of the first order nonlinear differential equation required in the MBWM.

4.4.4 Comparison between MBWM and APM

Figure 4.35 shows a symmetric force-displacement hysteresis loop, displayed by seismic isolators having post-hardening behavior at large displacements, such as high damping rubber bearings and wire rope isolators, simulated using the MBWM and the proposed APM. The values of the parameters adopted in the two mathematical models are listed in Table 4.10. In the APM, 50 1d elastic-perfectly plastic elements and 50 1d linear elastic gap elements have been used, that is, $N = 50$ and $M = 50$.

Table 4.10. MBWM and APM parameters | Hysteresis loop with post-hardening characteristics.

MBWM	f_y [N]	u_y [m]	α	A	β	γ	n	c_1	c_2
	2025	0.0015	0.2407	1	0.9	0.1	2	1300	500
APM	k_0 [N/m]	k_∞ [N/m]	c_1	c_2 [N/m]	c_3				
	780000	81000	784.8	140000	36.75				

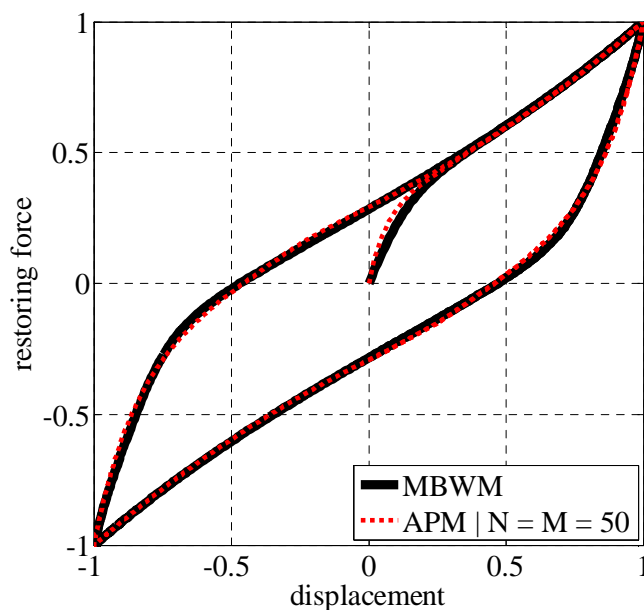
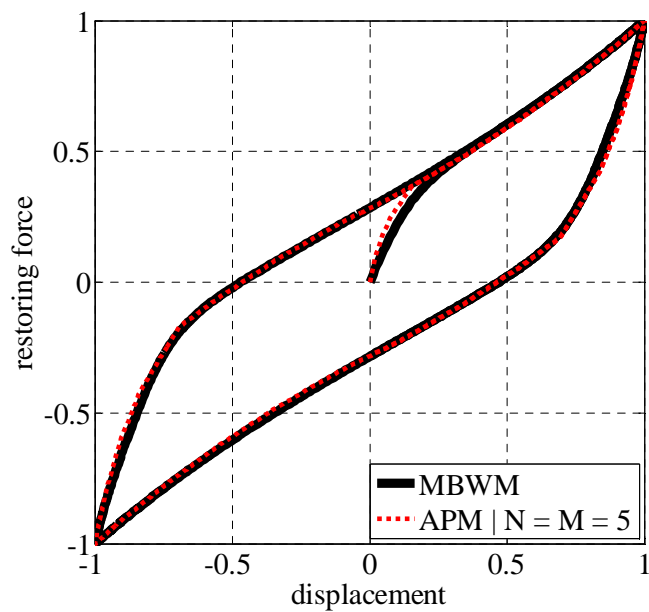


Figure 4.35. Symmetric hysteresis loop with post-hardening characteristics simulated adopting the MBWM and the proposed APM with $N = 50$ and $M = 50$.

Figure 4.36a shows the same force-displacement hysteresis loop simulated adopting 5 1d elastic-perfectly plastic elements and 5 1d linear elastic gap elements in the proposed PM, whereas Figure 4.36b shows the hysteresis loop obtained using 100 1d elastic-perfectly plastic elements and 100 1d linear elastic gap elements.

(a)



(b)

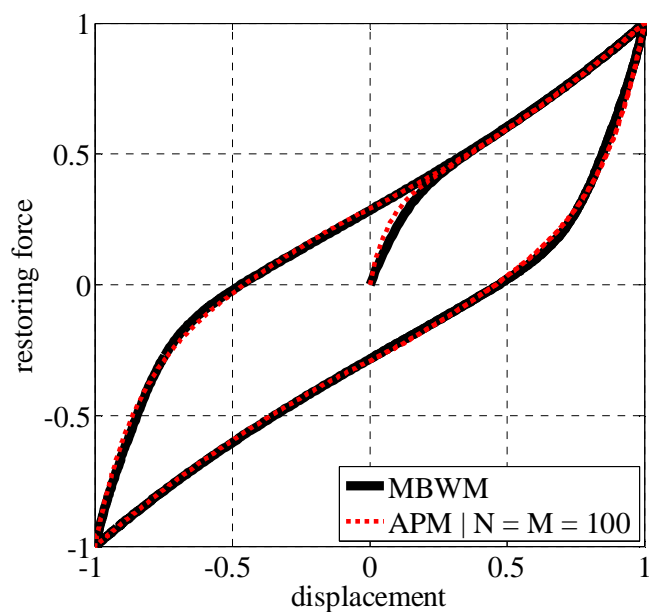


Figure 4.36. Symmetric hysteresis loop with post-hardening characteristics simulated adopting the MBWM and the proposed APM with (a) $N = M = 5$ and (b) $N = M = 100$.

Figure 4.37 shows a symmetric force-displacement hysteresis loop, displayed by seismic isolators having post-softening behavior at large displacements, such as unbounded elastomeric bearings with deformable reinforcing layers, simulated using the MBWM and the proposed APM. The values of the parameters adopted in the two mathematical models are listed in Table 4.11. In the APM, 50 1d elastic-perfectly plastic elements and 50 1d linear elastic gap elements have been used, that is, $N = 50$ and $M = 50$.

Table 4.11. MBWM and APM parameters | Hysteresis loop with post-softening characteristics.

MBWM	f_y [N]	u_y [m]	α	A	β	γ	n	c_1	c_2
	2025	0.0015	0.0481	1	0.9	0.1	2	-3000	500
APM	k_0 [N/m]	k_∞ [N/m]	c_1	c_2 [N/m]	c_3				
	2025000	64989	500	-1875000	8				

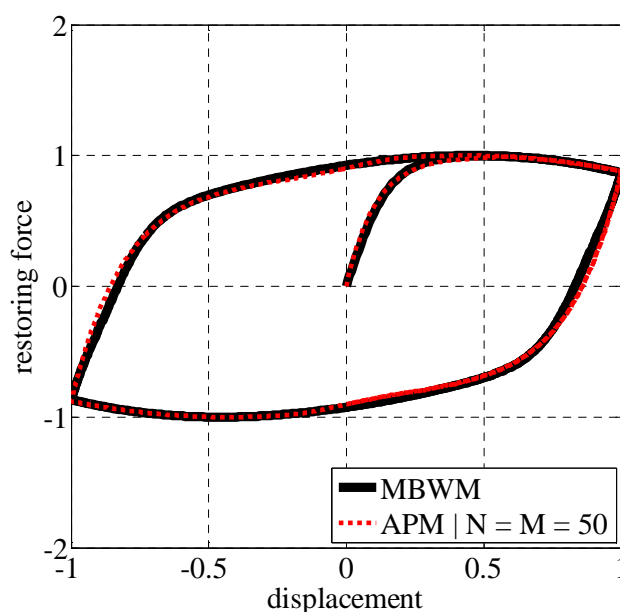
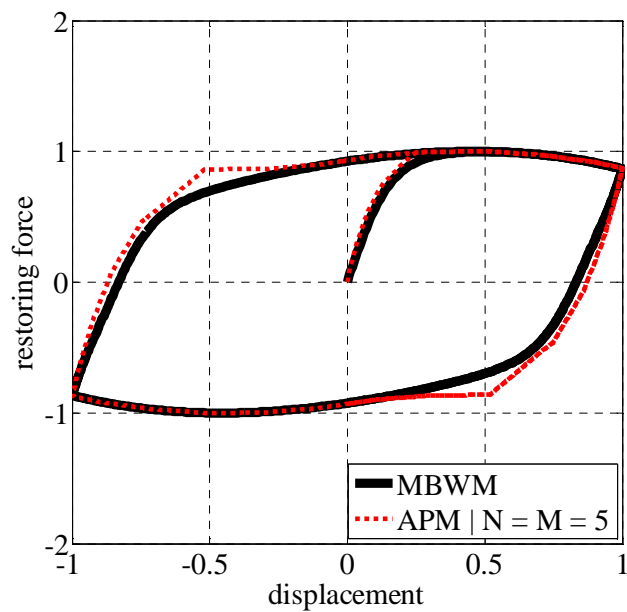


Figure 4.37. Symmetric hysteresis loop with post-softening characteristics simulated adopting the MBWM and the proposed APM with $N = 50$ and $M = 50$.

Figure 4.38a shows the same force-displacement hysteresis loop simulated adopting 5 1d elastic-perfectly plastic elements and 5 1d linear elastic gap elements in the proposed PM, whereas Figure 4.38b shows the hysteresis loop obtained using 100 1d elastic-perfectly plastic elements and 100 1d linear elastic gap elements.

(a)



(b)

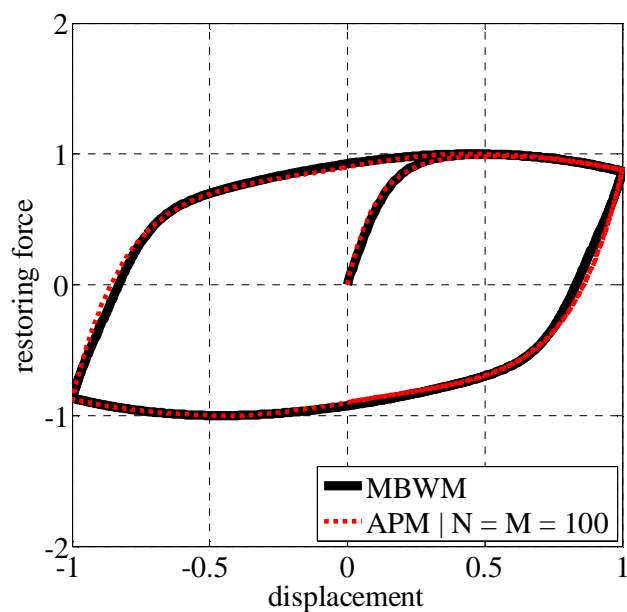


Figure 4.38. Symmetric hysteresis loop with post-softening characteristics simulated adopting the MBWM and the proposed APM with (a) $N = M = 5$ and (b) $N = M = 100$.

The theoretical force-displacement hysteresis loops produced by use of the MBWM and APM have been obtained, as done in experimental tests, by applying a sinusoidal harmonic displacement having amplitude equal to 0.01 m and frequency of 1 Hz.

It is worth to observe that the proposed mathematical model requires the evaluation of only 5 parameters whereas in the MBWM the number of parameters to be identified is equal to 9. In addition, it has to be noted that the proposed APM allows one to reduce the computational effort of a nonlinear time history analysis by avoiding, for each time step, the numerical solution of the first order nonlinear ordinary differential equation required by the MBWM.

Chapter 5

Verification of the Proposed Models

5.1 Introduction

In order to demonstrate the validity of the two advanced mathematical models, namely, Advanced Nonlinear Exponential Model (ANEM) and Advanced Parallel Model (APM), which are an improved version of the Nonlinear Exponential Model (NEM) and Parallel Model (PM), respectively, and are able to simulate the dynamic response of seismic isolators having softening behavior within the relatively large displacements range and a post-hardening or post-softening behavior at large displacements, in this chapter, the results predicted numerically are compared to the experimental ones obtained from horizontal dynamic tests performed on four Wire Rope Isolators (WRIs) and a Recycled Rubber-Fiber Reinforced Bearing (RR-FRB), as described in Chapter 3.

5.2 Simulation of Experimental Response of WRIs

5.2.1 Advanced Nonlinear Exponential Model

In what follows, the ANEM is used to predict the force-displacement hysteresis loops displayed by the four tested WRIs, namely, WRI PWHS 16010, WRI PWHS 16040, WRI PWHS 16040 S, and WRI PWHS 16060, in both two principal horizontal directions, namely, Roll and Shear directions, under different values of the vertical load. Then, a comparison between the experimental hysteresis loops, obtained testing WRI PWHS 16010 along the Roll direction, at small, relatively large, and large displacements, and those simulated by adopting the proposed ANEM and the Modified Bouc-Wen Model (MBWM), described in Chapter 4, is presented. Finally, the limitation of the proposed ANEM in predicting the stronger nonlinear stiffening behavior, shown by WRI PWHS 16040 at large horizontal displacements, is described.

5.2.1.1 WRI PWHS 16010

The geometrical characteristics of WRI PWHS 16010 and its two principal horizontal directions, namely, Roll and Shear directions, are shown in Figure 5.1.

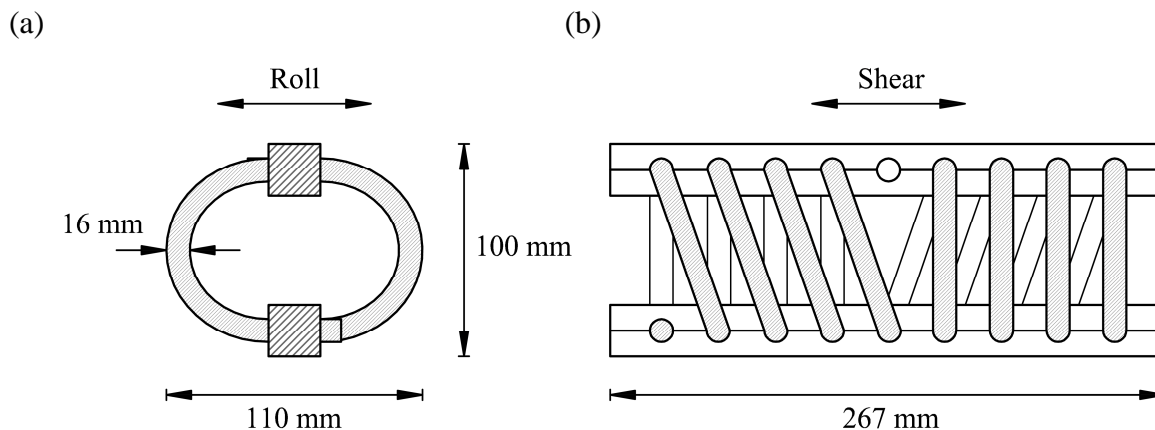


Figure 5.1. Geometrical characteristics and principal horizontal directions of WRI PWHS 16010:
(a) Roll and (b) Shear directions.

Figures 5.2, 5.3, and 5.4 give the comparisons of the analytical and experimental results obtained, in both Roll and Shear directions, for a frequency of 1 Hz and without the effect of the vertical load, at small (i.e., $A = 0.25$ cm), relatively large (i.e., $A = 0.5$ cm), and large (i.e., $A = 1$ cm) displacements, respectively. The force-displacement hysteresis loops have been simulated using the set of five model parameters listed in Table 5.1 and determined from the experimental loops having the largest amplitude, that is, $A = 1$ cm.

Table 5.1. ANEM parameters for WRI PWHS 16010 ($P_v = 0$ kN).

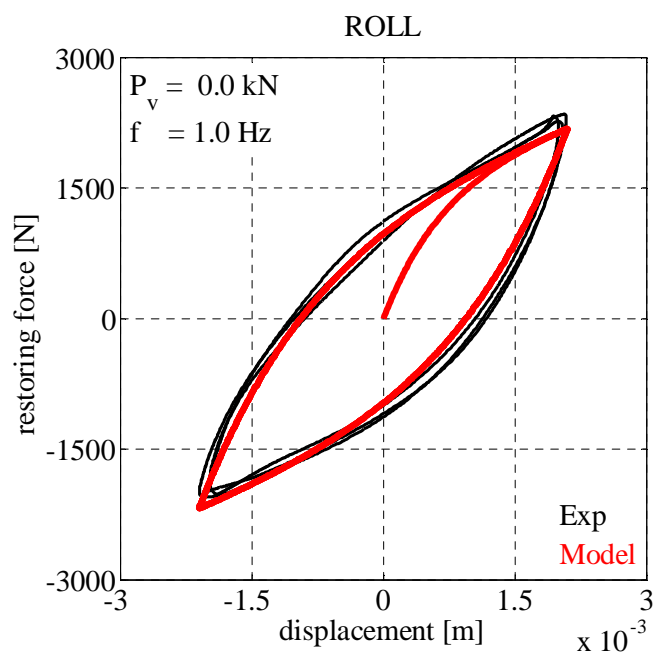
$P_v = 0$ kN	k_1 [N/m]	k_2 [N/m]	a	c [N/m]	d
Roll	2600000	300000	720	400000	35
Shear	1650000	200000	670	620000	58

Figure 5.5 shows the hysteresis force-displacement loops obtained for $P_v = 2$ kN. In order to account for the effect of the applied vertical load, the five model parameters, listed in Table 5.2, have been adjusted based on the experimental results.

Table 5.2. ANEM parameters for WRI PWHS 16010 ($P_v = 2$ kN).

$P_v = 2$ kN	k_1 [N/m]	k_2 [N/m]	a	c [N/m]	d
Roll	2100000	220000	710	160000	120
Shear	2000000	220000	900	650000	46

(a)



(b)

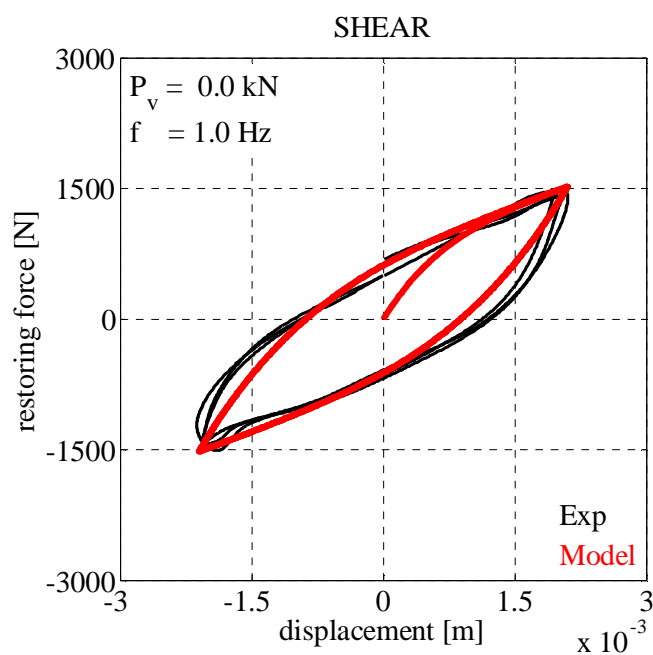
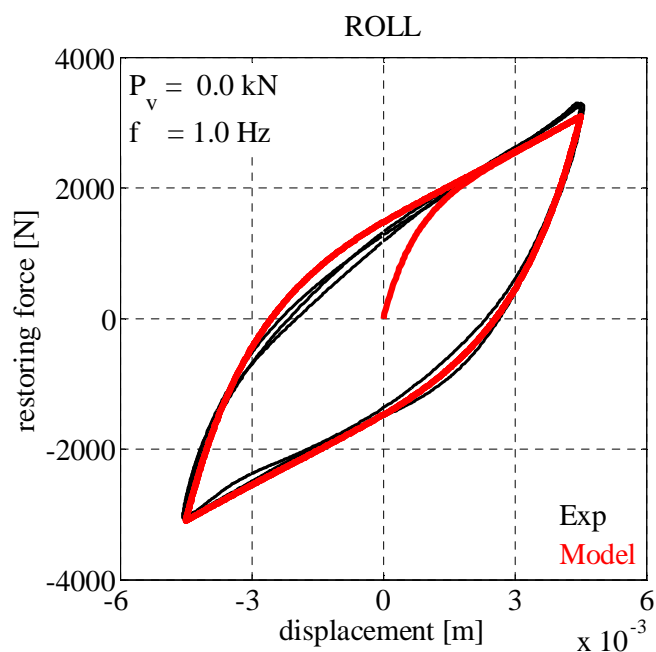


Figure 5.2. Analytical and experimental hysteresis loops of WRI PWHS 16010 obtained for $A = 0.25 \text{ cm}$, $f = 1 \text{ Hz}$, and $P_v = 0 \text{ kN}$ in (a) Roll and (b) Shear directions.

(a)



(b)

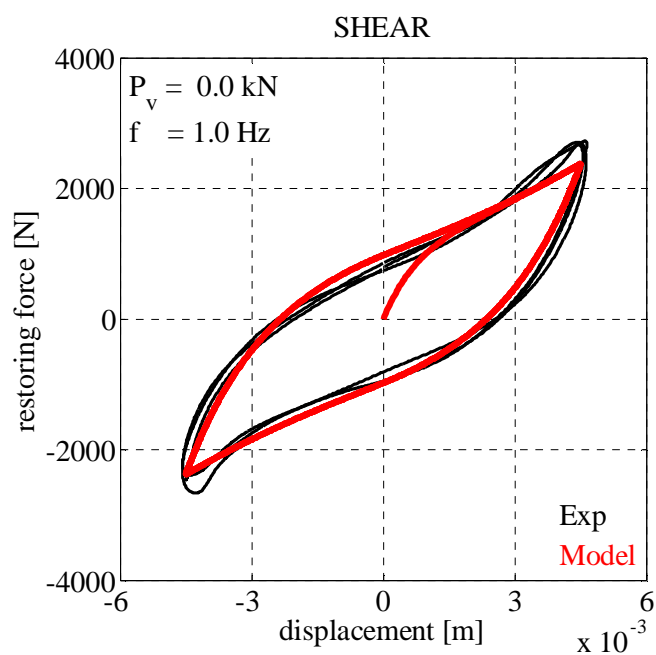
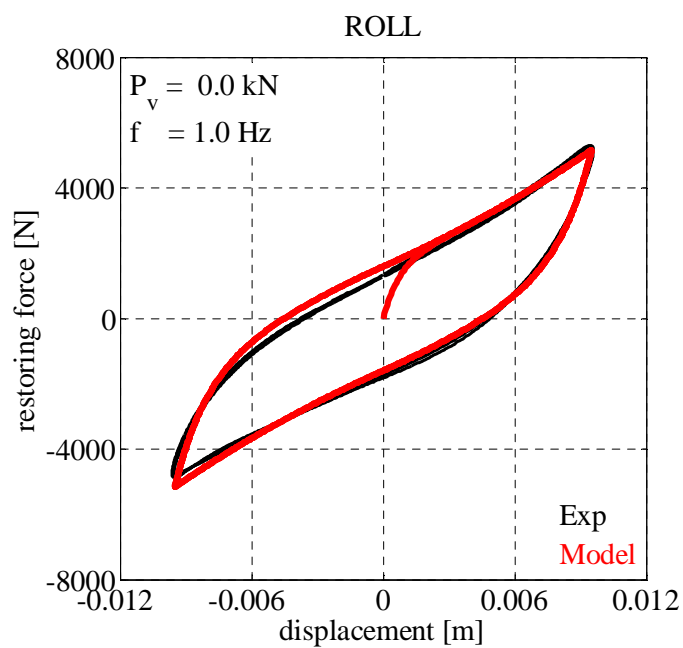


Figure 5.3. Analytical and experimental hysteresis loops of WRI PWHS 16010 obtained for $A = 0.5 \text{ cm}$, $f = 1 \text{ Hz}$, and $P_v = 0 \text{ kN}$ in (a) Roll and (b) Shear directions.

(a)



(b)

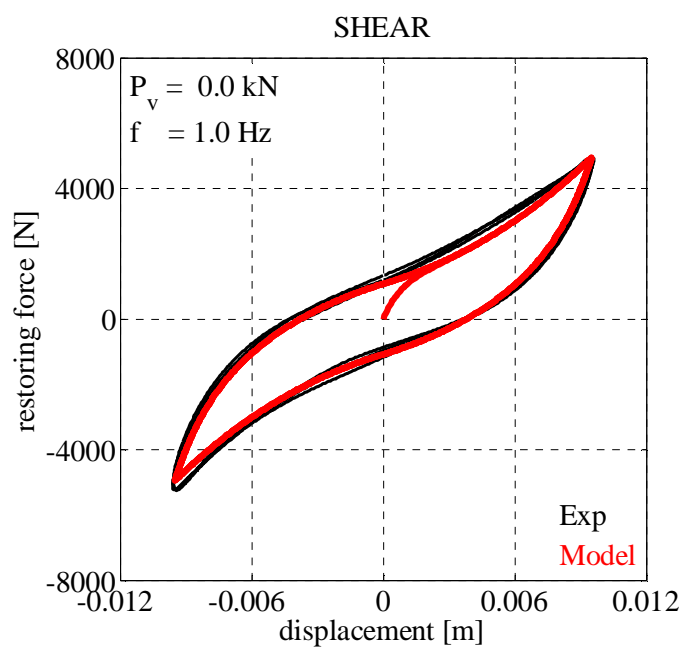
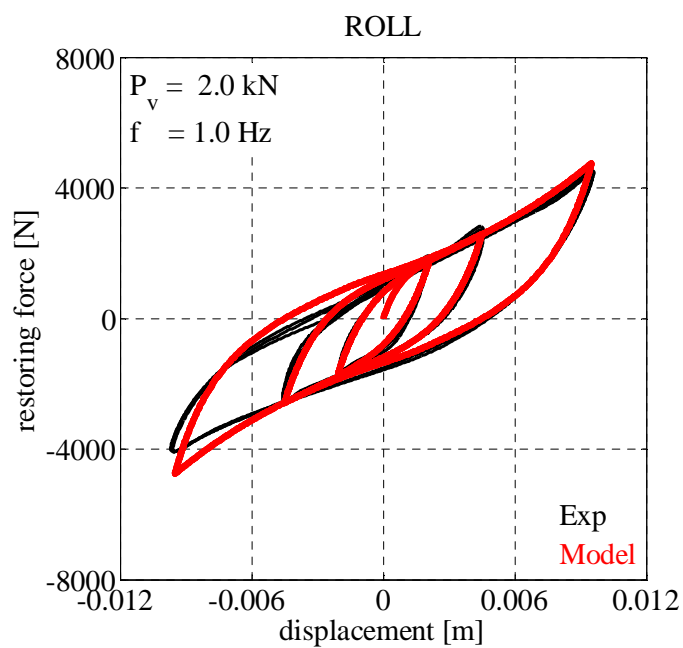


Figure 5.4. Analytical and experimental hysteresis loops of WRI PWHS 16010 obtained for $A = 1 \text{ cm}$, $f = 1 \text{ Hz}$, and $P_v = 0 \text{ kN}$ in (a) Roll and (b) Shear directions.

(a)



(b)

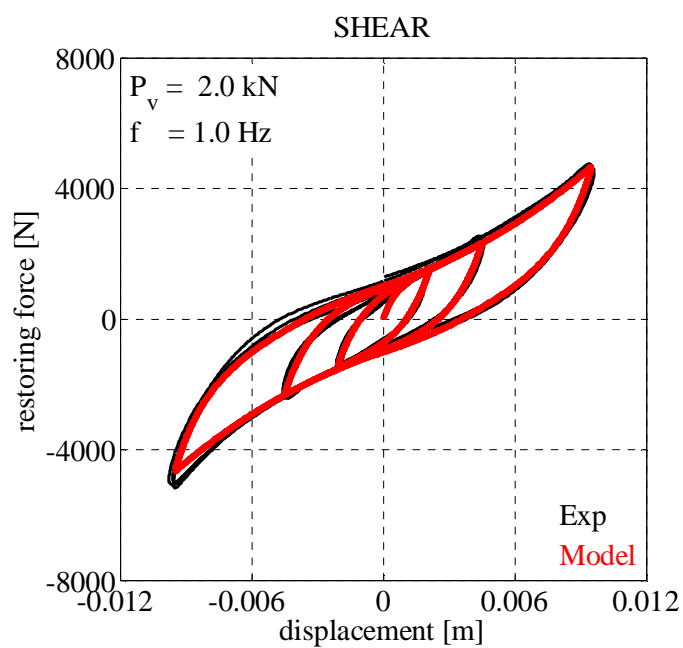


Figure 5.5. Analytical and experimental hysteresis loops of WRI PWHS 16010 obtained for $f = 1 \text{ Hz}$ and $P_v = 2 \text{ kN}$ in (a) Roll and (b) Shear directions.

5.2.1.2 WRI PWHS 16040

The geometrical characteristics of WRI PWHS 16040 and its two principal horizontal directions are shown in Figure 5.6.

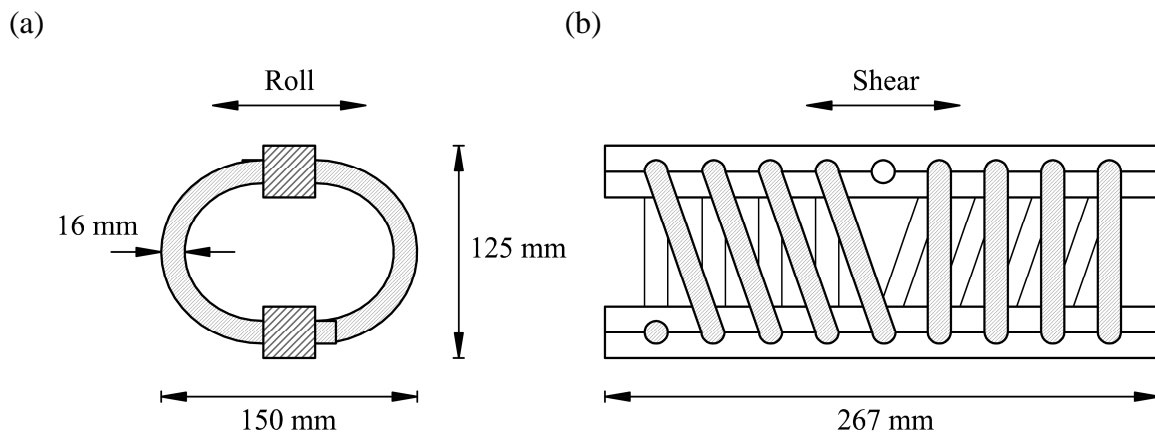


Figure 5.6. Geometrical characteristics and principal horizontal directions of WRI PWHS 16040:
(a) Roll and (b) Shear directions.

Figure 5.7 reveals the comparisons of the analytical and experimental results obtained, in both Roll and Shear directions, under a test frequency of 1 Hz and for two different displacement amplitudes, that is, $A = 1$ cm and $A = 3$ cm, without the effect of the vertical load. The force-displacement hysteresis loops have been simulated using the set of five model parameters listed in Table 5.3 and determined from the experimental loops having the largest amplitude, that is, $A = 3$ cm.

Table 5.3. ANEM parameters for WRI PWHS 16040 ($P_v = 0$ kN).

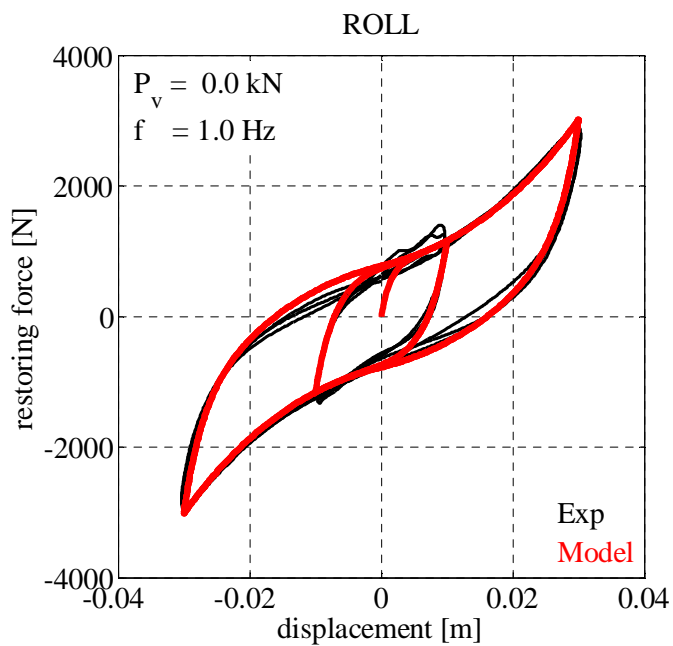
$P_v = 0$ kN	k_1 [N/m]	k_2 [N/m]	a	c [N/m]	d
Roll	600000	25000	370	80000	30
Shear	790000	54000	400	90000	25

Figure 5.8 shows the hysteresis force-displacement loops obtained for $P_v = 3$ kN. In order to account for the effect of the applied vertical load, the five model parameters, listed in Table 5.4, have been adjusted based on the experimental results.

Table 5.4. ANEM parameters for WRI PWHS 16040 ($P_v = 3$ kN).

$P_v = 3$ kN	k_1 [N/m]	k_2 [N/m]	a	c [N/m]	d
Roll	600000	16500	499.5	48000	30
Shear	553000	23400	504	72000	20

(a)



(b)

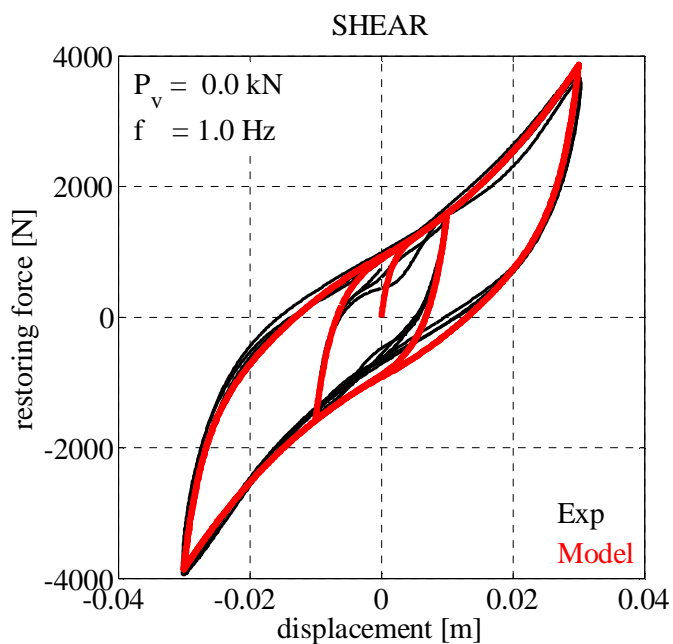
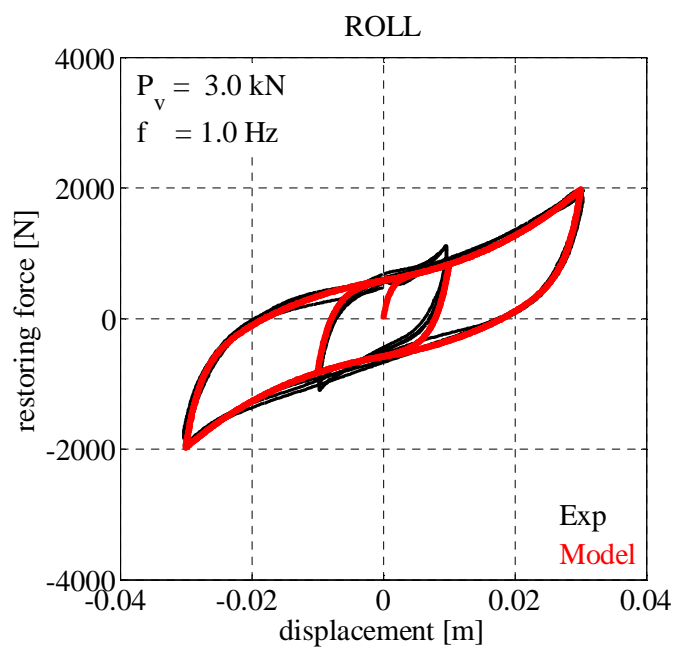


Figure 5.7. Analytical and experimental hysteresis loops of WRI PWHS 16040 obtained for $f = 1 \text{ Hz}$ and $P_v = 0 \text{ kN}$ in (a) Roll and (b) Shear directions.

(a)



(b)

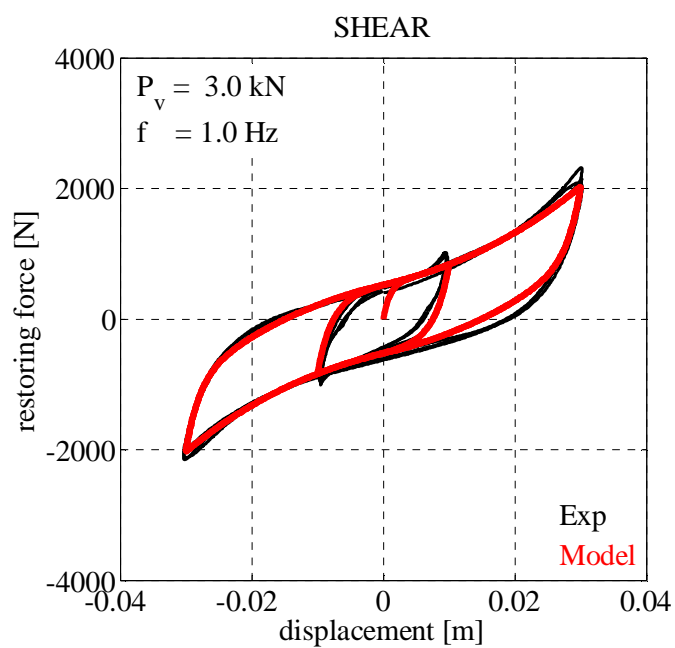


Figure 5.8. Analytical and experimental hysteresis loops of WRI PWHS 16040 obtained for $f = 1 \text{ Hz}$ and $P_v = 3 \text{ kN}$ in (a) Roll and (b) Shear directions.

5.2.1.3 WRI PWHS 16040 S

The geometrical characteristics of WRI PWHS 16040 S and its two principal horizontal directions are shown in Figure 5.9.

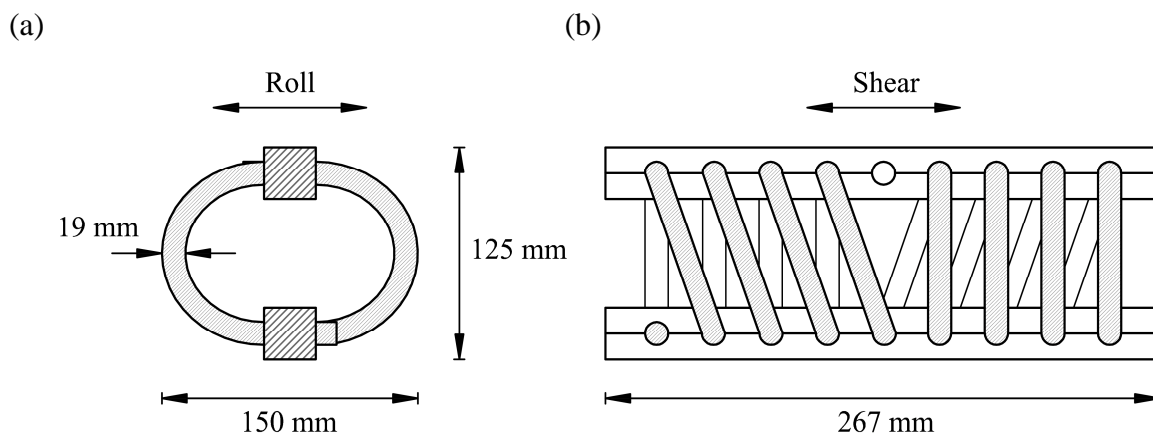


Figure 5.9. Geometrical characteristics and principal horizontal directions of WRI PWHS 16040 S:
(a) Roll and (b) Shear directions.

Figure 5.10 shows the comparisons of the analytical and experimental results obtained, in both Roll and Shear directions, under a test frequency of 1 Hz and for two different displacement amplitudes, that is, $A = 1$ cm and $A = 3$ cm, without the effect of the vertical load. The force-displacement hysteresis loops have been simulated using the set of five model parameters listed in Table 5.5 and determined from the experimental loops having the largest amplitude, that is, $A = 3$ cm.

Table 5.5. ANEM parameters for WRI PWHS 16040 S ($P_v = 0$ kN).

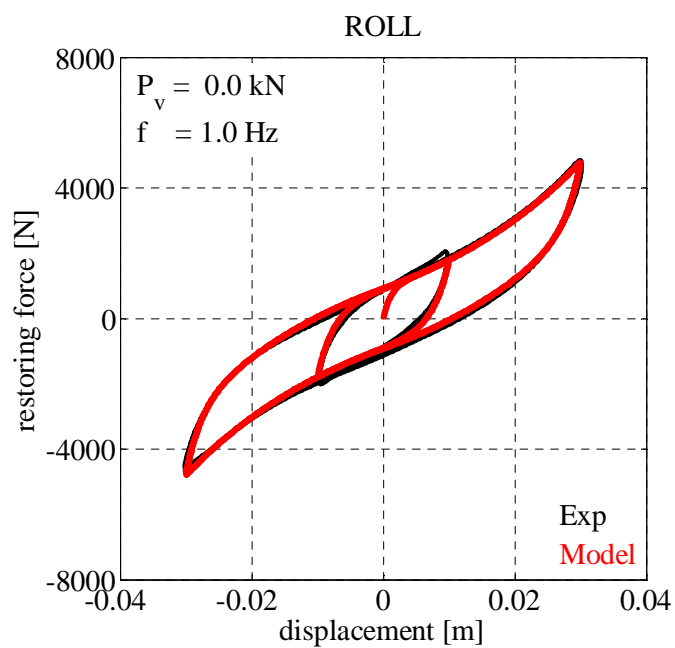
$P_v = 0$ kN	k_1 [N/m]	k_2 [N/m]	a	c [N/m]	d
Roll	900000	73000	450	70000	36
Shear	1000000	140000	380	30000	32

Figure 5.11 shows the hysteresis force-displacement loops obtained for $P_v = 2$ kN. In order to account for the effect of the applied vertical load, the five model parameters, listed in Table 5.6, have been adjusted based on the experimental results.

Table 5.6. ANEM parameters for WRI PWHS 16040 S ($P_v = 2$ kN).

$P_v = 2$ kN	k_1 [N/m]	k_2 [N/m]	a	c [N/m]	d
Roll	640000	39000	370	70000	30
Shear	700000	50000	340	95000	30

(a)



(b)

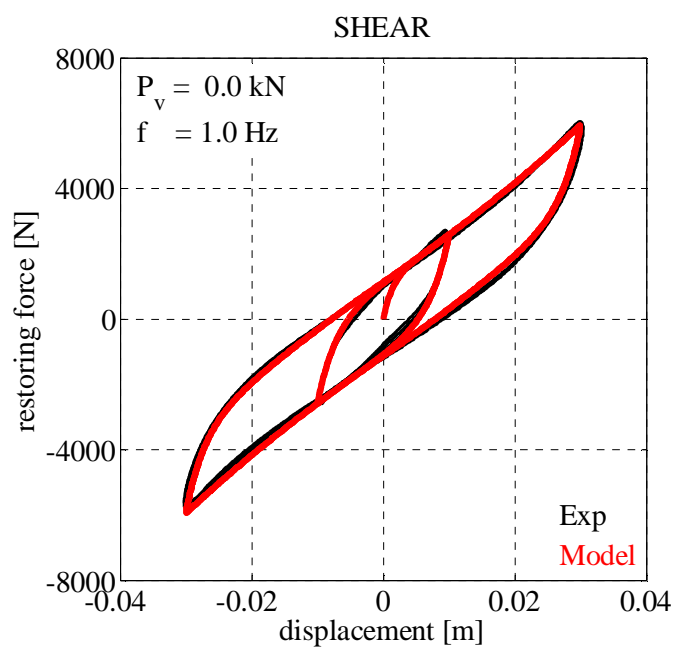
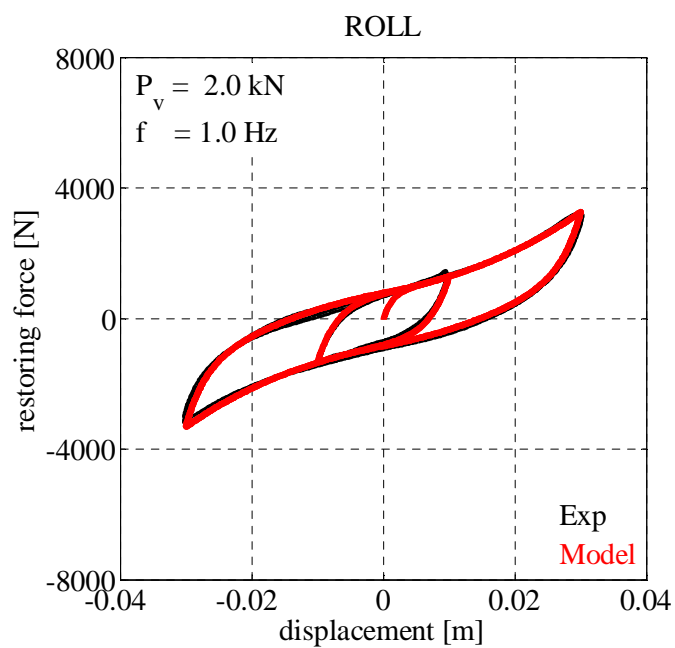


Figure 5.10. Analytical and experimental hysteresis loops of WRI PWHS 16040 S obtained for $f = 1 \text{ Hz}$ and $P_v = 0 \text{ kN}$ in (a) Roll and (b) Shear directions.

(a)



(b)

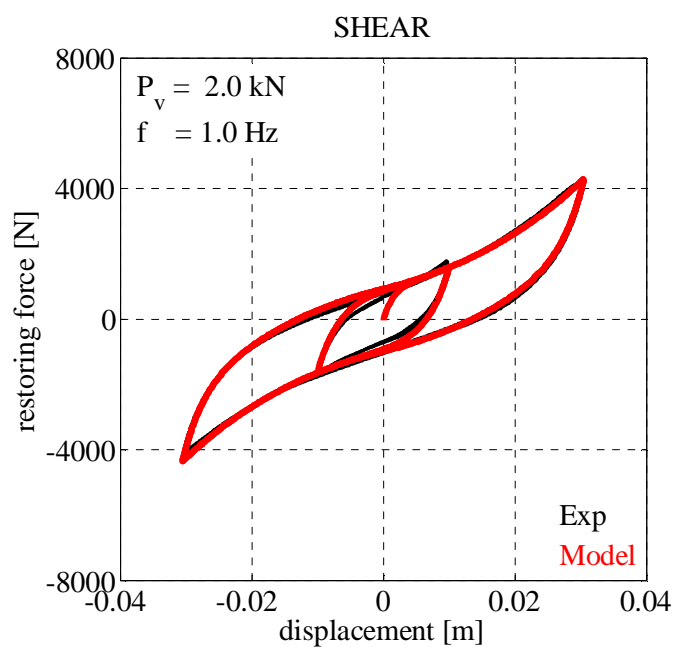


Figure 5.11. Analytical and experimental hysteresis loops of WRI PWHS 16040 S obtained for $f = 1 \text{ Hz}$ and $P_v = 2 \text{ kN}$ in (a) Roll and (b) Shear directions.

5.2.1.4 WRI PWHS 16060

The geometrical characteristics of WRI PWHS 16060 and its two principal horizontal directions are shown in Figure 5.12.

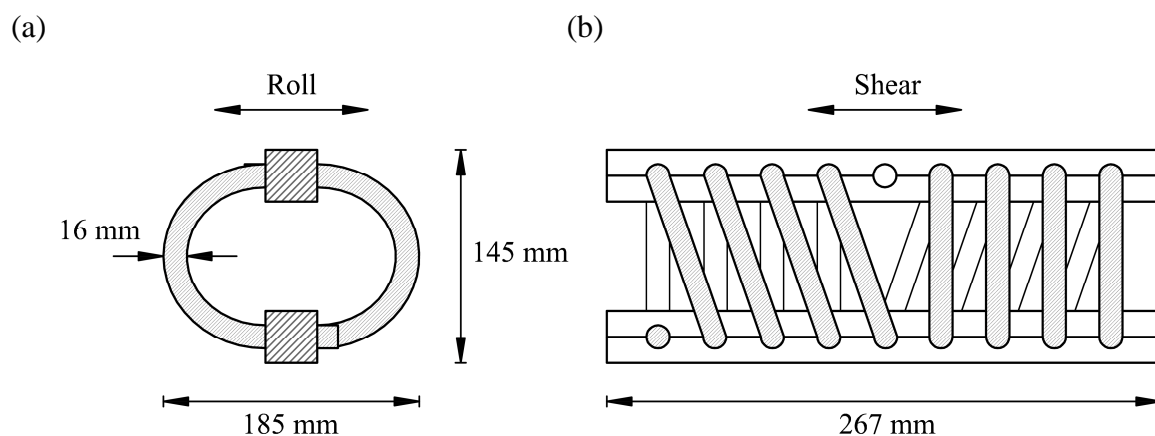


Figure 5.12. Geometrical characteristics and principal horizontal directions of WRI PWHS 16060:
(a) Roll and (b) Shear directions.

Figure 5.13 reveals the comparisons of the analytical and experimental results obtained, in both Roll and Shear directions, under a test frequency of 1 Hz and for two different displacement amplitudes, that is, $A = 1$ cm and $A = 4$ cm, without the effect of the vertical load. The force-displacement hysteresis loops have been simulated using the set of five model parameters listed in Table 5.7 and determined from the experimental loops having the largest amplitude, that is, $A = 4$ cm.

Table 5.7. ANEM parameters for WRI PWHS 16060 ($P_v = 0$ kN).

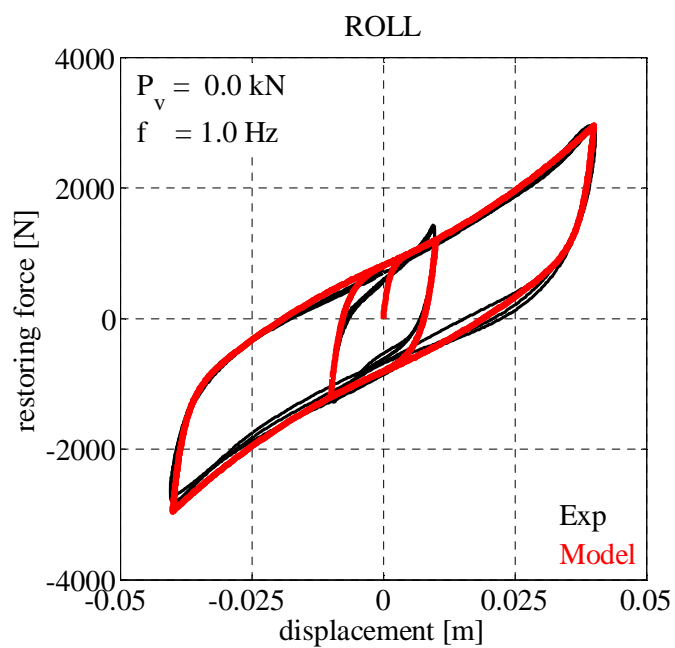
$P_v = 0$ kN	k_1 [N/m]	k_2 [N/m]	a	c [N/m]	d
Roll	850000	35000	500	65000	12
Shear	750000	25000	700	50000	20

Figure 5.14 shows the hysteresis force-displacement loops obtained for $P_v = 2$ kN. In order to account for the effect of the applied vertical load, the five model parameters, listed in Table 5.8, have been adjusted based on the experimental results.

Table 5.8. ANEM parameters for WRI PWHS 16060 ($P_v = 2$ kN).

$P_v = 2$ kN	k_1 [N/m]	k_2 [N/m]	a	c [N/m]	d
Roll	595000	15750	550	26000	15
Shear	320000	12000	300	32000	15

(a)



(b)

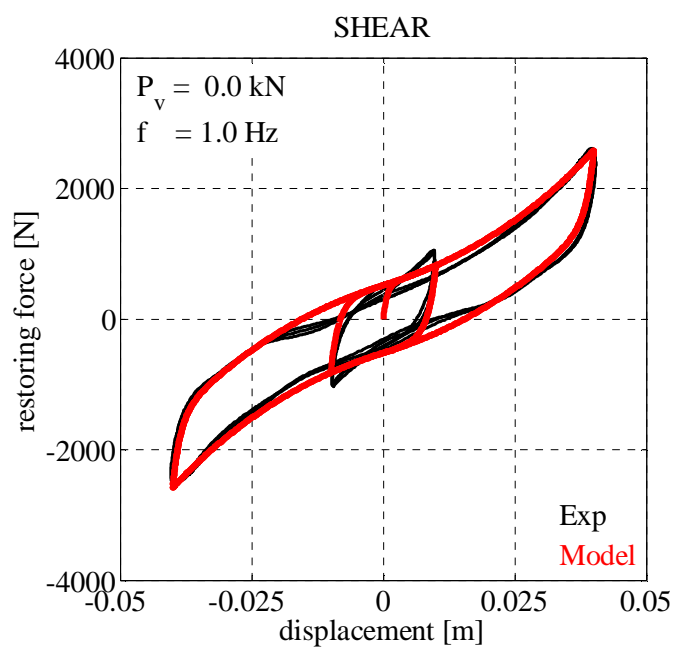
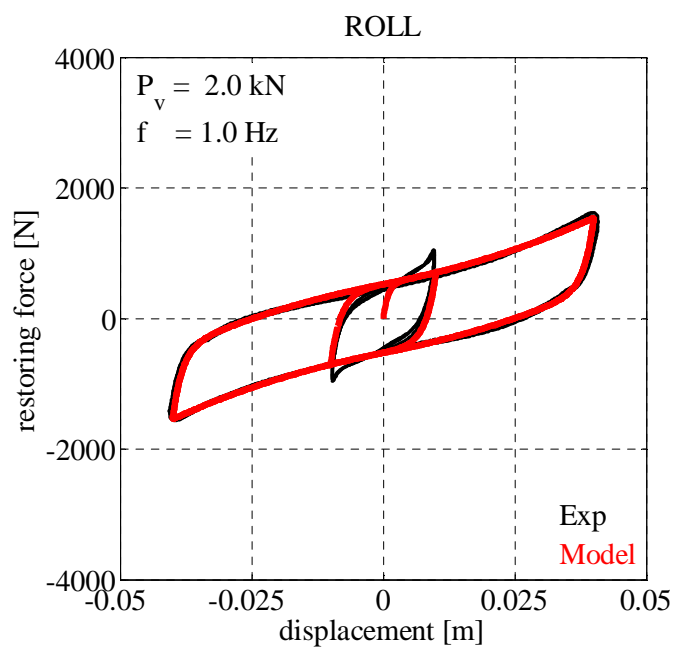


Figure 5.13. Analytical and experimental hysteresis loops of WRI PWHS 16060 obtained for $f = 1 \text{ Hz}$ and $P_v = 0 \text{ kN}$ in (a) Roll and (b) Shear directions.

(a)



(b)

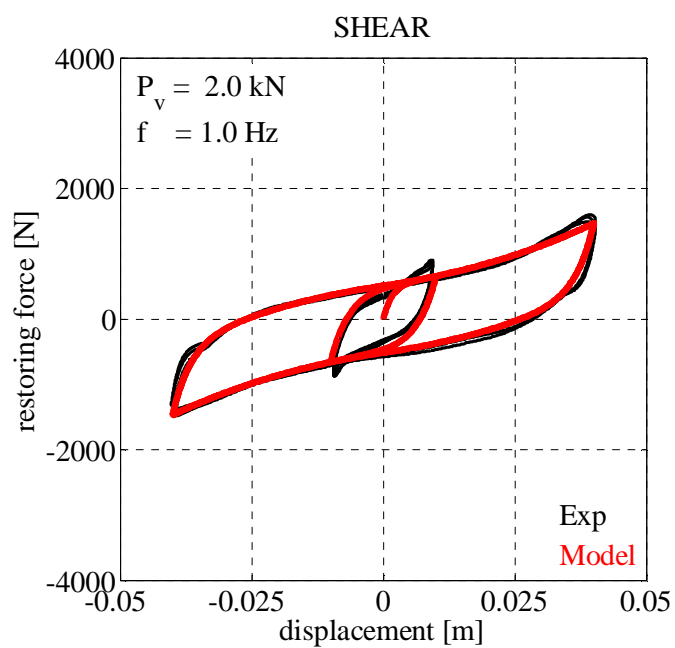


Figure 5.14. Analytical and experimental hysteresis loops of WRI PWHS 16060 obtained for $f = 1 \text{ Hz}$ and $P_v = 2 \text{ kN}$ in (a) Roll and (b) Shear directions.

5.2.1.5 Comparison with the MBWM

Table 5.9 shows the parameters of the proposed ANEM and the MBWM, described in Chapter 4, adopted to simulate the experimental response of WRI PWHS 16010 obtained applying, in Roll direction, a sinusoidal harmonic motion having frequency of 1 Hz, without the effect of the vertical load. These models parameters have been determined from the experimental loops having the largest amplitude, that is, $A = 1$ cm.

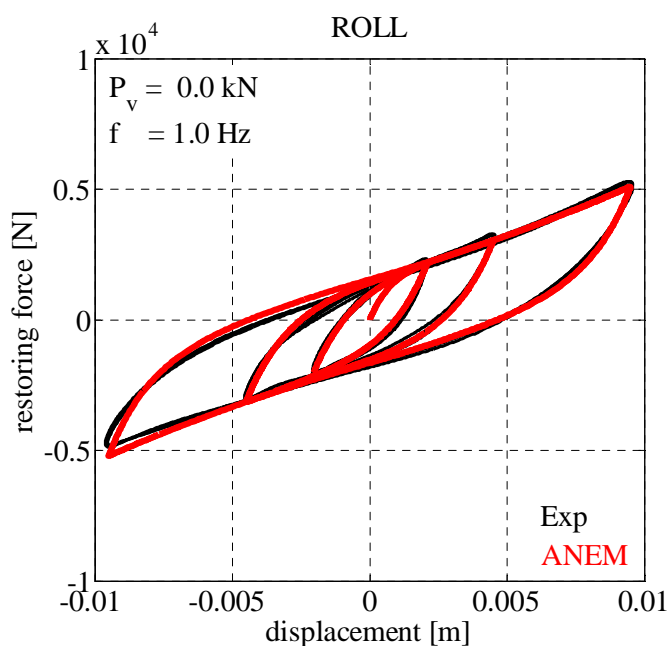
Table 5.9. MBWM and ANEM parameters for WRI PWHS 16010 ($P_v = 0$ kN).

MBWM	f_y [N]	u_y [m]	α	A	β	γ	n	c_1	c_2
	2025	0.0015	0.2407	1	0.1	0.9	2	1300	500
ANEM	k_1 [N/m]	k_2 [N/m]	a	c [N/m]	d				
	2600000	300000	720	400000	35				

Figures 5.15a and 5.15b compare the experimental hysteresis force-displacement loops with those predicted analytically using the proposed ANEM and the MBWM, respectively. It can be seen that both analytical models are able to well reproduce the experimental behavior of the tested device by capturing the smooth transition of the hysteresis loops from the small to the large displacements range using the set of parameters listed in Table 5.9.

It is worth to notice that the proposed ANEM requires the evaluation of only five parameters whereas in the MBWM the number of parameters to be identified is equal to nine.

(a)



(b)

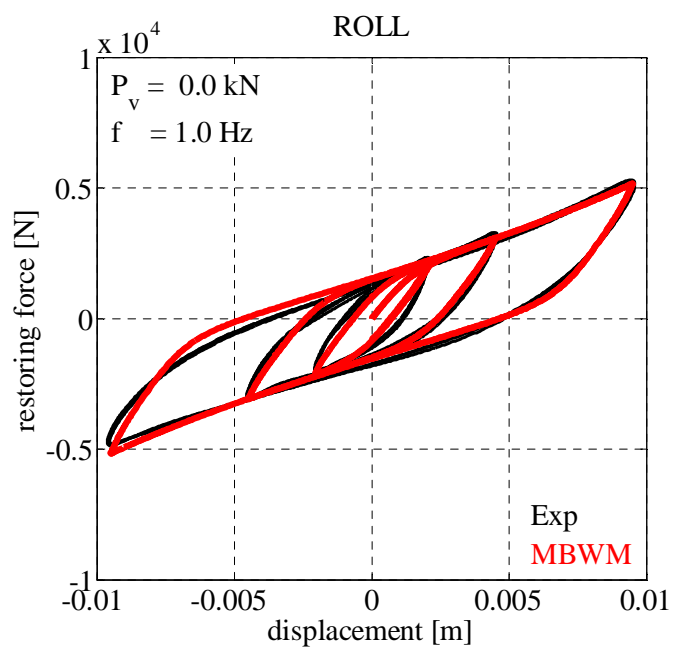


Figure 5.15. Comparisons of analytical and experimental hysteresis loops of WRI PWHS 16010:
(a) ANEM and (b) MBWM.

5.2.1.6 Limitation of the Proposed ANEM

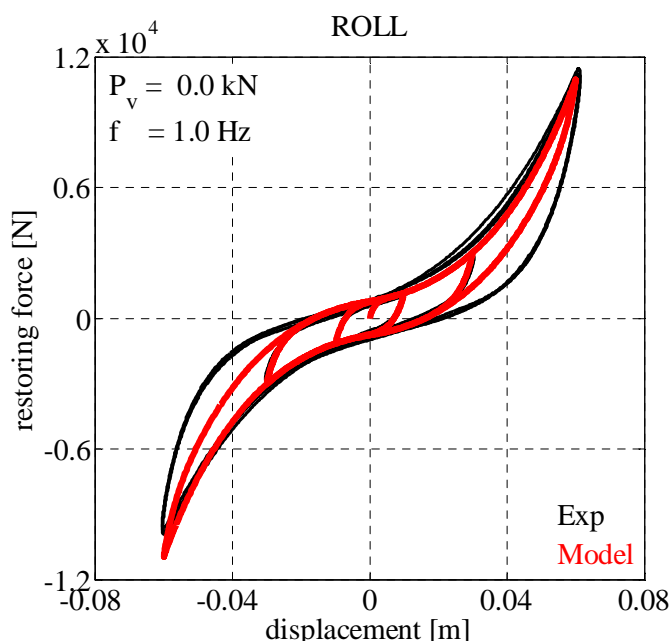
According to the experimental tests results, WRI PWHS 16040, 16040 S, and 16060 display a stronger nonlinear stiffening behavior and a slight variation of the hysteresis force-displacement loops shape at large horizontal displacements.

Figure 5.16 shows the comparisons of analytical and experimental hysteresis loops of WRI PWHS 16040 obtained applying a sinusoidal harmonic motion, in Roll and Shear directions, with a test frequency of 1 Hz, without the effect of the vertical load.

It can be observed that, adopting the five model parameters evaluated with respect to the experimental hysteresis loops having maximum displacement of 3 cm, the proposed analytical model cannot simulate correctly the dynamic behavior in the large displacements range. Moreover, using the five parameters calibrated by considering the hysteresis loops obtained for a displacement amplitude of 6 cm, it is not possible to adequately simulate the responses in the small and relatively large displacements ranges. Therefore, further work is required to improve the analytical model by including a procedure of updating the parameters to specify the shape of the hysteresis curve according to the maximum displacement at the point of loading or unloading.

In spite of this, the proposed analytical model can be adopted to simulate the dynamic behavior of WRIs because small or relatively large displacements are generally reached under the design earthquake.

(a)



(b)

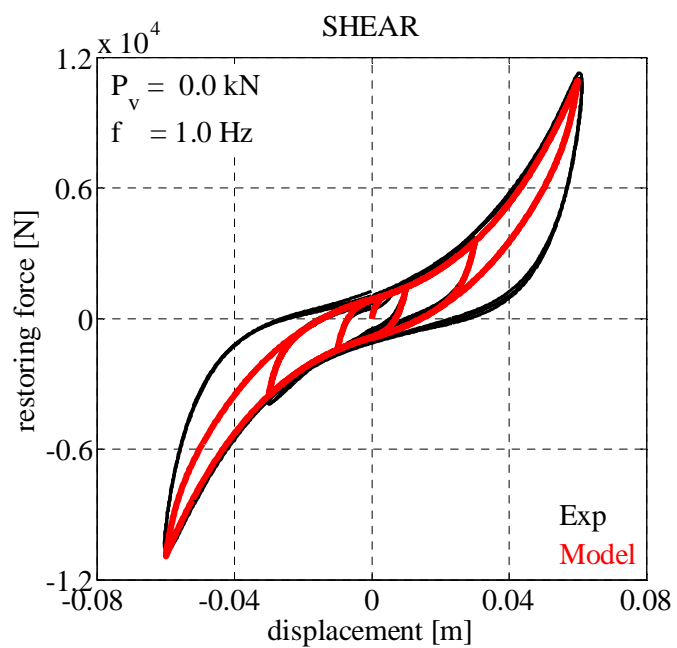


Figure 5.16. Comparisons of analytical and experimental hysteresis loops of WRI PWHS 16040 obtained at large displacements in (a) Roll and (b) Shear directions.

5.2.2 Advanced Parallel Model

5.2.2.1 WRI PWHS 16010

The geometrical characteristics of WRI PWHS 16010 and its two principal horizontal directions, namely, Roll and Shear directions, are shown in Figure 5.1.

Figures 5.17, 5.18, and 5.19 give the comparisons of the experimental and mathematical results obtained, in both Roll and Shear directions, for a frequency of 1 Hz and without the effect of the vertical load, at small (i.e., $A = 0.25$ cm), relatively large (i.e., $A = 0.5$ cm), and large (i.e., $A = 1$ cm) displacements, respectively. The hysteresis loops have been simulated using the set of five model parameters listed in Table 5.10, that have been determined from the experimental loops having the largest amplitude, that is, $A = 1$ cm, and adopting 50 elastic-perfectly plastic elements (i.e., $N = 50$) and 50 linear elastic gap elements (i.e., $M = 50$).

Table 5.10. APM parameters for WRI PWHS 16010 ($P_v = 0$ kN).

$P_v = 0$ kN	k_0 [N/m]	k_∞ [N/m]	c_1	c_2 [N/m]	c_3
Roll	2600000	300000	720	400000	35
Shear	1650000	200000	670	620000	58

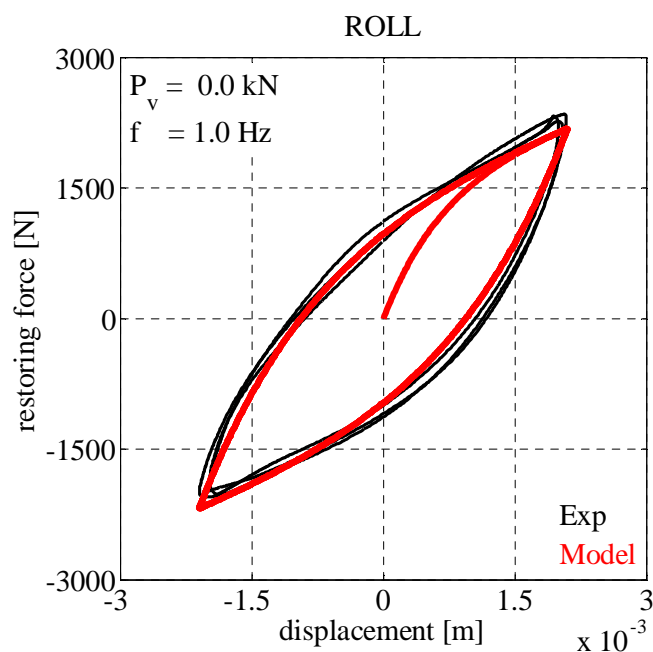
Figures 5.20, 5.21, and 5.22 show the same force-displacement hysteresis loops obtained adopting 5 elastic-perfectly plastic elements (i.e., $N = 5$) and 5 linear elastic gap elements (i.e., $M = 5$), whereas, in Figures 5.23, 5.24, and 5.25, 100 elastic-perfectly plastic elements (i.e., $N = 100$) and 100 linear elastic gap elements (i.e., $M = 100$) have been used in the proposed APM.

Figure 5.26 shows the hysteresis loops obtained for $P_v = 2$ kN. In order to account for the effect of the applied vertical load, the five model parameters, listed in Table 5.11, have been adjusted based on the experimental results. The hysteresis loops have been simulated using 50 elastic-perfectly plastic elements (i.e., $N = 50$) and 50 linear elastic gap elements (i.e., $M = 50$).

Table 5.11. APM parameters for WRI PWHS 16010 ($P_v = 2$ kN).

$P_v = 2$ kN	k_0 [N/m]	k_∞ [N/m]	c_1	c_2 [N/m]	c_3
Roll	2100000	220000	710	160000	120
Shear	2000000	220000	900	650000	46

(a)



(b)

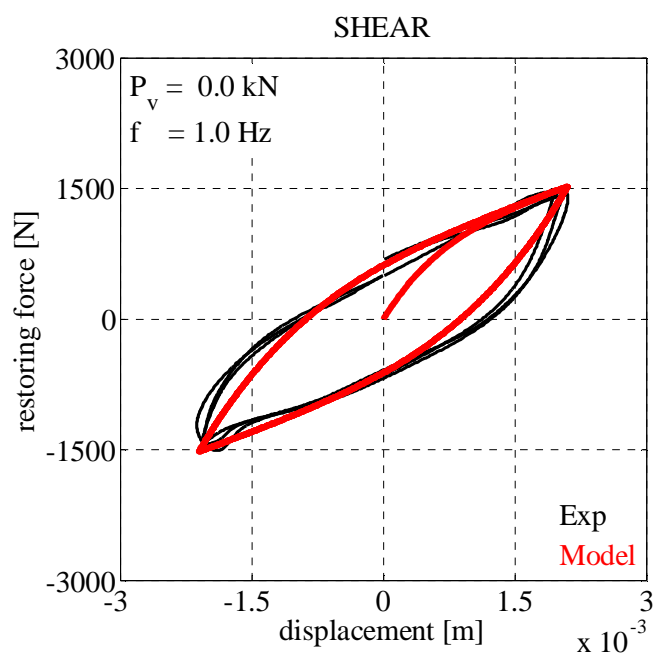
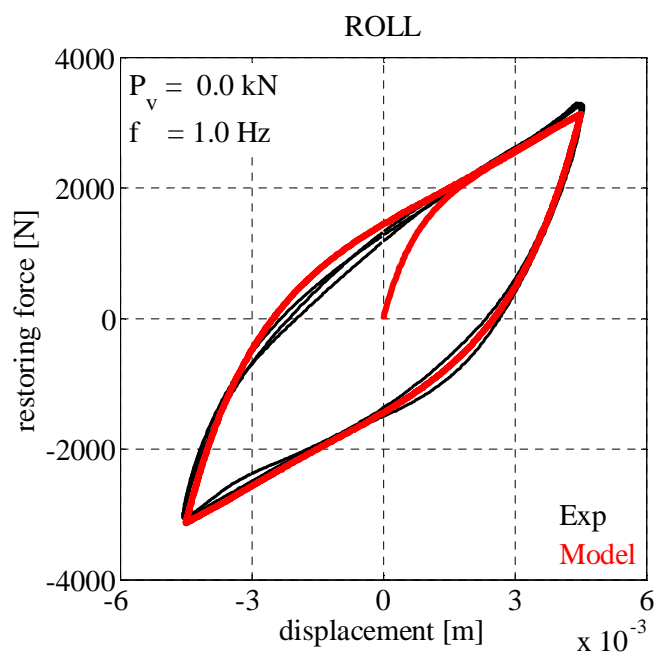


Figure 5.17. Experimental and mathematical hysteresis loops of WRI PWHS 16010 obtained for $A = 0.25$ cm, $f = 1$ Hz, and $P_v = 0$ kN ($N = 50$, $M = 50$) in (a) Roll and (b) Shear directions.

(a)



(b)

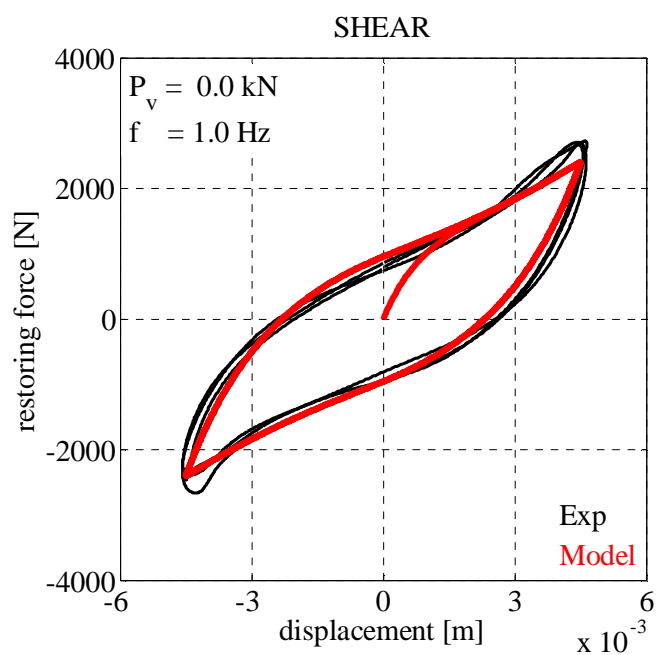
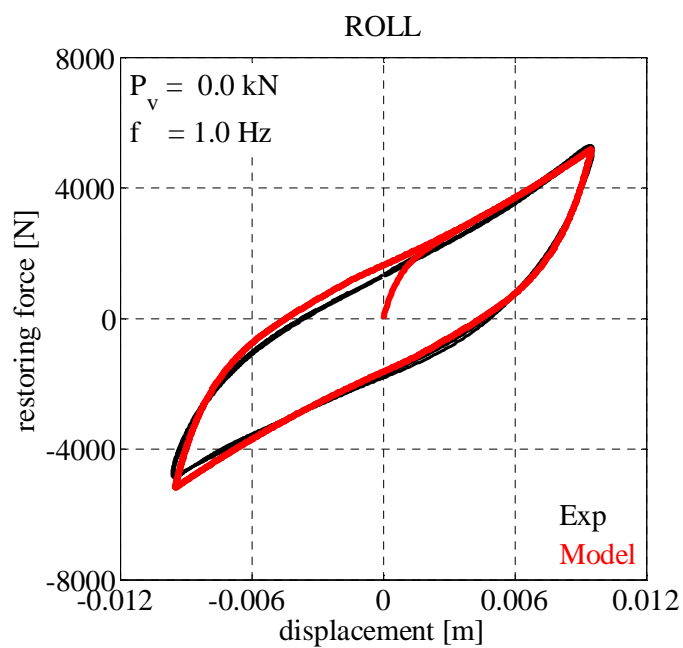


Figure 5.18. Experimental and mathematical hysteresis loops of WRI PWHS 16010 obtained for $A = 0.5 \text{ cm}$, $f = 1 \text{ Hz}$, and $P_v = 0 \text{ kN}$ ($N = 50$, $M = 50$) in (a) Roll and (b) Shear directions.

(a)



(b)

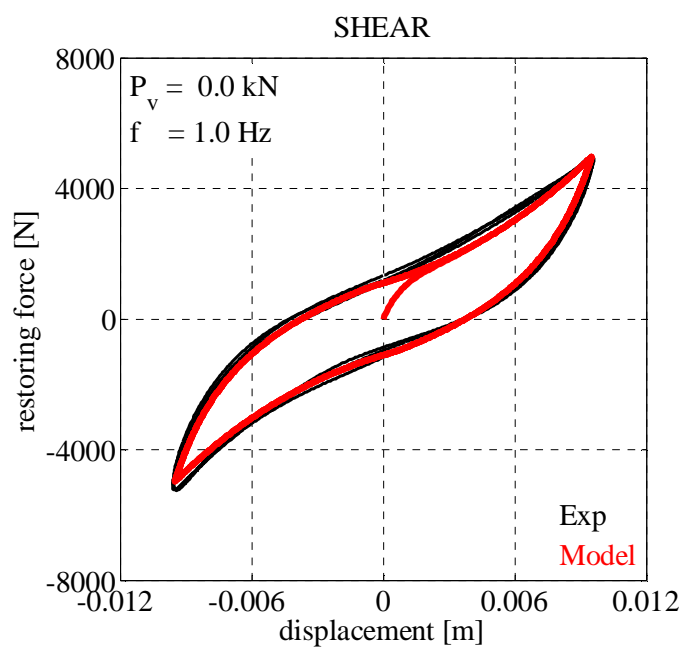
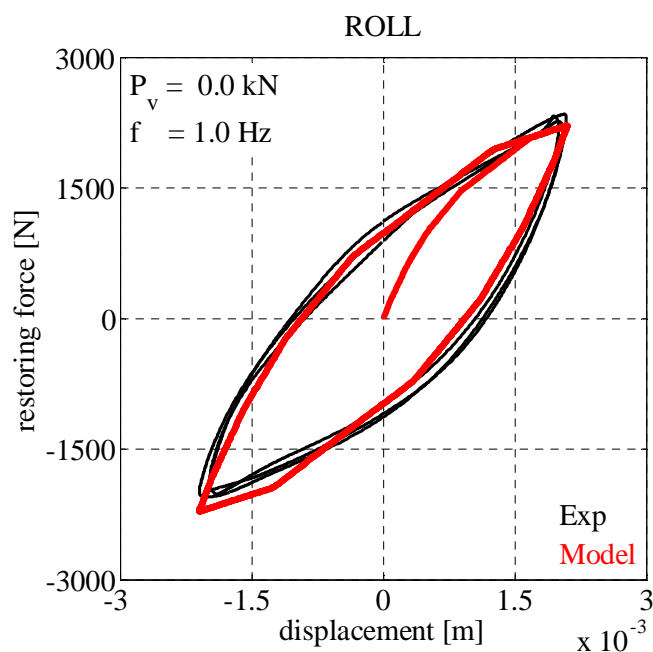


Figure 5.19. Experimental and mathematical hysteresis loops of WRI PWHS 16010 obtained for $A = 1 \text{ cm}$, $f = 1 \text{ Hz}$, and $P_v = 0 \text{ kN}$ ($N = 50$, $M = 50$) in (a) Roll and (b) Shear directions.

(a)



(b)

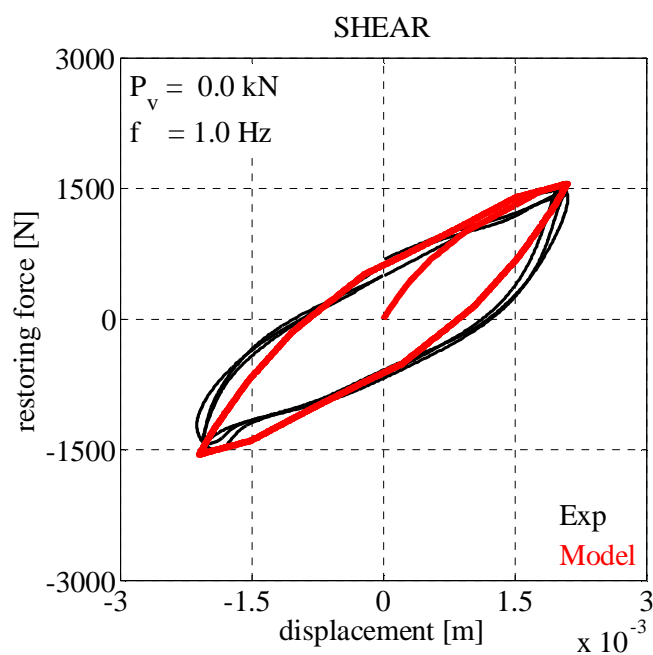
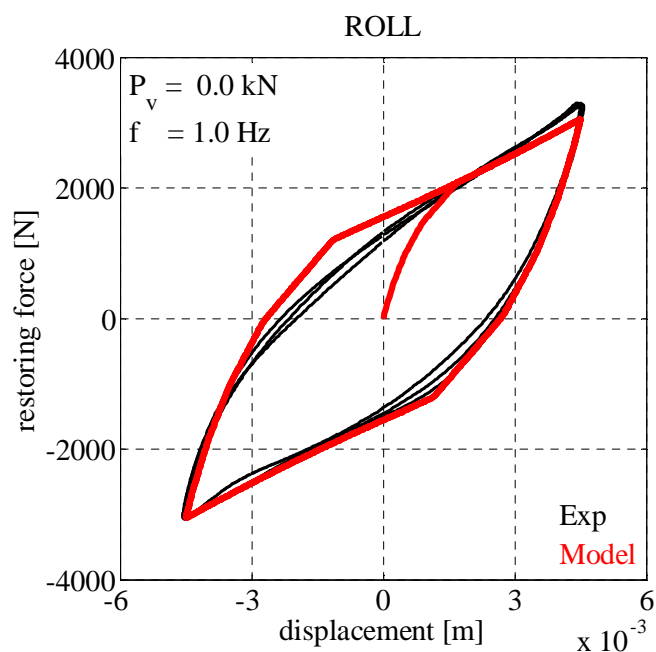


Figure 5.20. Experimental and mathematical hysteresis loops of WRI PWHS 16010 obtained for $A = 0.25 \text{ cm}$, $f = 1 \text{ Hz}$, and $P_v = 0 \text{ kN}$ ($N = 5$, $M = 5$) in (a) Roll and (b) Shear directions.

(a)



(b)

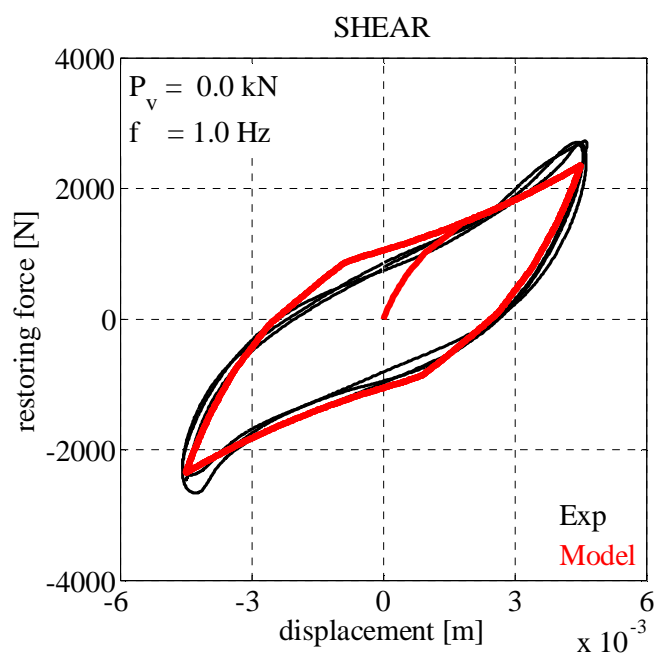
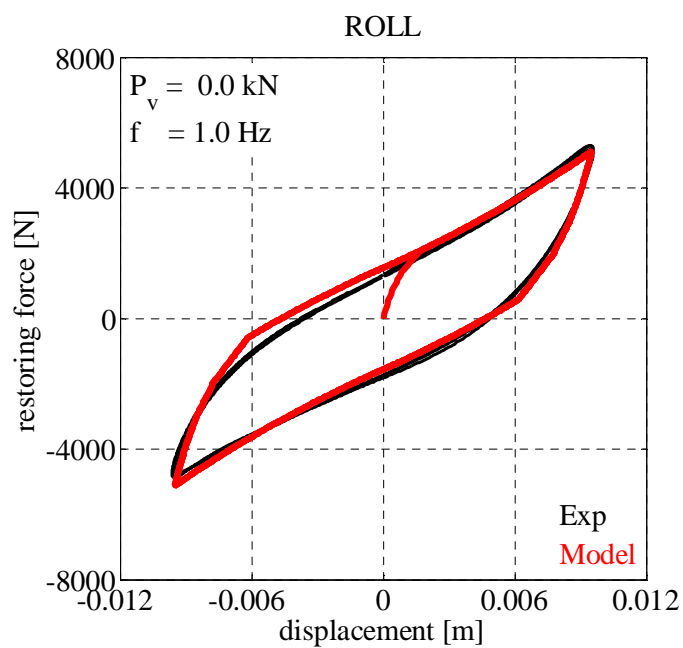


Figure 5.21. Experimental and mathematical hysteresis loops of WRI PWHS 16010 obtained for $A = 0.5 \text{ cm}$, $f = 1 \text{ Hz}$, and $P_v = 0 \text{ kN}$ ($N = 5$, $M = 5$) in (a) Roll and (b) Shear directions.

(a)



(b)

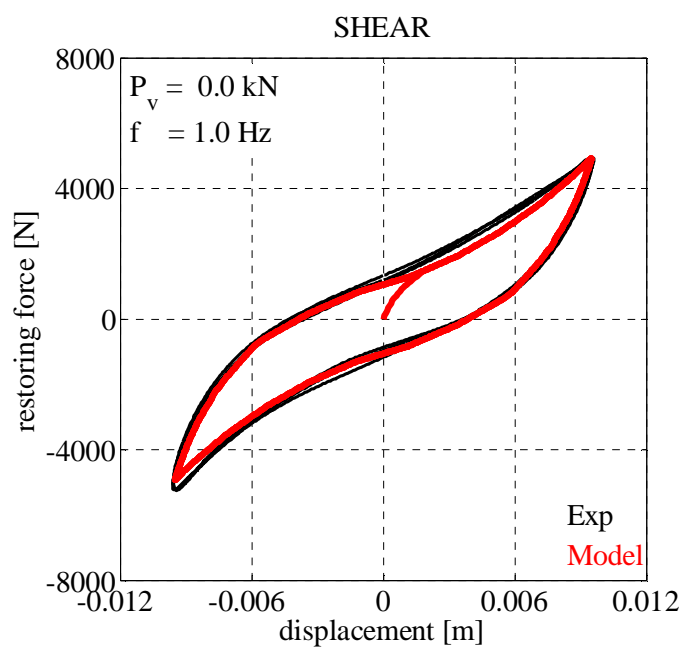
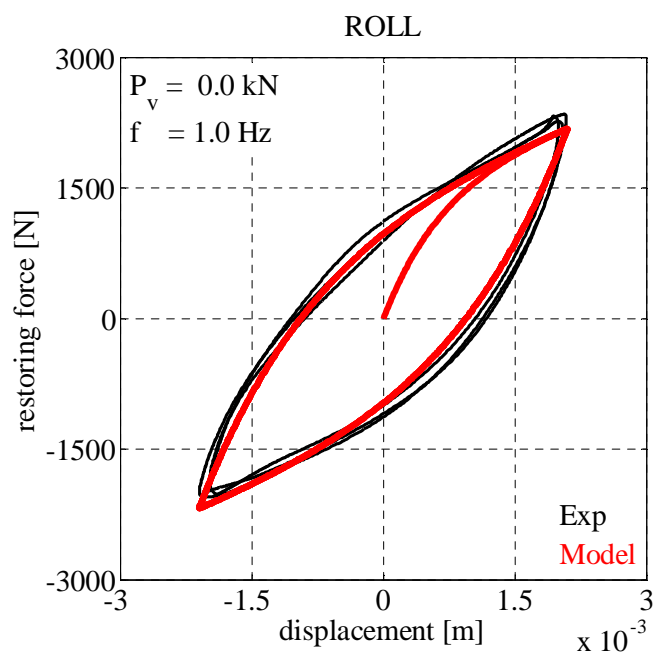


Figure 5.22. Experimental and mathematical hysteresis loops of WRI PWHS 16010 obtained for $A = 1 \text{ cm}$, $f = 1 \text{ Hz}$, and $P_v = 0 \text{ kN}$ ($N = 5$, $M = 5$) in (a) Roll and (b) Shear directions.

(a)



(b)

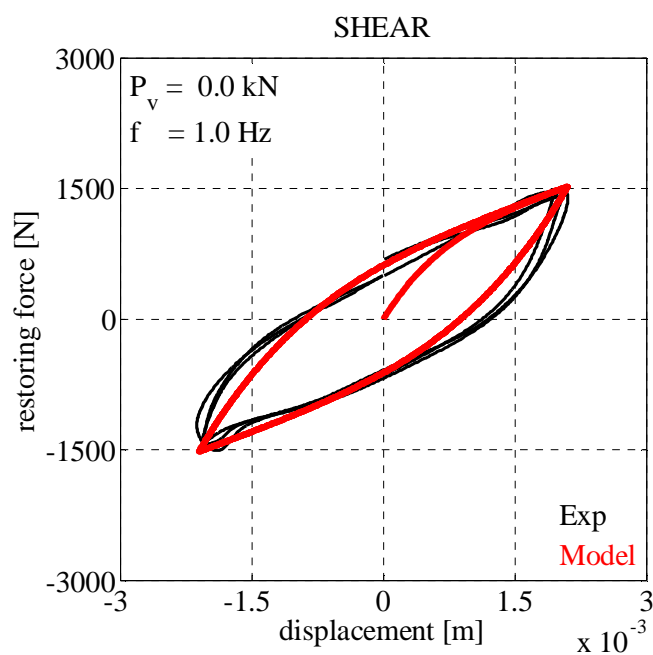
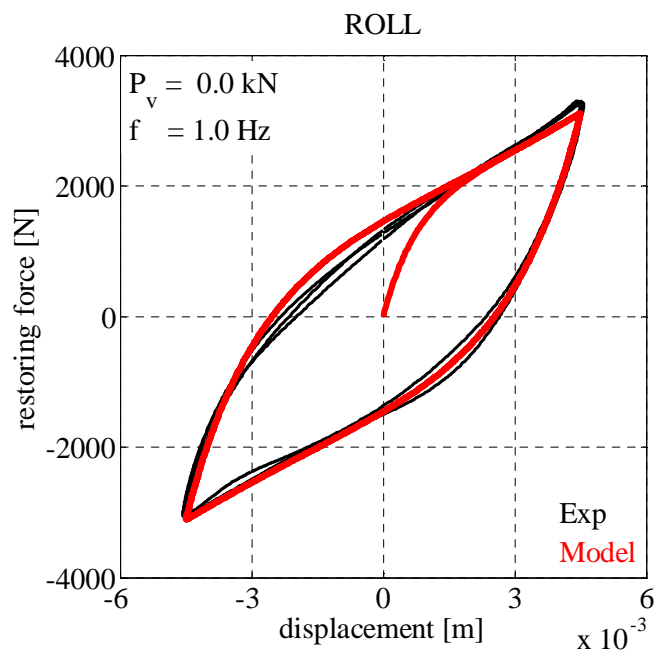


Figure 5.23. Experimental and mathematical hysteresis loops of WRI PWHS 16010 obtained for $A = 0.25$ cm, $f = 1$ Hz, and $P_v = 0$ kN ($N = 100$, $M = 100$) in (a) Roll and (b) Shear directions.

(a)



(b)

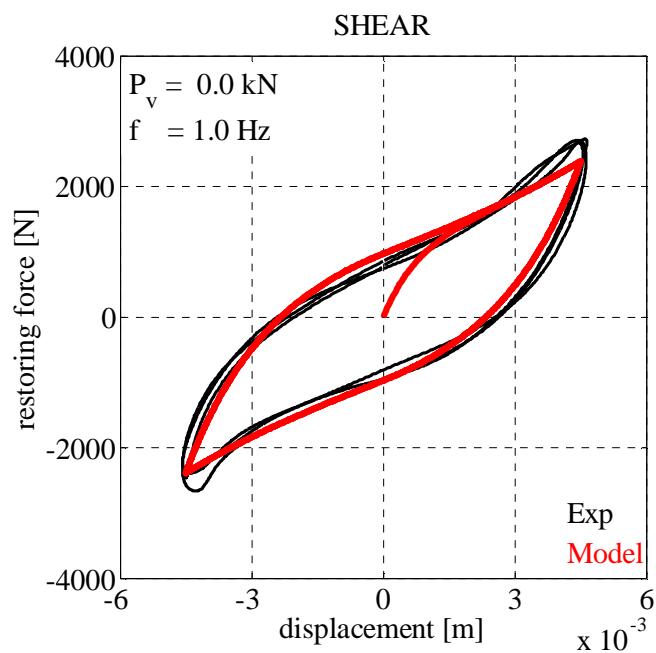
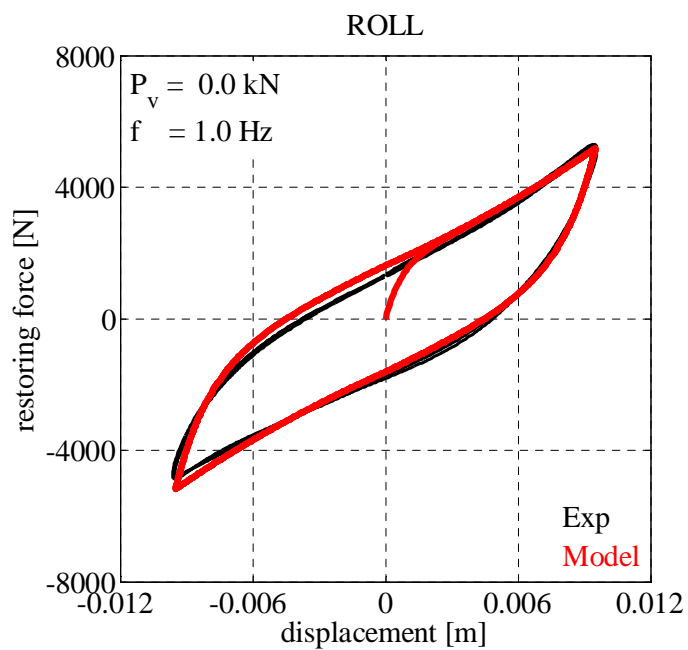


Figure 5.24. Experimental and mathematical hysteresis loops of WRI PWHS 16010 obtained for $A = 0.5 \text{ cm}$, $f = 1 \text{ Hz}$, and $P_v = 0 \text{ kN}$ ($N = 100$, $M = 100$) in (a) Roll and (b) Shear directions.

(a)



(b)

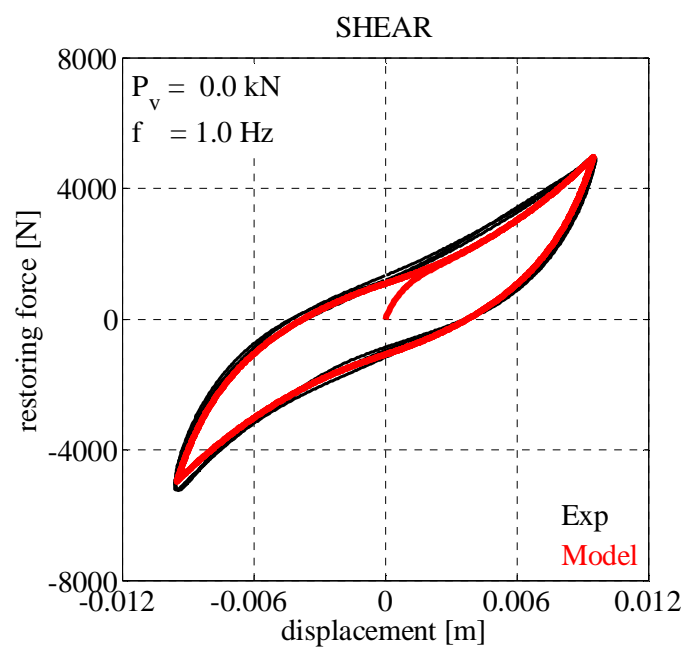
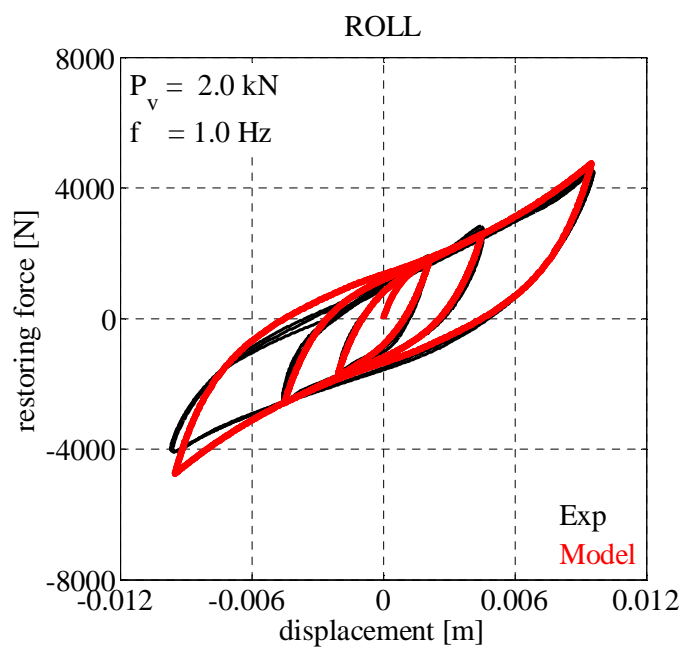


Figure 5.25. Experimental and mathematical hysteresis loops of WRI PWHS 16010 obtained for $A = 1 \text{ cm}$, $f = 1 \text{ Hz}$, and $P_v = 0 \text{ kN}$ ($N = 100$, $M = 100$) in (a) Roll and (b) Shear directions.

(a)



(b)

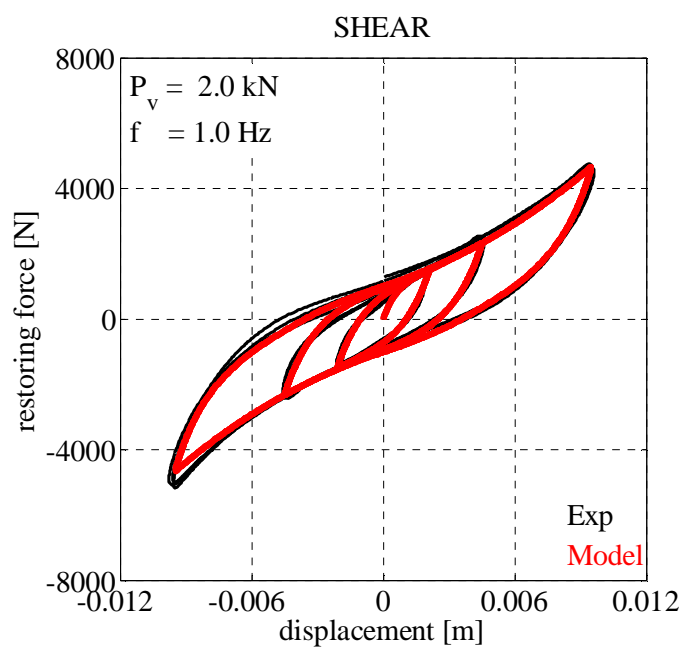


Figure 5.26. Experimental and mathematical hysteresis loops of WRI PWHS 16010 obtained for $f = 1 \text{ Hz}$ and $P_v = 2 \text{ kN}$ ($N = 50$, $M = 50$) in (a) Roll and (b) Shear directions.

5.2.2.2 WRI PWHS 16040

The geometrical characteristics of WRI PWHS 16040 and its two principal horizontal directions are shown in Figure 5.6.

Figure 5.27 reveals the comparisons of the experimental and mathematical results obtained, in both Roll and Shear directions, under a test frequency of 1 Hz and for two different displacement amplitudes, that is, $A = 1$ cm and $A = 3$ cm, without the effect of the vertical load. The force-displacement hysteresis loops have been simulated using the set of five model parameters listed in Table 5.12, which have been determined from the experimental loops having the largest amplitude, that is, $A = 3$ cm, and adopting 50 elastic-perfectly plastic elements (i.e., $N = 50$) and 50 linear elastic gap elements (i.e., $M = 50$).

Table 5.12. APM parameters for WRI PWHS 16040 ($P_v = 0$ kN).

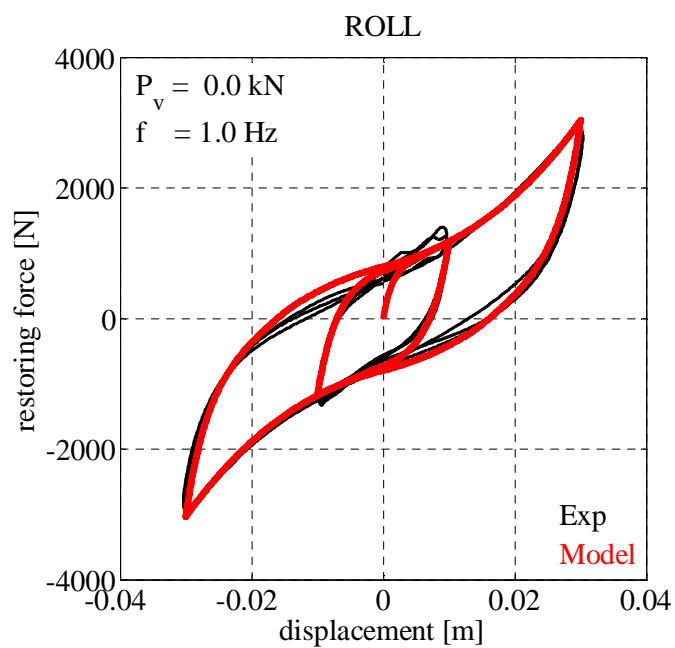
$P_v = 0$ kN	k_0 [N/m]	k_∞ [N/m]	c_1	c_2 [N/m]	c_3
Roll	600000	25000	370	80000	30
Shear	790000	54000	400	90000	25

Figure 5.28 shows the hysteresis force-displacement loops obtained for $P_v = 3$ kN. In order to account for the effect of the applied vertical load, the five model parameters, listed in Table 5.13, have been adjusted based on the experimental results. In the proposed APM, 50 elastic-perfectly plastic elements (i.e., $N = 50$) and 50 linear elastic gap elements (i.e., $M = 50$) have been adopted.

Table 5.13. APM parameters for WRI PWHS 16040 ($P_v = 3$ kN).

$P_v = 3$ kN	k_0 [N/m]	k_∞ [N/m]	c_1	c_2 [N/m]	c_3
Roll	600000	16500	499.5	48000	30
Shear	553000	23400	504	72000	20

(a)



(b)

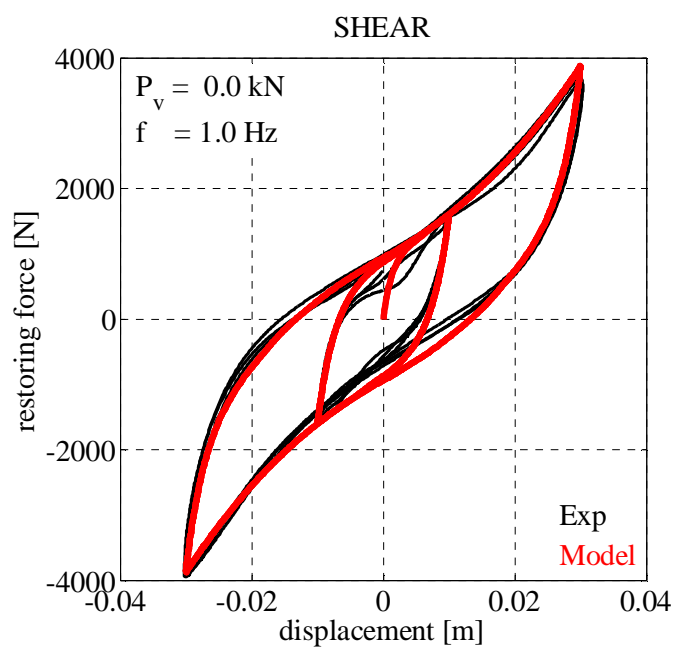
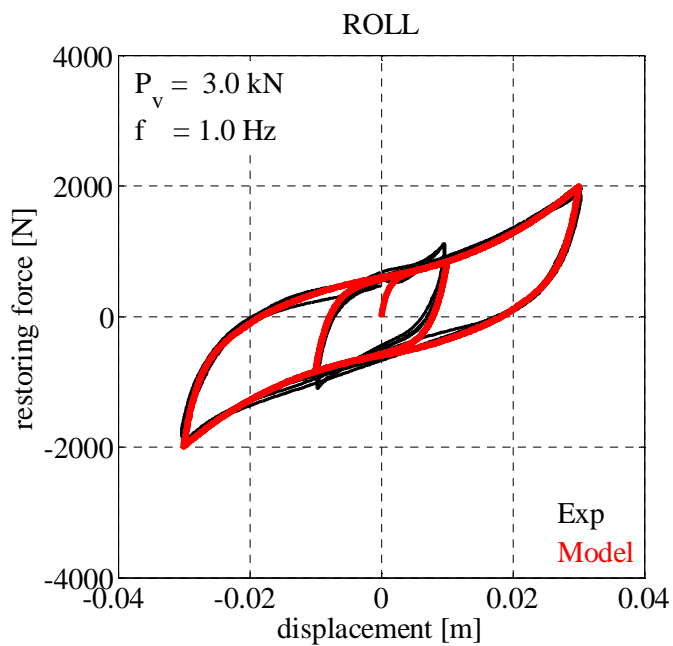


Figure 5.27. Experimental and mathematical hysteresis loops of WRI PWHS 16040 obtained for $f = 1 \text{ Hz}$ and $P_v = 0 \text{ kN}$ ($N = 50$, $M = 50$) in (a) Roll and (b) Shear directions.

(a)



(b)

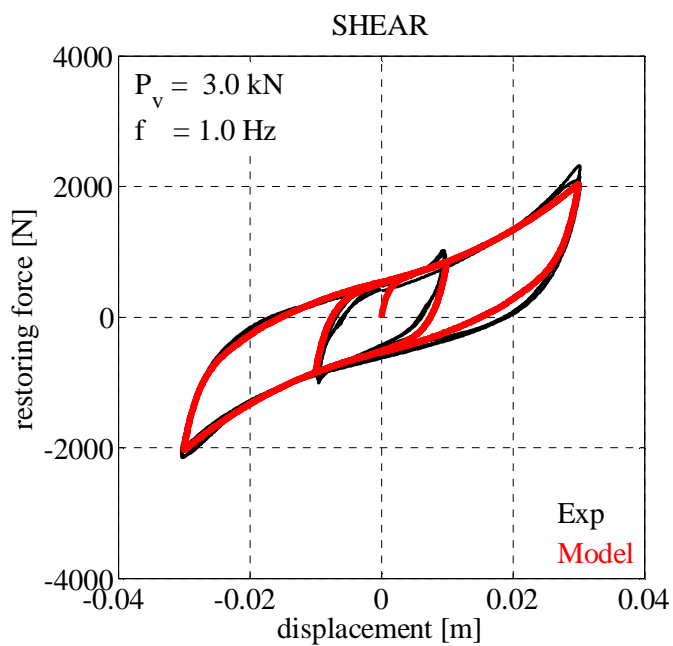


Figure 5.28. Experimental and mathematical hysteresis loops of WRI PWHS 16040 obtained for $f = 1 \text{ Hz}$ and $P_v = 3 \text{ kN}$ ($N = 50$, $M = 50$) in (a) Roll and (b) Shear directions.

5.2.2.3 WRI PWHS 16040 S

The geometrical characteristics of WRI PWHS 16040 S and its two principal horizontal directions are shown in Figure 5.9.

Figure 5.29 shows the comparisons of the experimental and mathematical results obtained, in both Roll and Shear directions, under a test frequency of 1 Hz and for two different displacement amplitudes, that is, $A = 1$ cm and $A = 3$ cm, without the effect of the vertical load. The force-displacement hysteresis loops have been simulated using the set of five model parameters listed in Table 5.14, which have been determined from the experimental loops having the largest amplitude, that is, $A = 3$ cm, and adopting 50 elastic-perfectly plastic elements (i.e., $N = 50$) and 50 linear elastic gap elements (i.e., $M = 50$).

Table 5.14. APM parameters for WRI PWHS 16040 S ($P_v = 0$ kN).

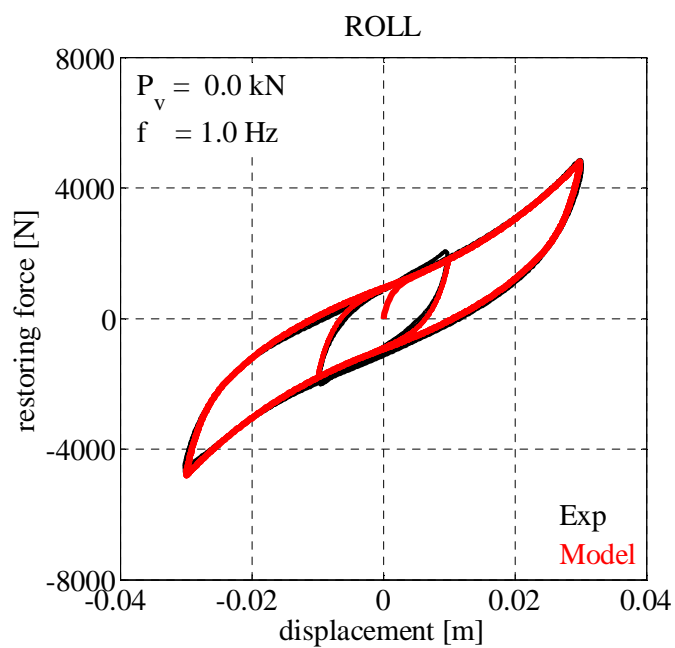
$P_v = 0$ kN	k_0 [N/m]	k_∞ [N/m]	c_1	c_2 [N/m]	c_3
Roll	900000	73000	450	70000	36
Shear	1000000	140000	380	30000	32

Figure 5.30 shows the hysteresis force-displacement loops obtained for $P_v = 2$ kN. In order to account for the effect of the applied vertical load, the five model parameters, listed in Table 5.15, have been adjusted based on the experimental results. In the proposed APM, 50 elastic-perfectly plastic elements (i.e., $N = 50$) and 50 linear elastic gap elements (i.e., $M = 50$) have been adopted.

Table 5.15. APM parameters for WRI PWHS 16040 S ($P_v = 2$ kN).

$P_v = 2$ kN	k_0 [N/m]	k_∞ [N/m]	c_1	c_2 [N/m]	c_3
Roll	640000	39000	370	70000	30
Shear	700000	50000	340	95000	30

(a)



(b)

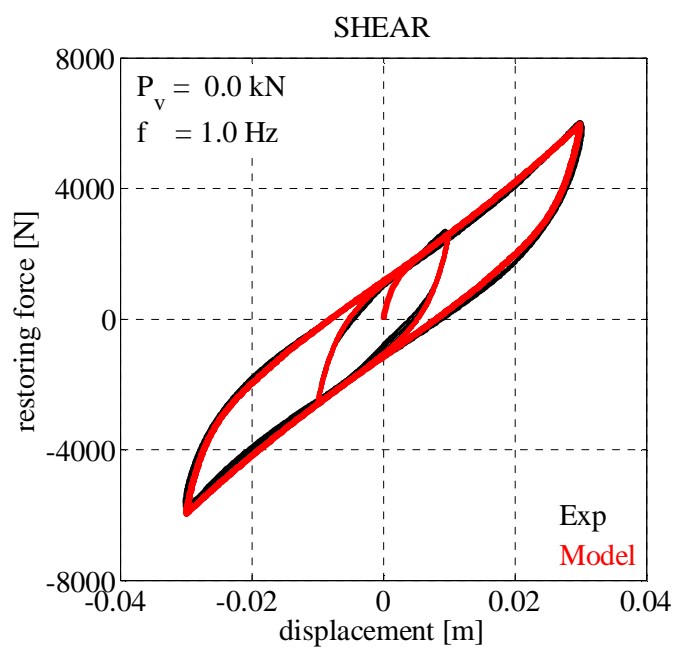
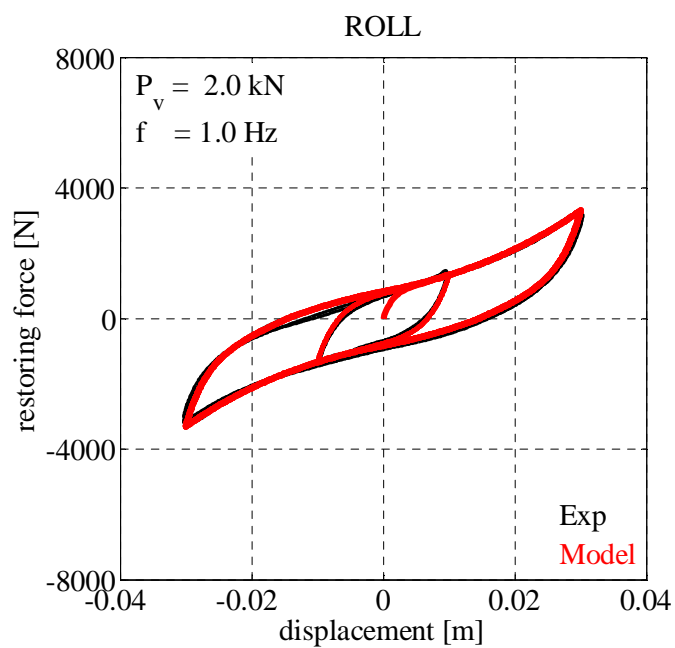


Figure 5.29. Experimental and mathematical hysteresis loops of WRI PWHS 16040 S obtained for $f = 1 \text{ Hz}$ and $P_v = 0 \text{ kN}$ ($N = 50$, $M = 50$) in (a) Roll and (b) Shear directions.

(a)



(b)

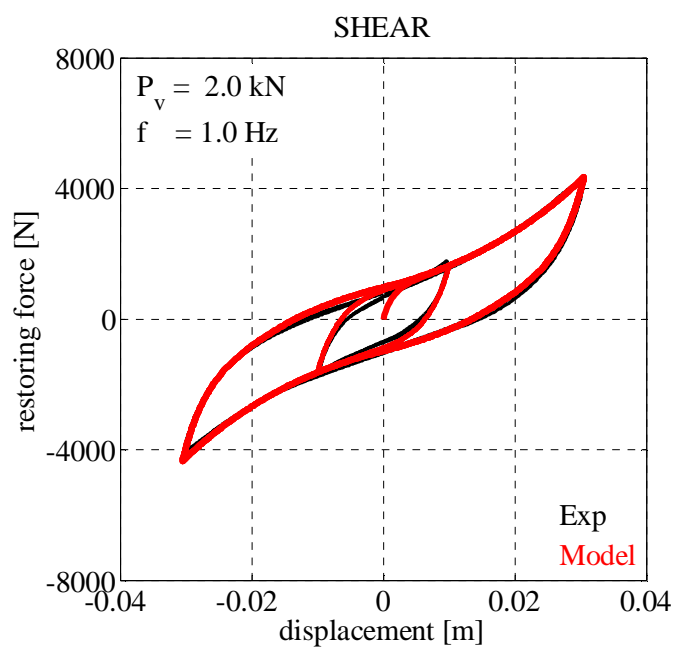


Figure 5.30. Experimental and mathematical hysteresis loops of WRI PWHS 16040 S obtained for $f = 1 \text{ Hz}$ and $P_v = 2 \text{ kN}$ ($N = 50$, $M = 50$) in (a) Roll and (b) Shear directions.

5.2.2.4 WRI PWHS 16060

The geometrical characteristics of WRI PWHS 16060 and its two principal horizontal directions are shown in Figure 5.12.

Figure 5.31 reveals the comparisons of the experimental and mathematical results obtained, in both Roll and Shear directions, under a test frequency of 1 Hz and for two different displacement amplitudes, that is, $A = 1$ cm and $A = 4$ cm, without the effect of the vertical load. The force-displacement hysteresis loops have been simulated using the set of five model parameters listed in Table 5.16, which have been determined from the experimental loops having the largest amplitude, that is, $A = 4$ cm, and adopting 50 elastic-perfectly plastic elements (i.e., $N = 50$) and 50 linear elastic gap elements (i.e., $M = 50$).

Table 5.16. APM parameters for WRI PWHS 16060 ($P_v = 0$ kN).

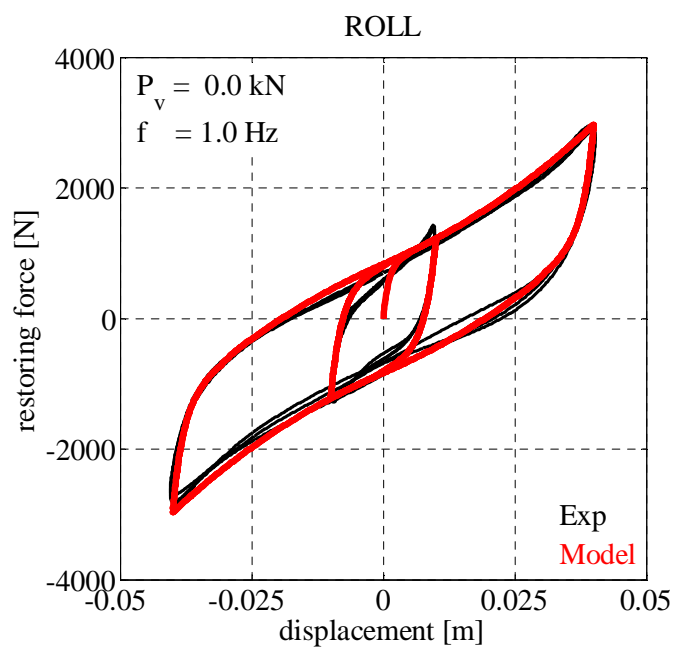
$P_v = 0$ kN	k_0 [N/m]	k_∞ [N/m]	c_1	c_2 [N/m]	c_3
Roll	850000	35000	500	65000	12
Shear	750000	25000	700	50000	20

Figure 5.32 shows the hysteresis force-displacement loops obtained for $P_v = 2$ kN. In order to account for the effect of the applied vertical load, the five model parameters, listed in Table 5.17, have been adjusted based on the experimental results. In the proposed APM, 50 elastic-perfectly plastic elements (i.e., $N = 50$) and 50 linear elastic gap elements (i.e., $M = 50$) have been adopted.

Table 5.17. APM parameters for WRI PWHS 16060 ($P_v = 2$ kN).

$P_v = 2$ kN	k_0 [N/m]	k_∞ [N/m]	c_1	c_2 [N/m]	c_3
Roll	595000	15750	550	26000	15
Shear	320000	12000	300	32000	15

(a)



(b)

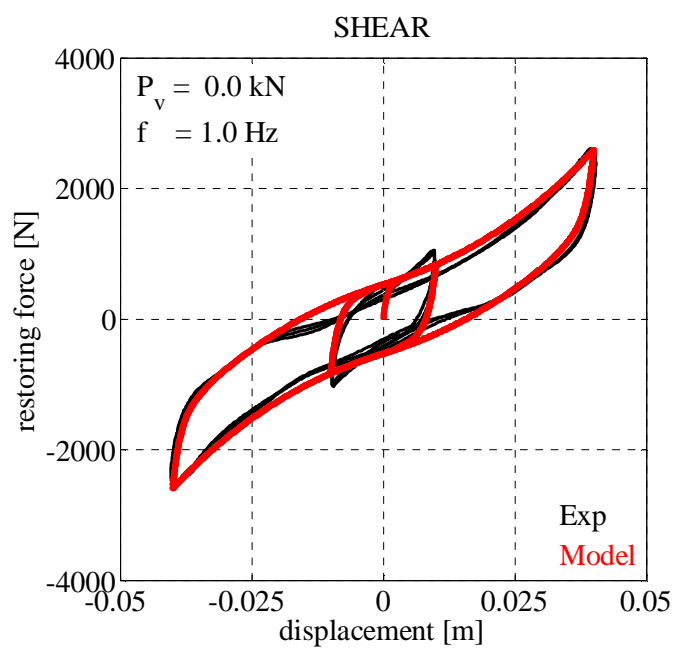
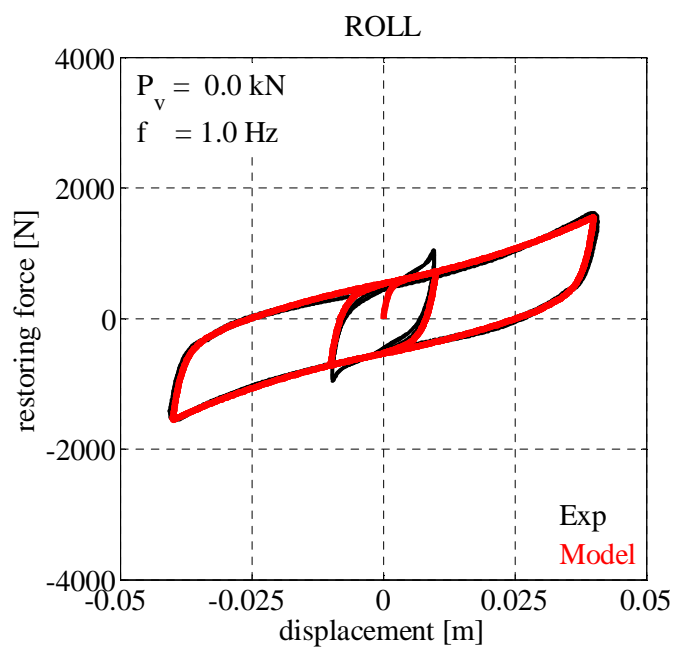


Figure 5.31. Experimental and mathematical hysteresis loops of WRI PWHS 16060 obtained for $f = 1 \text{ Hz}$ and $P_v = 0 \text{ kN}$ ($N = 50$, $M = 50$) in (a) Roll and (b) Shear directions.

(a)



(b)

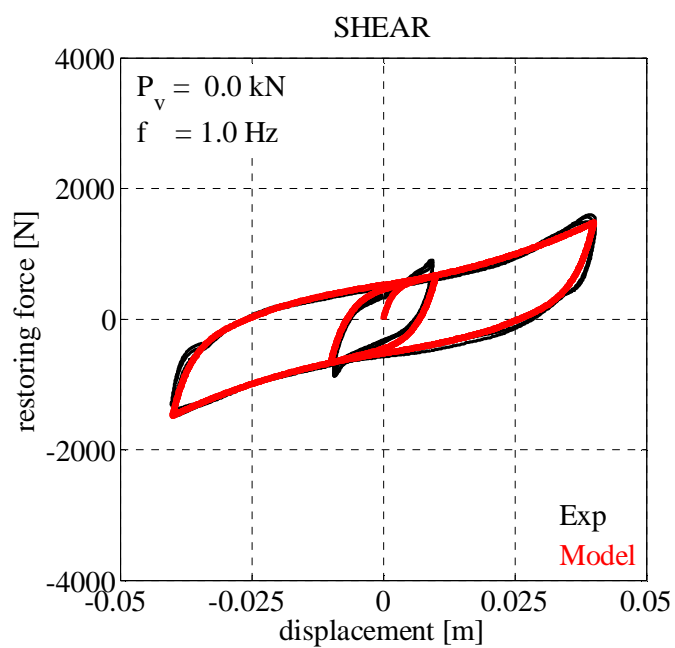


Figure 5.32. Experimental and mathematical hysteresis loops of WRI PWHS 16060 obtained for $f = 1 \text{ Hz}$ and $P_v = 2 \text{ kN}$ ($N = 50$, $M = 50$) in (a) Roll and (b) Shear directions.

5.3 Simulation of Experimental Response of RR-FRB

5.3.1 Advanced Nonlinear Exponential Model

The tested RR-FRB and the two different horizontal loading directions, namely, 0° and 45° directions, are shown in Figure 5.33.

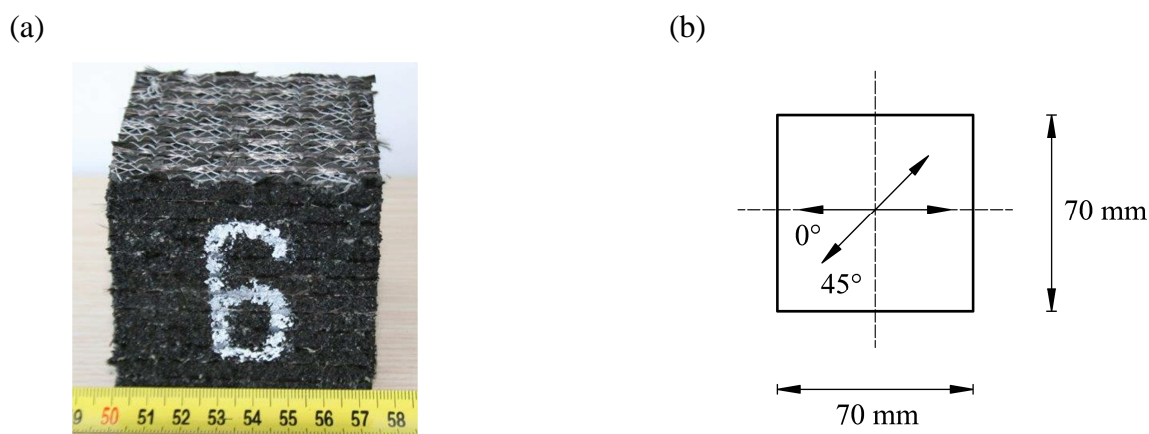


Figure 5.33. (a) Tested RR-FRB and (b) horizontal loading directions.

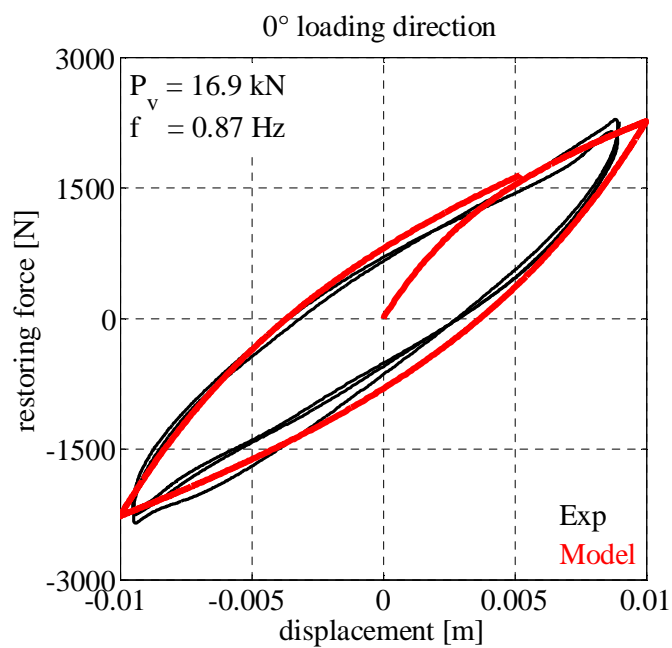
Figures 5.34, 5.35, 5.36, 5.37, 5.38, 5.39, 5.40 and 5.41 show the experimental and simulated hysteresis loops of RR-FRB obtained applying a sinusoidal harmonic motion having frequency of 0.87 Hz, under the effect of a vertical load of 16.9 kN, for a displacement amplitude A equal to 1 cm, 1.5 cm, 2 cm, 2.5 cm, 3 cm, 3.5 cm, 4 cm, and 4.5 cm, respectively, in both 0° and 45° horizontal loading directions.

The force-displacement hysteresis loops have been simulated using the set of five model parameters listed in Table 5.18 and determined from the experimental loops having the largest amplitude, that is, $A = 4.5$ cm.

Table 5.18. ANEM parameters for RR-FRB ($P_v = 16.9$ kN).

$P_v = 16.9$ kN	k_1 [N/m]	k_2 [N/m]	a	c [N/m]	d
0°	350000	38000	80	-20000	45
45°	250000	40000	70	-80000	12

(a)



(b)

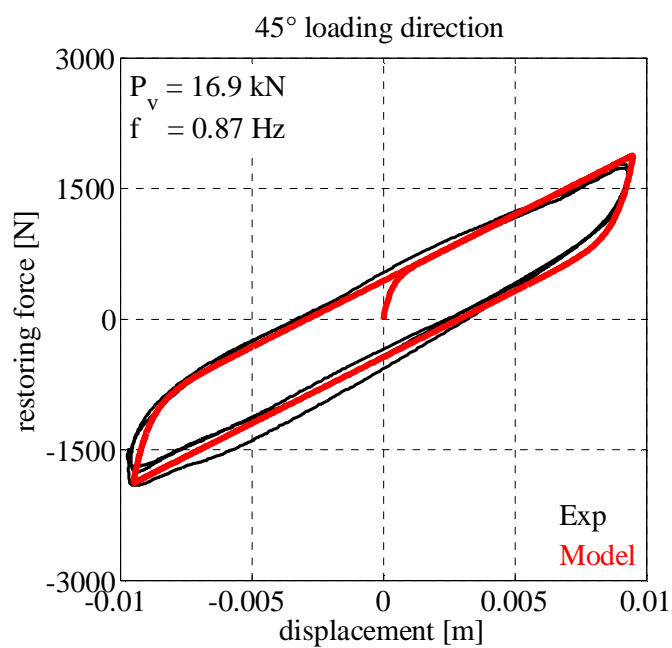
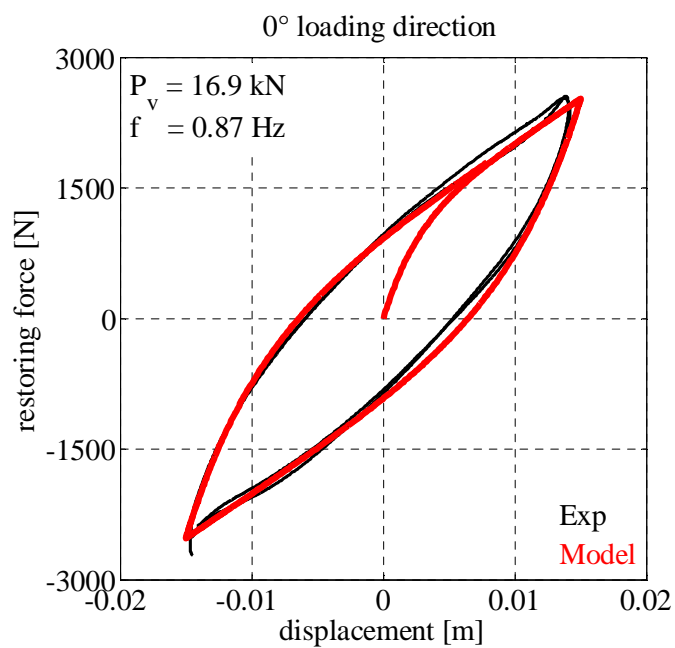


Figure 5.34. Analytical and experimental hysteresis loops of RR-FRB obtained for $A = 1 \text{ cm}$, $f = 0.87 \text{ Hz}$, and $P_v = 16.9 \text{ kN}$ in (a) 0° and (b) 45° loading directions.

(a)



(b)

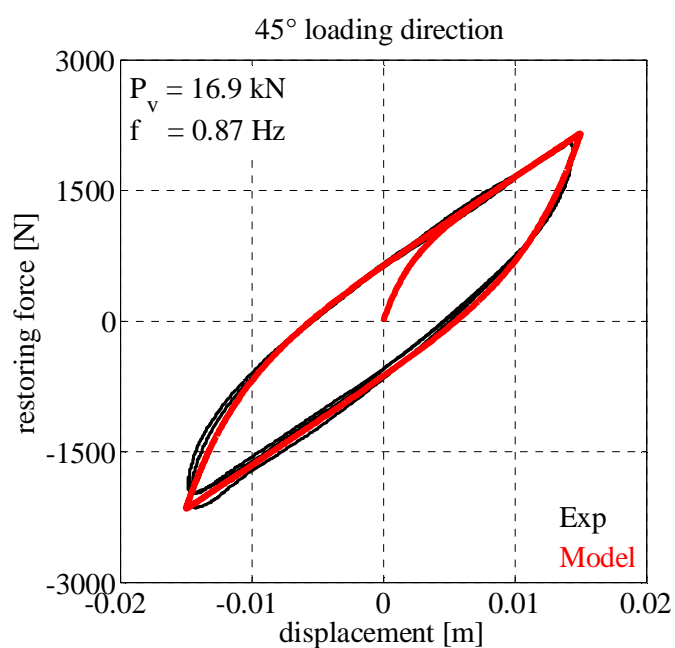
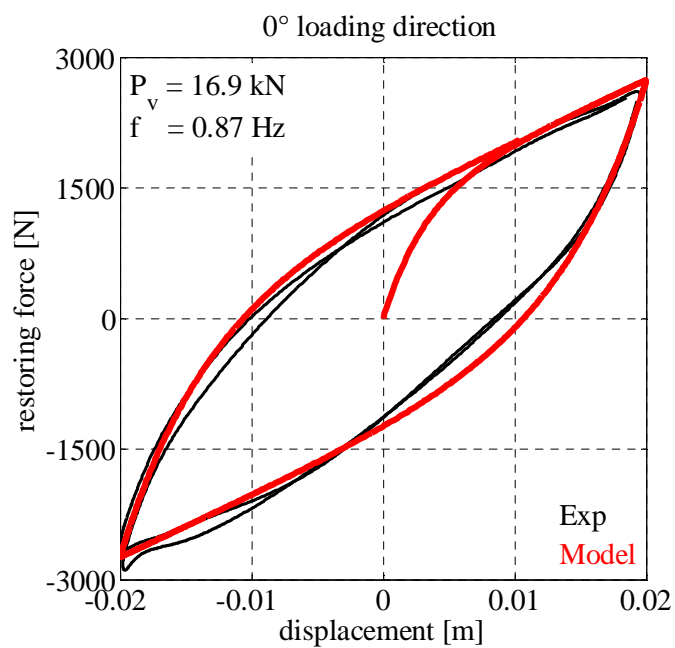


Figure 5.35. Analytical and experimental hysteresis loops of RR-FRB obtained for $A = 1.5 \text{ cm}$, $f = 0.87 \text{ Hz}$, and $P_v = 16.9 \text{ kN}$ in (a) 0° and (b) 45° loading directions.

(a)



(b)

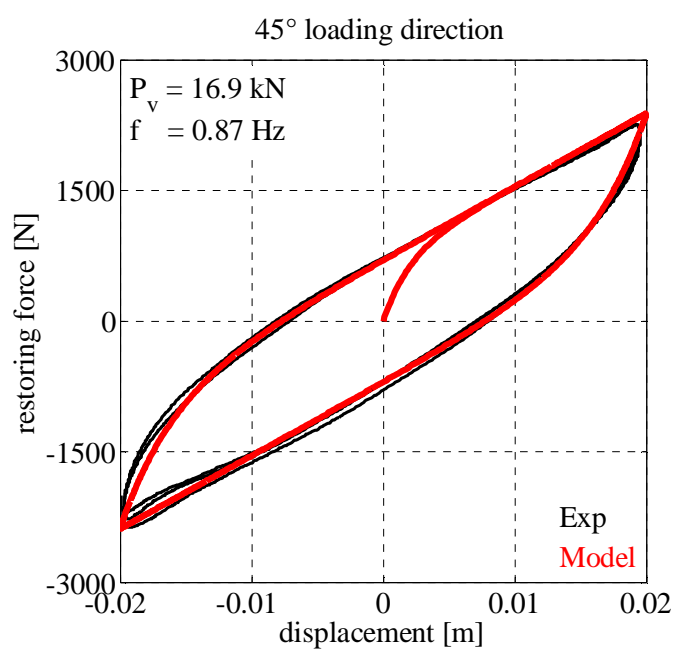
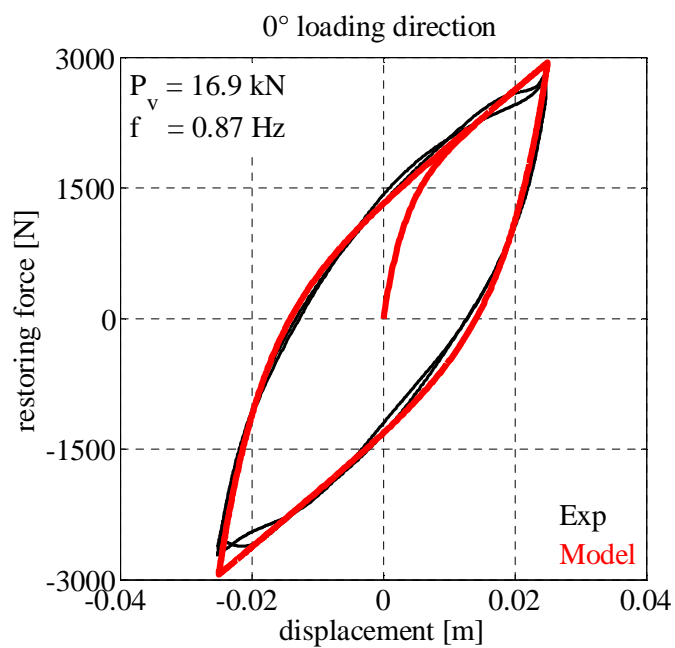


Figure 5.36. Analytical and experimental hysteresis loops of RR-FRB obtained for $A = 2 \text{ cm}$, $f = 0.87 \text{ Hz}$, and $P_v = 16.9 \text{ kN}$ in (a) 0° and (b) 45° loading directions.

(a)



(b)

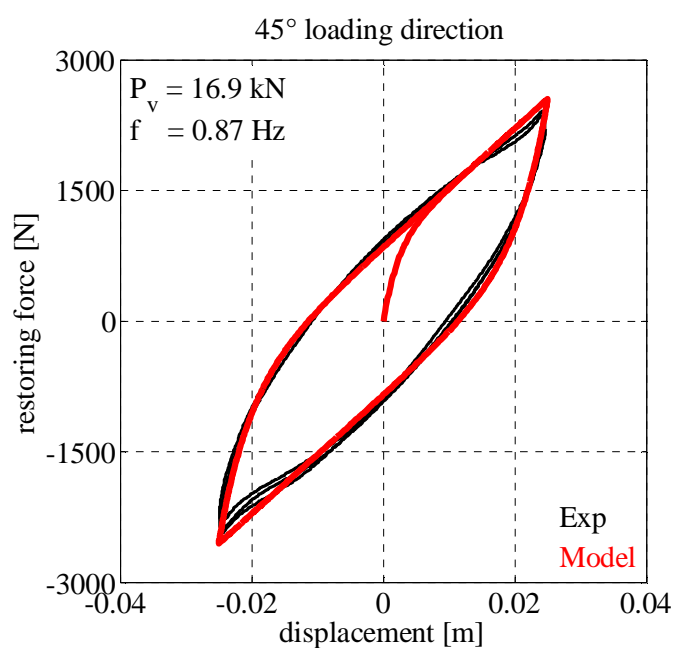
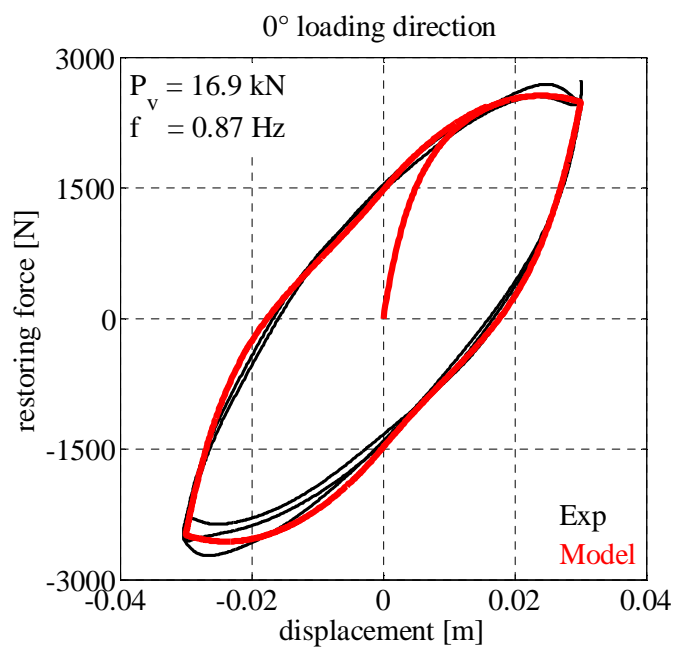


Figure 5.37. Analytical and experimental hysteresis loops of RR-FRB obtained for $A = 2.5 \text{ cm}$, $f = 0.87 \text{ Hz}$, and $P_v = 16.9 \text{ kN}$ in (a) 0° and (b) 45° loading directions.

(a)



(b)

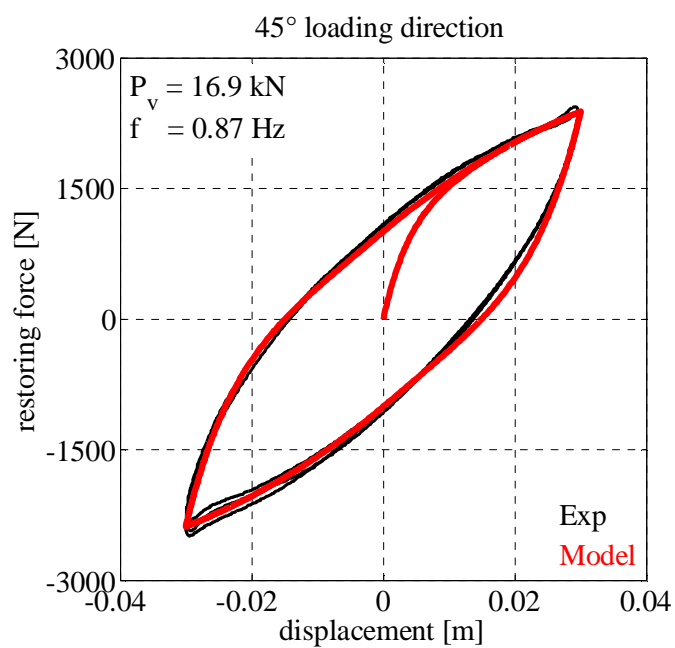
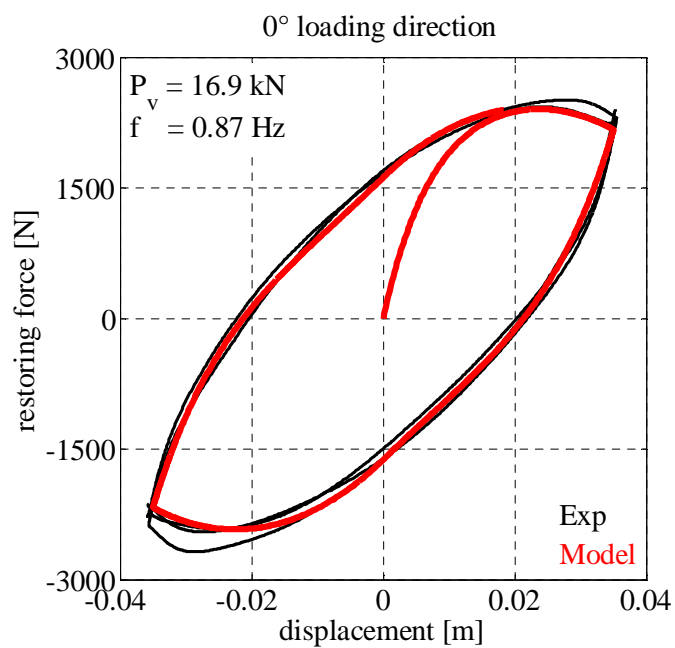


Figure 5.38. Analytical and experimental hysteresis loops of RR-FRB obtained for $A = 3 \text{ cm}$, $f = 0.87 \text{ Hz}$, and $P_v = 16.9 \text{ kN}$ in (a) 0° and (b) 45° loading directions.

(a)



(b)

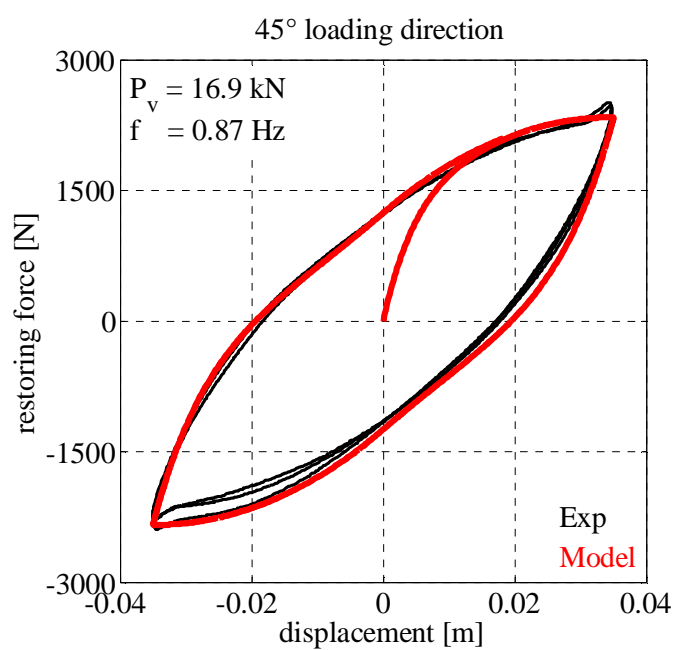
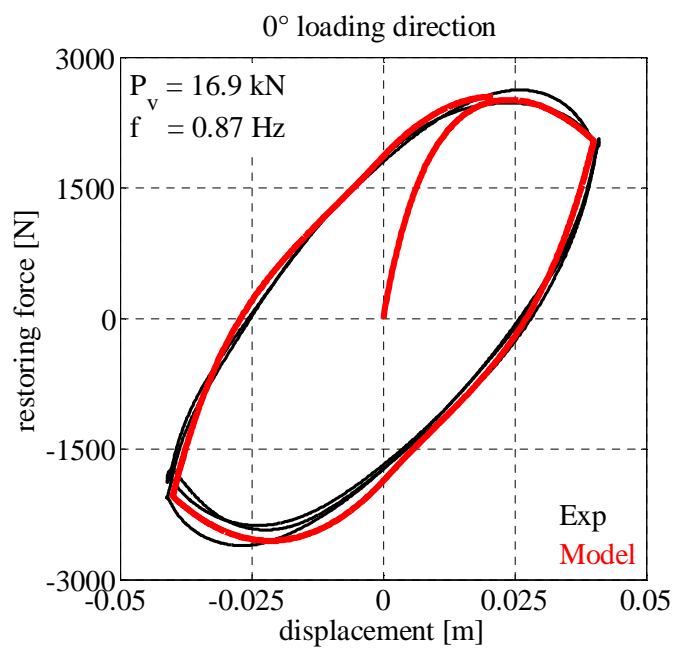


Figure 5.39. Analytical and experimental hysteresis loops of RR-FRB obtained for $A = 3.5 \text{ cm}$, $f = 0.87 \text{ Hz}$, and $P_v = 16.9 \text{ kN}$ in (a) 0° and (b) 45° loading directions.

(a)



(b)

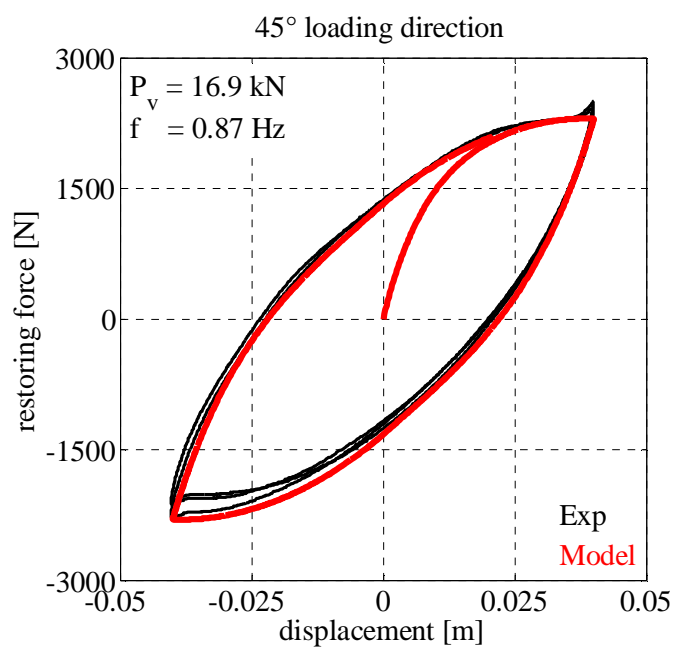
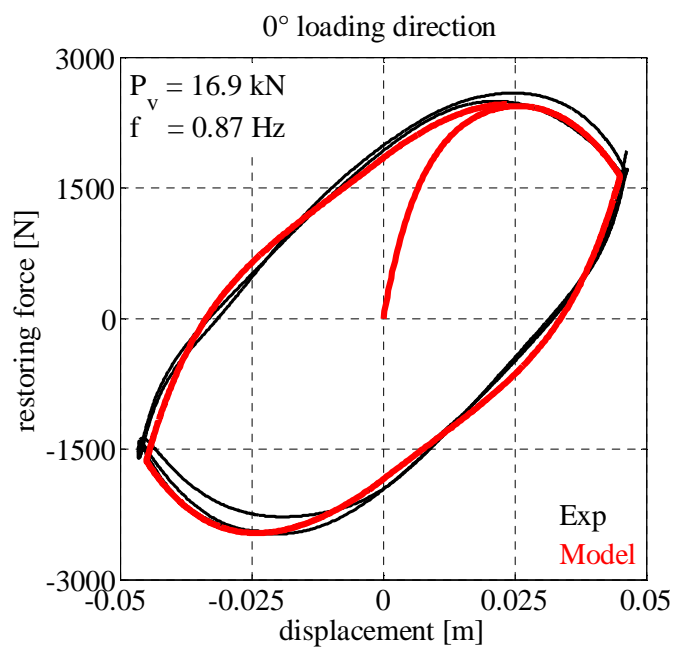


Figure 5.40. Analytical and experimental hysteresis loops of RR-FRB obtained for $A = 4 \text{ cm}$, $f = 0.87 \text{ Hz}$, and $P_v = 16.9 \text{ kN}$ in (a) 0° and (b) 45° loading directions.

(a)



(b)

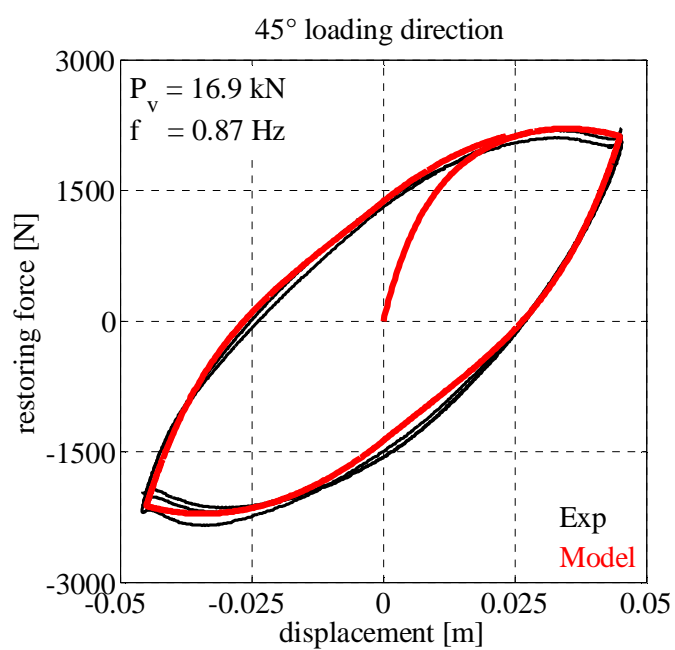


Figure 5.41. Analytical and experimental hysteresis loops of RR-FRB obtained for $A = 4.5 \text{ cm}$, $f = 0.87 \text{ Hz}$, and $P_v = 16.9 \text{ kN}$ in (a) 0° and (b) 45° loading directions.

5.3.2 Advanced Parallel Model

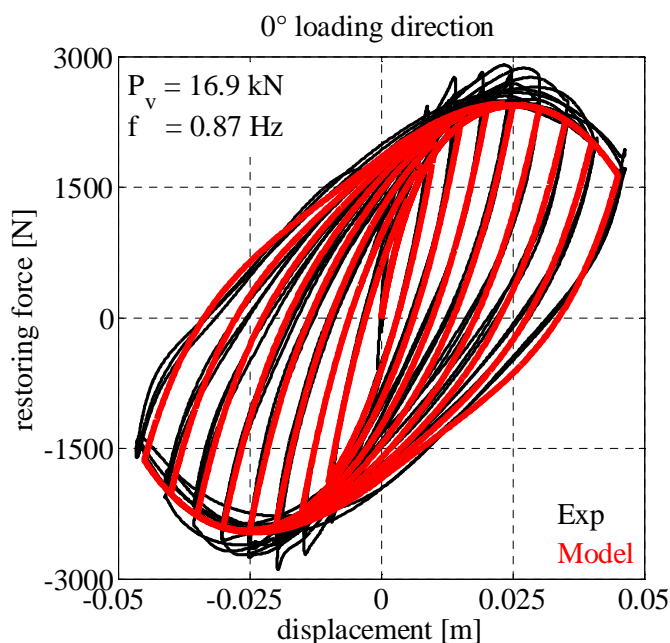
Figure 5.42a and 5.42b show the experimental and simulated hysteresis loops of RR-FRB obtained applying a sinusoidal harmonic motion having frequency of 0.87 Hz, under the effect of a vertical load of 16.9 kN, for a displacement amplitude A equal to 1 cm, 1.5 cm, 2 cm, 2.5 cm, 3 cm, 3.5 cm, 4 cm, and 4.5 cm, in 0° and 45° loading directions, respectively.

The force-displacement hysteresis loops have been simulated using the set of five model parameters listed in Table 5.19, which have been determined from the experimental loops having the largest amplitude, that is, $A = 4.5$ cm, and adopting 50 elastic-perfectly plastic elements (i.e., $N = 50$) and 50 linear elastic gap elements (i.e., $M = 50$).

Table 5.19. APM parameters for RR-FRB ($P_v = 16.9$ kN).

$P_v = 16.9$ kN	k_0 [N/m]	k_∞ [N/m]	c_1	c_2 [N/m]	c_3
0°	350000	38000	80	-20000	45
45°	250000	40000	70	-80000	12

(a)



(b)

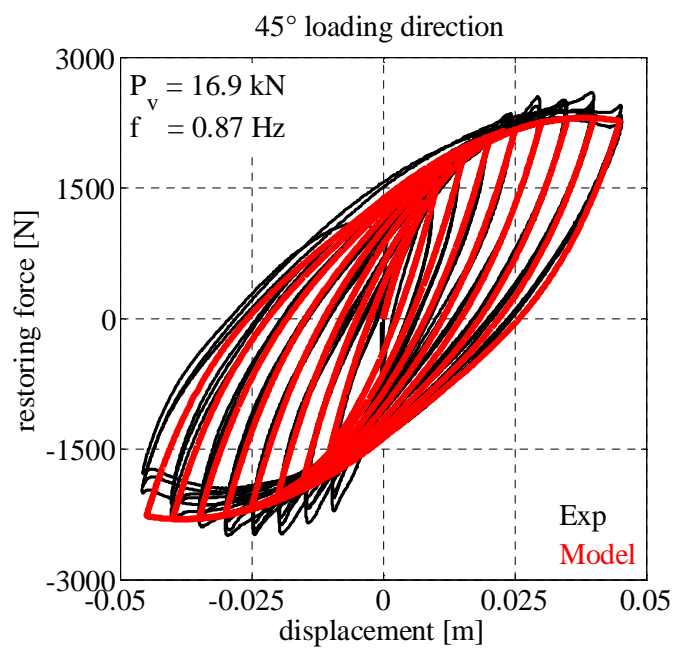


Figure 5.42. Experimental and mathematical hysteresis loops of RR-FRB obtained for $f = 0.87 \text{ Hz}$ and $P_v = 16.9 \text{ kN}$ ($N = 50, M = 50$) in (a) 0° and (b) 45° loading directions.

Chapter 6

Numerical Time Integration Methods

6.1 Introduction

Chapter 6 deals with the nonlinear response history analysis methods, required to solve the dynamic equilibrium equations of the discrete structural model of a seismically base-isolated structures, and is organized into three parts.

The first part presents a conventional non-partitioned solution method, developed by Nagarajaiah et al. (1991) specifically for the nonlinear time history analysis of base-isolated structures and implemented in the computer program 3D-BASIS-ME-MB (Tsopelas et al. 2005). For brevity, in this work, the latter implicit time integration method adopted in conjunction with the pseudo-force approach is called Pseudo-Force Method.

The second part presents a proposed partitioned solution approach, that is, a Mixed Explicit-Implicit time integration Method, characterized by two substeps called Explicit Integration Substep and Implicit Integration Substep.

The third part is concerned with the stability aspects, accuracy and computational efficiency of the proposed time integration method. First, a procedure to evaluate the critical time step is developed for 2d base-isolated structures and extended to the 3d case. Then, the proposed numerical time integration method is adopted to analyze four different 3d base-isolated structures subjected to bidirectional earthquake excitation and the numerical results are compared with those obtained by using the solution algorithm introduced by Nagarajaiah et al. (1991) in order to demonstrate the accuracy and the computational efficiency of the proposed method.

6.2 Conventional Non-Partitioned Solution Approach

6.2.1 Introduction

The response of real civil structures subjected to a large dynamic excitation, such as blast or seismic loading, often involves significant nonlinear behavior which generally includes the effects of large displacements and/or nonlinear material properties (Wilson 2002).

Direct time integration methods used to solve the nonlinear dynamic equilibrium equations of structures subjected to external excitation, that is, time-dependent applied forces and/or earthquake excitation, are basically categorized into two groups:

- explicit time integration methods, such as the central difference method;
- implicit time integration methods, such as the Newmark's method.

A time integration method is explicit if the solution at time $t + \Delta t$ is obtained by considering the equilibrium conditions at time t and the integration algorithm does not require factorization of the effective stiffness matrix (Dokainish and Subbarai 1989a).

A time integration method is implicit if the solution at time $t + \Delta t$ is evaluated by considering the equilibrium conditions at time $t + \Delta t$ and a set of simultaneous equations has to be solved at each time step wherein the effective stiffness matrix is a combination of the mass, damping and stiffness matrices (Dokainish and Subbarai 1989b).

In general, each type of time integration method has its own advantages and disadvantages. Explicit algorithms require a much lower computational effort per time step when compared with implicit methods but are conditionally stable. On the other hand, implicit algorithms can be designed to have unconditional stability, in linear analysis, so that the choice of time step size is limited by accuracy requirements only (Bathe 1996).

A conventional non-partitioned solution approach, characterized by the use of an implicit single-step time integration method adopted with the (modified) Newton-Raphson or the pseudo-force iteration procedure, is generally employed to solve the nonlinear dynamic equilibrium equations of seismically base-isolated structures subjected to earthquake excitation.

Nagarajaiah et al. (1989) investigated the use of an implicit time integration method adopted with the modified Newton-Raphson iteration procedure for the nonlinear dynamic analysis of

base-isolated structures with elastomeric or sliding bearings. This study reveals that the modified Newton-Raphson iteration method:

- converges when 3d base-isolated structures with elastomeric bearings are analyzed;
- does not converge when 3d base-isolated structures with sliding bearings are analyzed because of the severe nonlinearities involved.

Among conventional non-partitioned solution methods, the solution algorithm proposed by Nagarajaiah et al. (1991), which has been implemented in the computer program 3D-BASIS-ME-MB (Tsopelas et al. 2005), is presented in the following because specifically developed for nonlinear time history analysis of base-isolated structures with either elastomeric and/or sliding isolation systems. In this non-partitioned solution approach, the equations of motion are solved using the implicit unconditionally stable Newmark's constant average acceleration method, chosen because unconditionally stable for both positive and negative tangent stiffness (Cheng 1988), with the nonlinear forces being represented as pseudo-forces. An iterative procedure consisting of corrective pseudo-forces is employed within each time step until equilibrium is achieved. For brevity, in this work, the above-described implicit time integration method adopted in conjunction with the pseudo-force approach is referred to as the Pseudo-Force Method (PFM).

6.2.2 Pseudo-Force Method

The dynamic equilibrium equations of the 3d discrete structural model of an actual base-isolated structure written at time t and at time $t + \Delta t$ are:

$$\mathbf{m} \ddot{\mathbf{u}}(t) + \mathbf{c} \dot{\mathbf{u}}(t) + \mathbf{k} \mathbf{u}(t) + \mathbf{f}(t) = -\mathbf{m} \mathbf{r} \ddot{u}_g(t), \quad (6.1)$$

$$\mathbf{m} \ddot{\mathbf{u}}(t + \Delta t) + \mathbf{c} \dot{\mathbf{u}}(t + \Delta t) + \mathbf{k} \mathbf{u}(t + \Delta t) + \mathbf{f}(t + \Delta t) = -\mathbf{m} \mathbf{r} \ddot{u}_g(t + \Delta t). \quad (6.2)$$

Subtracting Equation (6.1) from Equation (6.2) gives the following incremental dynamic equilibrium equations:

$$\begin{aligned} \mathbf{m} \Delta \ddot{\mathbf{u}}(t + \Delta t) + \mathbf{c} \Delta \dot{\mathbf{u}}(t + \Delta t) + \mathbf{k} \Delta \mathbf{u}(t + \Delta t) + \Delta \mathbf{f}(t + \Delta t) = \\ -\mathbf{m} \mathbf{r} \ddot{u}_g(t + \Delta t) - \mathbf{m} \ddot{\mathbf{u}}(t) - \mathbf{c} \dot{\mathbf{u}}(t) - \mathbf{k} \mathbf{u}(t) - \mathbf{f}(t), \end{aligned} \quad (6.3)$$

with

$$\Delta \ddot{\mathbf{u}}(t + \Delta t) = \ddot{\mathbf{u}}(t + \Delta t) - \ddot{\mathbf{u}}(t), \quad (6.4)$$

$$\Delta \dot{\mathbf{u}}(t + \Delta t) = \dot{\mathbf{u}}(t + \Delta t) - \dot{\mathbf{u}}(t), \quad (6.5)$$

$$\Delta \mathbf{u}(t + \Delta t) = \mathbf{u}(t + \Delta t) - \mathbf{u}(t), \quad (6.6)$$

$$\Delta \mathbf{f}(t + \Delta t) = \mathbf{f}(t + \Delta t) - \mathbf{f}(t), \quad (6.7)$$

where $\Delta \ddot{\mathbf{u}}(t + \Delta t)$, $\Delta \dot{\mathbf{u}}(t + \Delta t)$, and $\Delta \mathbf{u}(t + \Delta t)$ are the incremental acceleration, velocity, and displacement vectors, respectively, and $\Delta \mathbf{f}(t + \Delta t)$ is the incremental nonlinear forces vector.

The coupled incremental nonlinear ordinary differential equations of the second order in time, given by Equation (6.3), can be solved adopting the implicit unconditionally stable Newmark's constant average acceleration method. This method is based on the assumption that the variation of acceleration over a time step is constant, equal to the average acceleration. Taking constant time steps, the expressions for the incremental velocity and acceleration vectors are:

$$\Delta \dot{\mathbf{u}}(t + \Delta t) = \frac{2}{\Delta t} \Delta \mathbf{u}(t + \Delta t) - 2 \dot{\mathbf{u}}(t), \quad (6.8)$$

$$\Delta \ddot{\mathbf{u}}(t + \Delta t) = \frac{4}{(\Delta t)^2} \Delta \mathbf{u}(t + \Delta t) - \frac{4}{\Delta t} \dot{\mathbf{u}}(t) - 2 \ddot{\mathbf{u}}(t). \quad (6.9)$$

Bringing the incremental nonlinear forces vector $\Delta \mathbf{f}(t + \Delta t)$ to the right hand side of Equation (6.3) and substituting the two expressions for $\Delta \dot{\mathbf{u}}(t + \Delta t)$ and $\Delta \ddot{\mathbf{u}}(t + \Delta t)$ into the incremental dynamic equilibrium equations gives:

$$\hat{\mathbf{k}} \Delta \mathbf{u}(t + \Delta t) = \hat{\mathbf{p}}(t + \Delta t), \quad (6.10)$$

where

$$\hat{\mathbf{k}} = \left[\frac{4}{(\Delta t)^2} \mathbf{m} + \frac{2}{\Delta t} \mathbf{c} + \mathbf{k} \right], \quad (6.11)$$

and

$$\begin{aligned} \hat{\mathbf{p}}(t + \Delta t) = & -\mathbf{m} \mathbf{r} \ddot{\mathbf{u}}_g(t + \Delta t) - \mathbf{m} \ddot{\mathbf{u}}(t) - \mathbf{c} \dot{\mathbf{u}}(t) - \mathbf{k} \mathbf{u}(t) - \mathbf{f}(t) \\ & - \Delta \mathbf{f}(t + \Delta t) + \mathbf{m} \left[\frac{4}{\Delta t} \dot{\mathbf{u}}(t) + 2 \ddot{\mathbf{u}}(t) \right] + 2 \mathbf{c} \dot{\mathbf{u}}(t). \end{aligned} \quad (6.12)$$

The incremental nonlinear forces vector $\Delta \mathbf{f}(t + \Delta t)$ can be function of both displacement and velocity vectors at time $t + \Delta t$. Thus, treating $\Delta \mathbf{f}(t + \Delta t)$ as incremental pseudo-forces vector and applying an iterative procedure in order to correct the latter within the time step until equilibrium is achieved allows one to evaluate $\Delta \mathbf{u}(t + \Delta t)$.

6.2.3 Solution Algorithm

The solution algorithm is given in the following:

1. Initial calculations:

1.1 Form mass matrix \mathbf{m} , damping matrix \mathbf{c} , and stiffness matrix \mathbf{k} .

1.2 Initialize displacement, velocity, and acceleration vectors $\mathbf{u}(0)$, $\dot{\mathbf{u}}(0)$, $\ddot{\mathbf{u}}(0)$.

1.3 Select time step Δt and calculate the integration constants:

$$a_1 = \frac{4}{(\Delta t)^2}, \quad a_2 = \frac{2}{\Delta t}, \quad a_3 = \frac{4}{\Delta t}.$$

1.4 Form the effective stiffness matrix:

$$\hat{\mathbf{k}} = a_1 \mathbf{m} + a_2 \mathbf{c} + \mathbf{k}.$$

1.5 Triangularize $\hat{\mathbf{k}}$ using Gaussian elimination:

$$\hat{\mathbf{k}} = \mathbf{L} \mathbf{D} \mathbf{L}^T.$$

2. Calculations for each time step:

2.1 Assume the incremental pseudo-forces vector $\Delta \mathbf{f}^i(t + \Delta t) = 0$ in iteration $i = 1$.

2.2 Calculate the effective load vector at time $t + \Delta t$:

$$\begin{aligned} \hat{\mathbf{p}}(t + \Delta t) = & -\mathbf{m} \mathbf{r} \ddot{\mathbf{u}}_g(t + \Delta t) - \mathbf{m} \ddot{\mathbf{u}}(t) - \mathbf{c} \dot{\mathbf{u}}(t) - \mathbf{k} \mathbf{u}(t) - \mathbf{f}(t) \\ & - \Delta \mathbf{f}^i(t + \Delta t) + \mathbf{m} [a_3 \dot{\mathbf{u}}(t) + 2 \ddot{\mathbf{u}}(t)] + 2 \mathbf{c} \dot{\mathbf{u}}(t). \end{aligned}$$

2.3 Solve for incremental displacement vector:

$$\mathbf{L} \mathbf{D} \mathbf{L}^T \Delta \mathbf{u}^i(t + \Delta t) = \hat{\mathbf{p}}(t + \Delta t).$$

2.4 Evaluate acceleration, velocity, and displacement vectors at time $t + \Delta t$:

$$\ddot{\mathbf{u}}(t + \Delta t) = \ddot{\mathbf{u}}(t) + a_1 \Delta \mathbf{u}^i(t + \Delta t) - a_3 \dot{\mathbf{u}}(t) - 2 \ddot{\mathbf{u}}(t),$$

$$\dot{\mathbf{u}}(t + \Delta t) = \dot{\mathbf{u}}(t) + a_2 \Delta \mathbf{u}^i(t + \Delta t) - 2\dot{\mathbf{u}}(t),$$

$$\mathbf{u}(t + \Delta t) = \mathbf{u}(t) + \Delta \mathbf{u}^i(t + \Delta t).$$

2.5 Compute the state of motion at each bearing and calculate the nonlinear restoring force of each isolator, using the unconditionally stable semi-implicit Runge-Kutta method if required.

2.6 Compute the incremental pseudo-forces vector $\Delta \mathbf{f}^{i+1}(t + \Delta t)$ at the mass center of the base isolation system.

2.7 Compute:

$$error = \left| \Delta \mathbf{f}^{i+1}(t + \Delta t) - \Delta \mathbf{f}^i(t + \Delta t) \right|,$$

where $|\cdot|$ is the euclidean norm.

2.8 If $error \geq tolerance$, further iteration is needed. Iterate starting from step 2.1 and use $\Delta \mathbf{f}^{i+1}(t + \Delta t)$ as incremental pseudo-forces vector and the state of motion at time t , that is, $\mathbf{u}(t)$, $\dot{\mathbf{u}}(t)$, and $\ddot{\mathbf{u}}(t)$.

2.9 If $error \leq tolerance$, no further iteration is needed. Update the nonlinear forces vector $\mathbf{f}(t + \Delta t) = \mathbf{f}(t) + \Delta \mathbf{f}^{i+1}(t + \Delta t)$ and go to step 2.1.

6.3 Proposed Partitioned Solution Approach

6.3.1 Introduction

In most practical civil engineering problems, the increasing complexity of structural models requires the use of a partitioned solution approach in which a discrete structural model is spatially decomposed into interacting components generically called *partitions*. The mathematical foundations of Domain Decomposition Methods (DDMs), which can be used in the framework of any discretization method for partial differential equations (finite elements, finite differences) to make their algebraic solution more efficient on parallel computer platforms, can be found in recent numerical analysis texts (Quarteroni and Valli 1999; Quarteroni 2014). The decomposition may be driven by physical or computational considerations (Felippa et al. 2001). For instance, in the nonlinear soil-structure interaction analysis, being the soil more flexible than the structure, the partitioning of the problem may be a natural choice. In the nonlinear dynamic analysis of a structure subjected to a localized impact, because a small part of the structure is expected to experience strong nonlinear behavior whereas the remaining part would deform into the elastic range, the decomposition of the structural model into two subdomains is driven by computational considerations (Brun et al. 2012): in this case, the use of different time steps and time integration methods (explicit or implicit methods) depending on parts of the analyzed structure instead of adopting a non-partitioned solution approach, that is, a conventional procedure adopting a single time integration method with a unique time step, can reduce the computational effort significantly. To overcome the limitations of conventional single-time step integration, partitioned time integration methods have been developed by several authors in the last 30 years to allow different time steps (multi-time step integration) or time integration algorithms (mixed time integration) or both to be used in different spatial subdomains of the mesh. Mixed time integration procedures using explicit and implicit time integration methods have been proposed by Hughes and Liu (1978), assuming the same time step for all the parts of the mesh. Early works of Belytshko et al. (1979) investigated the use of explicit time integration methods with different time steps according to the mesh subdivision and the finite elements size. Wu and Smolinski (2000) proposed a new explicit multi-time step integration method for solving structural dynamics problems derived from the modified trapezoidal rule method developed by Pezeshk and Camp (1995). All the previous multi-time step integration methods are essentially based on a nodal partition and prescribe the continuity of displacements,

velocities or accelerations at the interface in a strong way, by imposing the equality of subdomain kinematic quantities at the interface. Recently, new methods have been proposed allowing one to prescribe the continuity of those quantities in a weak way by means of Lagrange multipliers (Farhat and Roux 1991; Farhat et al. 1994; Gravouil and Combescure 2001; Combescure and Gravouil 2002; Herry et al. 2002).

In the following, a Mixed Explicit-Implicit time integration Method (MEIM) is proposed for predicting the nonlinear response of base-isolated structures subjected to earthquake excitation. Indeed, in the case of seismically isolated structures (buildings and bridges) the above-mentioned partitioned solution approach can be easily applied being the decomposition of the discrete structural model of such structures driven by physical considerations: the base isolation system is much more flexible than the superstructure to decouple the latter from the earthquake ground motion. Thus, an explicit conditionally stable time integration method can be used to evaluate the base isolation system response and an implicit unconditionally stable time integration method can be adopted to predict the superstructure response with the remarkable benefit in avoiding the iterative procedure within each time step of a nonlinear time history analysis required by conventional implicit time integration methods.

6.3.2 Proposed Mixed Explicit-Implicit Time Integration Method

The solution algorithm is characterized by two substeps called Explicit Integration Substep (EIS) and Implicit Integration Substep (IIS): in each time step of a nonlinear time history analysis, the nonlinear response of the base isolation system is computed first using the explicit time integration method, then the implicit method is adopted to evaluate the superstructure linear response.

6.3.2.1 Explicit Integration Substep

The explicit time integration method adopted to predict the response of the base isolation system is the second order Central Difference Method which is one of the most used among explicit methods in structural dynamics programs and is said to have the highest accuracy and maximum stability limit for any explicit method of order two (Krieg 1973).

In the EIS, the equations of motion at time t are used to evaluate the base isolation system displacement vector \mathbf{u}_b for time $t + \Delta t$. Hence, writing the first set of ntb dynamic equilibrium equations of the 3d discrete structural model at time t gives:

$$\mathbf{m}_b \ddot{\mathbf{u}}_b(t) + (\mathbf{c}_b + \mathbf{c}_1) \dot{\mathbf{u}}_b(t) + \mathbf{c}^T \dot{\mathbf{u}}_s(t) + (\mathbf{k}_b + \mathbf{k}_1) \mathbf{u}_b(t) + \mathbf{k}^T \mathbf{u}_s(t) + \mathbf{f}_n(t) = -\mathbf{m}_b \mathbf{r}_b \ddot{\mathbf{u}}_g(t). \quad (6.13)$$

This method is based on a finite difference approximation of the time derivatives of displacement, that is, velocity and acceleration. Taking constant time steps, the central difference expressions for velocity and acceleration vectors at time t are:

$$\dot{\mathbf{u}}_b(t) = \frac{1}{2 \Delta t} [\mathbf{u}_b(t + \Delta t) - \mathbf{u}_b(t - \Delta t)], \quad (6.14)$$

$$\ddot{\mathbf{u}}_b(t) = \frac{1}{(\Delta t)^2} [\mathbf{u}_b(t + \Delta t) - 2\mathbf{u}_b(t) + \mathbf{u}_b(t - \Delta t)]. \quad (6.15)$$

The error in the expressions (6.14) and (6.15) is of order $(\Delta t)^2$, so the error in \mathbf{u}_b is quartered when Δt is halved.

Substituting the relations for $\dot{\mathbf{u}}_b(t)$ and $\ddot{\mathbf{u}}_b(t)$, from Equations (6.14) and (6.15), respectively, into Equation (6.13), and rearranging terms, gives:

$$\hat{\mathbf{k}}_b \mathbf{u}_b(t + \Delta t) = \hat{\mathbf{p}}_b(t), \quad (6.16)$$

where

$$\hat{\mathbf{k}}_b = \left[\frac{1}{(\Delta t)^2} \mathbf{m}_b + \frac{1}{2\Delta t} (\mathbf{c}_b + \mathbf{c}_1) \right], \quad (6.17)$$

and

$$\begin{aligned} \hat{\mathbf{p}}_b(t) = & -\mathbf{m}_b \mathbf{r}_b \ddot{\mathbf{u}}_g(t) - \mathbf{c}^T \dot{\mathbf{u}}_s(t) - \mathbf{k}^T \mathbf{u}_s(t) - \mathbf{f}_n(t) \\ & + \left[\frac{2}{(\Delta t)^2} \mathbf{m}_b - \mathbf{k}_b - \mathbf{k}_1 \right] \mathbf{u}_b(t) \\ & + \left[-\frac{1}{(\Delta t)^2} \mathbf{m}_b + \frac{1}{2\Delta t} (\mathbf{c}_b + \mathbf{c}_1) \right] \mathbf{u}_b(t - \Delta t), \end{aligned} \quad (6.18)$$

from which $\mathbf{u}_b(t + \Delta t)$ can be evaluated.

In Equation (6.18), $\mathbf{u}_b(t - \Delta t)$, $\mathbf{u}_b(t)$, $\mathbf{u}_s(t)$, and $\dot{\mathbf{u}}_s(t)$ are assumed known from implementation of the procedure for the preceding time steps. In order to calculate the solution at time Δt , a special starting procedure must be used. Since $\mathbf{u}_b(0)$, $\dot{\mathbf{u}}_b(0)$, and $\ddot{\mathbf{u}}_b(0)$ are known at time $t = 0$, $\mathbf{u}_b(-\Delta t)$ can be obtained using the following relation (Bathe 1996):

$$\mathbf{u}_b(-\Delta t) = \mathbf{u}_b(0) - \Delta t \dot{\mathbf{u}}_b(0) + \frac{(\Delta t)^2}{2} \ddot{\mathbf{u}}_b(0). \quad (6.19)$$

The resultant nonlinear forces vector of the base isolation system \mathbf{f}_n depends on the response at time t and could be function of both displacement and velocity, according to the explicit nonlinear force-displacement relation used to model each seismic isolator. The base isolation system velocity vector at time t can be evaluated in terms of displacement vectors using the three-point backward difference approximation (D'Acunto 2012):

$$\dot{\mathbf{u}}_b(t) = \frac{1}{2\Delta t} [-4\mathbf{u}_b(t - \Delta t) + 3\mathbf{u}_b(t) + \mathbf{u}_b(t - 2\Delta t)]. \quad (6.20)$$

The error in the Equation (6.20) is of order $(\Delta t)^2$. It is worth noting that the base isolation system velocity vector at time t cannot be determined by using Equation (6.14) because $\mathbf{u}_b(t + \Delta t)$ is unknown.

6.3.2.2 Implicit Integration Substep

The implicit time integration method adopted to compute the linear response of the superstructure is the second order Newmark's Constant Average Acceleration Method which is one of the most effective and popular implicit methods, especially for the linear and nonlinear time history analysis of civil structures.

In the IIS, the equations of motion at time $t + \Delta t$ are used to evaluate the superstructure displacement vector \mathbf{u}_s for time $t + \Delta t$. Hence, writing the second set of nts dynamic equilibrium equations of the 3d discrete structural model at time $t + \Delta t$ gives:

$$\mathbf{m}_s \ddot{\mathbf{u}}_s(t + \Delta t) + \mathbf{c}_s \dot{\mathbf{u}}_s(t + \Delta t) + \mathbf{k}_s \mathbf{u}_s(t + \Delta t) + \mathbf{c} \dot{\mathbf{u}}_b(t + \Delta t) + \mathbf{k} \mathbf{u}_b(t + \Delta t) = -\mathbf{m}_s \mathbf{r}_s \ddot{\mathbf{u}}_g(t + \Delta t). \quad (6.21)$$

This method is based on the assumption that the variation of acceleration over a time step is constant, equal to the average acceleration. Taking constant time steps, the expressions for the superstructure velocity and acceleration vectors at time $t + \Delta t$ are:

$$\dot{\mathbf{u}}_s(t + \Delta t) = \frac{2}{\Delta t} [\mathbf{u}_s(t + \Delta t) - \mathbf{u}_s(t)] - \dot{\mathbf{u}}_s(t), \quad (6.22)$$

$$\ddot{\mathbf{u}}_s(t + \Delta t) = \frac{4}{(\Delta t)^2} [\mathbf{u}_s(t + \Delta t) - \mathbf{u}_s(t)] - \frac{4}{\Delta t} \dot{\mathbf{u}}_s(t) - \ddot{\mathbf{u}}_s(t). \quad (6.23)$$

Substitution of these two expressions for $\dot{\mathbf{u}}_s(t + \Delta t)$ and $\ddot{\mathbf{u}}_s(t + \Delta t)$ into Equation (6.21) gives:

$$\hat{\mathbf{k}}_s \mathbf{u}_s(t + \Delta t) = \hat{\mathbf{p}}_s(t + \Delta t), \quad (6.24)$$

where

$$\hat{\mathbf{k}}_s = \left[\frac{4}{(\Delta t)^2} \mathbf{m}_s + \frac{2}{\Delta t} \mathbf{c}_s + \mathbf{k}_s \right], \quad (6.25)$$

and

$$\begin{aligned} \hat{\mathbf{p}}_s(t + \Delta t) = & -\mathbf{m}_s \mathbf{r}_s \ddot{\mathbf{u}}_g(t + \Delta t) - \mathbf{c} \dot{\mathbf{u}}_b(t + \Delta t) - \mathbf{k} \mathbf{u}_b(t + \Delta t) \\ & + \left[\frac{4}{(\Delta t)^2} \mathbf{m}_s + \frac{2}{\Delta t} \mathbf{c}_s \right] \mathbf{u}_s(t) \\ & + \left[\frac{4}{\Delta t} \mathbf{m}_s + \mathbf{c}_s \right] \dot{\mathbf{u}}_s(t) + \mathbf{m}_s \ddot{\mathbf{u}}_s(t). \end{aligned} \quad (6.26)$$

In order to solve for $\mathbf{u}_s(t + \Delta t)$, first the base isolation system velocity vector at time $t + \Delta t$ has to be predicted. This vector can be computed in terms of displacement vectors using the three-point backward difference approximation (D'Acunto 2012):

$$\dot{\mathbf{u}}_b(t + \Delta t) = \frac{1}{2\Delta t} [-4\mathbf{u}_b(t) + 3\mathbf{u}_b(t + \Delta t) + \mathbf{u}_b(t - \Delta t)]. \quad (6.27)$$

The error in the Equation (6.27) is of order $(\Delta t)^2$.

The use of a modal representation for the superstructure, assumed to remain elastic, can reduce the computational cost of the nonlinear time history analysis.

6.3.3 Solution Algorithm

Recently developed time integration algorithms, such as those introduced by Noh and Bathe (2013) and Noh et al. (2013) for the analysis of wave propagation problems, are not adopted in this work because the main idea is reducing the computational effort required for the solution of nonlinear dynamic equilibrium equations of base-isolated structures, by coupling two of the most widely used time integration methods in the seismic analysis of civil structures. The proposed solution algorithm is given in the following:

1. Initial calculations:

1.1 Form superstructure mass matrix \mathbf{m}_s , damping matrix \mathbf{c}_s , and stiffness matrix \mathbf{k}_s and base isolation system mass matrix \mathbf{m}_b , damping matrix \mathbf{c}_b , and stiffness matrix \mathbf{k}_b .

1.2 Initialize superstructure displacement, velocity and acceleration vectors $\mathbf{u}_s(0)$, $\dot{\mathbf{u}}_s(0)$, $\ddot{\mathbf{u}}_s(0)$, and base isolation system displacement, velocity and acceleration vectors $\mathbf{u}_b(0)$, $\dot{\mathbf{u}}_b(0)$, $\ddot{\mathbf{u}}_b(0)$; then calculate:

$$\mathbf{u}_b(-\Delta t) = \mathbf{u}_b(0) - \Delta t \dot{\mathbf{u}}_b(0) + \frac{(\Delta t)^2}{2} \ddot{\mathbf{u}}_b(0).$$

1.3 Select time step Δt and calculate the integration constants:

$$a_1 = \frac{2}{(\Delta t)^2}, \quad a_2 = \frac{1}{(\Delta t)^2}, \quad a_3 = \frac{1}{2\Delta t}, \quad a_4 = \frac{4}{(\Delta t)^2}, \quad a_5 = \frac{2}{\Delta t}, \quad a_6 = \frac{4}{\Delta t}.$$

1.4 Form effective mass matrix and effective stiffness matrix:

$$\mathbf{m}^* = a_2 \mathbf{m}_b + a_3 (\mathbf{c}_b + \mathbf{c}_1),$$

$$\mathbf{k}^* = a_4 \mathbf{m}_s + a_5 \mathbf{c}_s + \mathbf{k}_s.$$

1.5 Triangularize \mathbf{m}^* and \mathbf{k}^* :

$$\mathbf{m}^* = \mathbf{L}_e \mathbf{D}_e \mathbf{L}_e^T,$$

$$\mathbf{k}^* = \mathbf{L}_i \mathbf{D}_i \mathbf{L}_i^T.$$

2. Calculations for each time step:

2.1 Compute the state of motion at each seismic isolation bearing at time t .

2.2 Compute the resultant nonlinear forces vector $\mathbf{f}_n(t)$ at the center of mass of the base isolation system.

2.3 Calculate the explicit integration substep effective load vector at time t :

$$\hat{\mathbf{p}}_b(t) = -\mathbf{m}_b \mathbf{r}_b \ddot{\mathbf{u}}_g(t) - \mathbf{c}^T \dot{\mathbf{u}}_s(t) - \mathbf{k}^T \mathbf{u}_s(t) - \mathbf{f}_n(t) + [a_1 \mathbf{m}_b - \mathbf{k}_b - \mathbf{k}_1] \mathbf{u}_b(t) + [-a_2 \mathbf{m}_b + a_3(\mathbf{c}_b + \mathbf{c}_1)] \mathbf{u}_b(t - \Delta t).$$

2.4 Solve for base isolation system displacement vector at time $t + \Delta t$:

$$\mathbf{L}_e \mathbf{D}_e \mathbf{L}_e^T \mathbf{u}_b(t + \Delta t) = \hat{\mathbf{p}}_b(t).$$

2.5 Evaluate base isolation system velocity and acceleration vectors at time t :

$$\dot{\mathbf{u}}_b(t) = a_3 [\mathbf{u}_b(t + \Delta t) - \mathbf{u}_b(t - \Delta t)],$$

$$\ddot{\mathbf{u}}_b(t) = a_2 [\mathbf{u}_b(t + \Delta t) - 2\mathbf{u}_b(t) + \mathbf{u}_b(t - \Delta t)].$$

2.6 Calculate the implicit integration substep effective load vector at time $t + \Delta t$:

$$\hat{\mathbf{p}}_s(t + \Delta t) = -\mathbf{m}_s \mathbf{r}_s \ddot{\mathbf{u}}_g(t + \Delta t) - a_3 \mathbf{c} [-4\mathbf{u}_b(t) + 3\mathbf{u}_b(t + \Delta t) + \mathbf{u}_b(t - \Delta t)] - \mathbf{k} \mathbf{u}_b(t + \Delta t) + [a_4 \mathbf{m}_s + a_5 \mathbf{c}_s] \mathbf{u}_s(t) + [a_6 \mathbf{m}_s + \mathbf{c}_s] \dot{\mathbf{u}}_s(t) + \mathbf{m}_s \ddot{\mathbf{u}}_s(t).$$

2.7 Solve for superstructure displacement vector at time $t + \Delta t$:

$$\mathbf{L}_i \mathbf{D}_i \mathbf{L}_i^T \mathbf{u}_s(t + \Delta t) = \hat{\mathbf{p}}_s(t + \Delta t).$$

2.8 Evaluate superstructure velocity and acceleration vectors at time $t + \Delta t$:

$$\dot{\mathbf{u}}_s(t + \Delta t) = a_5 [\mathbf{u}_s(t + \Delta t) - \mathbf{u}_s(t)] - \dot{\mathbf{u}}_s(t),$$

$$\ddot{\mathbf{u}}_s(t + \Delta t) = a_4 [\mathbf{u}_s(t + \Delta t) - \mathbf{u}_s(t)] - a_6 \dot{\mathbf{u}}_s(t) - \ddot{\mathbf{u}}_s(t).$$

3. Repetition for next time step: replace t by $t + \Delta t$ and repeat steps 2.1 - 2.8.

6.4 Stability Aspects, Accuracy and Computational Efficiency of the MEIM

6.4.1 Introduction

The proposed MEIM is conditionally stable because the second order central difference method is employed in the EIS to compute the nonlinear response of the base isolation system. Thus, in the following, a procedure to evaluate the critical time step is first developed for 2d base-isolated structures with linear isolation elements, neglecting the superstructure and base isolation system viscous damping, and then extended to the 3d case.

The proposed partitioned approach is then applied to determine the dynamic response of two 3d base-isolated structures subjected to a bidirectional earthquake excitation. The first structure is a two-story reinforced concrete structure with vertical geometric irregularity, the second one a four-story reinforced concrete structure without plan and vertical geometric irregularities. For each structure, two types of base isolation systems are considered, namely, base isolation system with lead rubber bearings and base isolation system with friction pendulum bearings. The latter kind of base isolation system allows one to investigate the use of the mixed time integration procedure also in the presence of isolators with very high initial stiffness for which the critical time step size could become smaller than the one used to define the ground acceleration accurately. The accuracy and the computational efficiency of the proposed MEIM are assessed by comparing the numerical results and the computational time with those obtained by using the PFM.

6.4.2 Evaluation of the Critical Time Step

6.4.2.1 2d Base-Isolated Structures

Considering the 2d discrete structural model of a base-isolated structure with only linear isolation elements and neglecting the superstructure and base isolation system viscous damping, Equation (6.13) at time t becomes:

$$m_b \ddot{u}_b(t) + (k_b + k_1) u_b(t) - k_1 u_1(t) = -m_b \ddot{u}_g(t). \quad (6.28)$$

The superstructure first floor displacement u_1 can be expressed in terms of u_b as follows:

$$u_1 = u_b + \alpha u_b, \quad (6.29)$$

where the first term is the base isolation system displacement relative to the ground whereas the last term is the superstructure first floor displacement relative to the base isolation system; generally, the latter is very small compared to the former, that is, $\alpha \ll 1$.

Dividing Equation (6.28) by m_b , the dynamic equilibrium equation becomes:

$$\ddot{u}_b(t) + \frac{(k_b - \alpha k_1)}{m_b} u_b(t) = -\ddot{u}_g(t). \quad (6.30)$$

Substituting the central difference expression for the acceleration at time t into Equation (6.30) and solving for $u_b(t + \Delta t)$ gives:

$$u_b(t + \Delta t) = \left[2 - \frac{\Delta t^2}{m_b} (k_b - \alpha k_1) \right] u_b(t) - u_b(t - \Delta t) - \Delta t^2 \ddot{u}_g(t). \quad (6.31)$$

Equation (6.31) can be reformulated into a recursive matrix form as follows:

$$\begin{Bmatrix} u_b(t + \Delta t) \\ u_b(t) \end{Bmatrix} = \mathbf{A} \begin{Bmatrix} u_b(t) \\ u_b(t - \Delta t) \end{Bmatrix} - \mathbf{L} \ddot{u}_g(t), \quad (6.32)$$

with:

$$\mathbf{A} = \begin{bmatrix} 2 - \frac{\Delta t^2}{m_b}(k_b - \alpha k_1) & -1 \\ 1 & 0 \end{bmatrix}, \quad (6.33)$$

$$\mathbf{L} = \begin{Bmatrix} \Delta t^2 \\ 0 \end{Bmatrix}, \quad (6.34)$$

where \mathbf{A} and \mathbf{L} are the integration approximation and load operators, respectively (Bathe 1996).

The stability of an integration method is determined by examining the behavior of the numerical solution for arbitrary initial conditions, thus it is possible to consider the integration of Equation (6.32) when load is absent, that is, $\ddot{u}_g(t) = 0$.

In this work, the numerical stability is analyzed by using the spectral decomposition of the matrix \mathbf{A} . Since the stability of an integration method depends only on the eigenvalues of the approximation operator \mathbf{A} , the following eigenvalue problem has to be solved:

$$\begin{bmatrix} 2 - \frac{\Delta t^2}{m_b}(k_b - \alpha k_1) & -1 \\ 1 & 0 \end{bmatrix} \mathbf{v} = \lambda \mathbf{v}. \quad (6.35)$$

The eigenvalues of the matrix \mathbf{A} are the roots of the following characteristic polynomial:

$$p(\lambda) = \det(\mathbf{A} - \lambda \mathbf{I}), \quad (6.36)$$

which, in this case, is defined as:

$$p(\lambda) = \left[2 - \frac{\Delta t^2}{m_b}(k_b - \alpha k_1) - \lambda \right] (-\lambda) + 1. \quad (6.37)$$

Thus, the two eigenvalues of \mathbf{A} are:

$$\lambda_1 = \left[1 - \frac{\Delta t^2}{2m_b}(k_b - \alpha k_1) \right] + \sqrt{\frac{1}{4} \left[2 - \frac{\Delta t^2}{m_b}(k_b - \alpha k_1) \right]^2 - 1}, \quad (6.38)$$

$$\lambda_2 = \left[1 - \frac{\Delta t^2}{2m_b}(k_b - \alpha k_1) \right] - \sqrt{\frac{1}{4} \left[2 - \frac{\Delta t^2}{m_b}(k_b - \alpha k_1) \right]^2 - 1}. \quad (6.39)$$

For stability, the absolute values of λ_1 and λ_2 have to be smaller than or equal to 1, that is, the spectral radius $\rho(\mathbf{A})$ of the approximation operator \mathbf{A} , defined as $\rho(\mathbf{A}) = \max_{i=1,2} |\lambda_i|$, must satisfy the condition $\rho(\mathbf{A}) \leq 1$. It follows from this condition that the critical time step Δt_{cr} is given by:

$$\Delta t_{cr} = \frac{T}{\pi} = 2 \sqrt{\frac{m_b}{k_b - \alpha k_1}}. \quad (6.40)$$

The same time step stability limit is also applicable when the viscous damping is not neglected (Bathe 1996).

It is important to observe that the highest horizontal stiffness of each seismic isolator has to be used in order to evaluate Δt_{cr} and that α can be assumed equal to zero. In practice, since all isolation bearings are modeled by a bilinear model in which the post-yield stiffness is generally smaller than the initial elastic stiffness (Naeim and Kelly 1999), the pre-yield stiffness of each isolator has to be chosen to determine Δt_{cr} .

6.4.2.2 3d Base-Isolated Structures

Considering the 3d discrete structural model of a base-isolated structure, the critical time step Δt_{cr} can be evaluated considering the lower natural period given by the following eigenvalue problem:

$$\mathbf{k}_b^h \boldsymbol{\Phi} = \mathbf{m}_b \boldsymbol{\Phi} \boldsymbol{\Omega}^2, \quad (6.41)$$

where \mathbf{k}_b^h is the stiffness matrix of the base isolation system assembled using the highest horizontal stiffness of each nonlinear element, $\boldsymbol{\Phi}$ is the modal matrix, and $\boldsymbol{\Omega}^2$ the spectral matrix of the eigenvalue problem.

6.4.3 Numerical Applications

In what follows, the PFM and the proposed MEIM are adopted to simulate the seismic response of two 3d base-isolated structures, namely, Structure A and Structure B, subjected to a bidirectional earthquake excitation, that is, the Northridge earthquake of January 17, 1994, for Structure A, and the Loma Prieta earthquake of October 17, 1989, for Structure B. For each structure, two types of base isolation systems are considered, namely, Lead Rubber Bearing System (LRBS) and Friction Pendulum Bearing System (FPBS).

6.4.3.1 Analysis of Base-Isolated Structures with LRBS

6.4.3.1.1 Analyzed 3d Base-Isolated Structure A

The superstructure is a two-story reinforced concrete structure with vertical geometric irregularity, plan dimensions 10 m x 8 m, and story height $h = 3.5$ m. The weight of the superstructure is 1802.9 kN and the first three natural periods are 0.15 s, 0.14 s, and 0.10 s, respectively. Each superstructure diaphragm mass includes the contributions of the dead load and live load on the floor diaphragm and the contributions of structural elements and nonstructural elements between floors.

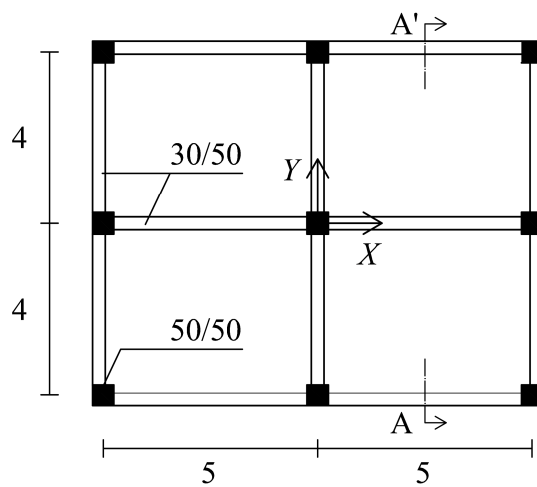
The base isolation system, having a total weight of 914.9 kN, consists of an orthogonal mesh of foundation beams having rectangular cross section with dimensions 30 cm x 50 cm, and 9 identical Lead Rubber Bearings (LRBs), positioned centrally under all columns.

The typical floor plan, the base floor plan, and a section of the analyzed 3d base-isolated structure are shown in Figure 6.1.

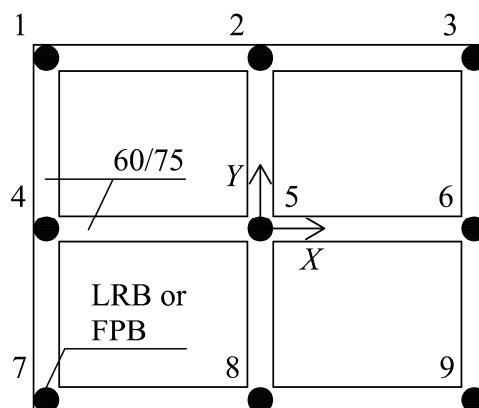
As a result of the kinematic constraints assumed in Chapter 2, the total number of dofs, defined relative to the ground, is equal to 9. Figure 6.2 shows the 3d discrete structural model of the analyzed base-isolated structure.

The base isolation system has been designed in order to provide an effective isolation period $T_{eff} = 2.25$ s and an effective viscous damping $\nu_{eff} = 0.15$ at the design displacement $d_d = 0.50$ m. Thus, each elastomeric bearing has a yield force $F_y = 31422$ N, a yield displacement $y = 0.017$ m and a post-yield to pre-yield stiffness ratio $\alpha = 0.10$.

(a)



(b)



(c)

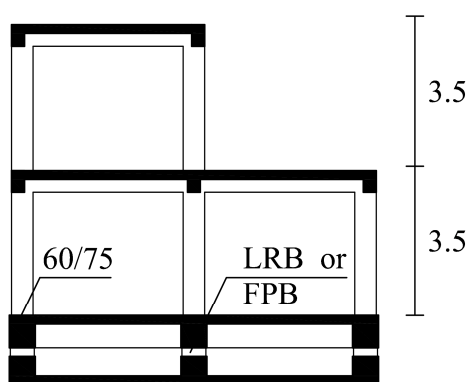


Figure 6.1. Structure A: (a) typical floor plan; (b) base floor plan; (c) section A-A'.

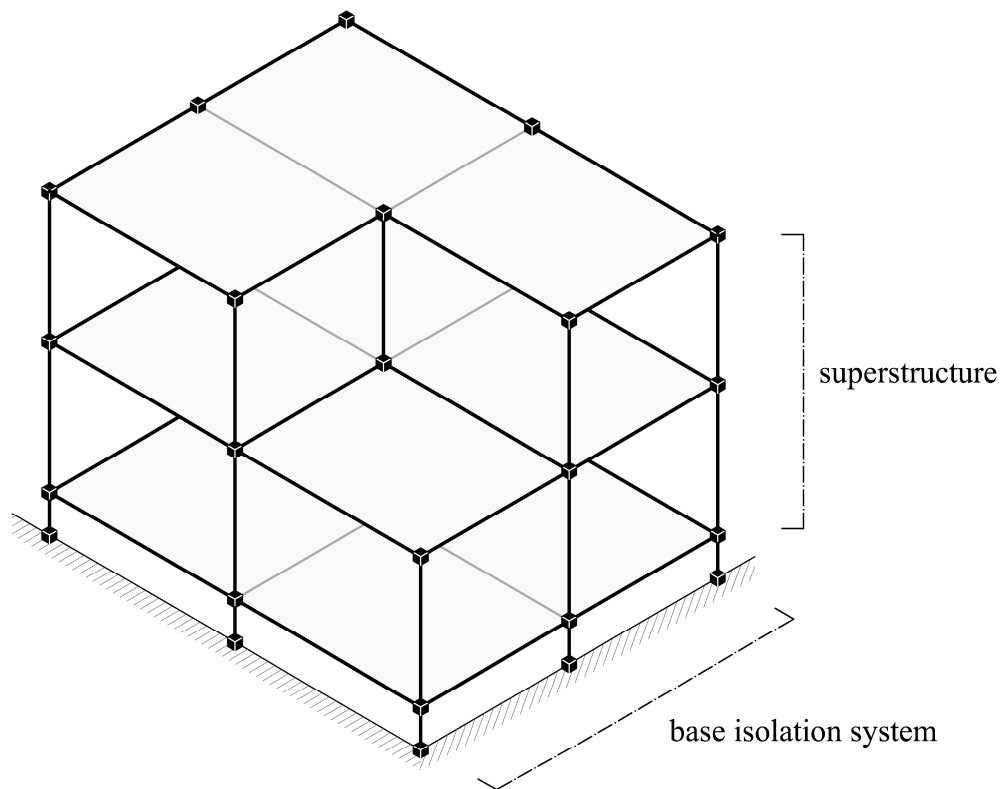


Figure 6.2. 3d discrete structural model of Structure A.

6.4.3.1.2 Analyzed 3d Base-Isolated Structure B

The superstructure is a four-story reinforced concrete structure with plan dimensions 19 m x 11 m, and story height $h = 3.5$ m. The weight of the superstructure is 9921.24 kN and the first three natural periods are 0.33 s, 0.33 s, and 0.26 s, respectively. Each superstructure diaphragm mass includes the contributions of the dead load and live load on the floor diaphragm and the contributions of structural elements and nonstructural elements between floors.

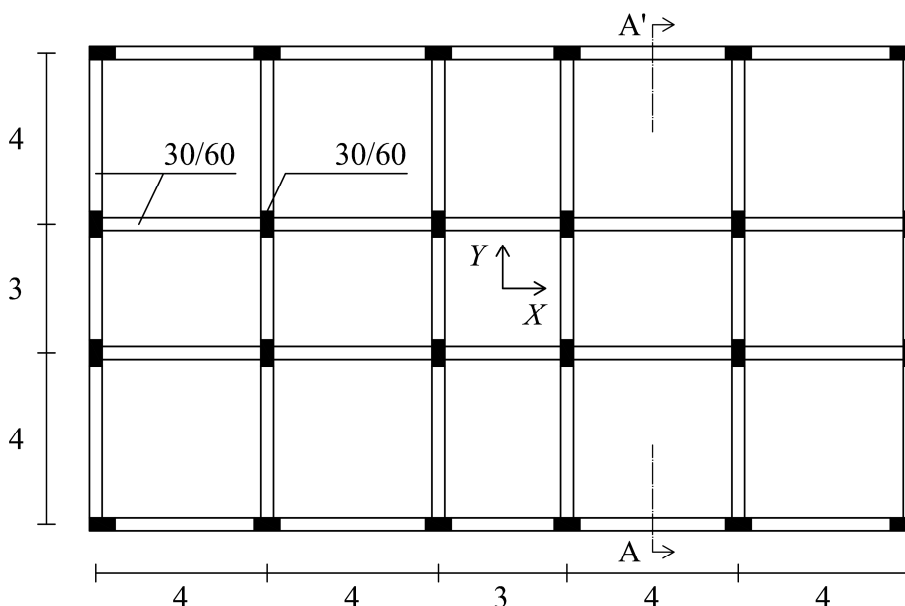
The base isolation system, having a total weight of 3006.44 kN, consists of an orthogonal mesh of foundation beams having rectangular cross section with dimensions 60 cm x 75 cm, and 24 identical Lead Rubber Bearings (LRBs), positioned centrally under all columns.

The typical floor plan, the base floor plan, and a section of the analyzed 3d base-isolated structure are shown in Figure 6.3.

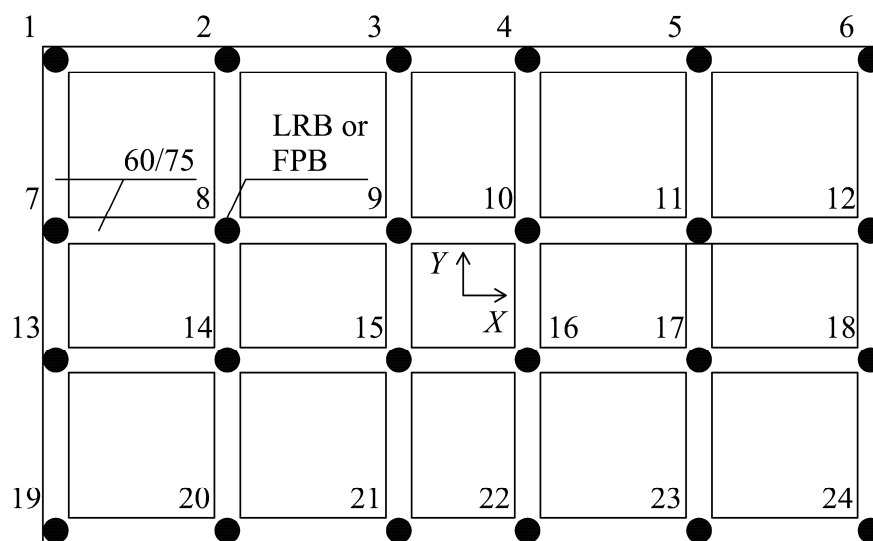
As a result of the kinematic constraints assumed in Chapter 2, the total number of dofs, defined relative to the ground, is equal to 15. Figure 6.4 shows the 3d discrete structural model of the analyzed base-isolated structure.

The base isolation system has been designed in order to provide an effective isolation period $T_{eff} = 2.50$ s and an effective viscous damping $\nu_{eff} = 0.15$ at the design displacement $d_d = 0.50$ m. Thus, each elastomeric bearing has a yield force $F_y = 45400.3$ N, a yield displacement $y = 0.017$ m, and a post-yield to pre-yield stiffness ratio $\alpha = 0.10$.

(a)



(b)



(c)

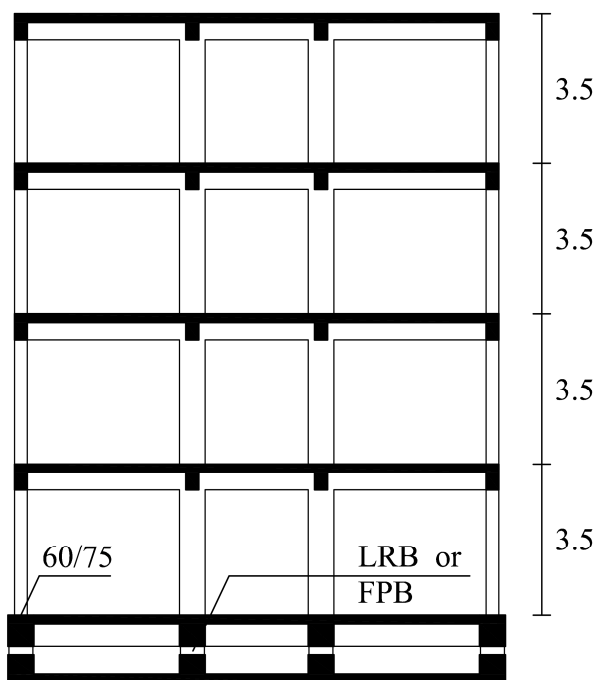


Figure 6.3. Structure B: (a) typical floor plan; (b) base floor plan; (c) section A-A'.

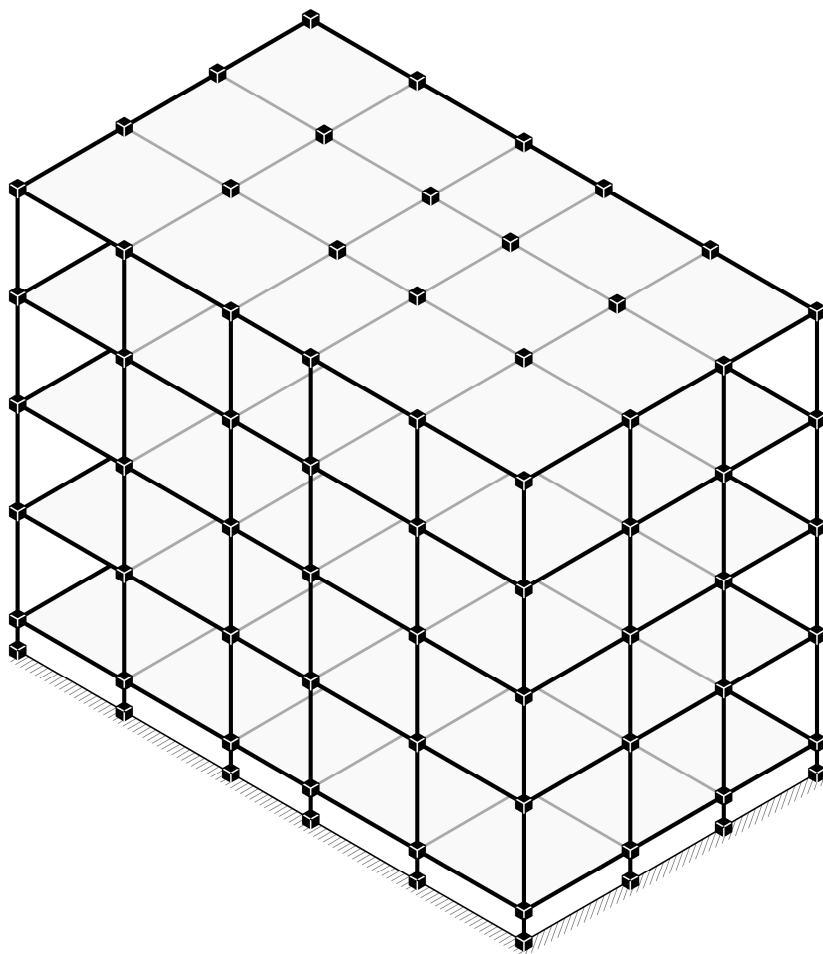


Figure 6.4. 3d discrete structural model of Structure B.

6.4.3.1.3 Model Adopted for Lead Rubber Bearings

The dynamic behavior of each LRB is simulated by using a mathematical model, introduced by Nagarajaiah et al. (1991) and described in Chapter 4, capable of predicting the biaxial behavior of elastomeric bearings. According to this model, the LRB nonlinear restoring forces along the orthogonal directions x and y are described by the following equations:

$$f_x = \alpha \frac{F_y}{y} u_x + (1 - \alpha) \frac{F_y}{y} z_x, \quad (6.42)$$

$$f_y = \alpha \frac{F_y}{y} u_y + (1 - \alpha) \frac{F_y}{y} z_y, \quad (6.43)$$

in which α is the post-yield to the pre-yield stiffness ratio, F_y is the yield force, y is the yield displacement, u_x and u_y represent the displacements of the isolation device in the x and y directions, respectively. The functions z_x and z_y , having the unit of displacement and accounting for the direction and biaxial interaction of hysteresis forces, are obtained solving the following coupled first order nonlinear ordinary differential equations proposed by Park et al. (1986):

$$\dot{z}_x = A \dot{u}_x - \beta |\dot{u}_x z_x| z_x - \gamma \dot{u}_x z_x^2 - \beta |\dot{u}_y z_y| z_x - \gamma \dot{u}_y z_x z_y, \quad (6.44)$$

$$\dot{z}_y = A \dot{u}_y - \beta |\dot{u}_y z_y| z_y - \gamma \dot{u}_y z_y^2 - \beta |\dot{u}_x z_x| z_y - \gamma \dot{u}_x z_x z_y, \quad (6.45)$$

in which A , β , and γ are parameters that control the shape of the hysteresis loop, \dot{u}_x and \dot{u}_y are the velocities that occur at the isolation device in x and y directions, respectively.

In the numerical applications presented in this work, the following values are adopted for the model parameters:

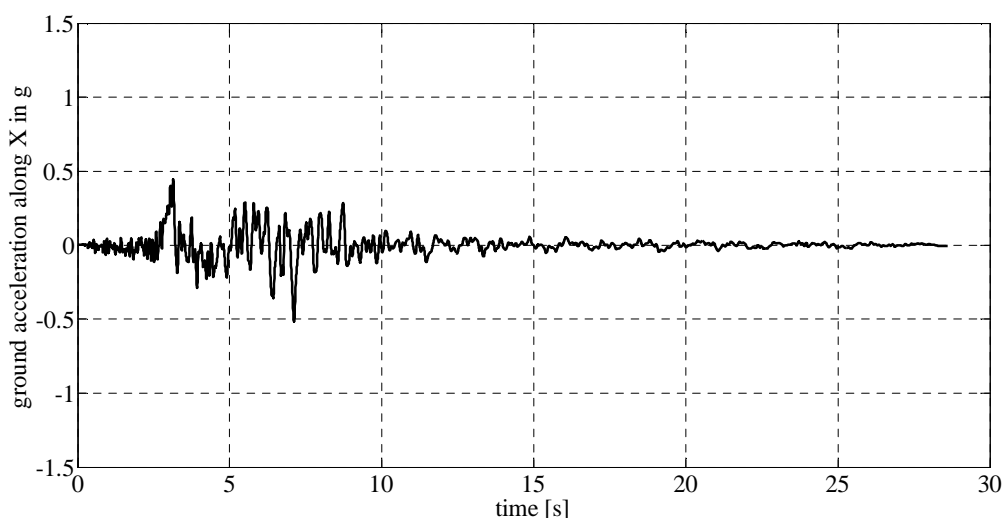
$$A = 1, \quad \beta = \frac{0.5}{y^2}, \quad \text{and} \quad \gamma = \frac{0.5}{y^2}.$$

The unconditionally stable semi-implicit Runge-Kutta method (Rosenbrock 1963) is employed to solve the differential equations governing the behavior of each nonlinear isolation element with a number of steps equal to 50.

6.4.3.1.4 Numerical Results for Structure A

Bidirectional earthquake excitation is imposed with component SN and SP of the 1994 Northridge motion applied along directions X and Y of the global coordinate system, respectively. The two components of the horizontal ground acceleration record, having time step equal to 0.005 s, are shown in Figure 6.5. It is important to note that normally 200 points per second are used to define accurately an acceleration record, and that the time step of the ground motion can be reduced through linear interpolation because it is generally assumed that the acceleration function is linear within each time increment (Wilson 2002).

(a)



(b)

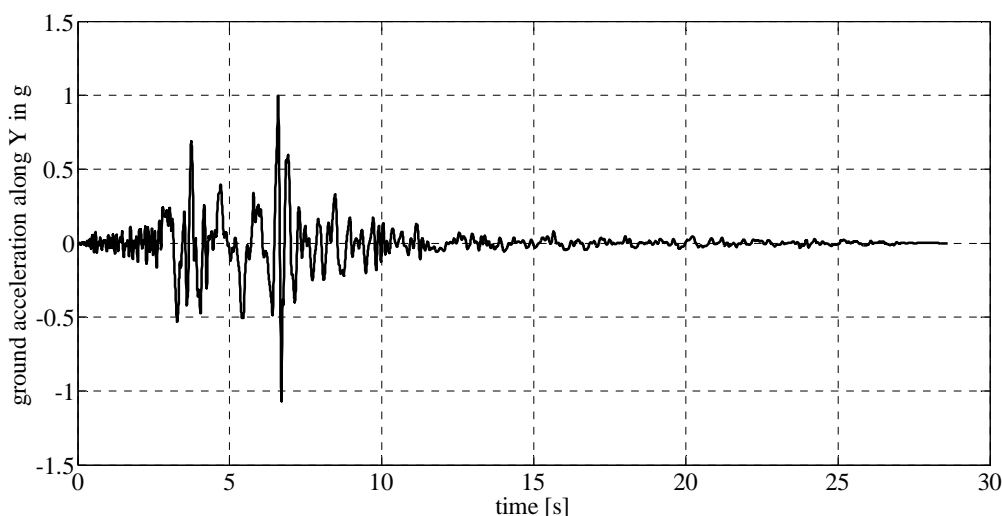


Figure 6.5. (a) SN and (b) SP component of horizontal ground acceleration recorded at the Jensen Filter Plant station during the Northridge earthquake of January 17, 1994.

Table 6.1 gives the Nonlinear Time History Analyses (NLTHAs) results obtained using the proposed MEIM and the PFM, both implemented on the same computer (Intel® Core™ i7-4700MQ processor, CPU at 2.40 GHz with 16 GB of RAM) by using the computer program Matlab and verified using SAP2000. In the PFM the adopted convergence tolerance value is equal to 10^{-8} .

Table 6.1. NLTHAs results with $\Delta t = 0.005$ s | Structure A with LRBS.

	<i>tct</i> [s]	<i>tctp</i> [%]	$u_x^{(MC_b)}$ [m]		$u_y^{(MC_b)}$ [m]		$\ddot{u}_x^{(MC_2)}$ [g]		$\ddot{u}_y^{(MC_2)}$ [g]	
			max	min	max	min	max	min	max	min
MEIM	45	18.44	0.3332	-0.3327	0.2286	-0.1787	0.5293	-0.4586	1.0986	-1.0783
PFM	244	-	0.3330	-0.3327	0.2287	-0.1787	0.5456	-0.4624	1.0874	-1.0399

The comparison of the maximum and minimum values of the base isolation system mass center (MC_b) displacements and superstructure second story mass center (MC_2) accelerations (relative to the ground) in x and y directions, obtained using the MEIM and PFM, reveals that the proposed method provides numerical results that are close enough to those obtained adopting the PFM.

As regards the stability of the MEIM, the critical time step Δt_{cr} , evaluated using Equation (6.40) and considering the lowest natural period given by the eigenvalue problem in Equation (6.41), is equal to 0.32 s. It is evident that, in this case, being the critical time step larger than the imposed ground acceleration time step, there are no stability problems.

As far as the computational efficiency is concerned, the total computational time, *tct*, required by the MEIM is significantly reduced in comparison to the PFM. It must be noted that the comparisons using the *tct* are meaningful only qualitatively because it depends on the CPU speed, memory capability and background processes of the computer used to obtain the previous results. To this end, in order to normalize the computational time results, Table 6.1 also shows the percentage of the MEIM *tct* evaluated with respect to the PFM *tct* as follows:

$$\text{MEIM } tctp [\%] = \frac{\text{MEIM } tct}{\text{PFM } tct} \cdot 100.$$

In addition, according to the numerical results listed in Table 6.2, the proposed MEIM, performed with a smaller time step, that is, $\Delta t = 0.001$ s, which allows one to minimize the error in Equations (6.20) and (6.27), requires less computational effort than the PFM even if the latter is performed using the larger time step, that is, $\Delta t = 0.005$ s. Indeed, the MEIM

$tctp$, referred to the PFM tct evaluated adopting $\Delta t = 0.005$ s, is equal to 90.16 %.

Table 6.2. NLTHAs results with $\Delta t = 0.001$ s | Structure A with LRBS.

	tct [s]	$tctp$ [%]	$u_x^{(MC_b)}$ [m]		$u_y^{(MC_b)}$ [m]		$\ddot{u}_x^{(MC_2)}$ [g]		$\ddot{u}_y^{(MC_2)}$ [g]	
			max	min	max	min	max	min	max	min
MEIM	220	26.79	0.3341	-0.3333	0.2292	-0.1794	0.5415	-0.4705	1.1285	-1.0728
PFM	821	-	0.3341	-0.3333	0.2292	-0.1794	0.5418	-0.4701	1.1274	-1.0743

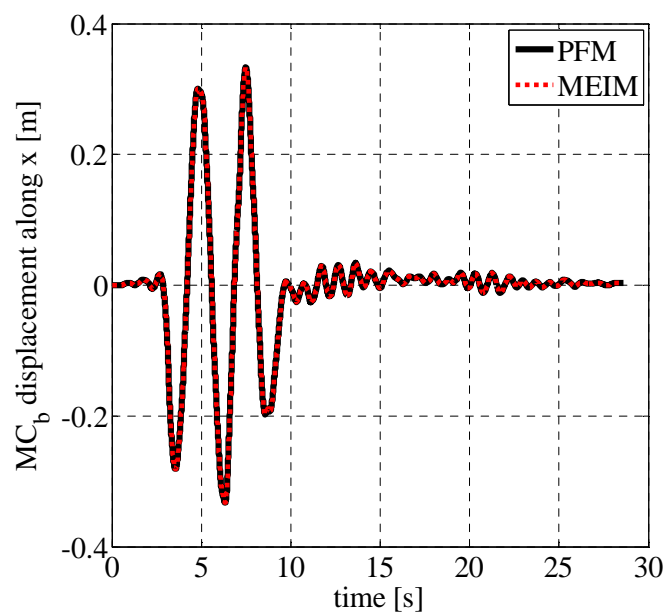
It can therefore be concluded that even when a time step smaller than the one used to define the ground acceleration accurately has to be adopted because of stability requirements, as in the case of base isolation systems having isolators with very high initial stiffness, such as sliding bearings, or very high stiffness at large displacements, such as high damping rubber bearings, the proposed method preserves its computational efficiency with respect to the PFM.

Figures 6.6, 6.7, and 6.8 illustrate, respectively, the displacement, velocity and acceleration time histories of the base isolation system mass center, whereas Figures 6.9, 6.10, and 6.11 show, respectively, the displacement, velocity and acceleration time histories of the superstructure second story mass center (relative to the ground).

In addition, Figures 6.12 and 6.13 illustrate, respectively, the force-displacement hysteresis loops displayed by Isolator 1 and Isolator 5, illustrated in Figure 6.1b.

It is evident the good agreement between responses computed using the proposed MEIM and the PFM.

(a)



(b)

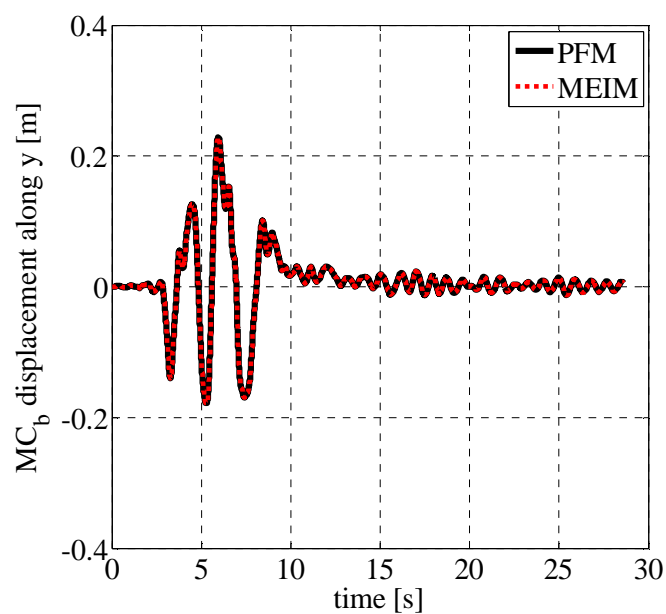
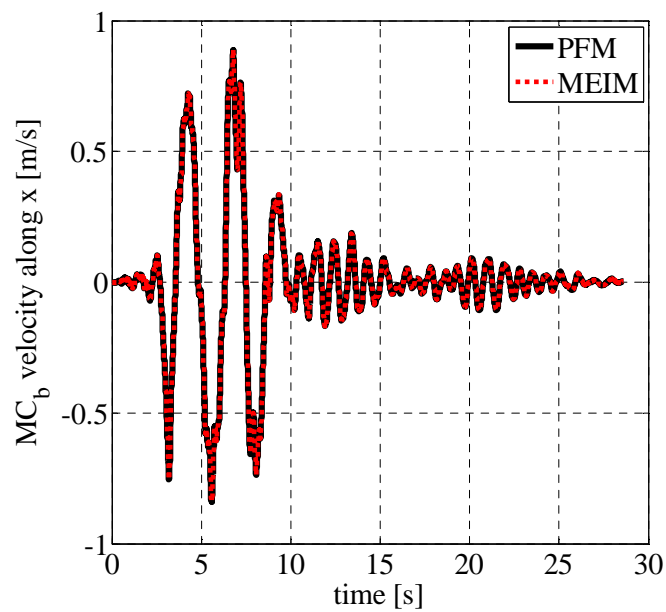


Figure 6.6. Displacement time history of the base isolation system mass center in (a) x and (b) y directions (Structure A with LRBS).

(a)



(b)

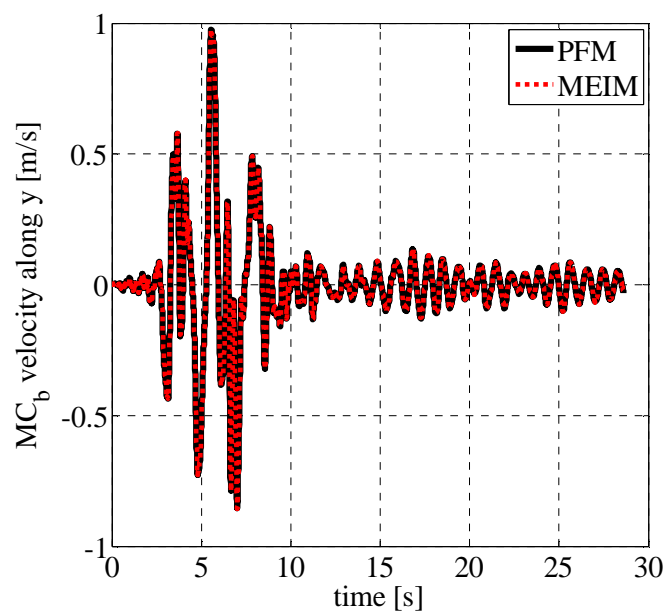
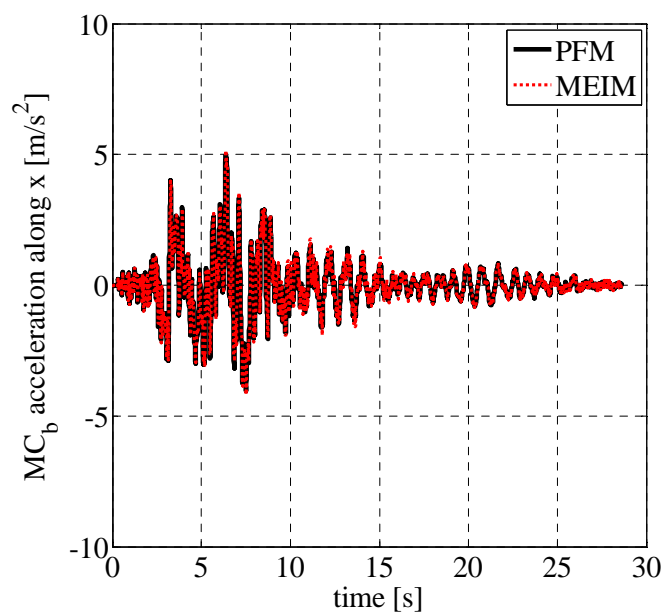


Figure 6.7. Velocity time history of the base isolation system mass center in (a) x and (b) y directions (Structure A with LRBS).

(a)



(b)

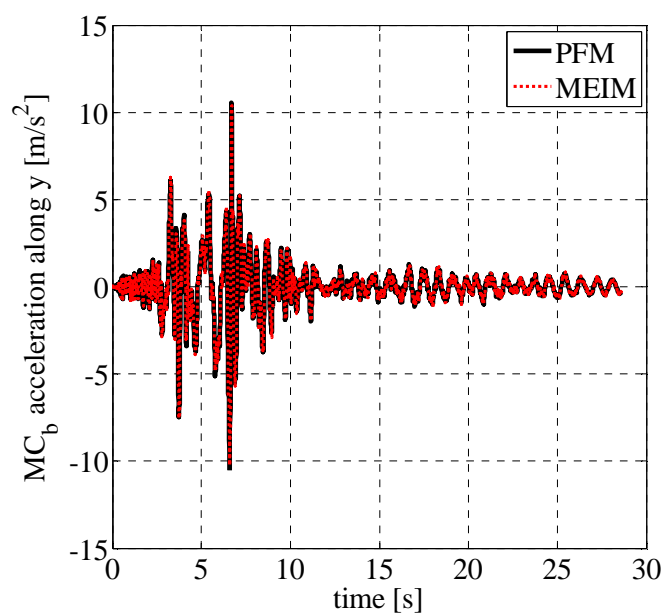
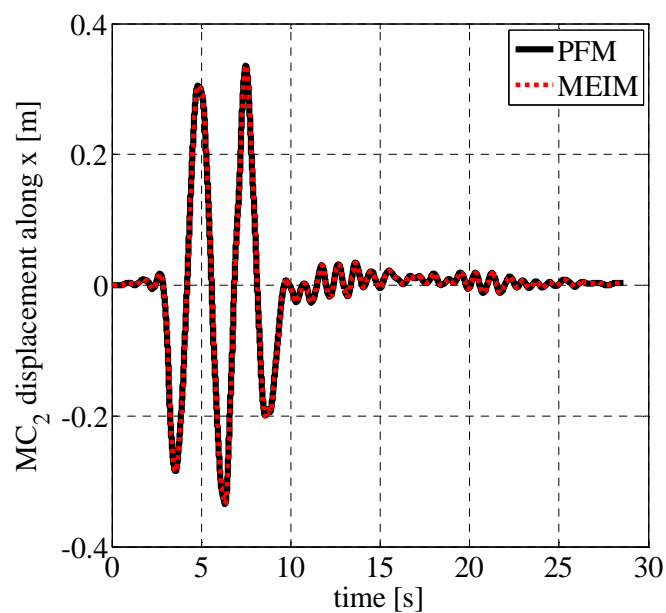


Figure 6.8. Acceleration time history of the base isolation system mass center in (a) x and (b) y directions (Structure A with LRBS).

(a)



(b)

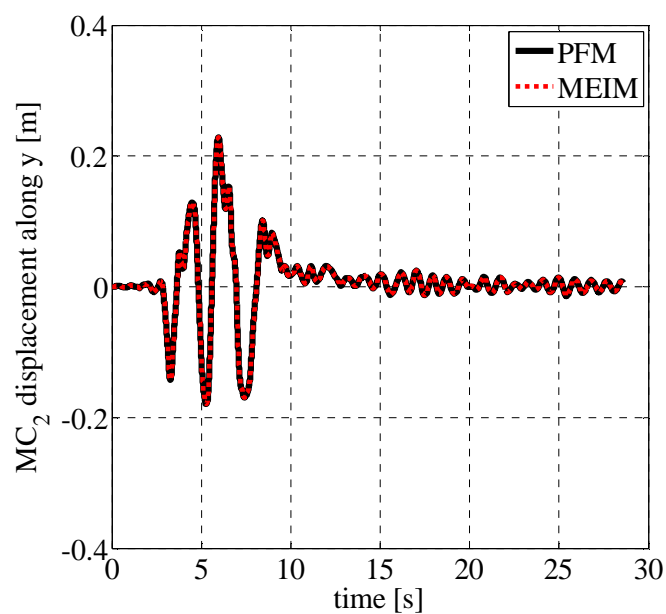
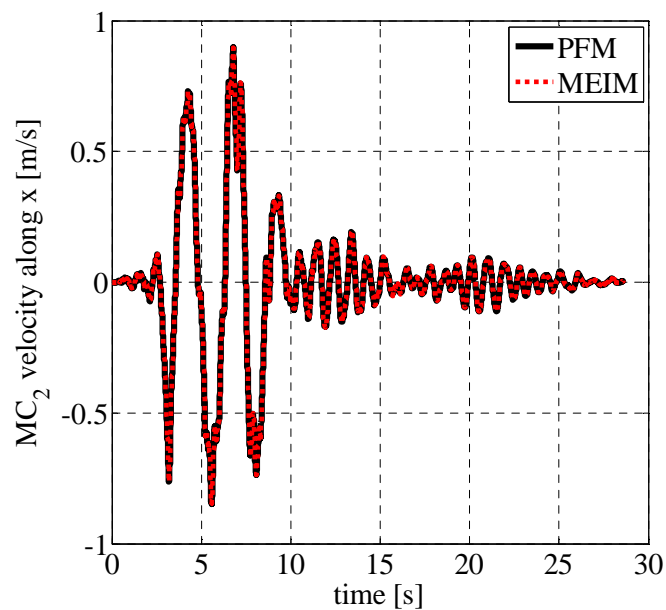


Figure 6.9. Displacement time history of the superstructure second story mass center in (a) x and (b) y directions (Structure A with LRBS).

(a)



(b)

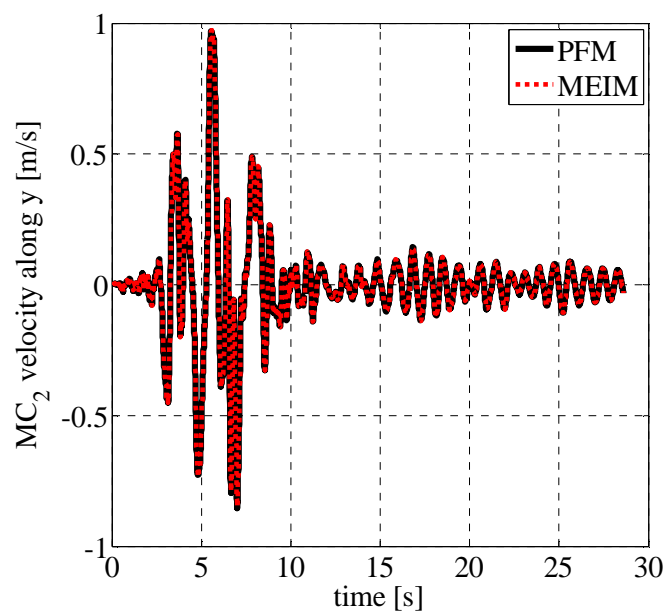
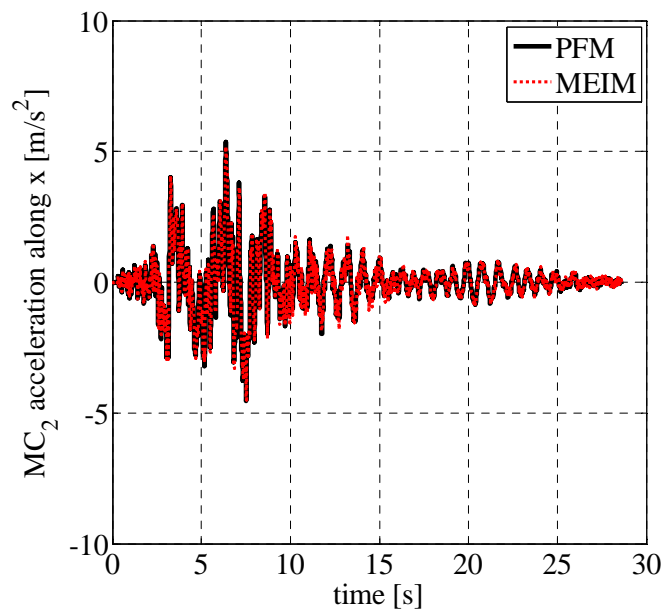


Figure 6.10. Velocity time history of the superstructure second story mass center in (a) x and (b) y directions (Structure A with LRBS).

(a)



(b)

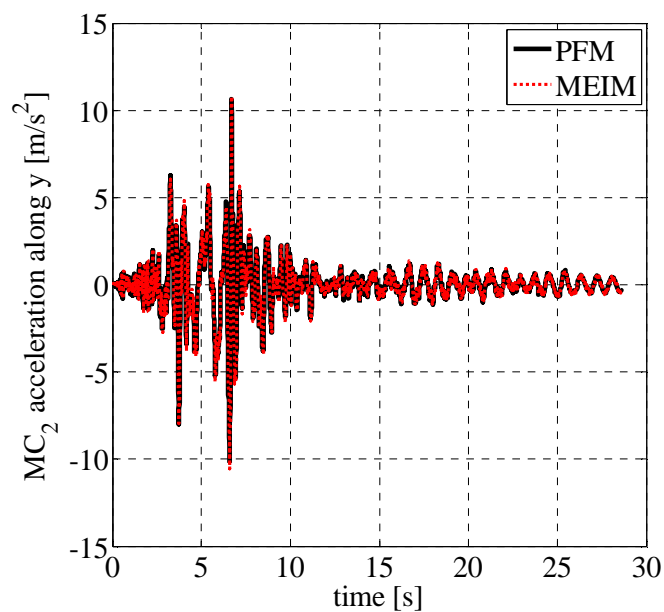
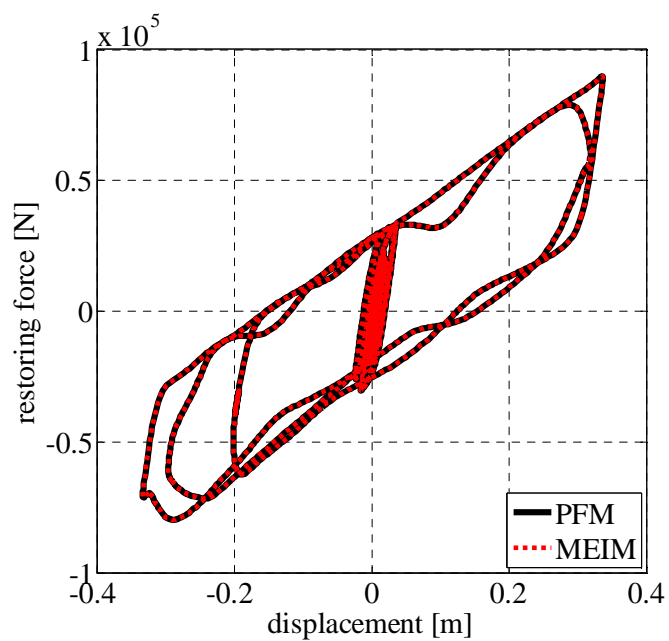


Figure 6.11. Acceleration time history of the superstructure second story mass center in (a) x and (b) y directions (Structure A with LRBS).

(a)



(b)

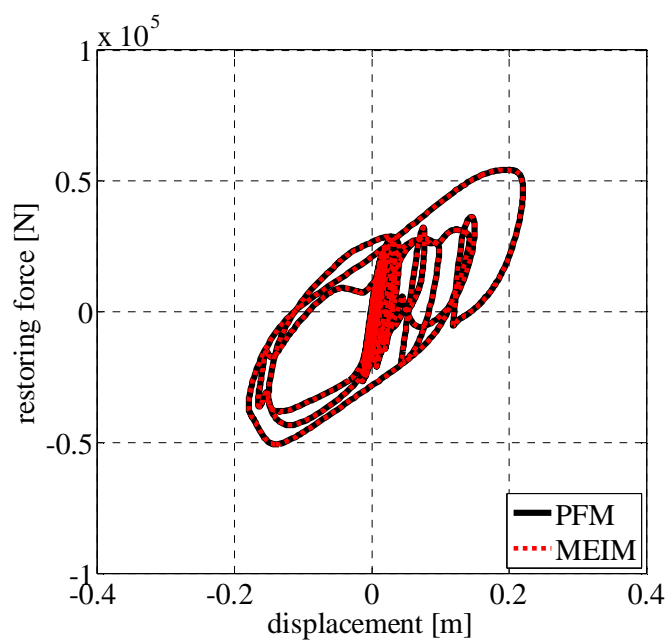
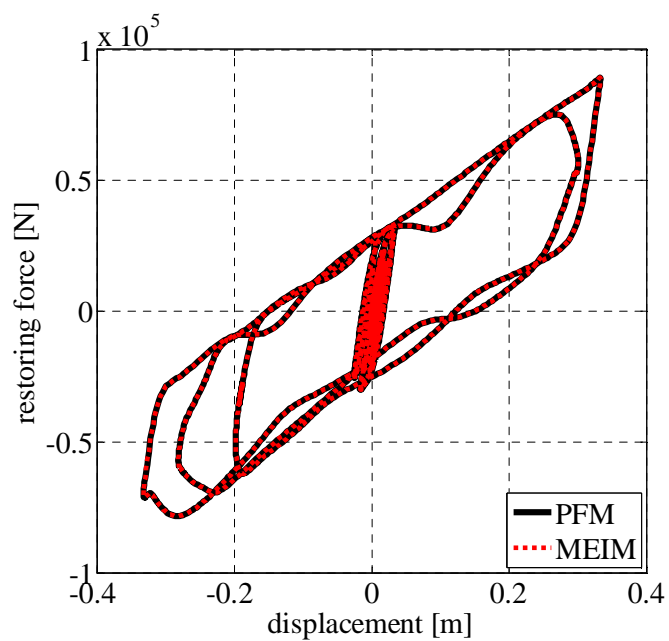


Figure 6.12. Hysteresis loop displayed by Isolator 1 in (a) x and (b) y directions (Structure A with LRBS).

(a)



(b)

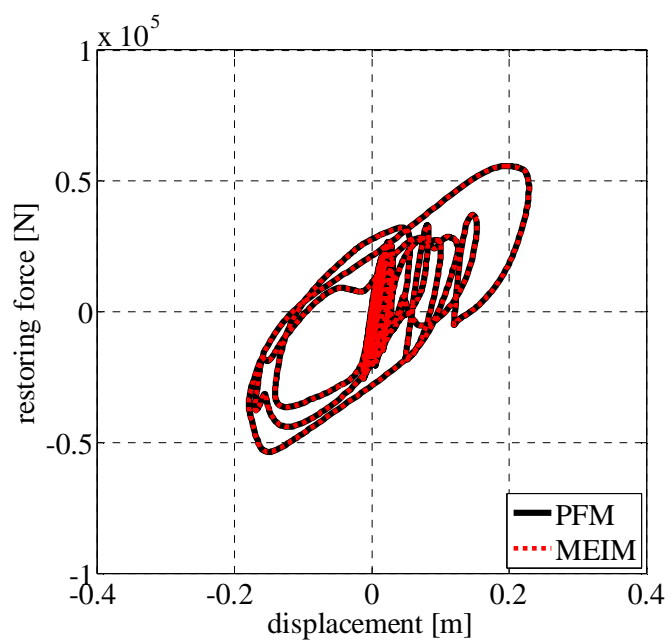
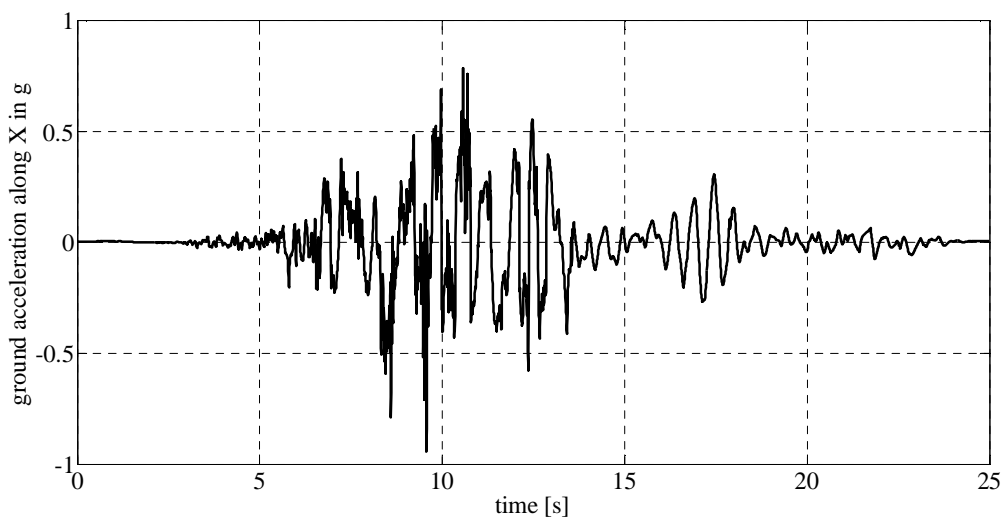


Figure 6.13. Hysteresis loop displayed by Isolator 5 in (a) x and (b) y directions (Structure A with LRBS).

6.4.3.1.5 Numerical Results for Structure B

Bidirectional earthquake excitation is imposed with component SN and SP of the 1989 Loma Prieta motion applied along directions X and Y of the global coordinate system, respectively. The two components of the horizontal ground acceleration record, having time step equal to 0.005 s, are shown in Figure 6.14. It is important to note that normally 200 points per second are used to define accurately an acceleration record, and that the time step of the ground motion can be reduced through linear interpolation because it is generally assumed that the acceleration function is linear within each time increment (Wilson 2002).

(a)



(b)

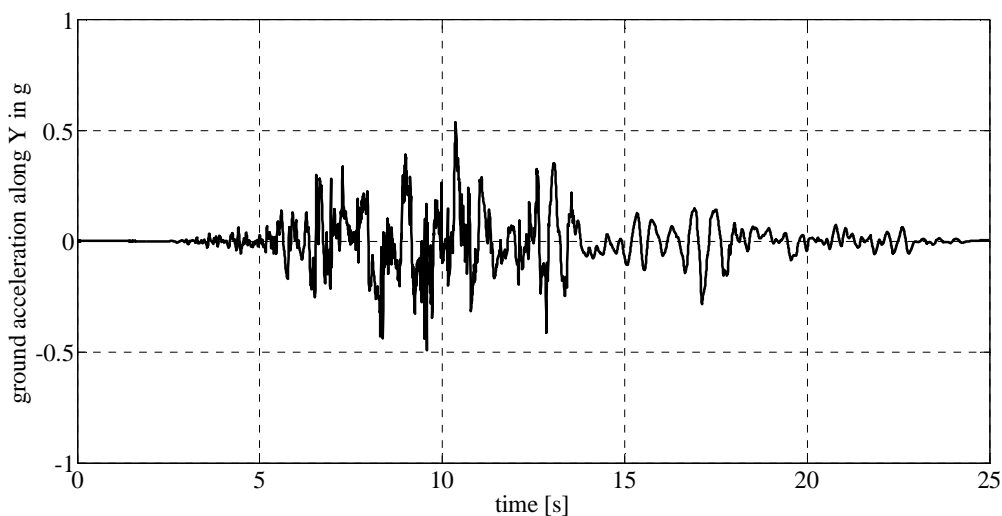


Figure 6.14. (a) SN and (b) SP component of horizontal ground acceleration recorded at the LGPC station during the Loma Prieta earthquake of October 17, 1989.

Table 6.3 gives the Nonlinear Time History Analyses (NLTHAs) results obtained using the proposed MEIM and the PFM, both implemented on the same computer (Intel® Core™ i7-4700MQ processor, CPU at 2.40 GHz with 16 GB of RAM) by using the computer program Matlab and verified using SAP2000. In the PFM the adopted convergence tolerance value is equal to 10^{-8} .

Table 6.3. NLTHAs results with $\Delta t = 0.005$ s | Structure B with LRBS.

	<i>tct</i> [s]	<i>tctp</i> [%]	$u_x^{(MC_b)}$ [m]		$u_y^{(MC_b)}$ [m]		$\ddot{u}_x^{(MC_4)}$ [g]		$\ddot{u}_y^{(MC_4)}$ [g]	
			max	min	max	min	max	min	max	min
MEIM	93.56	17.35	0.5643	-0.3957	0.3053	-0.2105	0.9210	-0.7925	0.4795	-0.5594
PFM	539	-	0.5642	-0.3958	0.3054	-0.2106	0.9266	-0.8062	0.4939	-0.5770

The comparison of the maximum and minimum values of the base isolation system mass center (MC_b) displacements and superstructure fourth story mass center (MC_4) accelerations (relative to the ground) in x and y directions, obtained using the MEIM and PFM, reveals that the proposed method provides numerical results that are close enough to those obtained adopting the PFM.

As regards the stability of the MEIM, the critical time step Δt_{cr} , evaluated using Equation (6.40) and considering the lowest natural period given by the eigenvalue problem in Equation (6.41), is equal to 0.12 s. It is evident that, in this case, being the critical time step larger than the imposed ground acceleration time step, there are no stability problems.

As far as the computational efficiency is concerned, the total computational time, *tct*, required by the MEIM is significantly reduced in comparison to the PFM. It must be noted that the comparisons using the *tct* are meaningful only qualitatively because it depends on the CPU speed, memory capability and background processes of the computer used to obtain the previous results. To this end, in order to normalize the computational time results, Table 6.3 also shows the percentage of the MEIM *tct* evaluated with respect to the PFM *tct* as follows:

$$\text{MEIM } tctp [\%] = \frac{\text{MEIM } tct}{\text{PFM } tct} \cdot 100.$$

In addition, according to the numerical results listed in Table 6.4, the proposed MEIM, performed with a smaller time step, that is, $\Delta t = 0.001$ s, which allows one to minimize the error in Equations (6.20) and (6.27), requires less computational effort than the PFM even if the latter is performed using the larger time step, that is, $\Delta t = 0.005$ s. Indeed, the MEIM

$tctp$, referred to the PFM tct evaluated adopting $\Delta t = 0.005$ s, is equal to 87.94 %.

Table 6.4. NLTHAs results with $\Delta t = 0.001$ s | Structure B with LRBS.

	tct [s]	$tctp$ [%]	$u_x^{(MC_b)}$ [m]		$u_y^{(MC_b)}$ [m]		$\ddot{u}_x^{(MC_4)}$ [g]		$\ddot{u}_y^{(MC_4)}$ [g]	
			max	min	max	min	max	min	max	min
MEIM	474	25.73	0.5651	-0.3957	0.3058	-0.2107	0.9408	-0.8372	0.4953	-0.5621
PFM	1842	-	0.5651	-0.3957	0.3058	-0.2107	0.9406	-0.8371	0.4935	-0.5628

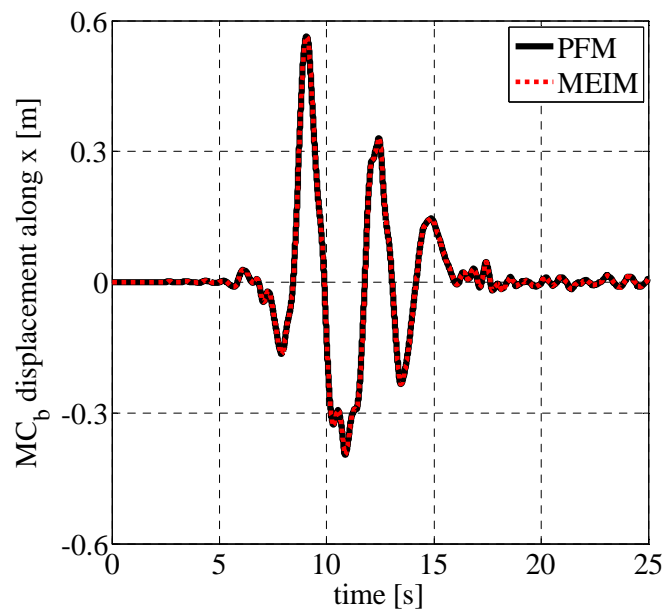
It can therefore be concluded that even when a time step smaller than the one used to define the ground acceleration accurately has to be adopted because of stability requirements, as in the case of base isolation systems having isolators with very high initial stiffness, such as sliding bearings, or very high stiffness at large displacements, such as high damping rubber bearings, the proposed method preserves its computational efficiency with respect to the PFM.

Figures 6.15, 6.16, and 6.17 illustrate, respectively, the displacement, velocity and acceleration time histories of the base isolation system mass center, whereas Figures 6.18, 6.19, and 6.20 show, respectively, the displacement, velocity and acceleration time histories of the superstructure fourth story mass center (relative to the ground).

In addition, Figures 6.21 and 6.22 illustrate, respectively, the force-displacement hysteresis loops displayed by Isolator 1 and Isolator 11, illustrated in Figure 6.3b.

It is evident the good agreement between responses computed using the proposed MEIM and the PFM.

(a)



(b)

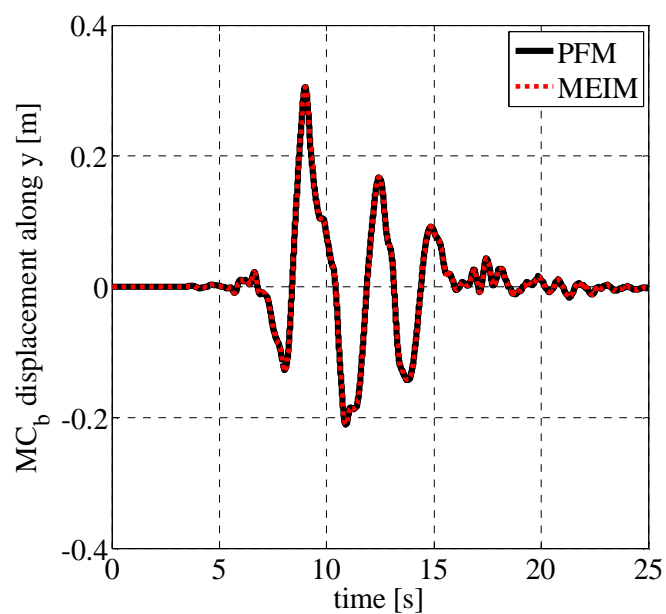
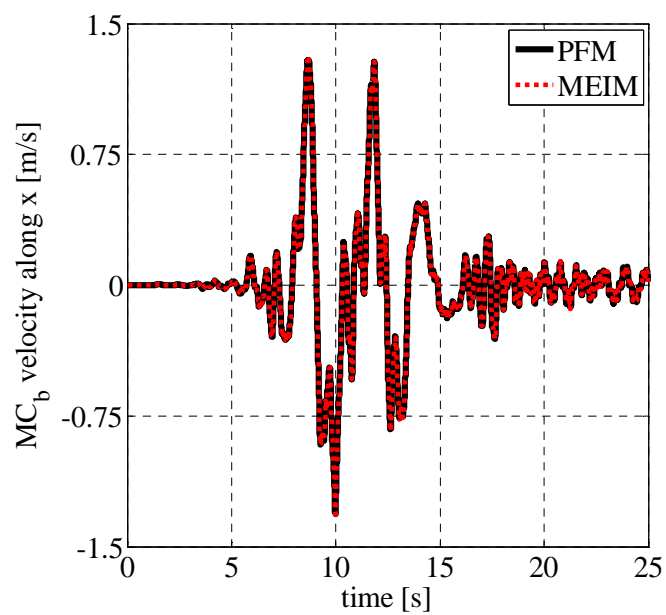


Figure 6.15. Displacement time history of the base isolation system mass center in (a) x and (b) y directions (Structure B with LRBS).

(a)



(b)

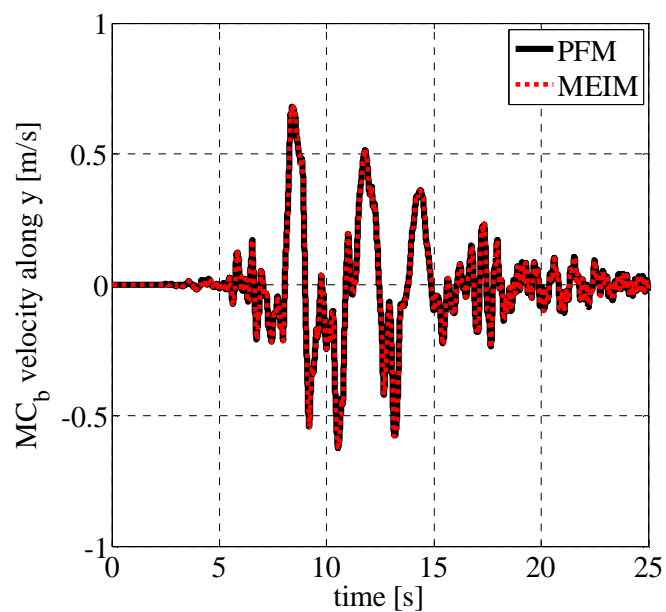
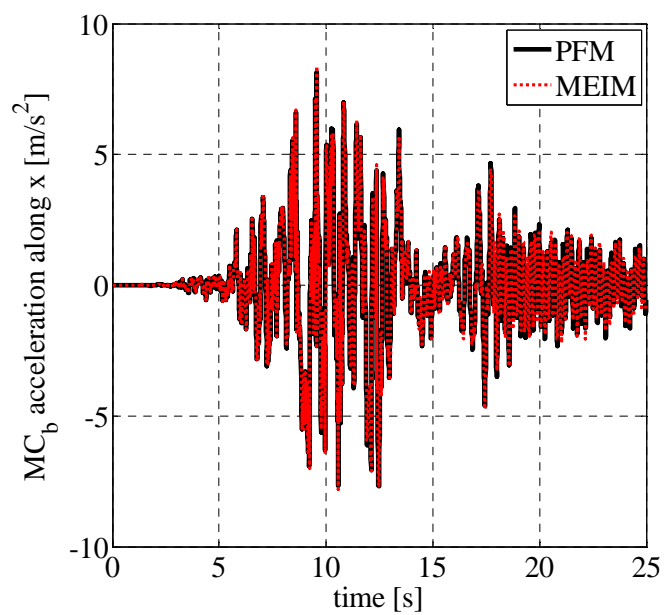


Figure 6.16. Velocity time history of the base isolation system mass center in (a) x and (b) y directions (Structure B with LRBS).

(a)



(b)

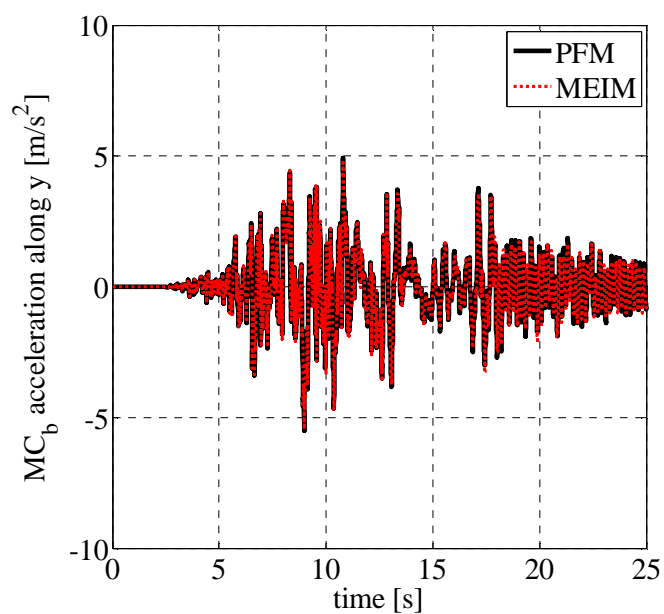
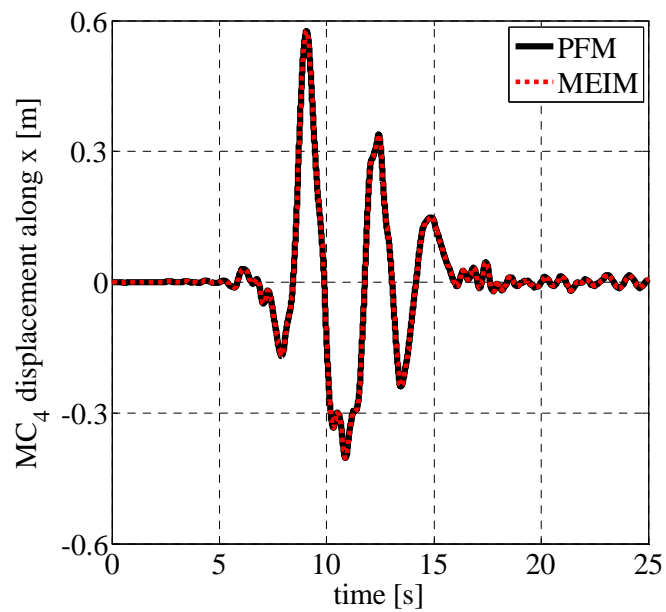


Figure 6.17. Acceleration time history of the base isolation system mass center in (a) x and (b) y directions (Structure B with LRBS).

(a)



(b)

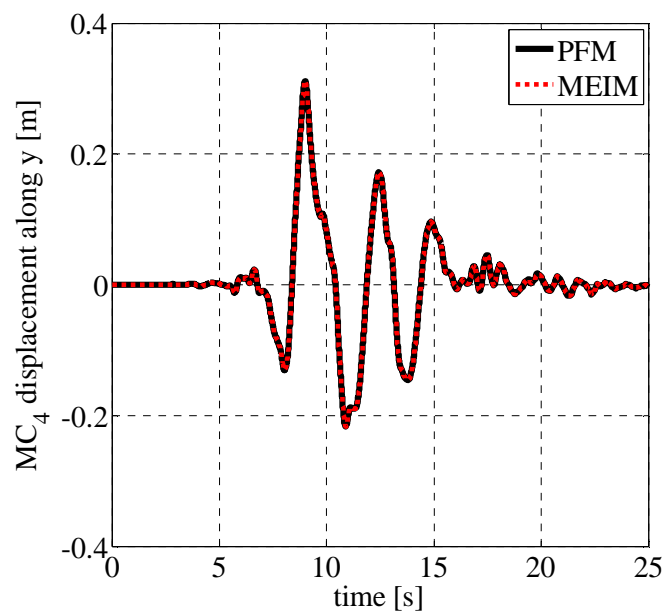
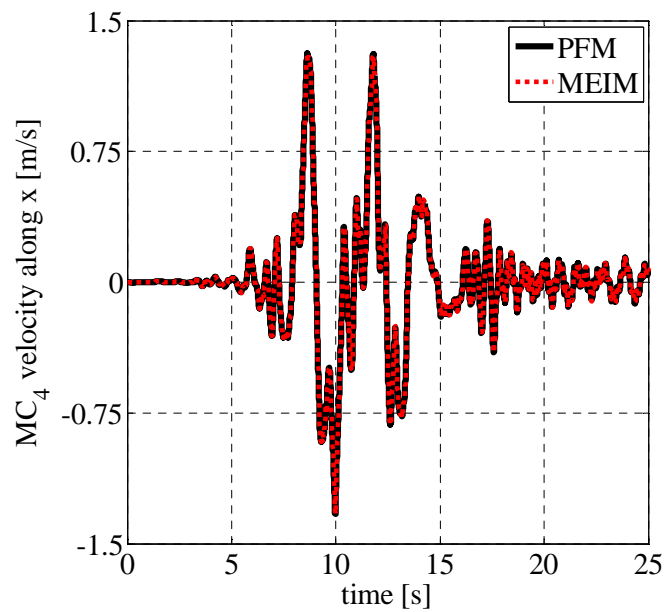


Figure 6.18. Displacement time history of the superstructure fourth story mass center in (a) x and (b) y directions (Structure B with LRBS).

(a)



(b)

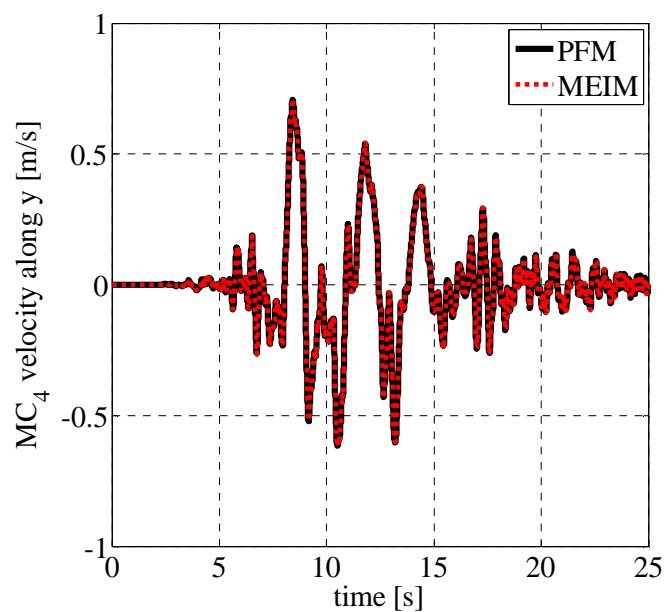
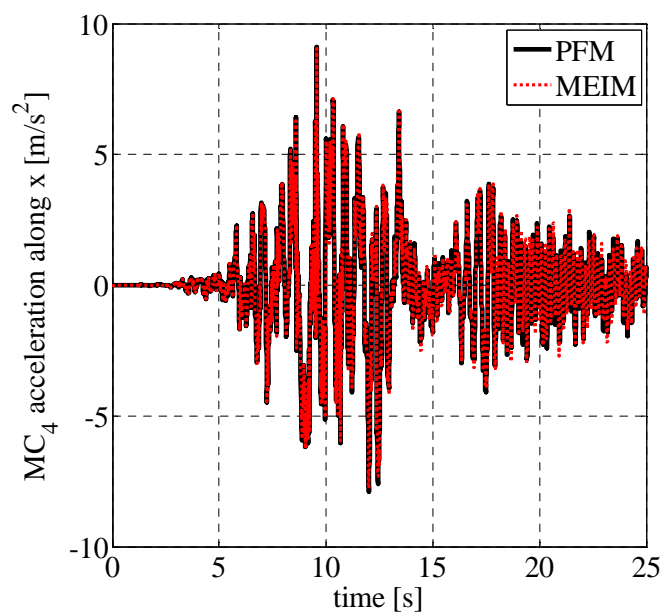


Figure 6.19. Velocity time history of the superstructure fourth story mass center in (a) x and (b) y directions (Structure B with LRBS).

(a)



(b)

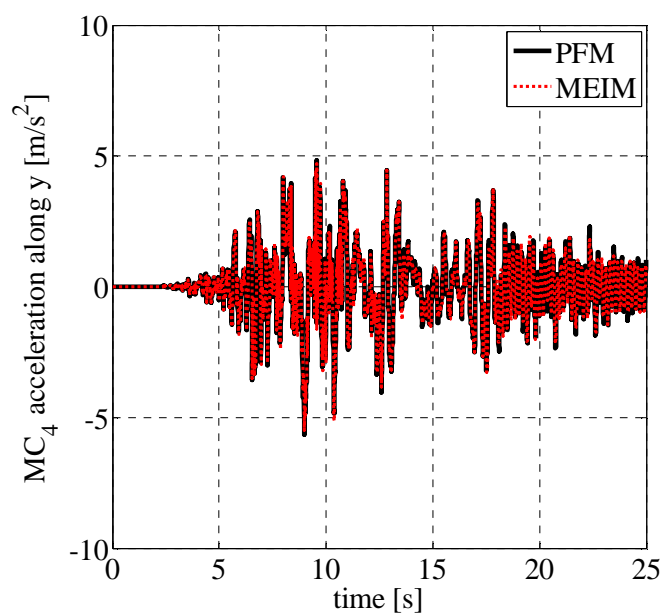
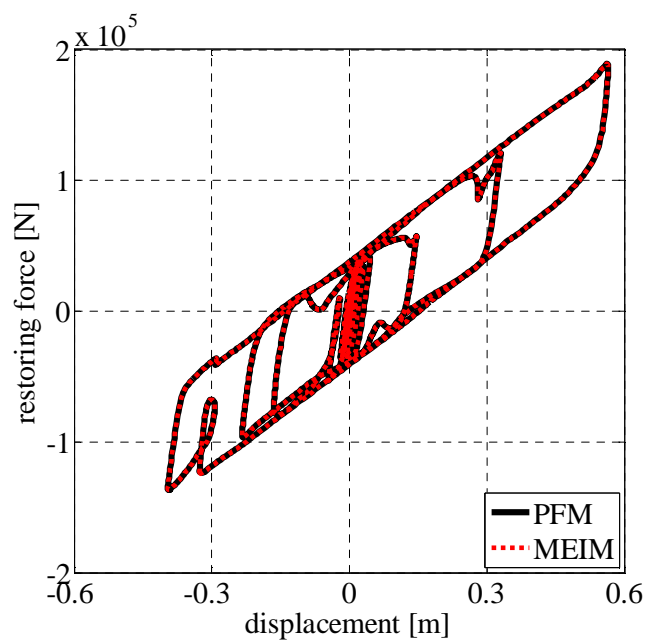


Figure 6.20. Acceleration time history of the superstructure fourth story mass center in (a) x and (b) y directions (Structure B with LRBS).

(a)



(b)

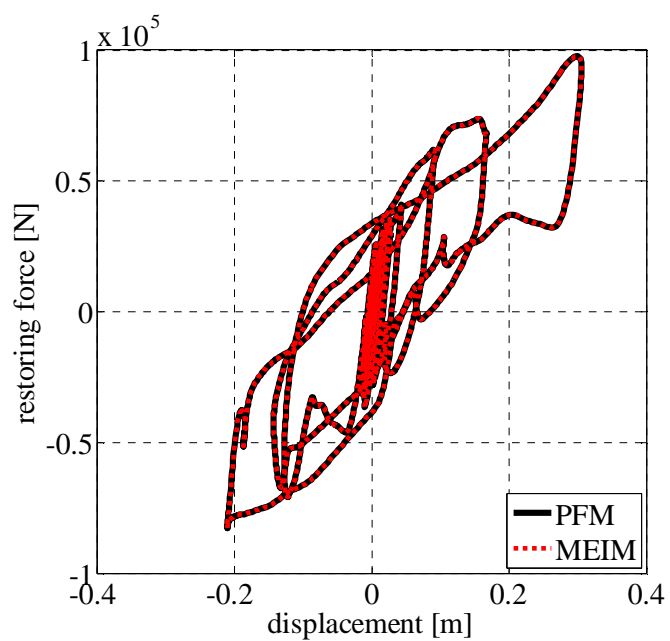
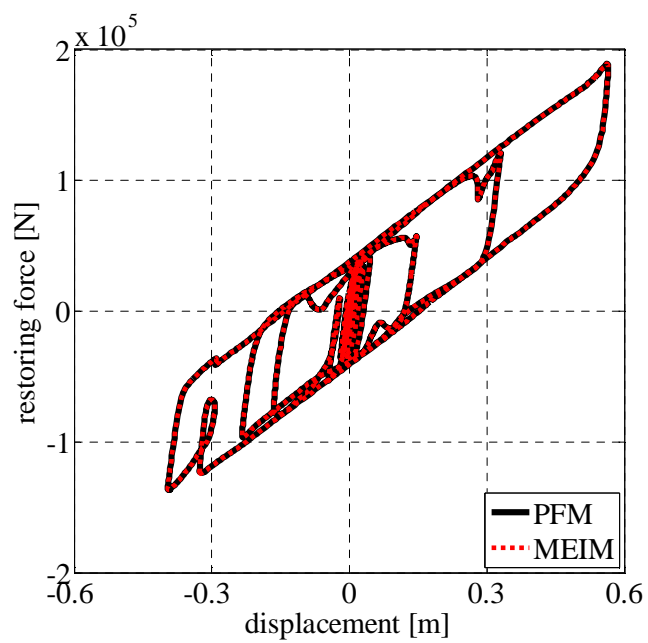


Figure 6.21. Hysteresis loop displayed by Isolator 1 in (a) x and (b) y directions (Structure B with LRBS).

(a)



(b)

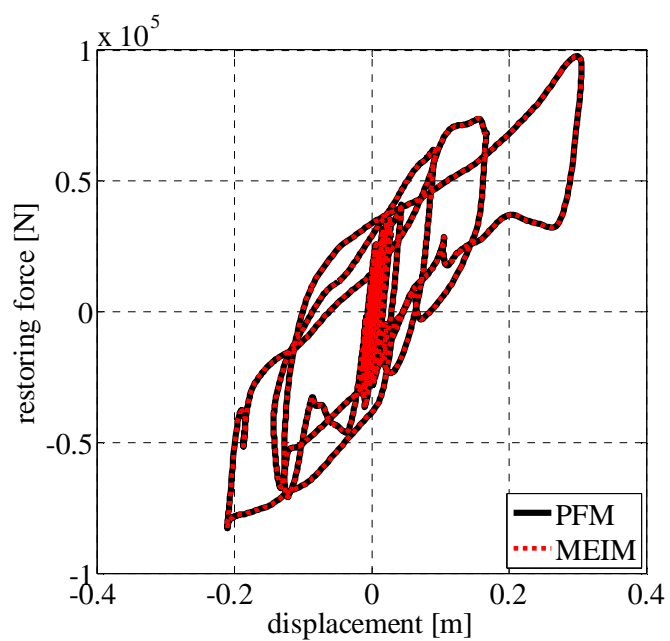


Figure 6.22. Hysteresis loop displayed by Isolator 11 in (a) x and (b) y directions (Structure B with LRBS).

6.4.3.2 Analysis of Base-Isolated Structures with FPBS

6.4.3.2.1 Analyzed 3d Base-Isolated Structure A

The superstructure is a two-story reinforced concrete structure with vertical geometric irregularity, plan dimensions 10 m x 8 m, and story height $h = 3.5$ m. The weight of the superstructure is 1802.9 kN and the first three natural periods are 0.15 s, 0.14 s, and 0.10 s, respectively. Each superstructure diaphragm mass includes the contributions of the dead load and live load on the floor diaphragm and the contributions of structural elements and nonstructural elements between floors.

The base isolation system, having a total weight of 914.9 kN, consists of an orthogonal mesh of foundation beams having rectangular cross section with dimensions 30 cm x 50 cm, and 9 identical Friction Pendulum Bearings (FPBs), positioned centrally under all columns.

The typical floor plan, the base floor plan, and a section of the analyzed 3d base-isolated structure are shown in Figure 6.1.

As a result of the kinematic constraints assumed in Chapter 2, the total number of dofs, defined relative to the ground, is equal to 9. Figure 6.2 shows the 3d discrete structural model of the analyzed base-isolated structure.

The base isolation system has been designed in order to provide an effective isolation period $T_{eff} = 2.25$ s and an effective viscous damping $\nu_{eff} = 0.10$ at the design displacement $d_d = 0.50$ m. Thus, each sliding bearing has a radius of curvature of the spherical concave surface $R = 1.25$ m, a sliding friction coefficient $\mu = 0.07$, and a yield displacement $y = 0.0002$ m. In the numerical application, the vertical load N carried by each device is assumed equal to the weight W acting on the isolator and the dependency of the sliding friction coefficient on bearing pressure and sliding velocity is neglected.

6.4.3.2.2 Analyzed 3d Base-Isolated Structure B

The superstructure is a four-story reinforced concrete structure with plan dimensions 19 m x 11 m, and story height $h = 3.5$ m. The weight of the superstructure is 9921.24 kN and the first three natural periods are 0.33 s, 0.33 s, and 0.26 s, respectively. Each superstructure diaphragm mass includes the contributions of the dead load and live load on the floor diaphragm and the contributions of structural elements and nonstructural elements between floors.

The base isolation system, having a total weight of 3006.44 kN, consists of an orthogonal mesh of foundation beams having rectangular cross section with dimensions 60 cm x 75 cm, and 24 identical Friction Pendulum Bearings (FPBs), positioned centrally under columns.

The typical floor plan, the base floor plan, and a section of the analyzed 3d base-isolated structure are shown in Figure 6.3.

As a result of the kinematic constraints assumed in Chapter 2, the total number of dofs, defined relative to the ground, is equal to 15. Figure 6.4 shows the 3d discrete structural model of the analyzed base-isolated structure.

The base isolation system has been designed in order to provide an effective isolation period $T_{eff} = 2.50$ s and an effective viscous damping $\nu_{eff} = 0.10$ at the design displacement $d_d = 0.50$ m. Thus, each sliding bearing has a radius of curvature of the spherical concave surface $R = 1.55$ m, and a sliding friction coefficient $\mu = 0.06$, and a yield displacement $y = 0.0001$ m. In the numerical application, the vertical load N carried by each device is assumed equal to the weight W acting on the isolator and the dependency of the sliding friction coefficient on bearing pressure and sliding velocity is neglected.

6.4.3.2.3 Model Adopted for Friction Pendulum Bearings

The dynamic behavior of each FPB is simulated by using a mathematical model, introduced by Constantinou et al. (1990) and described in Chapter 4, capable of predicting the biaxial behavior of sliding bearings. According to this model, the FPB nonlinear restoring forces along the orthogonal directions x and y are described by the following equations:

$$f_x = \frac{N}{R} u_x + \frac{\mu N}{y} z_x(u), \quad (6.46)$$

$$f_y = \frac{N}{R} u_y + \frac{\mu N}{y} z_y(u), \quad (6.47)$$

in which, N is the vertical load carried by the bearing, R is the radius of curvature of the spherical concave surface of the bearing, u_x and u_y represent the displacements of the isolation device in the x and y directions, respectively, y is the yield displacement, and μ is the sliding friction coefficient which depends on the value of bearing pressure and on the instantaneous velocity of sliding \dot{u} , given by:

$$\dot{u} = \sqrt{\dot{u}_x^2 + \dot{u}_y^2}, \quad (6.48)$$

where \dot{u}_x and \dot{u}_y are the velocities that occur at the isolation device in x and y directions, respectively.

The functions z_x and z_y , obtained by solving Equations (6.44) and (6.45), respectively, have the unit of displacement and account for the direction and biaxial interaction of hysteresis forces.

In the numerical applications, the following values are adopted for the model parameters in Equations (6.44) and (6.45):

$$A = 1, \beta = \frac{0.5}{y^2}, \text{ and } \gamma = \frac{0.5}{y^2}.$$

The unconditionally stable semi-implicit Runge-Kutta method (Rosenbrock 1963) is employed to solve the differential equations governing the behavior of each nonlinear isolation element with a number of steps equal to 50.

6.4.3.2.4 Numerical Results for Structure A

Bidirectional earthquake excitation is imposed with component SN and SP of the 1994 Northridge motion applied along directions X and Y of the global coordinate system, respectively. The two components of the horizontal ground acceleration record, having time step equal to 0.005 s, are shown in Figure 6.5. It is important to note that normally 200 points per second are used to define accurately an acceleration record, and that the time step of the ground motion can be reduced through linear interpolation because it is generally assumed that the acceleration function is linear within each time increment (Wilson 2002).

Table 6.5 gives the Nonlinear Time History Analyses (NLTHAs) results obtained using the proposed MEIM and the PFM, both implemented on the same computer (Intel® Core™ i7-4700MQ processor, CPU at 2.40 GHz with 16 GB of RAM) by using the computer program Matlab. In the PFM the adopted convergence tolerance value is equal to 10^{-6} .

Table 6.5. NLTHAs results with $\Delta t = 0.005$ s | Structure A with FPBS.

	tct [s]	$tctp$ [%]	$u_x^{(MC_b)}$ [m]		$u_y^{(MC_b)}$ [m]		$\ddot{u}_x^{(MC_2)}$ [g]		$\ddot{u}_y^{(MC_2)}$ [g]	
			max	min	max	min	max	min	max	min
MEIM	47	7.86	0.3312	-0.3138	0.2831	-0.2507	0.4708	-0.4772	1.1883	-0.9682
PFM	598	-	0.3310	-0.3137	0.2829	-0.2505	0.4729	-0.4164	1.0778	-1.1374

The comparison of the maximum and minimum values of the MC_b displacements and MC_2 accelerations (relative to the ground) in x and y directions, obtained using the MEIM and PFM, reveals that the proposed method provides numerical results that are close enough to those obtained adopting the PFM.

As regards the stability of the MEIM, the critical time step Δt_{cr} , evaluated using Equation (6.40) and considering the lowest natural period given by the eigenvalue problem in Equation (6.41), is equal to 0.015 s. It is evident that, in this case, being the critical time step larger than the imposed ground acceleration time step, there are no stability problems despite of the very high initial stiffness value of FPBs.

As far as the computational efficiency is concerned, the total computational time, tct , required by the MEIM is significantly reduced in comparison to the PFM. It must be noted that the comparisons using the tct are meaningful only qualitatively because it depends on the CPU speed, memory capability and background processes of the computer used to obtain the previous results. To this end, in order to normalize the computational time results, Table 6.5

also shows the percentage of the MEIM tct evaluated with respect to the PFM tct as follows:

$$\text{MEIM } tctp [\%] = \frac{\text{MEIM } tct}{\text{PFM } tct} \cdot 100 .$$

In addition, according to the numerical results listed in Table 6.6, the proposed MEIM, performed with a smaller time step, that is, $\Delta t = 0.001$ s, which allows one to minimize the error in Equations (6.20) and (6.27), requires less computational effort than the PFM even if the latter is performed using the larger time step, that is, $\Delta t = 0.005$ s. Indeed, the MEIM $tctp$, referred to the PFM tct evaluated adopting $\Delta t = 0.005$ s, is equal to 38.46 %.

Table 6.6. NLTHAs results with $\Delta t = 0.001$ s | Structure A with FPBS.

	tct [s]	$tctp$ [%]	$u_x^{(MC_b)}$ [m]		$u_y^{(MC_b)}$ [m]		$\ddot{u}_x^{(MC_2)}$ [g]		$\ddot{u}_y^{(MC_2)}$ [g]	
			max	min	max	min	max	min	max	min
MEIM	230	18.54	0.3312	-0.3139	0.2832	-0.2507	0.4779	-0.4692	1.2015	-0.9925
PFM	1240	-	0.3312	-0.3139	0.2832	-0.2507	0.4783	-0.4693	1.2067	-0.9835

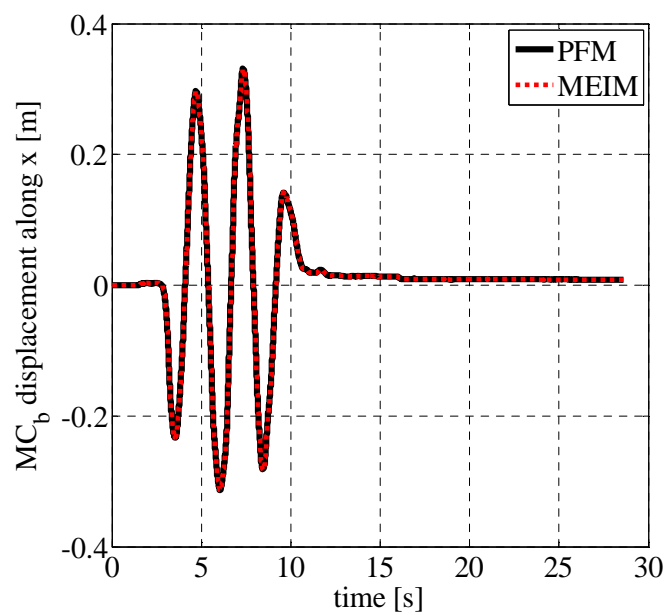
It can therefore be concluded that even when a time step smaller than the one used to define the ground acceleration accurately has to be adopted because of stability requirements, as in the case of base isolation systems having isolators with very high initial stiffness, such as sliding bearings, or very high stiffness at large displacements, such as high damping rubber bearings, the proposed method preserves its computational efficiency with respect to the PFM.

Figures 6.23, 6.24, and 6.25 illustrate, respectively, the displacement, velocity and acceleration time histories of the base isolation system mass center, whereas Figures 6.26, 6.27, and 6.28 show, respectively, the displacement, velocity and acceleration time histories of the superstructure second story mass center (relative to the ground).

In addition, Figures 6.29 and 6.30 illustrate, respectively, the force-displacement hysteresis loops displayed by Isolator 1 and Isolator 5, illustrated in Figure 6.1b.

It is evident the good agreement between responses computed using the proposed MEIM and the PFM.

(a)



(b)

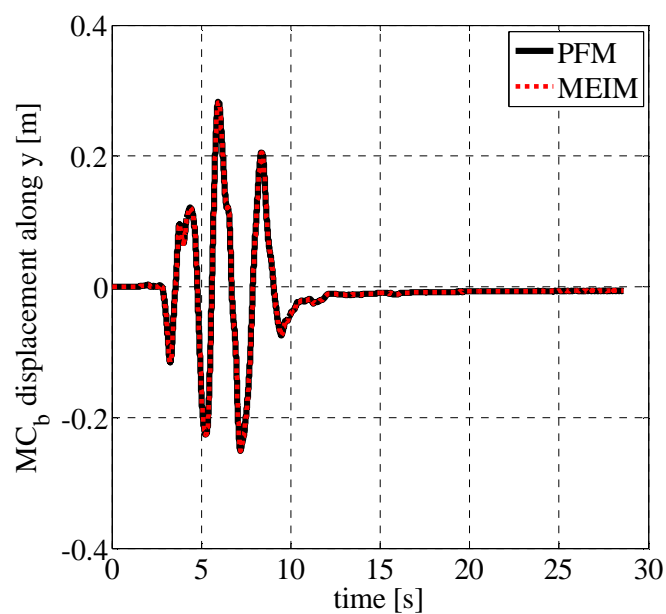
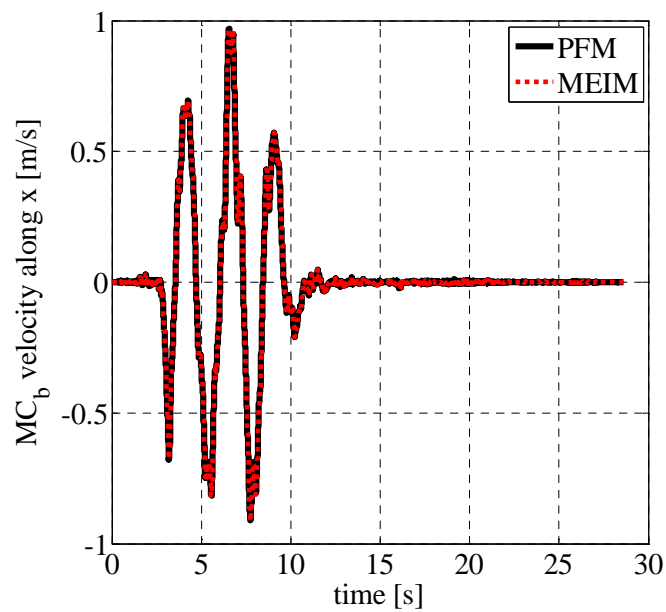


Figure 6.23. Displacement time history of the base isolation system mass center in (a) x and (b) y directions (Structure A with FPBS).

(a)



(b)

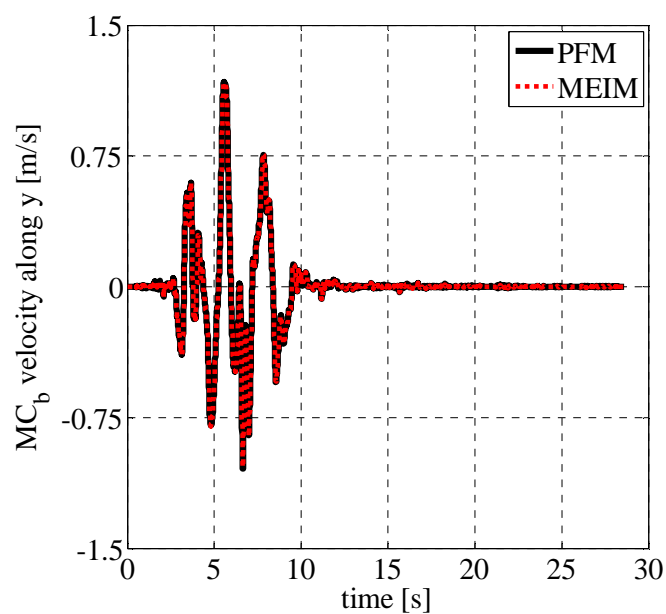
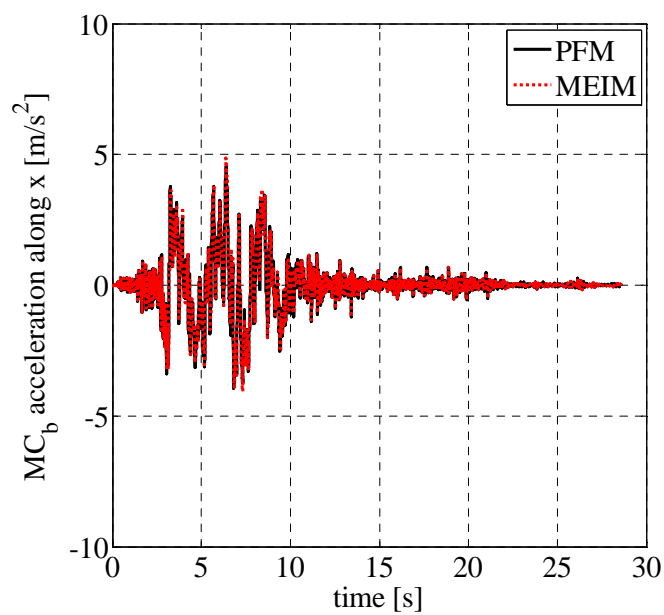


Figure 6.24. Velocity time history of the base isolation system mass center in (a) x and (b) y directions (Structure A with FPBS).

(a)



(b)

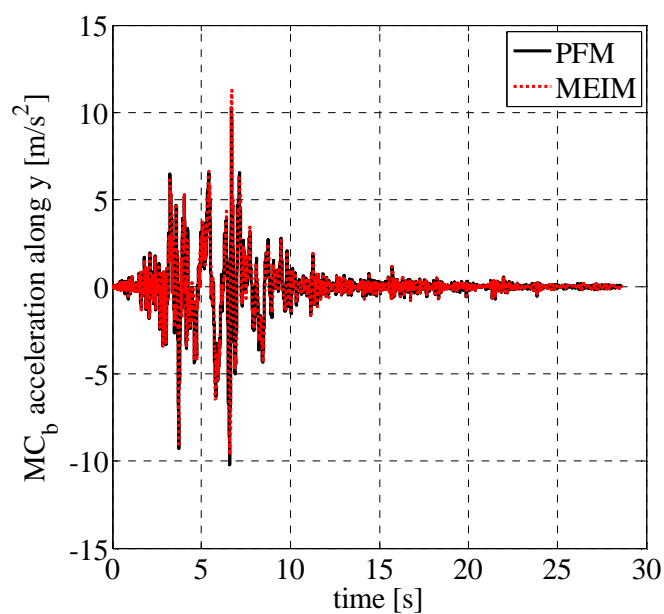
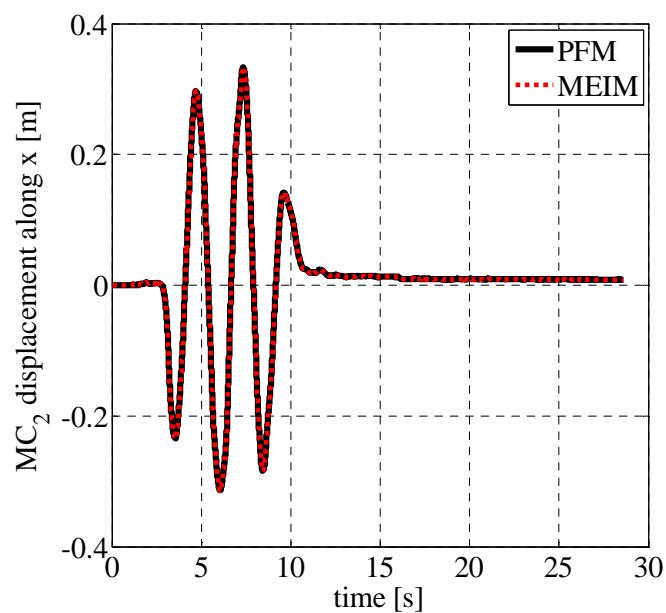


Figure 6.25. Acceleration time history of the base isolation system mass center in (a) x and (b) y directions (Structure A with FPBS).

(a)



(b)

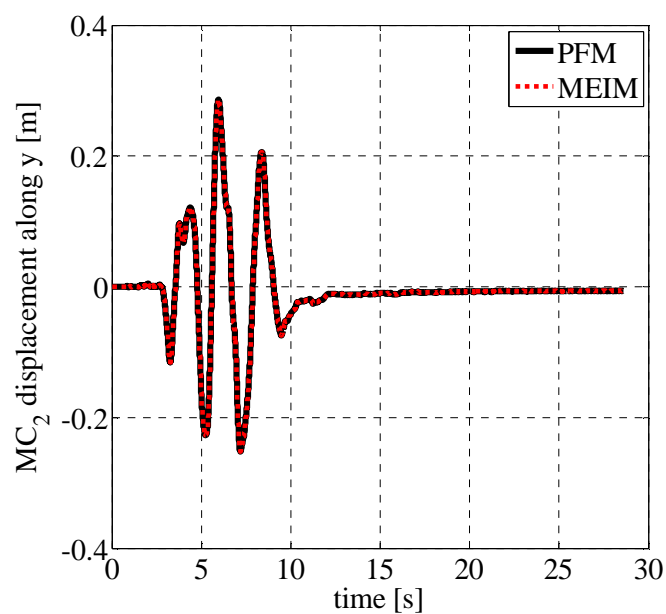
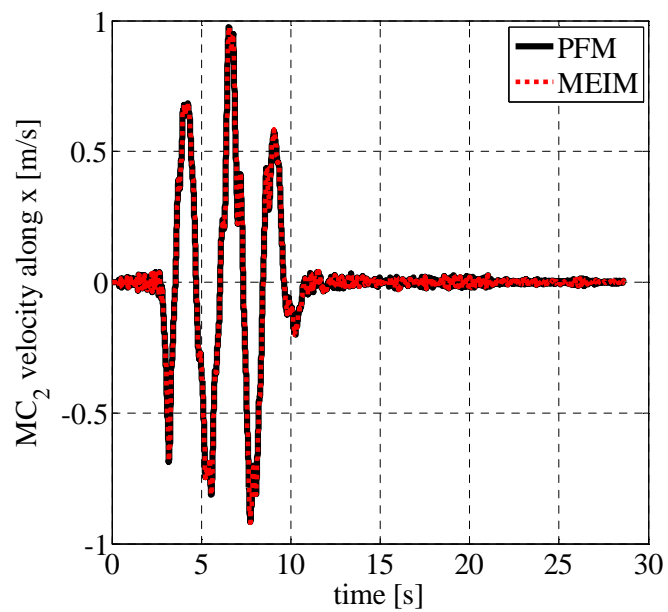


Figure 6.26. Displacement time history of the superstructure second story mass center in (a) x and (b) y directions (Structure A with FPBS).

(a)



(b)

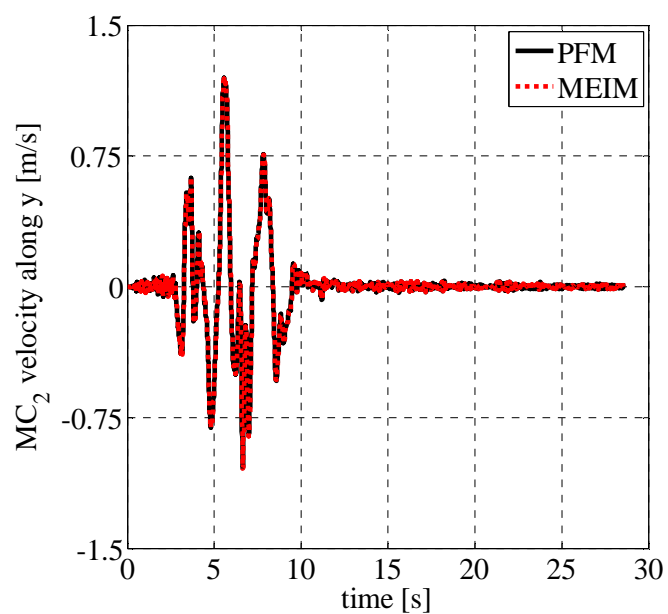
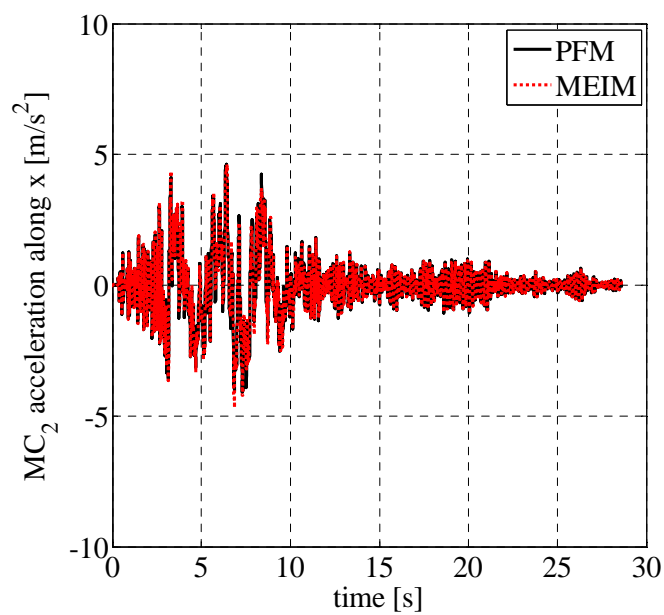


Figure 6.27. Velocity time history of the superstructure second story mass center in (a) x and (b) y directions (Structure A with FPBS).

(a)



(b)

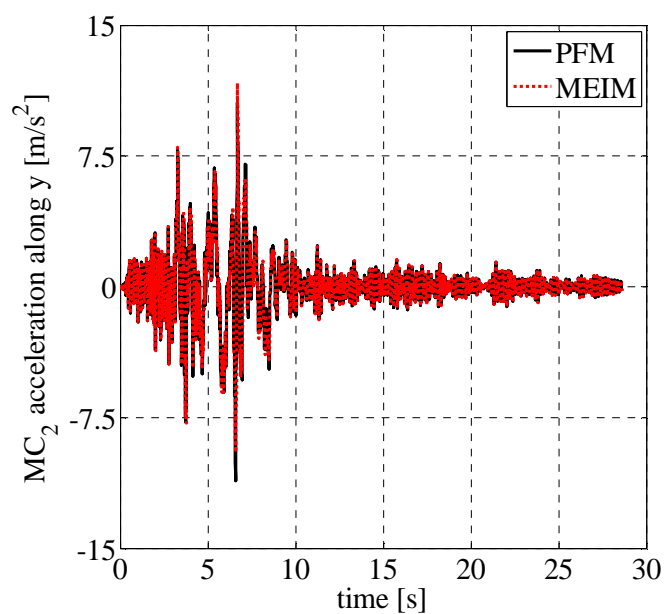
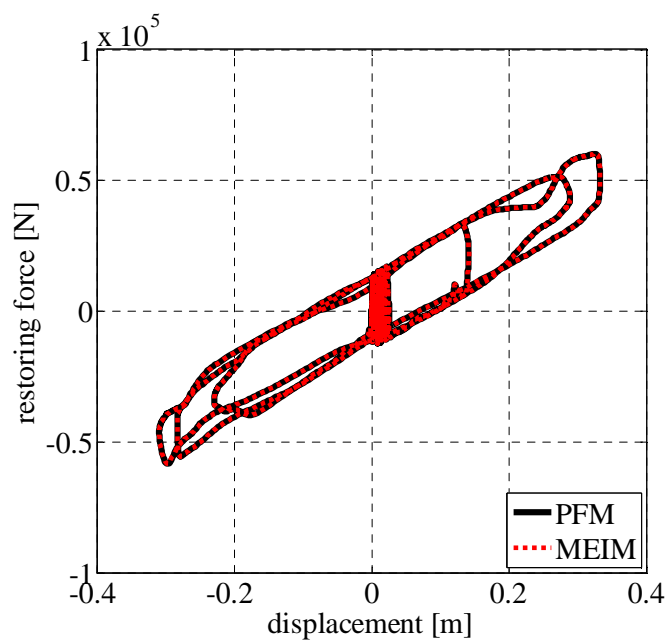


Figure 6.28. Acceleration time history of the superstructure second story mass center in (a) x and (b) y directions (Structure A with FPBS).

(a)



(b)

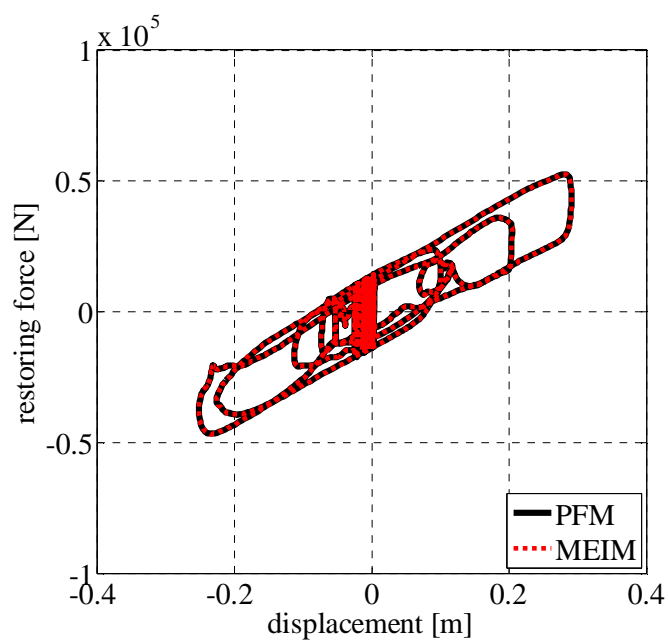
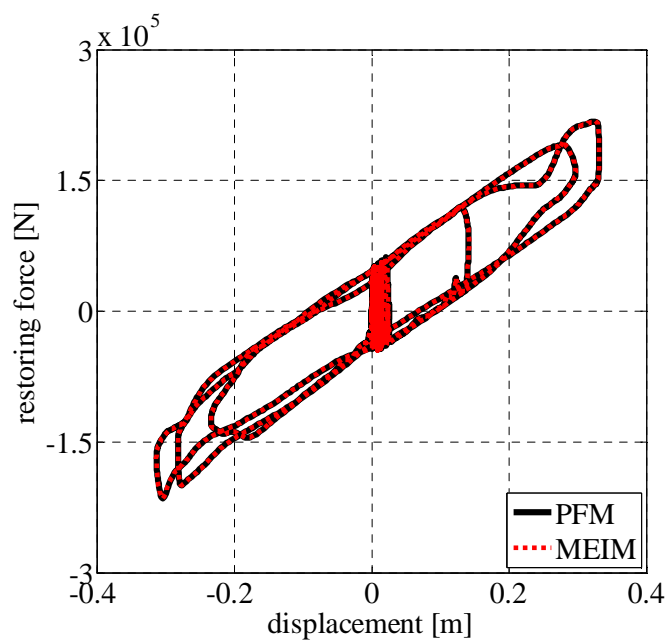


Figure 6.29. Hysteresis loop displayed by Isolator 1 in (a) x and (b) y directions (Structure A with FPBS).

(a)



(b)

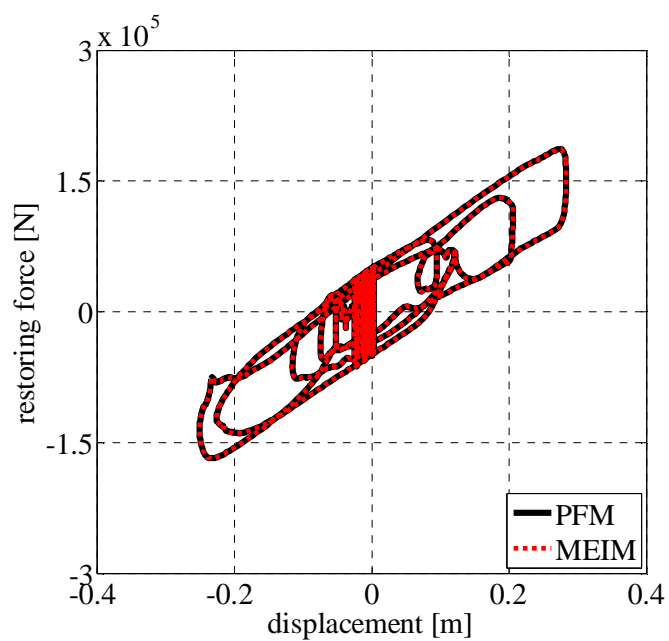


Figure 6.30. Hysteresis loop displayed by Isolator 5 in (a) x and (b) y directions (Structure A with FPBS).

6.4.3.2.5 Numerical Results for Structure B

Bidirectional earthquake excitation is imposed with component SN and SP of the 1989 Loma Prieta motion applied along directions X and Y of the global coordinate system, respectively. The two components of the horizontal ground acceleration record, having time step equal to 0.005 s, are shown in Figure 6.14. It is important to note that normally 200 points per second are used to define accurately an acceleration record, and that the time step of the ground motion can be reduced through linear interpolation because it is generally assumed that the acceleration function is linear within each time increment (Wilson 2002).

Table 6.7 gives the Nonlinear Time History Analyses (NLTHAs) results obtained using the proposed MEIM and the PFM, both implemented on the same computer (Intel® Core™ i7-4700MQ processor, CPU at 2.40 GHz with 16 GB of RAM) by using the computer program Matlab. In the PFM the adopted convergence tolerance value is equal to 10^{-6} .

Table 6.7. NLTHAs results with $\Delta t = 0.005$ s | Structure B with FPBS.

	tct [s]	$tctp$ [%]	$u_x^{(MC_b)}$ [m]		$u_y^{(MC_b)}$ [m]		$\ddot{u}_x^{(MC_4)}$ [g]		$\ddot{u}_y^{(MC_4)}$ [g]	
			max	min	max	min	max	min	max	min
MEIM	99.8	7.00	0.5642	-0.4575	0.2971	-0.1831	1.1373	-1.0563	0.5581	-0.7436
PFM	1425	-	0.5641	-0.4575	0.2970	-0.1839	1.1781	-1.1190	0.6006	-0.7293

The comparison of the maximum and minimum values of the MC_b displacements and MC_4 accelerations (relative to the ground) in x and y directions, obtained using the MEIM and PFM, reveals that the proposed method provides numerical results that are close enough to those obtained adopting the PFM.

As regards the stability of the MEIM, the critical time step Δt_{cr} , evaluated using Equation (6.40) and considering the lowest natural period given by the eigenvalue problem in Equation (6.41), is equal to 0.012 s. It is evident that, in this case, being the critical time step larger than the imposed ground acceleration time step, there are no stability problems despite of the very high initial stiffness value of FPBs.

As far as the computational efficiency is concerned, the total computational time, tct , required by the MEIM is significantly reduced in comparison to the PFM. It must be noted that the comparisons using the tct are meaningful only qualitatively because it depends on the CPU speed, memory capability and background processes of the computer used to obtain the previous results. To this end, in order to normalize the computational time results, Table 6.7

also shows the percentage of the MEIM tct evaluated with respect to the PFM tct as follows:

$$\text{MEIM } tctp [\%] = \frac{\text{MEIM } tct}{\text{PFM } tct} \cdot 100.$$

In addition, according to the numerical results listed in Table 6.8, the proposed MEIM, performed with a smaller time step, that is, $\Delta t = 0.001$ s, which allows one to minimize the error in Equations (6.20) and (6.27), requires less computational effort than the PFM even if the latter is performed using the larger time step, that is, $\Delta t = 0.005$ s. Indeed, the MEIM $tctp$, referred to the PFM tct evaluated adopting $\Delta t = 0.005$ s, is equal to 34.42 %.

Table 6.8. NLTHAs results with $\Delta t = 0.001$ s | Structure B with FPBS.

	tct [s]	$tctp$ [%]	$u_x^{(MC_b)}$ [m]		$u_y^{(MC_b)}$ [m]		$\ddot{u}_x^{(MC_4)}$ [g]		$\ddot{u}_y^{(MC_4)}$ [g]	
			max	min	max	min	max	min	max	min
MEIM	490.6	18.02	0.5590	-0.4466	0.2954	-0.1810	0.8799	-0.9578	0.5443	-0.6542
PFM	2722	-	0.5590	-0.4466	0.2954	-0.1810	0.8825	-0.9610	0.5452	-0.6547

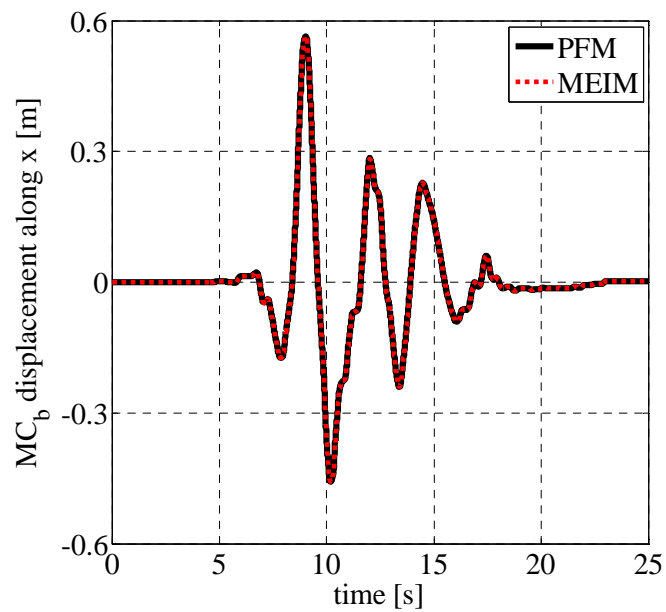
It can therefore be concluded that even when a time step smaller than the one used to define the ground acceleration accurately has to be adopted because of stability requirements, as in the case of base isolation systems having isolators with very high initial stiffness, such as sliding bearings, or very high stiffness at large displacements, such as high damping rubber bearings, the proposed method preserves its computational efficiency with respect to the PFM.

Figures 6.31, 6.32, and 6.33 illustrate, respectively, the displacement, velocity and acceleration time histories of the base isolation system mass center, whereas Figures 6.34, 6.35, and 6.36 show, respectively, the displacement, velocity and acceleration time histories of the superstructure fourth story mass center (relative to the ground).

In addition, Figures 6.37 and 6.38 illustrate, respectively, the force-displacement hysteresis loops displayed by Isolator 1 and Isolator 11, illustrated in Figure 6.3b.

It is evident the good agreement between responses computed using the proposed MEIM and the PFM.

(a)



(b)

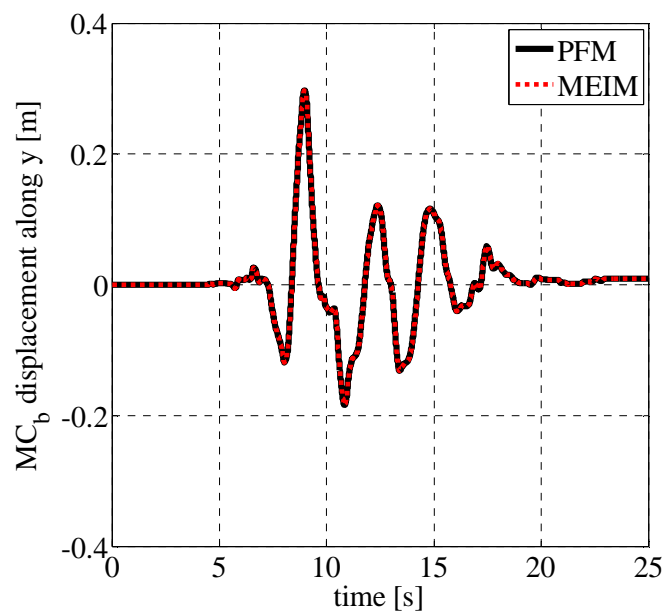
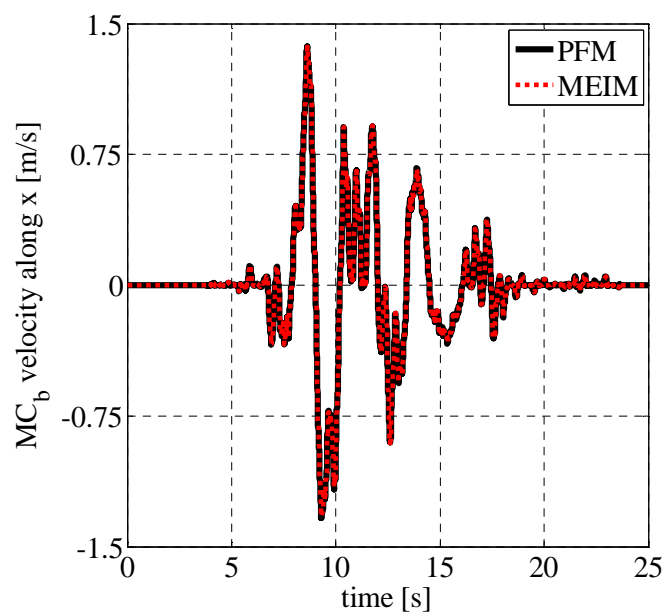


Figure 6.31. Displacement time history of the base isolation system mass center in (a) x and (b) y directions (Structure B with FPBS).

(a)



(b)

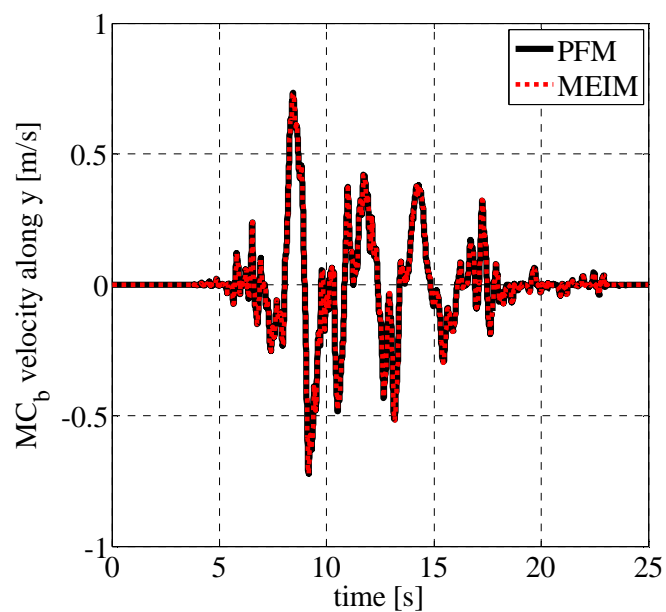
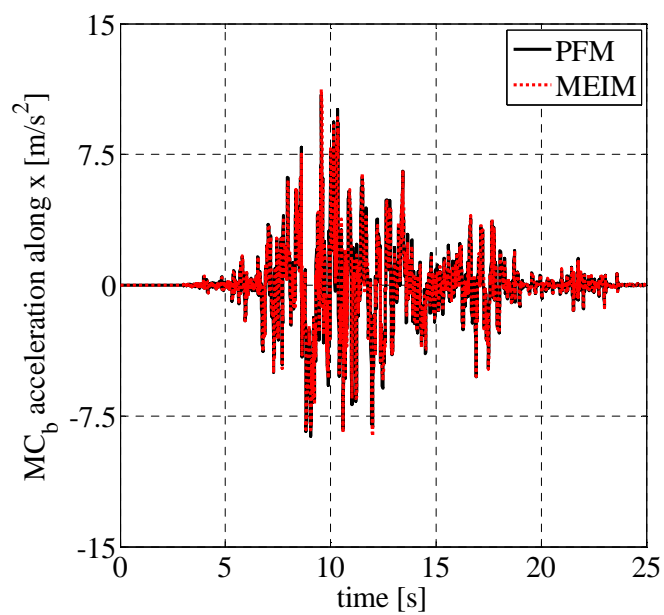


Figure 6.32. Velocity time history of the base isolation system mass center in (a) x and (b) y directions (Structure B with FPBS).

(a)



(b)

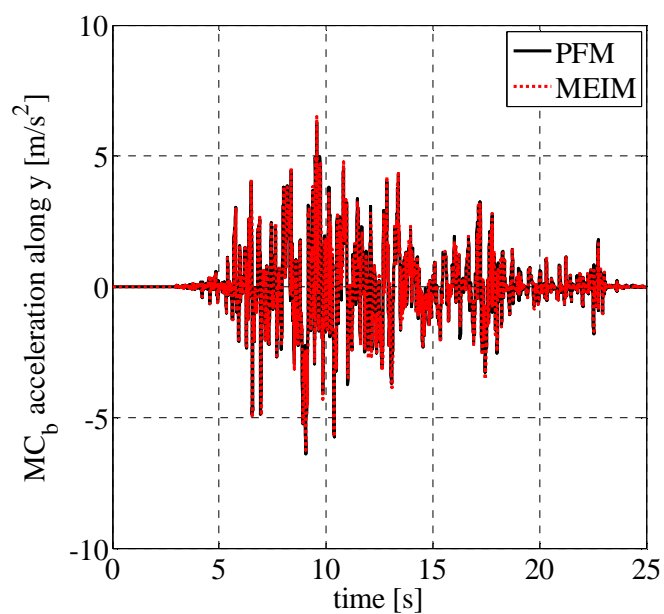
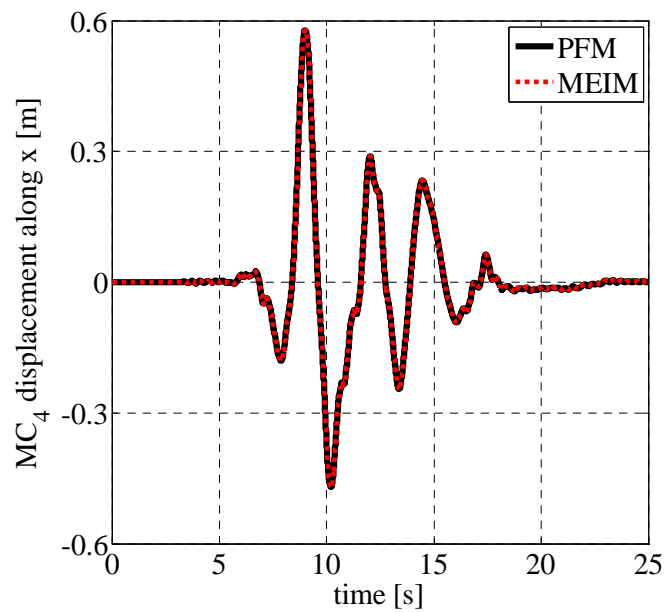


Figure 6.33. Acceleration time history of the base isolation system mass center in (a) x and (b) y directions (Structure B with FPBS).

(a)



(b)

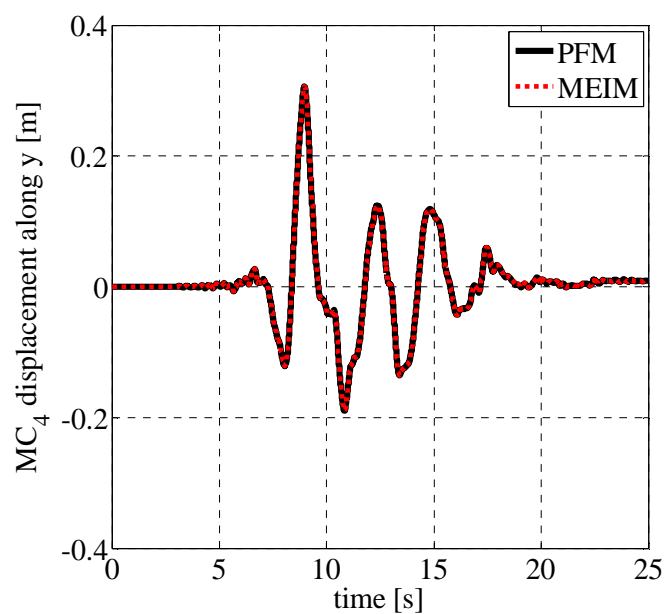
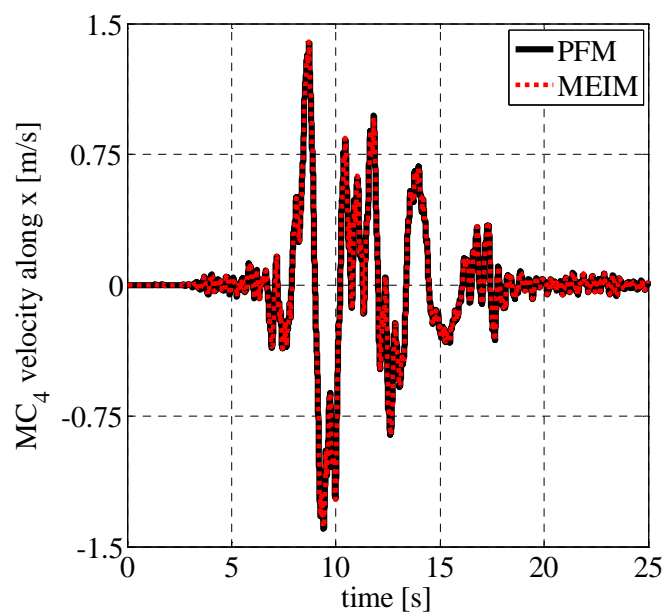


Figure 6.34. Displacement time history of the superstructure fourth story mass center in (a) x and (b) y directions (Structure B with FPBS).

(a)



(b)

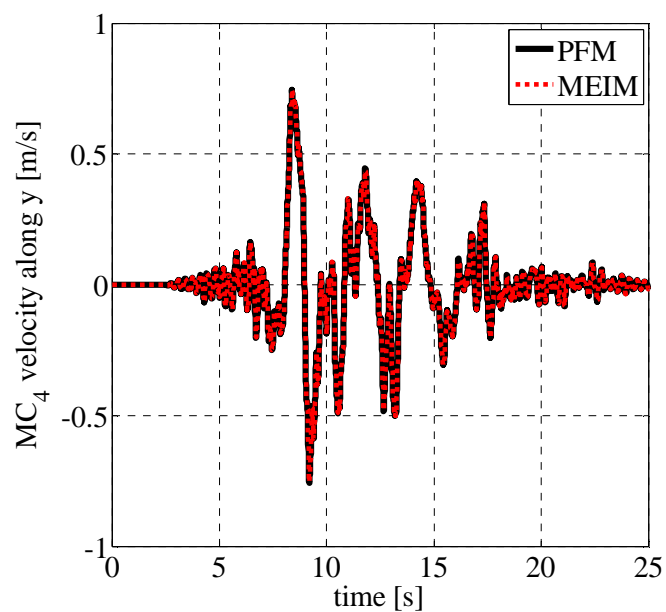
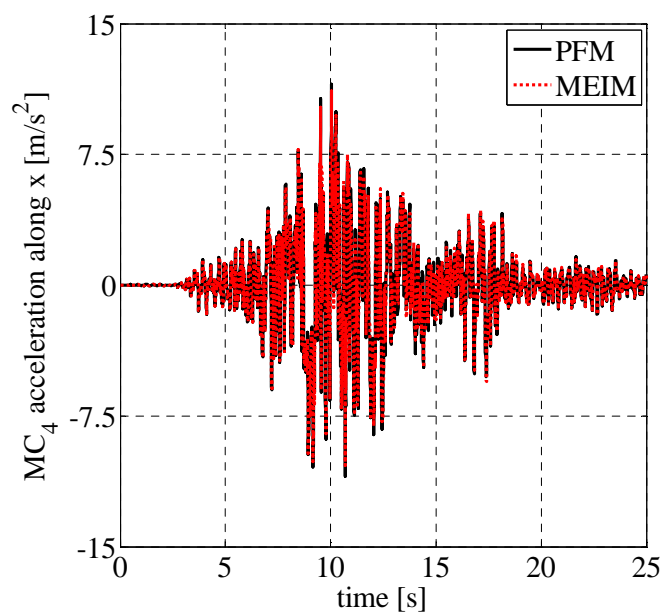


Figure 6.35. Velocity time history of the superstructure fourth story mass center in (a) x and (b) y directions (Structure B with FPBS).

(a)



(b)

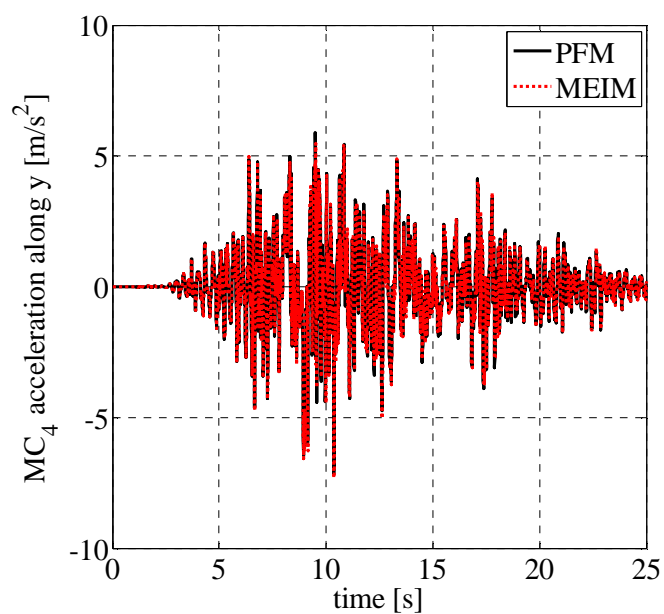
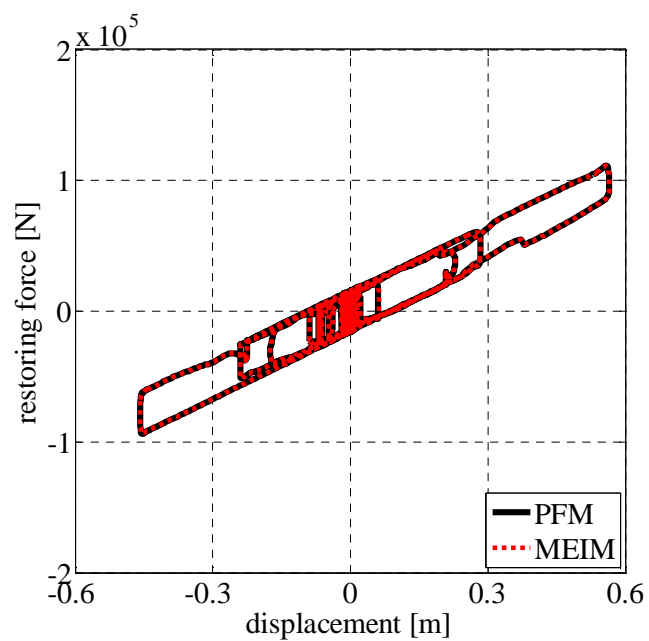


Figure 6.36. Acceleration time history of the superstructure fourth story mass center in (a) x and (b) y directions (Structure B with FPBS).

(a)



(b)

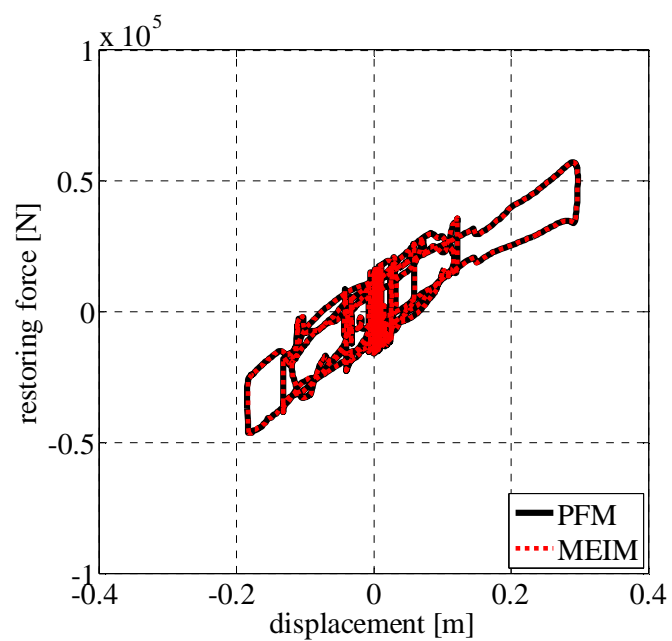
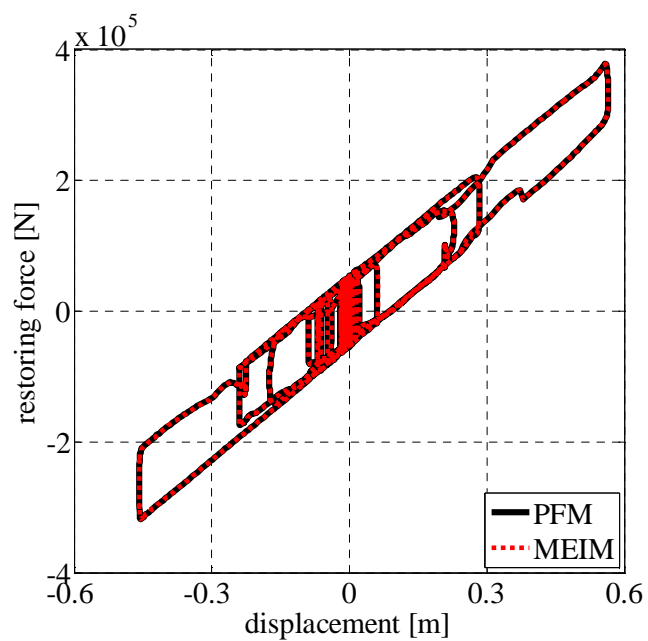


Figure 6.37. Hysteresis loop displayed by Isolator 1 in (a) x and (b) y directions (Structure B with FPBS).

(a)



(b)

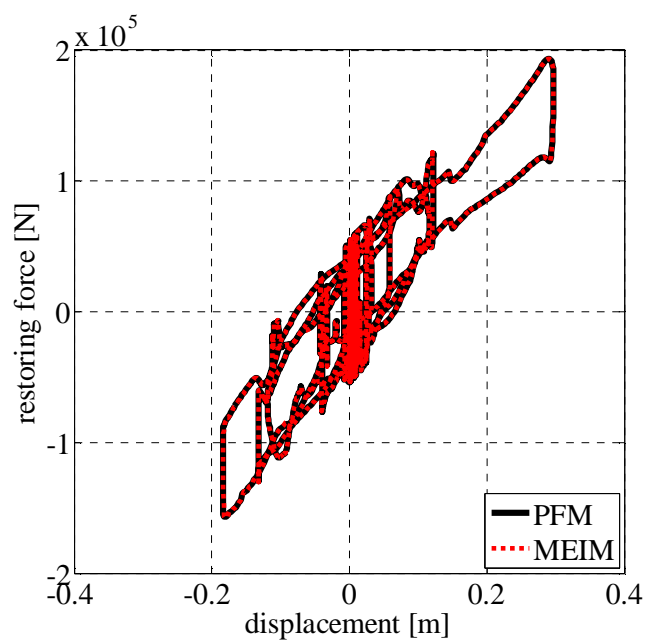


Figure 6.38. Hysteresis loop displayed by Isolator 11 in (a) x and (b) y directions (Structure B with FPBS).

Chapter 7

Speeding Up Nonlinear Dynamic Analysis Using the MEIM and NEM

7.1 Introduction

In Chapter 7, the nonlinear dynamic response of a 3d seismically base-isolated structure subjected to harmonic earthquake excitation is predicted using the Pseudo-Force Method (PFM), described in 6.2.2, and the proposed Mixed Explicit-Implicit time integration Method (MEIM), presented in 6.3.2. In order to simulate the nonlinear dynamic behavior of each seismic isolator within the relatively large displacements range, generally reached under the design earthquake, the Bouc-Wen Model (BWM), described in 4.2.1.1, and the proposed Nonlinear Exponential Model (NEM), presented in 4.3.1.1, are adopted. More specifically, the former is used when the nonlinear time history analysis is performed with the PFM (PFM-BWM), whereas the latter is employed when the nonlinear dynamic analysis is carried out using the MEIM (MEIM-NEM). The main aim of the following numerical application is to demonstrate how the significant reduction of the computational effort, due to the use of the proposed partitioned solution approach and nonlinear analytical model, makes the nonlinear dynamic analysis almost as fast as a linear dynamic analysis.

7.2 Numerical Application

7.2.1 Analyzed 3d Base-Isolated Structure

In the following, the analyzed 3d structure, seismically isolated by adopting a lead rubber bearing system, is described.

The superstructure is a four-story reinforced concrete structure with plan dimensions 19 m x 11 m, and story height $h = 3.5$ m. The weight of the superstructure is 9921.24 kN and the first three natural periods are 0.33 s, 0.33 s, and 0.26 s, respectively. Each superstructure diaphragm mass includes the contributions of the dead load and live load on the floor diaphragm and the contributions of structural elements and nonstructural elements between floors.

The base isolation system, having a total weight of 3006.44 kN, consists of an orthogonal mesh of foundation beams having rectangular cross section with dimensions 60 cm x 75 cm, and 24 identical Lead Rubber Bearings (LRBs), positioned centrally under all columns.

The typical floor plan, the base floor plan, and a section of the analyzed 3d base-isolated structure are shown in Figure 6.3.

As a result of the kinematic constraints assumed in Chapter 2, the total number of dofs, defined relative to the ground, is equal to 15. Figure 6.4 shows the 3d discrete structural model of the analyzed base-isolated structure.

The base isolation system has been designed in order to provide an effective isolation period $T_{eff} = 2.50$ s and an effective viscous damping $\nu_{eff} = 0.15$ at the design displacement $d_d = 0.50$ m. Thus, each elastomeric bearing has a yield force $f_y = 45400.3$ N, a yield displacement $u_y = 0.017$ m, and a post-yield to pre-yield stiffness ratio $\alpha = 0.10$.

7.2.2 Analytical Models Parameters

Table 7.1 shows the parameters of the two uniaxial analytical models adopted to simulate the dynamic behavior of each LRB, that is, the differential equation BWM, described in 4.2.1.1, and the proposed NEM, presented in 4.3.1.1.

Table 7.1. BWM and NEM parameters.

BWM	f_y [N]	u_y [m]	α	A	β	γ	n
	45400.29	0.0171	0.10	1	0.5	0.5	2
NEM	k_1 [N/m]	k_2 [N/m]	a				
	4513479	265498	50				

Figure 7.1 illustrates the force-displacement hysteresis loops produced by use of the BWM and NEM. They are obtained, as done in experimental tests, by applying a sinusoidal harmonic displacement having amplitude equal to 0.50 m and frequency of 0.40 Hz. It can be seen that the two analytical models adopting the parameters listed in Table 7.1 can reproduce a hysteresis loop having the same area and effective stiffness.

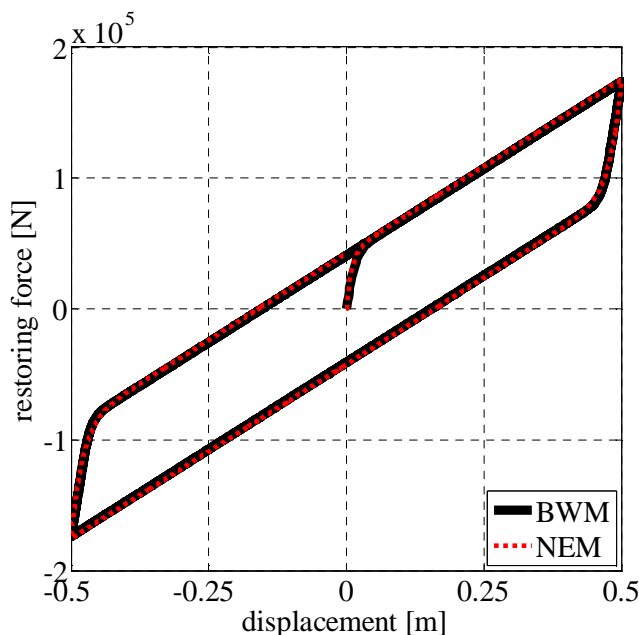
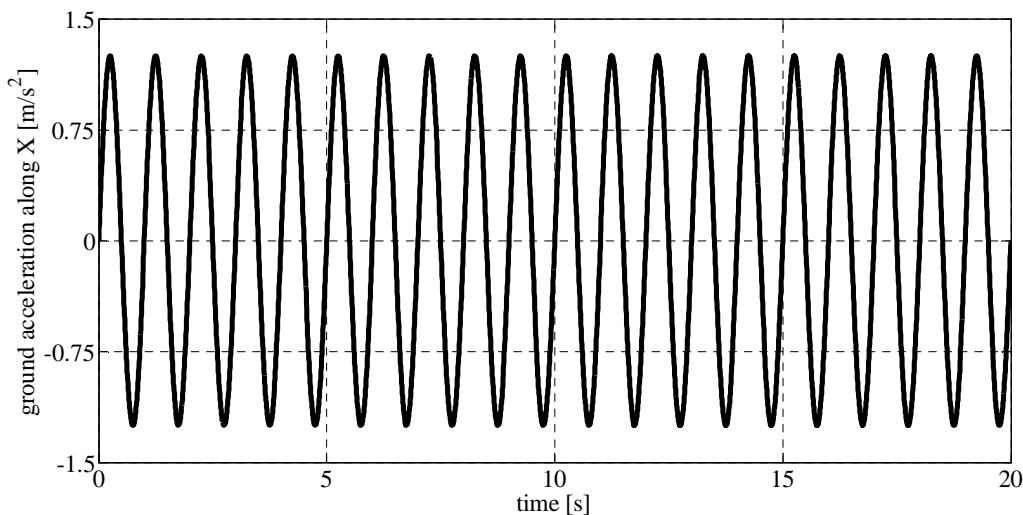


Figure 7.1. Hysteresis loop simulated using the BWM and the NEM.

7.2.3 Dynamic Response of the 3d Base-Isolated Structure

Harmonic ground motion, having amplitude $\ddot{u}_{g0} = 2.5 \text{ m/s}^2$, frequency $\omega_g = 2\pi \text{ rad/s}$, and time duration $t_d = 20 \text{ s}$, is imposed with an angle α_g , that is, the angle that the epicentral direction forms with the X -axis, equal to $\pi/6$. The time step of the harmonic earthquake excitation is chosen equal to 0.005 s because normally 200 points per second are used to define accurately an acceleration record (Wilson 2002). The two components of the horizontal harmonic ground acceleration are shown in Figure 7.2.

(a)



(b)

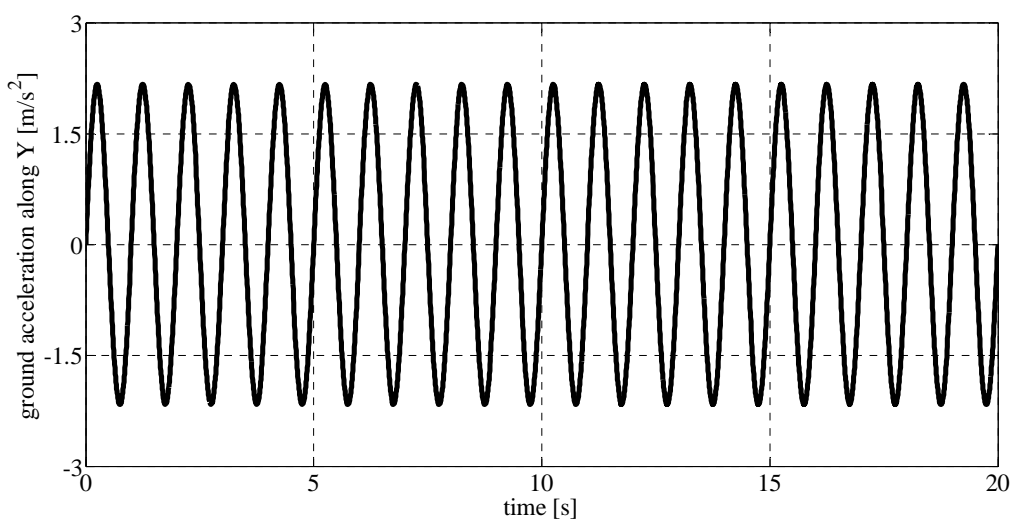


Figure 7.2. (a) X and (b) Y components of the applied horizontal harmonic ground acceleration.

Table 7.2 gives the Nonlinear Time History Analyses (NLTHAs) results obtained using the PFM-BWM and the proposed MEIM-NEM, both implemented on the same computer (Intel® Core™ i7-4700MQ processor, CPU at 2.40 GHz with 16 GB of RAM) by using the computer program Matlab and verified using SAP2000. In the PFM-BWM, the adopted convergence tolerance value is equal to 10^{-8} , and the unconditionally stable semi-implicit Runge-Kutta method (Rosenbrock 1963) is employed to solve the differential equations governing the behavior of each nonlinear isolation element with a number of steps equal to 50.

Table 7.2. NLTHAs results with $\Delta t = 0.005$ s.

	tct [s]	$tctp$ [%]	$u_x^{(MC_b)}$ [m]		$u_y^{(MC_b)}$ [m]		$\ddot{u}_x^{(MC_4)}$ [g]		$\ddot{u}_y^{(MC_4)}$ [g]	
			max	min	max	min	max	min	max	min
MEIM-NEM	1.25	0.33	0.073	-0.060	0.095	-0.140	0.323	-0.331	0.512	-0.527
PFM-BWM	373.24	-	0.071	-0.065	0.099	-0.146	0.329	-0.342	0.591	-0.562

The comparison of the maximum and minimum values of the base isolation system mass center (MC_b) displacements and superstructure fourth story mass center (MC_4) accelerations (relative to the ground) in x and y directions, obtained using the PFM-BWM and the MEIM-NEM, reveals that the proposed partitioned solution approach and analytical model provide numerical results that are close enough to those obtained adopting the PFM-BWM.

As regards the stability of the MEIM, the critical time step Δt_{cr} , evaluated using Equation (6.40) and considering the lowest natural period given by the eigenvalue problem in Equation (6.41), is equal to 0.12 s. It is clear that the low stiffness value of the base isolation system allows one to have a critical time step considerably larger than the imposed ground acceleration time step, thus avoiding stability problems.

As far as the computational efficiency is concerned, the total computational time, tct , required by the MEIM-NEM is significantly reduced in comparison to the PFM-BWM. It must be noted that the comparisons using the tct are meaningful only qualitatively because it depends on the CPU speed, memory capability and background processes of the computer used to obtain the previous results. To this end, in order to normalize the computational time results, Table 7.2 also shows the percentage of the MEIM-NEM tct evaluated with respect to the PFM-BWM tct as follows:

$$\text{MEIM-NEM } tctp \text{ [\%]} = \frac{\text{MEIM-NEM } tct}{\text{PFM-BWM } tct} \cdot 100.$$

In addition, according to the numerical results listed in Table 7.3, the proposed MEIM-NEM, performed with a smaller time step, that is, $\Delta t = 0.001$ s, requires less computational effort than the PFM-BWM even if the latter is performed using the larger time step, that is, $\Delta t = 0.005$ s. Indeed, the MEIM-NEM $tctp$, referred to the PFM-BWM tct evaluated adopting $\Delta t = 0.005$ s, is equal to 1.53 %.

Table 7.3. NLTHAs results with $\Delta t = 0.001$ s.

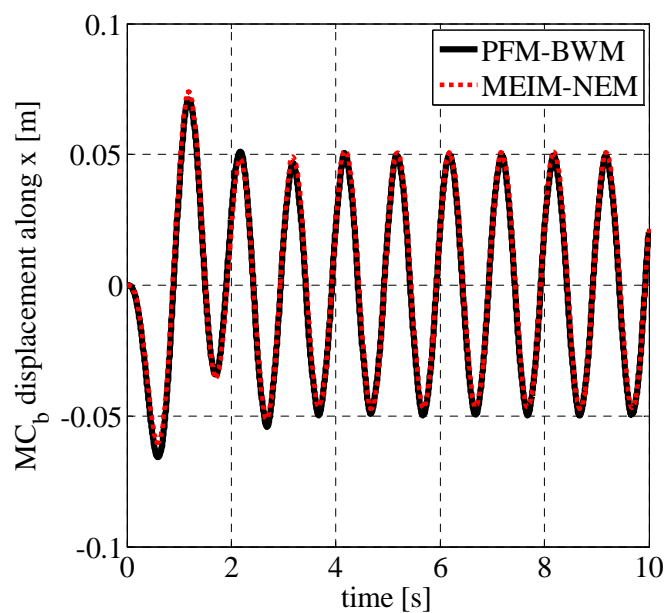
	tct [s]	$tctp$ [%]	$u_x^{(MC_b)}$ [m]		$u_y^{(MC_b)}$ [m]		$\ddot{u}_x^{(MC_4)}$ [g]		$\ddot{u}_y^{(MC_4)}$ [g]	
			max	min	max	min	max	min	max	min
MEIM-NEM	5.73	1.53	0.073	-0.060	0.095	-0.140	0.325	-0.325	0.514	-0.510

Figures 7.3, 7.4, and 7.5 illustrate, respectively, the displacement, velocity, and acceleration time histories of the base isolation system mass center, for a time duration of the harmonic earthquake excitation $t_d = 10$ s, whereas Figures 7.6, 7.7, and 7.8 show, respectively, the displacement, velocity, and acceleration time histories of the superstructure fourth story mass center (relative to the ground).

Furthermore, Figures 7.9 and 7.10 illustrate, respectively, the force-displacement hysteresis loops displayed by Isolator 1 and Isolator 11, illustrated in Figure 6.3b.

It is evident the good agreement between responses computed using the proposed MEIM-NEM and the PFM-BWM.

(a)



(b)

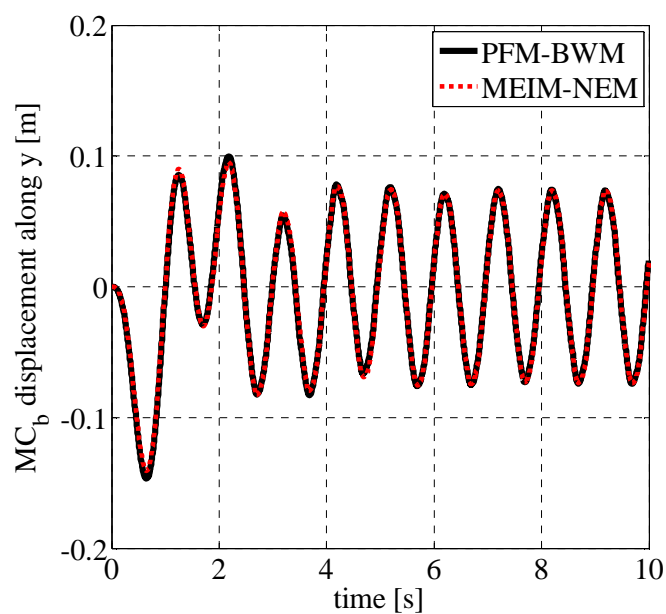
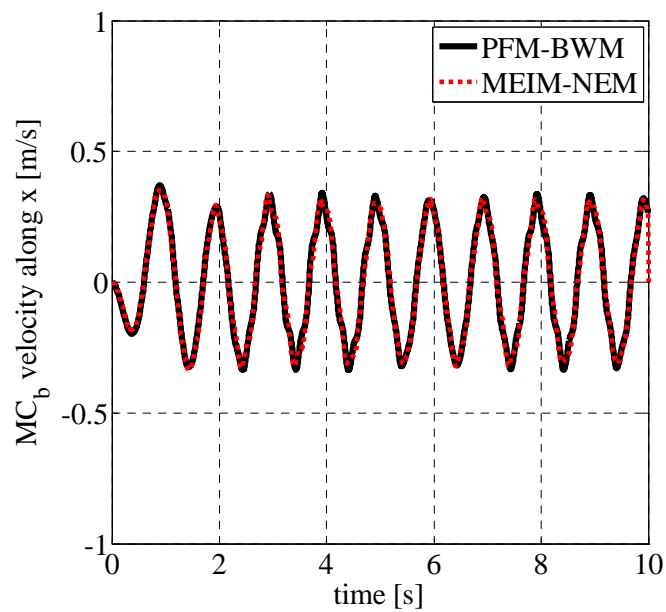


Figure 7.3. Displacement time history of the base isolation system mass center in (a) x and (b) y directions.

(a)



(b)

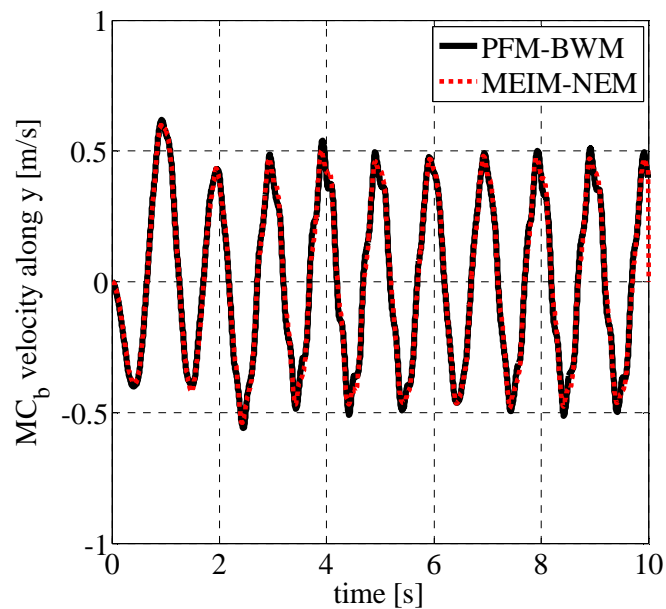
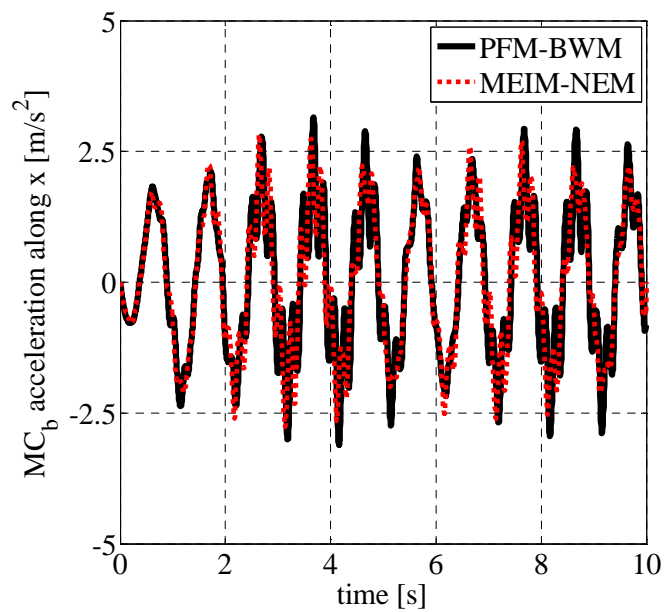


Figure 7.4. Velocity time history of the base isolation system mass center in (a) x and (b) y directions.

(a)



(b)

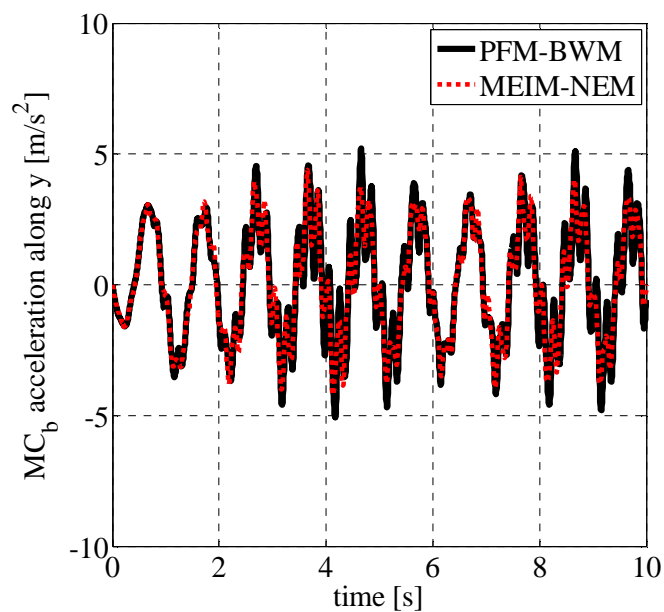
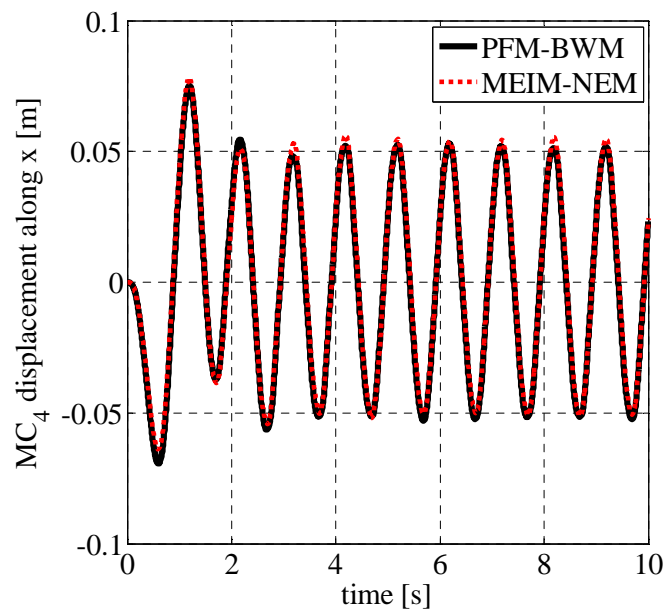


Figure 7.5. Acceleration time history of the base isolation system mass center in (a) x and (b) y directions.

(a)



(b)

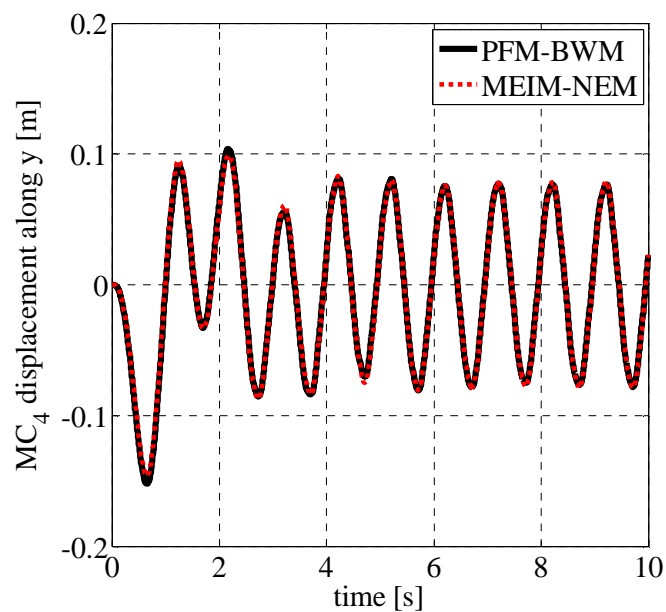
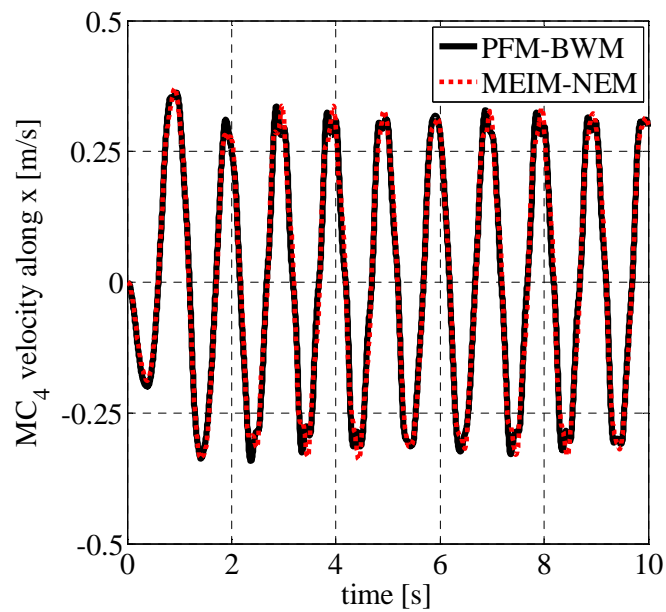


Figure 7.6. Displacement time history of the superstructure fourth story mass center in (a) x and (b) y directions.

(a)



(b)

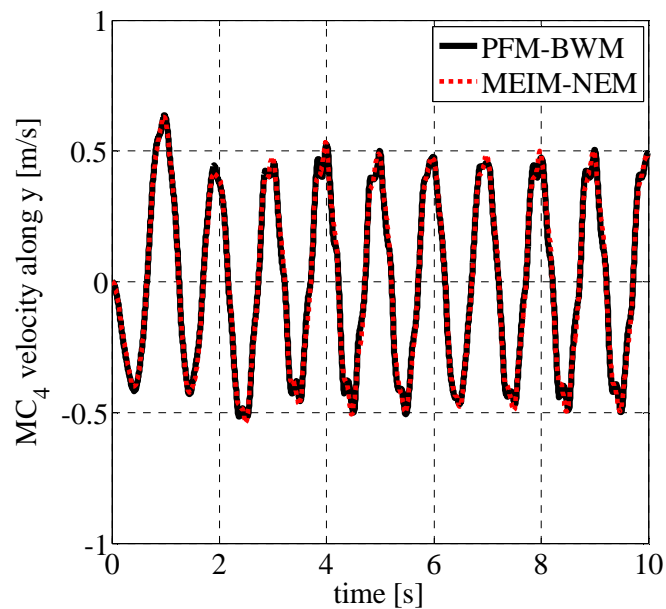
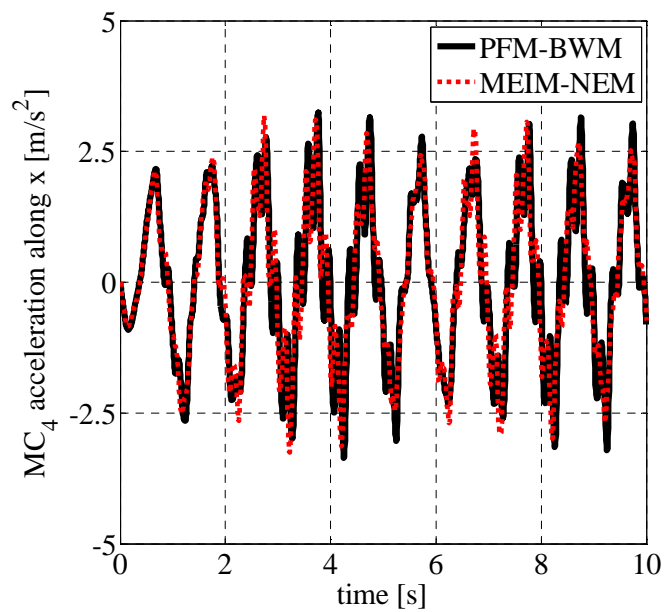


Figure 7.7. Velocity time history of the superstructure fourth story mass center in (a) x and (b) y directions.

(a)



(b)

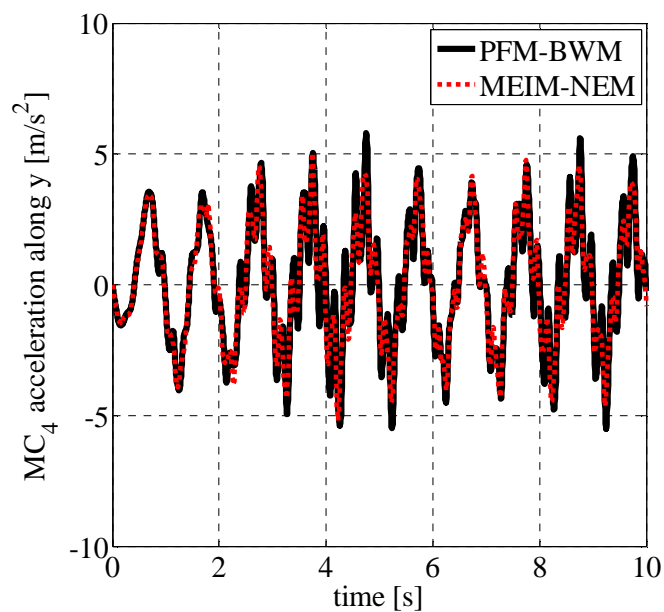
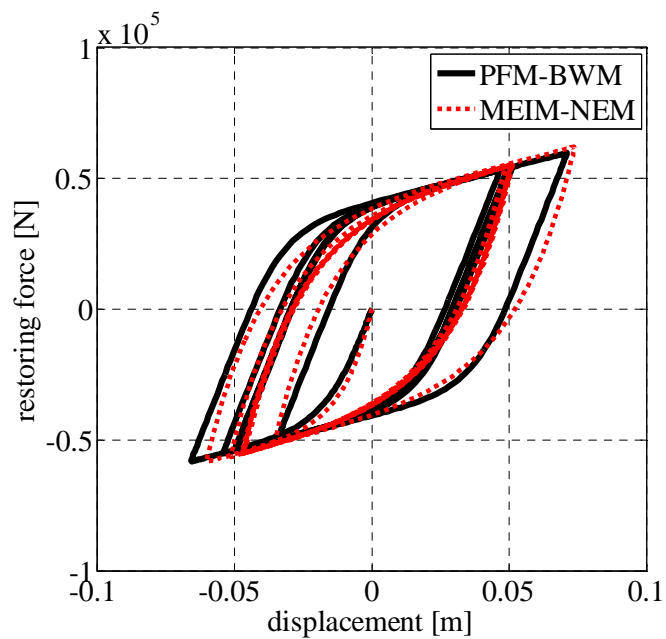


Figure 7.8. Acceleration time history of the superstructure fourth story mass center in (a) x and (b) y directions.

(a)



(b)

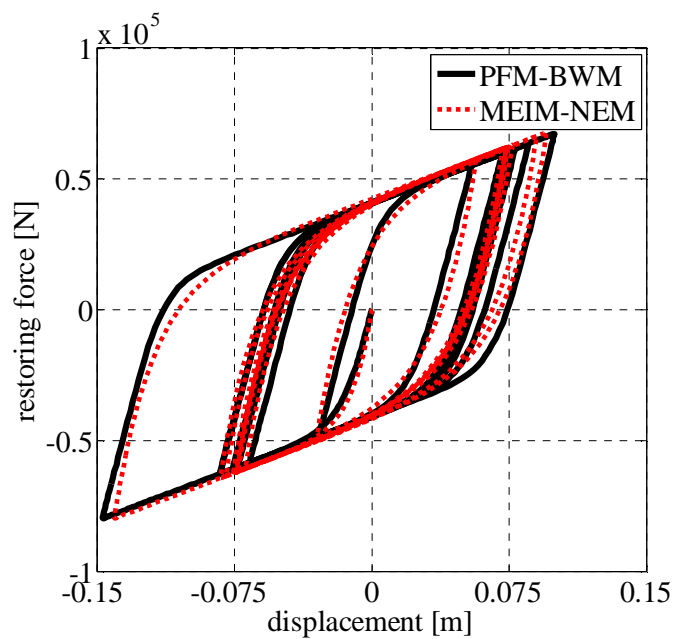
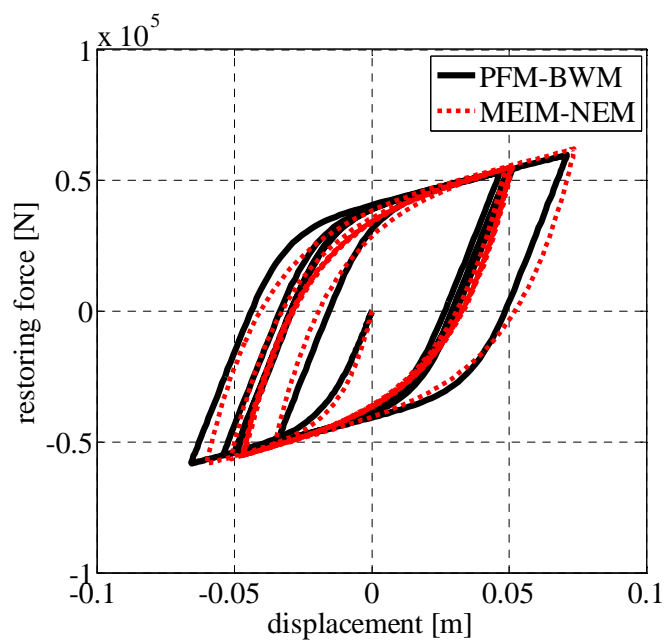


Figure 7.9. Hysteresis loop displayed by Isolator 1 in (a) x and (b) y directions.

(a)



(b)

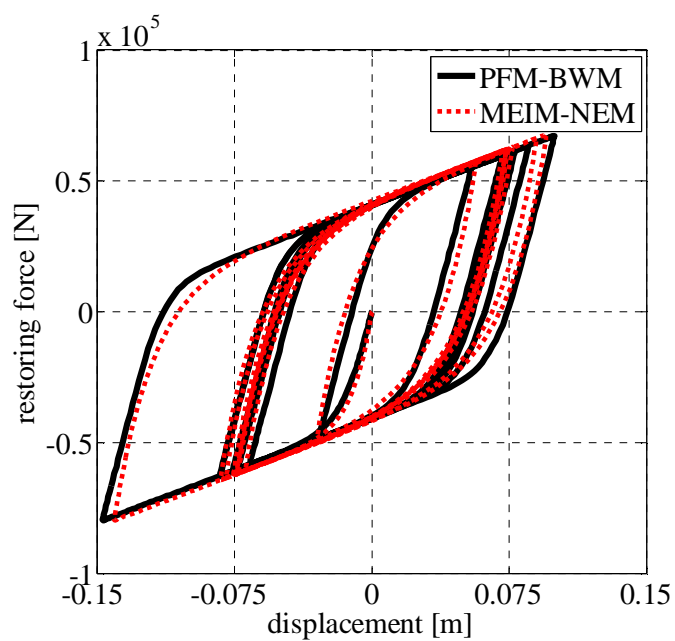


Figure 7.10. Hysteresis loop displayed by Isolator 11 in (a) x and (b) y directions.

Chapter 8

Conclusions

8.1 Summary of the Dissertation

In this dissertation, five mathematical models, namely, Nonlinear Exponential Model, Advanced Nonlinear Exponential Model, Parallel Model, Advanced Parallel Model, and 2d Parallel Model, and a Mixed Explicit-Implicit time integration Method have been proposed for the nonlinear time history analysis of seismically base-isolated structures with the main aim of simulating the nonlinear dynamic behavior of seismic isolators at both small and large displacements and reducing numerical computations making the nonlinear dynamic analysis almost as fast as a linear dynamic analysis.

8.1.1 Mathematical Models

The proposed Nonlinear Exponential Model (NEM) and Parallel Model (PM) are able to predict the dynamic behavior of seismic isolation devices displaying symmetric softening force-displacement loops with bilinear characteristics, such as elastomeric bearings and wire rope isolators, or rigid-plastic characteristics, such as sliding bearings, within a relatively large displacements range, generally reached under the design dynamic loading. The PM can be easily implemented in existing nonlinear finite element computer programs. Both models need only three parameters to be identified from experimental tests, whereas in the widely used uniaxial differential equation Bouc-Wen Model (BWM) the number of parameters to be identified is equal to seven for both elastomeric and sliding bearings and wire rope isolators. In addition, the presented models allow one to reduce the computational effort of a nonlinear time history analysis by avoiding, at each time step, the numerical solution of the first order nonlinear ordinary differential equation required by the BWM to evaluate the hysteretic variable.

The proposed Advanced Nonlinear Exponential Model (ANEM) and Advanced Parallel Model (APM), which are an improved version of the NEM and PM, respectively, can predict

the uniaxial dynamic response of seismic isolators having hardening or softening behavior at large displacements. The APM can be easily implemented in existing nonlinear finite element computer programs. Both models require the evaluation of only five model parameters whereas in the Modified Bouc-Wen Model (MBWM), described in 4.2.1.2, the number of parameters to be identified is equal to nine. Furthermore, the two proposed models are able to capture the smooth transition of the hysteresis loops from the small to the large displacements range using only one set of parameters evaluated from the experimental hysteresis loops with the largest amplitude. Compared to the MBWM, the proposed models do not require the numerical solution of a first order nonlinear ordinary differential equation at each time step of the analysis, thus decreasing the computational effort.

The experimental hysteresis loops obtained from cyclic dynamic tests, performed on four Wire Rope Isolators (WRIs) and a Recycled Rubber-Fiber Reinforced Bearing (RR-FRB), have been simulated adopting the presented models in order to demonstrate their accuracy. Good agreement between the experimental and numerical results has been obtained.

The proposed 2d Parallel Model (2d PM) is able to take into account the transverse biaxial interaction between the nonlinear hysteretic restoring forces along two orthogonal directions, within a relatively large displacements range. It can be easily implemented in existing nonlinear finite element computer programs. This model requires the evaluation of only five model parameters and, compared to the 2d BWM, it does not require the numerical solution of two coupled first order nonlinear ordinary differential equations at each time step of a nonlinear dynamic analysis.

8.1.2 Numerical Method

A Mixed Explicit-Implicit time integration Method (MEIM) has been proposed for predicting the nonlinear response of base-isolated structures subjected to earthquake excitation.

Adopting a partitioned solution approach, currently used in most practical civil engineering problems, the discrete structural model of a typical 3d base-isolated structure has been decomposed into two substructures, namely, the superstructure and the base isolation system. Being the base isolation system much more flexible than the superstructure to decouple the latter from the earthquake ground motion, an explicit conditionally stable time integration method, that is, the central difference method, has been employed to evaluate the nonlinear base isolation system response and an implicit unconditionally stable time integration method, that is, the Newmark's constant average acceleration method, has been adopted to predict the

linear superstructure response with the remarkable benefit of avoiding the iterative procedure within each time step of a nonlinear time history analysis required by conventional non-partitioned solution approaches.

In order to investigate the accuracy, the stability and the computational efficiency of the proposed method, the dynamic response of two 3d base-isolated structures, subjected to bidirectional earthquake excitation, has been analyzed using the MEIM. Two types of base isolation systems have been considered for both structures, namely, base isolation system with lead rubber bearings and base isolation system with friction pendulum bearings. The latter allowed one to investigate the use of the mixed time integration procedure in presence of isolators with very high initial stiffness. The accuracy and the computational efficiency of the proposed MEIM have been assessed by comparing the results with those obtained by using the solution algorithm specifically developed by Nagarajaiah et al. (1991) for the analysis of base-isolated structures. For brevity, in this dissertation, the latter implicit time integration method adopted in conjunction with the pseudo-force approach has been referred to as the Pseudo-Force Method (PFM).

From the numerical results presented in this thesis, the following conclusions can be drawn:

- as regards the accuracy, the proposed MEIM provides results that are close enough to those obtained adopting the PFM, for both two values of time step adopted in the nonlinear time history analyses of the selected 3d base-isolated structures. Both numerical methods, implemented on the same computer by using the computer program Matlab, have been verified using SAP2000;
- as far as the stability is concerned, the proposed MEIM is conditionally stable because the central difference method is employed to predict the nonlinear response of the base isolation system. The low stiffness value of the base isolation system with lead rubber bearings allows one to have a critical time step considerably larger than the imposed ground acceleration record time step. Furthermore, the critical time step continues to be larger than the ground acceleration time step also in the case of base isolation system with friction pendulum bearings in spite of their very high initial stiffness;
- regarding the computational efficiency, the total computational time, t_{ct} , required by the MEIM is significantly reduced in comparison to the PFM. In addition, the MEIM, performed with a smaller time step ($\Delta t = 0.001$ s), requires less computational effort than

the PFM even if the latter is performed using a larger time step ($\Delta t = 0.005$ s). It transpires that even when the critical time step size arising from stability requirements becomes smaller than the one used to accurately define the ground acceleration, as in the case of base isolation systems having isolators with very high initial stiffness (e.g., sliding bearings) or very high stiffness at large displacements (e.g., high damping rubber bearings), the proposed method preserves its computational efficiency with respect to conventional implicit time integration methods.

It follows that the proposed MEIM can be effectively adopted in the context of earthquake engineering structural applications being a very efficient solution approach for the nonlinear time history analysis of base-isolated structures under seismic loads.

8.1.3 Making the NLTHA almost as fast as a LTHA

The proposed MEIM and NEM have been adopted to perform the Nonlinear Time History Analysis (NLTHA) of a 3d seismically base-isolated structure with Lead Rubber Bearings (LRBs) in order to demonstrate the significant reduction of the computational effort which makes the NLTHA almost as fast as a Linear Time History Analysis (LTHA).

From the numerical results presented in this thesis, the following conclusions can be drawn:

- the presented MEIM and NEM provide results that are close enough to those obtained adopting the PFM and the BWM, for both time step values used in the NLTHAs of the analyzed 3d base-isolated structure with LRBs;
- the low stiffness value of the base isolation system with LRBs allows one to have a critical time step considerably larger than the imposed ground acceleration time step, thus avoiding stability problems in the MEIM;
- the tct required by the MEIM-NEM is significantly reduced in comparison to the PFM-BWM: the MEIM-NEM total computational time percentage, $tctp$, evaluated with respect to the PFM-BWM tct for a $\Delta t = 0.005$ s, is equal to 0.33 %. In addition, the MEIM-NEM, performed with a smaller time step, that is, $\Delta t = 0.001$ s, requires less computational effort than the PFM-BWM even if the latter is performed using the larger time step (i.e., $\Delta t = 0.005$ s): indeed, the MEIM-NEM $tctp$, referred to the PFM-BWM tct evaluated adopting $\Delta t = 0.005$ s, is equal to 1.53 %.

8.2 Recommendations for Future Research

8.2.1 Mathematical Models

In order to accurately predict the dynamic response of WRIs in the large displacements range, further work is required to improve the mathematical models, that is, ANEM and APM, by including a procedure of updating the parameters to specify the shape of the hysteresis curve according to the maximum displacement at the point of loading or unloading. In addition, further work is required in order to verify the proposed 2d PM by comparing the numerical results with those obtained experimentally.

8.2.2 Numerical Method

The proposed solution algorithm could be improved in order to take into account the nonlinear behavior of the superstructure, thus allowing one to analyze the response of base-isolated structures under extreme earthquake excitations. In addition, recently developed explicit and implicit time integration algorithms, such as those introduced by Noh and Bathe (2013) and Noh et al. (2013) for the analysis of wave propagation problems, could be adopted in the explicit and implicit substeps, respectively, in order to improve stability, accuracy and computational efficiency of the proposed partitioned solution approach.

References

Alessandri S, Giannini R, Paolacci F, Amoretti M and Freddo A (2015a) Seismic retrofitting of an HV circuit breaker using base isolation with wire ropes. Part 2: Shaking-table test validation. *Engineering Structures* 98: 263-274.

Alessandri S, Giannini R, Paolacci F and Malena M (2015b) Seismic retrofitting of an HV circuit breaker using base isolation with wire ropes. Part 1: Preliminary tests and analyses. *Engineering Structures* 98: 251-262.

Alhan C and Gavin H (2004) A parametric study of linear and non-linear passively damped seismic isolation systems for buildings. *Engineering Structures* 26: 485-497.

Asher JW, Van Volkinburg DR, Mayes R, Kelly RL, Sveinsson BI and Hussain S (1990) Seismic isolation design of the USC university hospital. Proceedings of the 4th US National Conference on Earthquake Engineering, California, USA.

Bathe KJ (1996) *Finite Element Procedures*. Prentice Hall, Englewood Cliffs, NJ, USA.

Belytschko T, Yen HJ and Mullen R (1979) Mixed methods for time integration. *Computer Methods in Applied Mechanics and Engineering* 17(18): 259-275.

Bouc R (1971) Modele mathematique d'hysteresis. *Acustica* 24: 16-25.

Bozorgnia Y and Bertero VV (2004) *Earthquake Engineering: From Engineering Seismology to Performance-Based Engineering*. CRC Press, New York, NY, USA.

Brun M, Batti A, Limam A and Gravouil A (2012) Explicit/implicit multi-time step co-computations for blast analyses on a reinforced concrete frame structure. *Finite Elements in Analysis and Design* 52: 41-59.

Built SM (1982) Lead-rubber dissipators for the base isolation of bridge structures. Report No. 289, Department of Civil Engineering, University of Auckland, New Zealand.

References

Calabrese A, Serino G, Strano S and Terzo M (2013) Investigation of the seismic performances of an FRBs base isolated steel frame through hybrid testing. Proceedings of the World Congress on Engineering, London, UK.

Cheng M (1988) Convergence and stability of step by step integration for model with negative stiffness. *Earthquake Engineering and Structural Dynamics* 16(1): 227-244.

Chopra AK (2012) *Dynamics of Structures: Theory and Applications to Earthquake Engineering*, 4th edn. Prentice Hall, Englewood Cliffs, NJ, USA.

Combescure A and Gravouil A (2002) A numerical scheme to couple subdomains with different time-steps for predominantly linear transient analysis. *Computer Methods in Applied Mechanics and Engineering* 191: 1129-1157.

Constantinou MC and Adnane MA (1987) Dynamics of soil-base-isolated-structure systems: evaluation of two models for yielding systems. Report No. 4 to NSF, Drexel University, Philadelphia, PA, USA.

Constantinou MC, Mokha A and Reinhorn AM (1990) Teflon bearings in base isolation II: Modeling. *Journal of Structural Engineering ASCE* 116(2): 455-474.

Constantinou MC, Whittaker AS, Kalpakidis Y, Fenz DM and Warn GP (2007) Performance of seismic isolation hardware under service and seismic loading. Report No. MCEER-07-0012, State University of New York, Buffalo, NY, USA.

D'Acunto B (2012) *Computational Partial Differential Equations for Engineering Science*. Nova Science Publishers, New York, NY, USA.

Demetriades GF, Constantinou MC and Reinhorn AM (1993) Study of wire rope systems for seismic protection of equipment in buildings. *Engineering Structures* 15(5): 321-334.

Di Donna M and Serino G (2002) Base isolation of high-voltage equipment: comparison between two different solutions. Proceedings of the 7th International Conference on Probabilistic Methods Applied to Power Systems, Napoli, Italy.

Dokainish MA and Subbaraj K (1989a) A survey of direct time-integration methods in computational structural dynamics - I. Explicit methods. *Computers and Structures* 32(6): 1371-1386.

References

Dokainish MA and Subbaraj K (1989b) A Survey of direct time-integration methods in computational structural dynamics - II. Implicit methods. *Computers and Structures* 32(6): 1387-1401.

Farhat C, Crivelli L and Roux FX (1994) A transient FETI methodology for large-scale parallel implicit computations in structural mechanics. *International Journal for Numerical Methods in Engineering* 37: 1945-1975.

Farhat C and Roux FX (1991) A method of finite element tearing and interconnecting and its parallel solution algorithm. *International Journal for Numerical Methods in Engineering* 32: 1205-1227.

Felippa CA, Park KC and Farhat C (2001) Partitioned analysis of coupled mechanical systems. *Computer Methods in Applied Mechanics and Engineering* 190: 3247-3270.

Gravouil A and Combescure A (2001) Multi-time-step explicit-implicit method for non-linear structural dynamics. *International Journal for Numerical Methods in Engineering* 50: 199-225.

Hills DA (1971) *Heat Transfer and Vulcanization of Rubber*. Elsevier, London, UK.

Herry B, Di Valentin L and Combescure A (2002) An approach to the connection between subdomains with non-matching meshes for transient mechanical analysis. *International Journal for Numerical Methods in Engineering* 55: 973-1003.

Huang WH (2002) Bi-directional testing, modeling, and system response of seismically isolated bridges. Ph.D. Thesis, University of California, Berkeley, CA, USA.

Huang WH, Fenves GL, Whittaker AS and Mahin SA (2000) Characterization of seismic isolation bearings from bidirectional testing. *Proceedings of the 12th World Conference on Earthquake Engineering*, Auckland, New Zealand.

Hughes TJR and Liu WK (1978) Implicit-explicit finite elements in transient analysis: implementation and numerical examples. *Journal of Applied Mechanics* 45: 375-378.

Hwang JS, Wu JD, Pan TC and Yang G (2002) A mathematical hysteretic model for elastomeric isolation bearings. *Earthquake Engineering and Structural Dynamics* 31: 771-789.

References

Jangid RS and Datta TK (1995) Performance of base isolation systems for asymmetric building subject to random excitation. *Engineering Structures* 17(6): 443-454.

Kelly JM (1997) *Earthquake-resistant Design with Rubber*. Springer-Verlag, London, UK.

Kelly JM and Konstantinidis D (2007) Low-cost seismic isolators for housing in highly-seismic developing countries. *Proceedings of the 10th World Conference on Seismic Isolation, Energy Dissipation and Active Vibrations Control of Structures*, Istanbul, Turkey.

Kelly JM and Takhirov SM (2001) Analytical and experimental study of fiber-reinforced elastomeric isolators. PEER Report 2001/11, University of California, Berkeley, CA, USA.

Kelly JM and Takhirov SM (2002) Analytical and experimental study of fiber-reinforced strip isolators. PEER Report 2002/11, University of California, Berkeley, CA, USA.

Kikuchi M and Aiken ID (1997) An analytical hysteresis model for elastomeric seismic isolation bearings. *Earthquake Engineering and Structural Dynamics* 26: 215-231.

Krieg RD (1973) Unconditional stability in numerical time integration methods. *Journal of Applied Mechanics* 40: 417-421.

Mokha A, Constantinou MC and Reinhorn AM (1991) Further results on frictional properties of teflon bearings. *Journal of Structural Engineering ASCE* 117(2): 622-626.

Mordini A and Strauss A (2008) An innovative earthquake isolation system using fibre reinforced rubber bearings. *Engineering Structures* 30: 2739-2751.

Mroz A (1963) Non-associated flow rules in plasticity. *Journal de Mecanique* 2: 21-42.

Muscolino G (1990) Dynamic response of multiply connected primary-secondary systems. *Earthquake Engineering and Structural Dynamics* 19: 205-216.

Naeim F (2001) *The Seismic Design Handbook*, 2nd edn. Springer Science+Business Media, New York, NY, USA.

Naeim F and Kelly JM (1999) *Design of Seismic Isolated Structures: From Theory to Practice*. John Wiley and Sons Inc, Hoboken, NJ, USA.

Nagarajaiah S, Reinhorn AM and Constantinou MC (1989) Nonlinear dynamic analysis of three dimensional base isolated structures (3DBASIS). Report No. NCEER-89-0019, National

References

Center for Earthquake Engineering Research, State University of New York, Buffalo, NY, USA.

Nagarajaiah S, Reinhorn AM and Constantinou MC (1991) Nonlinear dynamic analysis of 3-D base-isolated structures. *Journal of Structural Engineering ASCE* 117(7): 2035-2054.

Nelson RB and Dorfmann A (1995) Parallel elastoplastic models of inelastic material behavior. *Journal of Engineering Mechanics ASCE* 121(10): 1089-1097.

Ni YQ, Ko JM, Wong CW and Zhan S (1999) Modelling and identification of a wire-cable vibration isolator via a cyclic loading test. Part 1: experiments and model development. *Journal of Systems and Control Engineering* 213(I3): 163-171.

Noh G and Bathe KJ (2013) An explicit time integration scheme for the analysis of wave propagations. *Computers and Structures* 129: 178-193.

Noh G, Ham S and Bathe KJ (2013) Performance of an implicit time integration scheme in the analysis of wave propagations. *Computers and Structures* 123: 93-105.

Owen DRJ, Prakash A and Zienkiewicz OC (1974) Finite element analysis of non-linear composite materials by use of overlay systems. *Computer and Structures* 4: 1251-1267.

Ozdemir H (1976) Nonlinear transient dynamic analysis of yielding structures. Ph.D. Thesis, University of California, Berkeley, CA, USA.

Pagano S, Russo R, Strano S and Terzo M (2013) Non-linear modelling and optimal control of a hydraulically actuated seismic isolator test rig. *Mechanical Systems and Signal Processing* 35(1-2): 255-278.

Pagano S, Russo M, Strano S and Terzo M (2014) A mixed approach for the control of a testing equipment employed for earthquake isolation systems. *Journal of Mechanical Engineering Science* 228(2): 246-261.

Pande GN, Owen DRJ and Zienkiewicz OC (1977) Overlay models in time-dependent nonlinear material analysis. *Computer and Structures* 7: 435-443.

Park YJ, Wen YK and Ang AHS (1986) Random vibration of hysteretic systems under bi-directional ground motions. *Earthquake Engineering and Structural Dynamics* 14: 543-557.

References

Pezeshk S and Camp CV (1995) An explicit time integration technique for dynamics analyses. *International Journal for Numerical Methods in Engineering* 38: 2265-2281.

Piersol AG and Paez TL (2009) *Harris' Shock and Vibration Handbook*, 6th edn. McGraw-Hill, New York, NY, USA.

Quarteroni A (2014) *Numerical Models for Differential Problems*, 2nd edn. Springer-Verlag, Milano, Italy.

Quarteroni A and Valli A (1999) *Domain Decomposition Methods for Partial Differential Equations*. Oxford Science Publications, Oxford, UK.

Rosenbrock HH (1963) Some general implicit processes for the numerical solution of differential equations. *Computing Journal* 5:329-330.

Russo G and Pauletta M (2013) Sliding instability of fiber-reinforced elastomeric isolators in unbonded application. *Engineering Structures* 48: 70-80.

Russo G, Pauletta M and Cortesia A (2013) A study on experimental shear behaviour of fiber-reinforced elastomeric isolators with various fiber layouts, elastomers and aging conditions. *Engineering and Structures* 52: 422-33.

Russo G, Pauletta M, Cortesia A and Dal Bianco A (2008) Experimental behavior of carbon fiber reinforced isolators. *Proceedings of the 2008 Seismic Engineering International Conference Commemorating the 1908 Messina and Reggio Calabria Earthquake*, Reggio Calabria, Italy.

Serino G, Bettinali F and Bonacina G (1995a) Seismic base isolation of gas insulated electrical substations: comparison among different solutions. *Proceedings of the 4th US Conference Sponsored by the ASCE Technical Council on Lifeline Earthquake Engineering*, San Francisco, CA, USA.

Serino G, Bonacina G and Bettinali F (1995b) Passive protection devices for high-voltage equipment: design procedures and performance evaluation. *Proceedings of the 4th US Conference Sponsored by the ASCE Technical Council on Lifeline Earthquake Engineering*, San Francisco, CA, USA.

References

Spizzuoco M, Calabrese A and Serino G (2014) Innovative low-cost recycled rubber-fiber reinforced isolator: experimental tests and finite element analyses. *Engineering Structures* 76: 99-111.

Spizzuoco M, Quaglini V, Calabrese A, Serino G and Zambrano C (2016) Study of wire rope devices for improving the re-centering capability of base isolated buildings. *Structural Control and Health Monitoring*, in press, ISSN: 15452255, DOI: 10.1002/stc.1928.

Strano S and Terzo M (2014) A multi-purpose seismic test rig control via a sliding mode approach. *Structural Control and Health Monitoring* 21: 1193-1207.

Tarics AG, Way D and Kelly JM (1984) The implementation of base isolation for the foothill communities law and justice center. Report to the National Science Foundation.

Tinker ML and Cutchins MA (1992) Damping phenomena in a wire rope vibration isolation system. *Journal of Sound and Vibration* 157(1): 7-18.

Toopchi-Nezhad H, Tait MJ and Drysdale RG (2007) Testing and modeling of square carbon fiber -reinforced elastomeric seismic isolators. *Structural Control and Health Monitoring* 15(6): 876-900.

Toopchi-Nezhad H, Tait MJ and Drysdale RG (2008) Lateral response evaluation of fiber-reinforced neoprene seismic isolators utilized in an unbonded application. *Journal of Structural Engineering ASCE* 134(10): 1627-1638.

Toopchi-Nezhad H, Tait MJ and Drysdale RG (2009) Shake table study on an ordinary low-rise building seismically isolated with SU-FREIs (stable unbonded fiber-reinforced elastomeric isolators). *Earthquake Engineering and Structural Dynamics* 38(11): 1335-1357.

Toopchi-Nezhad H, Tait MJ and Drysdale RG (2011) Bonded versus unbonded strip fiber reinforced elastomeric isolators: finite element analysis. *Composite Structures* 93: 850-859.

Tsai CS, Chiang TC, Chen BJ and Lin SB (2003) An advanced analytical model for high damping rubber bearings. *Earthquake Engineering and Structural Dynamics* 32: 1373-1387.

Tsopelas PC, Roussis PC, Constantinou MC, Buchanan R and Reinhorn AM (2005) 3D-BASIS-ME-MB: Computer program for nonlinear dynamic analysis of seismically isolated structures. Report No. MCEER-05-0009, State University of New York, Buffalo, NY, USA.

References

Vaiana N, Filippou FC and Serino G (2017a) Nonlinear dynamic analysis of base-isolated structures using a partitioned solution approach and an exponential model. Proceedings of the 19th International Conference on Earthquake and Structural Engineering, London, UK.

Vaiana N, Filippou FC and Serino G (2017b) Nonlinear dynamic analysis of base-isolated structures using a mixed integration method: stability aspects and computational efficiency. Proceedings of the 19th International Conference on Earthquake Engineering, Barcelona, Spain.

Vaiana N and Serino G (2017a) Simulation of dynamic behavior of seismic isolators using a parallel elasto-plastic model. Proceedings of the 19th International Conference on Earthquake and Structural Engineering, London, UK.

Vaiana N and Serino G (2017b) An advanced exponential model for seismic isolators having hardening or softening behavior at large displacements. Proceedings of the 19th International Conference on Earthquake Engineering, Barcelona, Spain.

Vaiana N and Serino G (2017c) Speeding up nonlinear time history analysis of base-isolated structures using a nonlinear exponential model. Proceedings of the 19th International Conference on Earthquake Engineering, Barcelona, Spain.

Vaiana N, Spizzuoco M and Serino G (2016) A parallel model for predicting the horizontal dynamic behavior of helical wire rope isolators. Proceedings of the 4th International Conference on Advances in Civil, Structural and Environmental Engineering, Rome, Italy.

Vaiana N, Spizzuoco M and Serino G (2017c) Influence of displacement amplitude and vertical load on the horizontal dynamic and static behavior of helical wire rope isolators. Proceedings of the 19th International Conference on Earthquake and Structural Engineering, London, UK.

Vaiana N, Spizzuoco M and Serino G (2017d) Wire rope isolators for seismically base-isolated lightweight structures: experimental characterization and mathematical modeling. *Engineering Structures* 140: 498-514.

Way D and Jeng V (1989) N-Pad, A three-dimensional program for the analysis of base isolated structures. Proceedings of American Society of Civil Engineers Structures Congress, San Francisco, CA, USA.

References

Wen YK (1976) Method for random vibration of hysteretic systems. *Journal of the Engineering Mechanics Division* 102(EM2): 249-263.

Wen YK (1980) Equivalent linearization for hysteretic systems under random excitation. *Journal of Applied Mechanics* 47: 150-154.

Wilson EL (2002) *Three-Dimensional Static and Dynamic Analysis of Structures*, 3rd edn. Computers and Structures Inc, Berkeley, CA, USA.

Wu YS and Smolinski P (2000) A multi-time step integration algorithm for structural dynamics based on the modified trapezoidal rule. *Computer Methods in Applied Mechanics and Engineering* 187: 641-660.